

Some pages of this thesis may have been removed for copyright restrictions.

If you have discovered material in AURA which is unlawful e.g. breaches copyright, (either yours or that of a third party) or any other law, including but not limited to those relating to patent, trademark, confidentiality, data protection, obscenity, defamation, libel, then please read our [Takedown Policy](#) and [contact the service](#) immediately

Various Techniques and Procedures for Refining ERS-1 Orbits

Simon Ehlers

Doctor of Philosophy

The University of Aston in Birmingham

December 1993

This copy of the thesis has been supplied on condition that anyone who consults it is understood to recognise that its copyright rests with its author and that no quotation from this thesis and no information derived from it may be published without proper acknowledgement.

The University of Aston in Birmingham
Various Techniques and Procedures for Refining ERS-1 Orbits

Simon Ehlers

Doctor of Philosophy

December 1993

The satellite ERS-1 was launched in July 1991 in a period of high solar activity. Sparse laser tracking and the failure of the experimental microwave system (PRARE) compounded the orbital errors which resulted from mismodelling of atmospheric density and hence surface forces.

Three attempts are presented here to try and refine the coarse laser orbits of ERS-1, made prior to the availability of the full altimetric dataset. The results of the first attempt indicate that by geometrically modelling the satellite shape some improvement in orbital precision may be made for *any* satellite; especially one where no area tables already exist. The second and third refinement attempts are based on the introduction of data from some second satellite; in these examples SPOT-2 and TOPEX/Poseidon are employed.

With SPOT-2 the method makes use of the orbital similarities to produce along-track corrections for the more fully tracked SPOT-2. Transferring these corrections to ERS-1 produces improvements in the precise orbits thus determined. With TOPEX/Poseidon the greater altitude results in a more precise orbit (gravity field and atmospheric errors are of less importance). Thus, by computing height differences at crossover points of the TOPEX/Poseidon and ERS-1 ground tracks the poorer orbit of ERS-1 may be improved by the addition of derived radial corrections.

In the positive light of all three results several potential modifications are suggested and some further avenues of investigation indicated.

Keywords:

- skin-surface forces,
- along-track acceleration corrections,
- dual-crossovers,
- SPOT-2,
- TOPEX/Poseidon.

for Joanna

Acknowledgements

I wish to thank Andrew Sinclair and Graham Appleby of the Royal Greenwich Observatory (UK) for providing processed laser normal points, station coordinates, flux, geomagnetic and polar motion information, planetary positions and other necessary data. The dependence of this work on such data cannot be overstressed. My thanks also, to the Centre National d'Etudes Spatiales (France) for the SPOT-2 DORIS Doppler data and required associated information and to SERC/MoD for funding the research. Finally, thankyou to Philip Moore, for the combination of patience and persistence which ensured the completion of the work described herein.

Contents

Thesis Summary	2
Dedication	3
Acknowledgements	4
Contents	5
List of Figures	8
List of Tables	11
1 Introduction	13
2 Precise Orbit Determination	17
2.1 Stating the problem and summarizing the solution	17
2.2 The force model	18
2.2.1 The earth's gravitational potential	18
2.2.2 Solid earth and ocean tides	19
2.2.3 Third body attraction	20
2.2.4 Atmospheric drag and lift	21
2.2.5 Direct solar radiation pressure	22
2.2.6 Earth reflected albedo and infra-red forces	23
2.3 Least squares minimisation	24
2.4 Integrating the force model	27
2.5 Saw-tooth drag modifications	30
2.6 Station coordinates	34

3	Surface Force Modelling	36
3.1	Errors in modelled surface-forces	36
3.2	Surface forces considered in terms of the momentum exchanged .	38
3.2.1	Direct solar radiation pressure	38
3.2.2	Free molecular aerodynamics	41
3.3	The GUESS area-table software	45
3.4	Evaluation of the area tables: theory	47
3.5	Further developments	53
3.6	Verification of the GUESS software	55
4	ERS-1 orbits	56
4.1	The ERS-1 satellite	56
4.2	A geometric model of ERS-1	59
4.3	Area tables for ERS-1	63
4.4	Precise orbit determinations for ERS-1 using GUESS tables . . .	68
5	Long-Arc Refinement using Dual-Crossover Data	78
5.1	Non-dynamic long-arc refinement	78
5.2	Altimetry and dual-crossovers	78
5.3	Simulating the crossover data	80
5.4	The determination of an analytic expression for the radial error .	91
5.5	Method of solution	100
5.6	Modifications to the solution procedure	104
5.7	Discussion of results	107
5.8	Conclusions	118
6	Tracking the French satellite SPOT-2	120
6.1	Introducing the next two chapters	120
6.2	SPOT-2 and the DORIS system	121
6.3	The Doppler effect and beats: some theory	124
6.4	Amending the SATAN-A package	128
6.5	Producing area tables for SPOT-2	135
6.6	Precise orbit determinations for SPOT-2	140

7	Improving ERS-1 orbits with SPOT-2 tracking data	147
7.1	Correcting for density mismodelling	147
7.2	Along-track acceleration corrections	149
7.3	Application of the above method to some SPOT-2 long-arcs	152
7.4	Employing these SPOT-2 corrections within ERS-1 orbits	162
8	Conclusions	168
8.1	Modifications to the SATAN-A suite	168
8.2	A re-iteration of the main results obtained	169
8.3	Directions of future work	171
	Bibliography	174

List of Figures

2.1	The three body system.	21
2.2	An example of the step function for drag scale factors over the period MJD 48687 to MJD 48692.	31
2.3	The saw-tooth approach to computing drag scale factors over the period MJD 48464.8 to MJD 48470.8.	33
3.1	Incident and post-impact solar flux on a plane surface.	39
3.2	Force from a single aerodynamic particle on a flat plate.	41
3.3	The incident velocity \underline{u} and the Cartesian system for the particular velocity $\underline{\omega}$	42
3.4	The satellite-fixed coordinate system.	46
3.5	The angles defining both the sun position (α, β) and the incident flux vector (γ, δ)	48
3.6	Enclosing the projected surface elements in boxes within the projective $OX_V OY_V$ -plane.	49
3.7	The wedge associated with a projected surface element and the angles θ, ϕ, ψ and Ω	50
3.8	The vector equation for a point on the edge of a triangle.	51
4.1	The network of laser stations ranging to ERS-1.	57
4.2	The ERS-1 satellite.	58
4.3	The ERS-1 model and satellite-fixed coordinate system.	60
4.4	Satellite-fixed and axial systems for ERS-1.	61
4.5	Region of interest for the aerodynamic flux incident on ERS-1.	66
4.6	An example of the variation in the effective cross-sectional area of ERS-1 over part of the long-arc from MJD 48628 to MJD 48633.	70

4.7	The converged drag-scale factors with and without GUESS tables for a selection of the long-arcs considered.	76
5.1	A comparison of simulated true and perturbed ephemerides for the satellite TOPEX/Poseidon.	83
5.2	A comparison of simulated true and perturbed ephemerides for the satellite ERS-1.	84
5.3	Geometric estimation of a dual-crossover point (Northern hemisphere, ERS-1 descending arc).	86
5.4	Geographic location of simulated single-crossovers over the oceans for ERS-1.	90
5.5	Geographic location of simulated single-crossovers over the oceans for TOPEX/Poseidon.	90
5.6	Geographic location of simulated dual-crossovers over the oceans for ERS-1 and TOPEX/Poseidon.	91
5.7	Computation of the length of arc U	103
5.8	Some of the higher standard errors for the solution S3, prior to suppressing the parameter C_2^T	109
5.9	ERS-1 radial residuals after correction for the solution S1.	111
5.10	The highest standard errors for solutions to ERS-1 parameters.	111
5.11	ERS-1 radial residuals after correction for the solution S2.	112
5.12	ERS-1 radial residuals after correction for the solution S3.	113
5.13	TOPEX/Poseidon radial residuals after correction, for the solution S3.	114
5.14	The highest standard errors for the simultaneous solutions.	114
5.15	Illustrating the triangular weighting procedure.	116
5.16	ERS-1 radial residuals after correction, for constrained version of the solution S2.	117
5.17	ERS-1 radial residuals after correction, for constrained version of the solution S3.	118
6.1	The SPOT-2 satellite.	122
6.2	Positioning and coverage of DORIS orbit determination beacons by February 1992.	123

6.3	The Doppler effect.	125
6.4	An example illustrating how two frequencies may interact to produce beats.	126
6.5	The satellite-beacon range vector.	128
6.6	The geometric model of SPOT-2 in the satellite-fixed system.	136
6.7	Solar Flux F10.7 for May 1990 and January and February 1992, emphasizing the converged long-arc periods.	141
6.8	Geomagnetic indices for May 1990 and January and February 1992, emphasizing the converged long-arc periods.	142
6.9	Drag-scale factors, C_D , for the eight SPOT-2 long-arcs considered.	145
7.1	Example slope for a single pass of range-rate residuals.	151
7.2	All $(\bar{l}, \Delta T)$ pairs, over three converged five-day SPOT-2 long-arcs.	154
7.3	Smoothed $(\bar{l}, \Delta T)$ pairs, over the same three arcs.	157
7.4	Detail of smoothed data showing single versus spliced polynomial fits from the SPOT-2 arc of MJD 48628 to MJD 48633.	158
7.5	Expected corrections, using area tables, with computed solution, for the three SPOT-2 arcs.	159
7.6	Comparison of expected corrections obtained with and without the use of GUESS tables from the arc starting on MJD 48628.	160
7.7	C_D values for SPOT-2.	163

List of Tables

4.1	Cross sectional area for ERS-1 (in square metres) as viewed from the sun.	65
4.2	Cross sectional area for ERS-1 (in square metres) as viewed along the incident aerodynamic flux vector.	67
4.3	Solution details for converged ERS-1 long-arcs, July to October inclusive, 1991.	71
4.4	The Root Mean Square of fit (in centimetres) for the converged ERS-1 long-arcs by solution method and geographical location. . .	73
4.5	The value of the solar radiation coefficient, C_{R_s} , solved for both with and without GUESS generated tables.	74
5.1	Numbers of laser-range passes and observations for ERS-1 between MJD 48500 and MJD 48506.	82
5.2	Summary of simulated crossover data used.	89
5.3	RMS of fit of the calculated radial error, from the unconstrained solutions, to the simulated values.	110
5.4	RMS of fit of the calculated radial error, from the constrained solutions, to the simulated values.	117
6.1	Cross sectional area for SPOT-2 (in square metres) as viewed from the sun.	137
6.2	Cross sectional area for SPOT-2 (in square metres) as viewed along the incident aerodynamic flux vector.	138
6.3	Solution details for converged SPOT-2 long-arcs, May 1990 and January and February 1992.	140
6.4	The Root Mean Square of fit for the SPOT-2 long-arcs both with and without GUESS generated tables in millimetres per second. .	143

6.5	The value of the solar radiation coefficient, C_R , solved for both with and without GUESS generated tables.	144
7.1	Summary of contributing stations, passes and range-rate measurements from SPOT-2.	153
7.2	RMS of orbital fits for SPOT-2 (millimetres/second).	161
7.3	Summary of contributing stations, passes and SLR measurements from ERS-1.	162
7.4	RMS of orbital fits for ERS-1 (centimetres), using only SLR tracking data in the convergence process.	164
7.5	RMS of fit of altimetry and crossover data for ERS-1 (centimetres) for the original converged orbits.	166

Chapter 1

Introduction

Data generated by earth satellites is very diverse, being concerned both with the physical environment of the satellite, and with returning information about the earth around which the satellites orbit. Thus, topics covered include atmospheric studies, the measurement of the earth's magnetic field, topographical images, altimetric information for use in mapping, oceanic studies and other geodetic projects. There is a certain teleological element to much of this though, since in order to fully utilise this information, a precise determination of the satellite's position is required. Therefore, as the knowledge of the earth's shape and structure, as evinced by the gravity field, increases so does the accuracy with which the orbit may be computed. Similarly, as the orbital accuracy increases, so does that of the physical constants (for instance the gravity field coefficients).

In addition to the accuracy of the physical constants, the quality of any precise orbit determination rests upon the accuracy of the model used to plot the course of the satellite; by far the most common approach being to fit the model to the observation data by means of some weighted linear least squares minimisation technique. Currently, this model is relatively weakest in the areas of atmospheric density and satellite-atmospheric reactions [Renard, 1990]. This is largely due to the difficulty in either accurately measuring atmospheric density and particle-surface interactions at the satellite, or correctly simulating the conditions attained at these locations within the laboratory situation. This weakness is *relative* since it is only recently [Klinkrad *et al.*, 1990] that the gravitational component has been recovered accurately enough so that errors in it are now lower than the magnitudes of lesser forces, such as drag and solar radiation pressure. However,

now that such accuracy is attainable in the gravity field, it becomes necessary to either improve on atmospheric models or to somehow circumvent the need for such improvements.

The aim of this thesis is to address these relative weaknesses by considering the specific case of the satellite ERS-1. ERS-1 orbits suffer particularly both from deficiencies in the thermospheric models currently used to determine atmospheric density and from a general sparsity of and geographical bias in the tracking data. In this thesis, three distinct but potentially combinable methods are considered, in order to see if they offer ways of refining the initially poor ERS-1 long-arcs orbits. In the first of these, the simple drag model currently used is modified to take account of surface-interaction coefficients in a more complex momentum-exchange based model. In contrast to this, both the second and third approaches differ from the first in that they do not directly improve the orbital determination model, but rather suggest ways of introducing information from some second satellite into the orbital procedure. In each case the second satellite is more densely tracked than ERS-1 and possesses other differences which make it suitable for the chosen method. Thus, the second method uses height differences with TOPEX/Poseidon which, at an altitude of some 1335 km, is far less affected by the atmosphere; avoiding the inherent weakness in thermospheric models. In contrast, the third method employs the SPOT-2 satellite, which is in a similar orbit to ERS-1 but does not suffer from the sparse and geographically biased tracking which troubles ERS-1.

In order to allow these methods to be developed, the main body of the thesis begins in Chapter 2 with a description of the orbit determination model employed at ASTON. It must be recognised that this model is continually undergoing minor alterations, as subroutines are updated and the modifications required by each new satellites are included. However, the overall technique does not change and the model employed remains basically the same.

Having elaborated upon the existing model, the first refinement method is described and tested in Chapters 3 and 4 respectively. The former contains the theory which elaborates the necessary equations for the forces due to both atmospheric resistance and direct solar pressure. Further, it includes a full description of the method of determining satellite area tables which may be used to com-

pute the surface areas required by these equations. This theory is then used to produce the GUESS software which is used for generating the tables required by the amended orbital determination routine. Chapter 4 begins by applying this software to ERS-1 and then continues with a description of the modifications to the orbital package necessary to employ the GUESS tables. The latter half of the chapter then considers several long-arc orbits, comparing the results obtained between the original and modified approaches.

The second refinement technique is described in Chapter 5, along with the results of its application to ERS-1 and TOPEX/Poseidon. However, since the latter satellite had not been launched at the time of the study, simulated data is employed throughout. Two orbital ephemeris are determined, one for ERS-1 and one for TOPEX/Poseidon, from which the height differences are computed at points where the two ground-tracks intersect. Two such simulated sets are used — one representing the observation data (which would be derived from actual altimeter measurements) and the other the calculated values (as obtained from the orbital model). The differences between these are then considered as a measure of the radial error in the two orbits. Whence, by writing the radial error as a harmonic expansion, it is possible to solve for the harmonic coefficients. These in turn allow for correction terms to be determined for both satellites at specific times. By adding such terms to the orbit of the relevant satellite, a refined or corrected orbit may be obtained. Where, as in this case, the orbit of the additional satellite is much superior to that of ERS-1, it is hoped that the orbital accuracy of the worse orbit may be improved to the order of the better one.

The third and final method is covered in Chapter 7. However, prior to this, Chapter 6 first describes both SPOT-2 and its tracking system, together with the modifications required to determine orbits for this satellite. In addition, this chapter contains the results of running the GUESS software to produce area tables for SPOT-2 as well as the results of converging several orbits both with and without these tables. Chapter 7 continues by developing the method of determining along-track acceleration corrections from SPOT-2, following an idea of Ridgway *et al.* [1990]. Then the method is tested for three long-arcs where data was available for both ERS-1 and SPOT-2.

Having considered all three approaches and the results obtained, it is then

possible to suggest where further development or testing of each method may be useful. In addition, some overall assessment of just how much each technique can contribute to improving poor orbits may be made, at least in the case of the satellite ERS-1.

Chapter 2

Precise Orbit Determination

2.1 Stating the problem and summarizing the solution

The problem of precise orbit determination is to determine the path of an Earth satellite by modelling its motion from estimated parameters, such as initial position and velocity, and observed data, for instance solar flux and geomagnetic indices. This chapter outlines the method employed by the SATAN-A suite of programs, as used at Aston University (SATellite ANalysis at Aston), so that subsequent developments may be related to it.

First, the force model is outlined, by considering the major forces acting upon an Earth satellite. Secondly, the correction process is explained, by which an improved set of model parameters is obtained. This process employs a linear least squares differentiated correction technique which minimises the residuals to the tracking data in the correction program ORBCORR of the SATAN-A suite. Finally, the prediction routine is described. This is contained in the program ORBPRED which integrates ahead using a Gauss-Jackson numerical integrator to compute ephemeris and partial derivatives over the span of the arc being determined. Here, *arc* means the satellite path over some period of time, with *long-arc* usually denoting an orbit of several days in length.

It is important to emphasize that the prediction-correction process described is an iterative one and that the aim is to improve on rather than fully determine the many model parameters involved. Thus the whole of this thesis is only part of

a continuing and evolving process, and not a finished or completed idea in itself.

2.2 The force model

The force model \underline{F} , used by the prediction program, has six components. Three of these are gravitational in origin: the attraction of the Earth (\underline{F}_G), variations in this due to solid and ocean tides (\underline{F}_{ET}) and attractions of other bodies in the solar system (\underline{F}_{TB}). The other three (known as skin forces [Klinkrad *et al.*, 1990], arising as they do from surface-particle interactions) are atmospheric resistance (drag and lift, \underline{F}_D), direct solar radiation pressure (\underline{F}_R) and Earth-reflected infrared and albedo forces (\underline{F}_{AlbIR}). These are modelled as follows.

2.2.1 The earth's gravitational potential

By far the greatest force acting on a low Earth satellite arises from the attraction due to the Earth's mass. It is known that any two point masses m and M exert a mutually attracting force of magnitude

$$F = \frac{GmM}{r^2}$$

where r is the distance between the masses and G is the universal gravitational constant. From this, using Newton's second law, it may be deduced that the mass m experiences an acceleration of magnitude

$$a = \frac{GM}{r^2}$$

due to the attracting force exerted by the mass M . Equally, the acceleration vector may be written as a potential $\underline{a} = \nabla V$ where

$$V = \frac{GM}{r}.$$

Further, it may be shown that this potential satisfies Laplace's equation — namely that $\nabla^2 = 0$ — and hence is harmonic.

Now for a non-particular mass, such as that of the Earth, the potential may be expanded as a triple integral

$$V = G \int_x \int_y \int_z \frac{\rho(x, y, z)}{r(x, y, z)} dx dy dz \quad (2.1)$$

where $\rho(x, y, z)$ is the density at the point (x, y, z) within the Earth's mass, a distance $r(x, y, z)$ from the external attracted mass m . Since $dM = \rho(x, y, z) dx dy dz$ is also a point mass, the total potential of Equation 2.1 also satisfies Laplace's equation.

Because of the physical significance, it is more usual to work in a spherical coordinate system rather than a Cartesian one. In such a system, Laplace's equation may be written

$$\frac{\partial}{\partial r} \left(r^2 \frac{\partial V}{\partial r} \right) + \frac{1}{\cos \phi} \frac{\partial}{\partial \phi} \left(\cos \phi \frac{\partial V}{\partial \phi} \right) + \frac{1}{\cos^2 \phi} \frac{\partial^2 V}{\partial \lambda^2} = 0 \quad (2.2)$$

where ϕ and λ are latitude and longitude respectively in a geocentric Earth-fixed coordinate system and r is the separation of the attracted point mass m from the Earth's centre (the origin of the system).

A solution to Equation 2.2 is obtained by assuming that it takes the separable form

$$V = R(r)\Phi(\phi)\Lambda(\lambda)$$

and solving the resulting differential equations independently for $R(r)$, $\Phi(\phi)$ and $\Lambda(\lambda)$. Such a process results in the following expression for the potential V

$$V = \frac{GM_e}{r} \left(\sum_{l=0}^{\infty} \sum_{m=0}^l \left(\frac{R_e}{r} \right)^l P_{l,m}(\sin \phi) (C_{l,m} \cos m\lambda + S_{l,m} \sin m\lambda) \right) \quad (2.3)$$

[Kaula, 1966, pp.4-6] where M_e is the Earth's mass and R_e its mean radius. The functions $P_{l,m}$ are the associated Legendre polynomials and $C_{l,m}$ and $S_{l,m}$ are the harmonic coefficients which collectively define a given gravity field. This is the form of V most usually employed in expressing the gravitational force \underline{F}_G on an Earth satellite,

$$\underline{F}_G = m\nabla V.$$

2.2.2 Solid earth and ocean tides

The Earth is not a rigid body, rather it is deformed by the attractions of other masses in the solar system: notably the sun and moon. These cause movements in both the solid Earth and in the oceans. Such effects are called tides and these perturb the underlying gravitational attraction as expressed by \underline{F}_G .

In the SATAN-A suite, the frequency dependent portion of the solid Earth tides is modelled by variations in the harmonic coefficients $C_{l,m}$ and $S_{l,m}$, while

the frequency independent part is modelled as another potential,

$$U_2 = \sum_{j=\substack{\text{sun,} \\ \text{moon}}} \frac{GM_j}{r_j^3} \frac{R_e^5}{r^3} k_2 \left(\frac{3}{2} \cos^2 s - \frac{1}{2} \right)$$

where s is the angle subtended by the sun/moon and satellite at the earth's centre, k_2 the second degree Love number and r_j is the geocentric sun/moon distance [Lambeck, 1980].

Having deformed the solid Earth, the ocean tides are then determined using a global circulation model such as that due to Schwiderski [1978]. The full tidal force, \underline{F}_{ET} , is the cumulative total of these three components. It is worth stating that, in addition to their contribution to the force model, tidal deformations displace the positions of the observation stations for satellite tracking data and hence must also be accounted for during the correction part of the iterative process. Finally, for this subsection, we note that the SATAN-A suite currently makes no allowance for ocean loading (the effect of the oceans' mass on the solid earth beneath).

2.2.3 Third body attraction

In addition to the Earth, several other bodies in the solar system are sufficiently massive to exert a significant gravitational attraction on an Earth satellite. However, unlike the Earth, such bodies are considered only as point masses due to the distances involved. Other satellite groups such as GSFC/NASA and Texas University are attempting to determine a low degree harmonic expansion for the gravitational attraction of the moon and future adaptations of the SATAN-A suite may also see such changes, together with the inclusion of tidal perturbations, for this and other bodies. However, at present, the accuracy of the force model does not appear to wholly justify such an elaboration.

The bodies currently included as perturbing point masses are the sun and moon and the four planets: Venus, Mars, Jupiter and Saturn. Each of these is taken in turn and, together with the satellite and the Earth, is considered in the manner of the classic three-body problem [Brouwer and Clemence, 1961, pp.249-251]. The force of such a body on the satellite may be computed as follows.

Let \underline{x} , \underline{x}_e and \underline{x}_j be the position vectors of satellite, Earth and third body respectively in some inertial reference frame (see Section 2.4 below), as illustrated

in Figure 2.1, so that Newton's laws of motion may be applied. Then the resultant

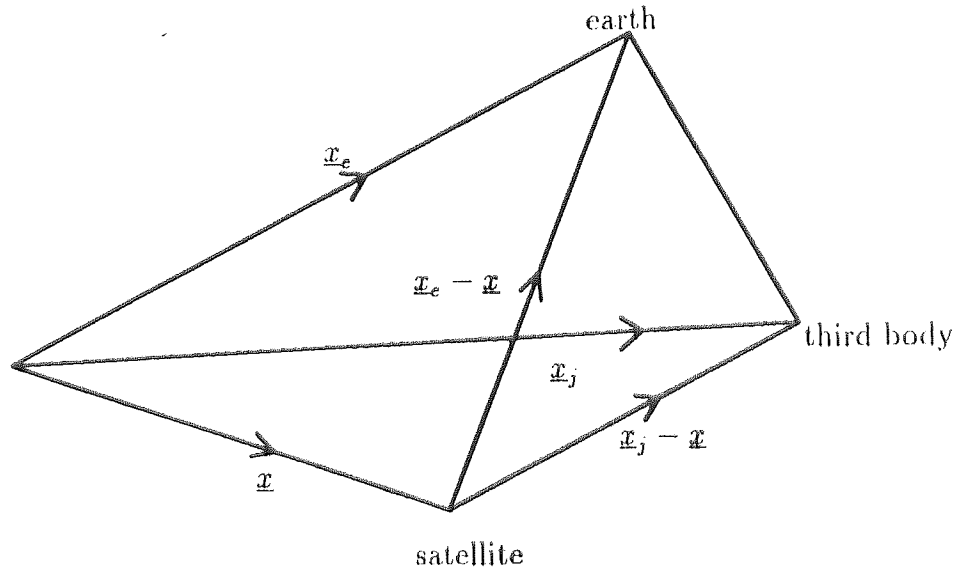


Figure 2.1: The three body system.

satellite acceleration due to all forces arising from point mass attractions in this system is

$$\ddot{\underline{x}} = G \left(\frac{M_e(\underline{x}_e - \underline{x})}{|\underline{x}_e - \underline{x}|^3} + \frac{M_j(\underline{x}_j - \underline{x})}{|\underline{x}_j - \underline{x}|^3} \right) \quad (2.4)$$

where M_j is the mass of the third body, all other variables being already defined.

This acceleration is converted to the geocentric frame by considering the geocentric satellite position vector, $\underline{x} - \underline{x}_e$ so that the acceleration in this frame is $\ddot{\underline{x}} - \ddot{\underline{x}}_e$.

Given an expression for $\ddot{\underline{x}}_e$ similar to Equation 2.4 the desired acceleration becomes

$$\ddot{\underline{x}} - \ddot{\underline{x}}_e = G(M_e + m) \frac{(\underline{x}_e - \underline{x})}{|\underline{x}_e - \underline{x}|^3} + GM_j \left(\frac{(\underline{x}_j - \underline{x}_e) - (\underline{x} - \underline{x}_e)}{|(\underline{x}_j - \underline{x}_e) - (\underline{x} - \underline{x}_e)|^3} - \frac{(\underline{x}_j - \underline{x}_e)}{|\underline{x}_j - \underline{x}_e|^3} \right)$$

the first part of which is already accounted by the $C_{0,0}$ term in the harmonic expansion of the gravitational potential (Equation 2.3). Thus the required third body force is

$$\underline{F}_{TB} = G \sum_j M_j \left(\frac{(\underline{x}_j - \underline{x}_e) - (\underline{x} - \underline{x}_e)}{|(\underline{x}_j - \underline{x}_e) - (\underline{x} - \underline{x}_e)|^3} - \frac{(\underline{x}_j - \underline{x}_e)}{|\underline{x}_j - \underline{x}_e|^3} \right)$$

where the sum over j is taken over the six bodies listed above.

2.2.4 Atmospheric drag and lift

All Earth satellites moving within the atmosphere experience a force due to the surface impingement of charged and uncharged particles. This force is predominantly retarding (drag), acting contrary to the velocity of the satellite relative to

the atmosphere (\underline{v}_r). However, there is also a component perpendicular to this (lift) which produces effects in the radial and across track directions.

Before this study, the SATAN-A suite of programs had assumed that the lift force was negligible, modelling the drag force as a function of atmospheric density (ρ) and effective area of the satellite perpendicular to the direction of travel (A_D):

$$\underline{F}_D = -\frac{1}{2}\rho C_D A_D v_r \underline{v}_r \quad (2.5)$$

where $v_r = |\underline{v}_r|$ and C_D is a drag (or ballistic) coefficient which varies with the surface characteristics of the satellite and the atmosphere's constituents [Cook, 1965]. The minus sign indicates that the force opposes the direction of travel.

Because of the lack of detailed knowledge of the atmosphere [Ries, 1992] it is usual to solve for C_D either as a linear function of time (drag and drag-rate) or a number of parameters forming a step function over time (as illustrated in Figure 2.2). A third method, solving for the points of a "saw-tooth" function, is developed and detailed later in this chapter (see Section 2.5). Much of this thesis is centred around ways of avoiding or overcoming this deficiency in knowledge about the atmosphere, such as using a different force model for drag (see Chapters 3 and 4) or transferring information from a second satellite (as attempted in Chapters 5 to 7).

2.2.5 Direct solar radiation pressure

The flux emitted by the sun, diminishing (in accordance with the inverse square law) with increasing distance from its source, gives rise to two skin forces. The first of these is due to the flux which arrives at the satellite directly from the sun, known as direct solar radiation pressure.

In addition to the distance factor, this force depends on the relative positions of the satellite with respect to the Earth's shadow, and the surface area and shape as viewed from the sun. To allow for the Earth's shadow, a variable μ (the shadow factor) is used, ranging from zero in the Earth's umbra to one in full sunlight. The intervening penumbral region is computed for a spherical Earth of some mean polar radius. In this area the shadow factor varies smoothly between the two extremes.

Given these considerations, the direct solar radiation pressure is modelled as

$$\underline{F}_R = -\nu PC_R A_R \underline{e}_s \quad (2.6)$$

where P is the solar flux per unit area at the satellite, A_R is the effective satellite surface area perpendicular to some unit satellite-to-sun vector \underline{e}_s and C_R is the radiation coefficient, allowing for the interactions between photons and satellite surface [Aksnes, 1976]. Again, as with the drag force of Equation 2.5, the minus sign indicates that the force acts in an opposite direction to the vector \underline{e}_s .

2.2.6 Earth reflected albedo and infra-red forces

The sixth and final force, modelled in the prediction program (and the second of the two forces arising from solar flux) arises from the energy re-emitted (infra-red) or reflected (albedo) by the Earth.

The infra-red component is always present — even for a satellite in the umbra of the Earth — but the albedo force comes only from those regions of the Earth which are visible from both sun and satellite at the same instant. Effectively (for a spherical Earth), this implies regions of the Earth visible from the satellite when the satellite is also visible from the sun. As with the direct solar radiation pressure force, \underline{F}_R , a shadow function smooths the albedo contribution in an idealised penumbral region.

In order to model these forces, the surface of the Earth visible from the satellite is divided into a number of areas which are equal when projected into a plane perpendicular to the geocentric satellite position vector along a line parallel to this vector. There are thirteen such areas in the current version of the SATAN-A package.

If the area of any one such is denoted dA_i then the force arising from this region is

$$d\underline{F}_i = -(\gamma C_R P \cos \theta + P_{IR}) \left(\frac{\cos \alpha A_R dA_i}{\pi c d^2} \right) \underline{e}_d$$

where C_R and P are as above (Section 2.2.5, Equation 2.6), γ is the albedo of the surface element i — incorporating the shadow factor ν — and P_{IR} is the emitted infra-red radiation, interpolated from tables [Vonder Haar and Suomi, 1971]. Further, θ is the angle between the surface normal and the geocentric position of the sun, α that between the same normal and the satellite geocentric

position vector, A_R the area of the satellite perpendicular to a satellite-to-earth unit vector \underline{e}_d and d the distance between satellite and earth surface-element. The sum of these elemental forces provides the total force due to indirect solar radiation,

$$\underline{F}_{AlbIR} = \sum_{i=1}^{13} dF_i$$

completing the force model as currently used by the prediction program.

2.3 Least squares minimisation

As has been indicated, the precise orbit determination routine, as embodied by the SATAN-A package, works by iterating a prediction-correction process. In order to see the values that the predicting program must produce, it is first necessary to consider what the correcting program requires.

The correction program ORBCORR, developed from one written by Andrew Sinclair and Graham Appleby of the Royal Greenwich Observatory (RGO) [Sinclair and Appleby, 1986], centres around a least squares minimisation by which the force model parameters of the previous section can be modified to produce an orbital ephemeris more closely matching the observed data. The basic concept is the minimisation of the weighted square residuals,

$$\sum_i w_i (O_i - C_i)^2 \quad (2.7)$$

where w_i are the weights and C_i are the computed values corresponding to the observations O_i at times t_i . Thus, the sum is taken over all observations, i .

We suppose that an orbit may be modelled using a set of true parameters $\underline{P}^* = \{p_k : p_k \in \underline{P}\}$. In practice these values are not precisely known, but are related to an equivalent set of best approximations, \underline{P}^0 say, where $\underline{P}^* = \underline{P}^0 + \underline{\Delta P}$. Given such a relationship, it may be possible to determine a solution set closer to the true values than \underline{P}^0 , provided $\underline{\Delta P}$ can be calculated sufficiently accurately.

Let, $C_i = C_i(\underline{P}^*)$, since the computed values are ideally produced from the true parameters. Then Equation 2.7 may be minimised in the usual way by differentiating with respect to each model parameter and setting all the resulting equations identically to zero:

$$\sum_i w_i (O_i - C_i(\underline{P}^*)) \frac{\partial C_i(\underline{P}^*)}{\partial p_k} = 0 \quad \forall p_k \in \underline{P}. \quad (2.8)$$

The partial derivatives are computed with respect to the variables $p_k \in \underline{P}$, of which \underline{P}^* and \underline{P}^0 are subsets evaluated at fixed values of the p_k 's. Both $C_i(\underline{P}^*)$ and $\frac{\partial}{\partial p_k} C_i(\underline{P}^*)$ must be expanded in terms of \underline{P}^0 and $\underline{\Delta P}$, since \underline{P}^* is not known and we wish to determine $\underline{\Delta P}$. Such an expansion may be achieved using Taylor's series, thus:

$$\begin{aligned} C_i(\underline{P}^*) &= C_i(\underline{P}^0 + \underline{\Delta P}) \\ &= C_i(\underline{P}^0) + \frac{dC_i(\underline{P}^0)}{d\underline{P}} \cdot \underline{\Delta P} + O(\underline{\Delta P}^2) \\ \frac{\partial C_i(\underline{P}^*)}{\partial p_k} &= \frac{\partial C_i(\underline{P}^0 + \underline{\Delta P})}{\partial p_k} \\ &= \frac{\partial C_i(\underline{P}^0)}{\partial p_k} + \frac{\partial}{\partial p_k} \left(\frac{dC_i(\underline{P}^0)}{d\underline{P}} \cdot \underline{\Delta P} \right) + O(\underline{\Delta P}^3) \end{aligned}$$

where terms in $\underline{\Delta P}^2$ and above are multi-dimensional matrices. Linearising the problem, to avoid dealing with such matrices, results in the following expressions

$$\begin{aligned} C_i(\underline{P}^*) &\approx C_i(\underline{P}^0) + \frac{dC_i(\underline{P}^0)}{d\underline{P}} \cdot \underline{\Delta P} \\ \frac{\partial C_i(\underline{P}^*)}{\partial p_k} &\approx \frac{\partial C_i(\underline{P}^0)}{\partial p_k}. \end{aligned} \quad (2.9)$$

This linearisation also means that a solution to $\underline{\Delta P}$ may not lead to an exact value of \underline{P}^* and is therefore the reason for the iteration of the two programs which ideally produces diminishing corrections, $\underline{\Delta P}$, so converging on a value as close to \underline{P}^* as is possible.

By substituting Equation 2.9 into Equation 2.8, neglecting the higher order terms and assuming equality, we obtain

$$\sum_i w_i \left(O_i - C_i(\underline{P}^0) - \frac{dC_i(\underline{P}^0)}{d\underline{P}} \cdot \underline{\Delta P} \right) \frac{\partial C_i(\underline{P}^0)}{\partial p_k} = 0 \quad \forall p_k \in \underline{P}$$

which must be solved if $\underline{\Delta P}$ is to be calculated. This system of equations may be expressed more succinctly in matrix form,

$$N \underline{\Delta P} = \underline{b}$$

where $N = (n_{jk})$ is composed of elements

$$n_{jk} = \sum_i \frac{\partial C_i(\underline{P}^0)}{\partial p_j} \frac{\partial C_i(\underline{P}^0)}{\partial p_k}$$

and each element (row) of the column vector \underline{b} is defined to be

$$b_j = \sum_i w_i (O_i - C_i(\underline{P}^0)) \frac{\partial C_i(\underline{P}^0)}{\partial p_j}.$$

Thus, each b_j is a sum of the products of the weighted residuals, $w_i (O_i - C_i)$ and the partial derivatives $\frac{\partial}{\partial p_j} C_i(\underline{P}^0)$.

These equations are known as the normal equations and, by construction, N is a symmetric positive definite matrix [Sernesi, 1993, p.236] and is therefore invertible — provided that the model is not over-parameterised; that is there are no linear dependencies in the row space of N [Chatfield and Collins, 1986, p.16]. So a set of parameter corrections may be determined from

$$\underline{\Delta P} = N^{-1} \underline{b}$$

and these being added onto the prior set \underline{P} , a new best estimate is produced, from which the whole process may be repeated, beginning again with the prediction program.

In order to produce the values of $C_i(\underline{P}^0)$ and $\frac{\partial}{\partial p_j} C_i(\underline{P}^0)$ the correction routine uses values of $\underline{x}(t_i)$, $\dot{\underline{x}}(t_i)$ and, $\frac{\partial}{\partial p_k} \underline{x}(t_i)$ for each observation time t_i . Thus, these variables are the required output of the correction routine. Here $\underline{x}(t_i)$ is the satellite position, $\dot{\underline{x}}(t_i)$ its velocity and $\frac{\partial}{\partial p_k} \underline{x}(t_i)$ the partial derivatives of $\underline{x}(t_i)$ with respect to all the model parameters for which a solution is to be sought. It is emphasized that the partial derivatives calculated in the prediction stage are for the force model parameters *only*. Further, it is possible (and desirable in terms of saved processing time) not to produce partial derivatives of those parameters for which a solution is not required.

The correction program determines the required terms for the least squares minimisation, $C_i(\underline{P}^0)$ and $\frac{\partial}{\partial p_j} C_i(\underline{P}^0)$, as follows. Taking each data type separately, first O_i is obtained by reading the data and, where necessary, adding on any corrections. The aim is to produce a value which corresponds (in the manner in which it has been obtained) to its computed equivalent. For example, an observed laser range will be affected by the troposphere. However, the calculated range will not show this effect, so the observed range is corrected to remove the effect by adding a value stored in the same observation record in the data files. These correction values are computed from models, from meteorological data, or measured directly by satellite or station at the observation time.

The calculated value is evaluated from the satellite ephemeris: position and velocity vectors. In the case of laser data, altimetry and crossovers, the partial derivatives of the calculated value, required to form the normal equations, are computed from

$$\frac{\partial C_i}{\partial p_k} = \frac{\partial C_i}{\partial \underline{x}} \frac{\partial \underline{x}}{\partial p_k} = \frac{\partial C_i}{\partial x} \frac{\partial x}{\partial p_k} + \frac{\partial C_i}{\partial y} \frac{\partial y}{\partial p_k} + \frac{\partial C_i}{\partial z} \frac{\partial z}{\partial p_k} \quad (2.10)$$

the values of $\frac{\partial}{\partial \underline{x}} C_i$ being determined from the values of C_i . Their computation is dependent upon the data type. Thus, for example, if the data type is laser range data, then the value of C_i is a range measurement, ρ say. This may be written

$$\rho^2 = (x - x_b)^2 + (y - y_b)^2 + (z - z_b)^2$$

where $\underline{x} = (x, y, z)$ and $\underline{x}_b = (x_b, y_b, z_b)$ are the satellite position vector and station coordinate vector respectively. Then the partial derivatives of this calculated range are of the form

$$\frac{\partial C_i}{\partial x} = \frac{\partial \rho}{\partial x} = \frac{1}{2\rho} \left(2\rho \frac{\partial \rho}{\partial x} \right) = \frac{1}{2\rho} \frac{\partial \rho^2}{\partial x} = \frac{x - x_b}{\rho}$$

with similar results for y and z :

$$\frac{y - y_b}{\rho} \quad \text{and} \quad \frac{z - z_b}{\rho}$$

respectively; thus determining $\frac{\partial}{\partial \underline{x}} C_i$. Combining this value, using Equation 2.10, with the partial derivatives $\frac{\partial}{\partial p_k} \underline{x}$, output by the ORBPRED program, provides the full required partial derivative. Both the computation of $\frac{\partial}{\partial \underline{x}} C_i$ and the combination of this with the partial derivatives from the ORBPRED routine are carried out within the ORBCORR program. In contrast, where the parameter p_k is *not* one of those in the force model of Section 2.2, the entire partial derivative is computed within the ORBCORR program: for example, where a solution is sought to one or more laser station coordinates, or to the pole position. Having produced the required components for the matrix N and vector \underline{b} , the matrix inversion process — currently a technique due to Choleski is employed [Burden and Faires, 1989, p.370] — produces the correction vector as described above.

2.4 Integrating the force model

The computation of the satellite ephemeris, $\underline{x}(t_i)$ and $\dot{\underline{x}}(t_i)$, and partial derivatives, $\frac{\partial}{\partial p_k} \underline{x}(t_i)$, required by the correction program, ORBCORR of Section 2.3, is carried

out in ORBPRED, using some prior set of model parameters, \underline{P}^0 , and the force model \underline{F} of Section 2.2.

The prior set of parameters consists of an initial state vector ($\underline{x}(0), \dot{\underline{x}}(0)$), drag and radiation coefficients (C_{D_i}, C_R) gravity field coefficients ($C_{l,m}, S_{l,m}$) and all other model variables. In practice it is not usual to solve for the harmonic coefficients $C_{l,m}$ and $S_{l,m}$ over a single arc since solutions to these generally require more data to be meaningful. Thus, these coefficients are more often taken to be known fixed values. In addition to the prior parameter set (\underline{P}^0) the prediction program requires various auxiliary data such as planetary positions (for the third body force, \underline{F}_{TB}), solar flux and geomagnetic data (for atmospheric density models) and fluctuations in time and polar positions (for converting to an inertial reference frame). Further, it requires that the user specify which of various models should be used (for tides, density etc.) and exactly what output (ground-tracks, projected state vectors etc.) is desired. Finally, as its main input, the prediction program takes a file of dates at which the ephemeris and partial derivatives are to be computed. These dates must all be in chronological order in the same time-scale.

In order to employ the force model in a Newtonian fashion, all computations must be carried out in an inertial frame of reference. That is a coordinate system fixed in both time and space, and uniformly varying coordinates for position and time. In order to facilitate this, various timescales are next considered and a uniformly continuous one is chosen. Following this, the spatial frame of reference that will be used is also defined.

Within the observation data, allowance is made for several timescales to be used, but all are variations of universal time (UT) and international atomic time (TAI). The former is measured from Greenwich mean sidereal time (GMST) and hence is based upon diurnal stellar motions [Astronomical Almanac, 1987]. Consequently it is not uniformly continuous due to variations in the Earth's rotation rate and axial position. Conversely, TAI is measured in multiples of the atomic SI (Système Internationale) second from a base date on January the 1st in 1972, hence *is* uniformly continuous.

UT is further subdivided into UT0, based on location and UT1 which has been corrected for polar-meridian motions and therefore is observer independent,

though still non-uniform. There is also UTC which differs from UT by at most 0.9 seconds SI and is an integer number of seconds SI different from TAI. This relationship is maintained by introducing leap seconds (finite discontinuities) in UTC, usually at the end of December and or June [Astronomical Almanac, 1987]. To produce a uniformly varying timescale with the minimum adjustment, all observation times are corrected to what is termed ATC. This differs from TAI by a fixed number of seconds SI and is equal to UTC at the start time of the long arc being determined.

The inertial reference frame currently in widespread use among the precise orbit determination community is J2000 which is defined as follows. The Z-axis is the mean Earth pole, normal to the equatorial plane while the X-axis points to the vernal equinox (first point in Aries). The time at which these axes are fixed is Julian Date (JD) 2451545.0 which is noon on the 1st January 2000 A.D. All integration within the prediction program takes place in this system, though two other systems are also used in the computation process. These are the Earth fixed system (with coordinates: latitude, longitude and radial distance) and the frame-of-date system (as for J2000, but fixed at the time of observation/computation, rather than in 2000 A.D.). Clearly the latter one is also inertial for any given date, but is different for each date considered.

Rotation between these systems is effected by matrix multiplication where the matrices are determined each time the observation (or computation) date alters. Briefly, movement between the inertial frames is due to precession and nutation — the time varying effects of the sun and moon which cause irregularities in the Earth's rotation and polar position. On the other hand, movement between the Earth-fixed and frame-of-date systems arises from the time of day involved and also from variations in polar motion.

Having decided upon an inertial reference frame and devised a way in which to convert to and from it, it is possible to employ Newton's laws to integrate the force model

$$\underline{F} = \underline{F}(\underline{x}(t), \dot{\underline{x}}(t), \underline{P}, t)$$

thus obtaining the satellite velocity,

$$\dot{\underline{x}}(t) = \frac{1}{m} \int_{t_0}^t \underline{F}(\underline{x}(s), \dot{\underline{x}}(s), \underline{P}, s) ds$$

and position,

$$\underline{x}(t) = \int_{t_0}^t \dot{\underline{x}}(s) ds.$$

The partial derivatives are found similarly:

$$\frac{\partial \underline{x}(t)}{\partial p_k} = \int_{t_0}^t \left(\frac{1}{m} \int_{t_0}^s \frac{\partial}{\partial p_k} F(\underline{x}(u), \dot{\underline{x}}(u), \underline{P}, u) du \right) ds.$$

In practice, since F is not defined analytically but only at a series of points, a numerical integration technique is used. That currently employed is an eighth order Gauss-Jackson integrator which predicts one step ahead from the previous eight steps. In order to start this off at the beginning of the arc the first eight steps must be produced in some other manner. To this end a procedure based upon difference approximations is used, iterating until the values converge. The prediction program works by integrating every ‘n’ seconds (where ‘n’ takes a value determined by the user). After each new point has been found, the observation dates are considered and the values of $\underline{x}(t_i)$, $\dot{\underline{x}}(t_i)$ and $\frac{\partial}{\partial p_k} \underline{x}(t_i)$ are interpolated at such dates as fall in the central interval of the current eight points. When all dates and all steps have been considered the program terminates.

2.5 Saw-tooth drag modifications

Before proceeding with the main body of the thesis which focuses on three attempts to improve long-arc orbit determination, the basic suite described above underwent two major modifications. The first of these, already mentioned in Section 2.2.4 above, is the implementation of a saw-tooth option for the drag scale factors, C_{D_i} . It is important to note that throughout this thesis “saw-tooth” refers to the pattern of drag scale factors here described and *not* to the discontinuous waveform referred to as saw-tooth by physicists, engineers, applied mathematicians and their ilk.

As has already been indicated in Section 2.2.4, there were two existing approaches to solving for drag scale factors in the SATAN-A suite at the start of this study. A comparison of the two, carried out by Rothwell [1989], indicated that although solving for just two parameters, namely an initial value and a rate of change, provided a continuous C_D , a solution involving multiple factors in the form of a step function (see Figure 2.2) provided better orbits. Here better means

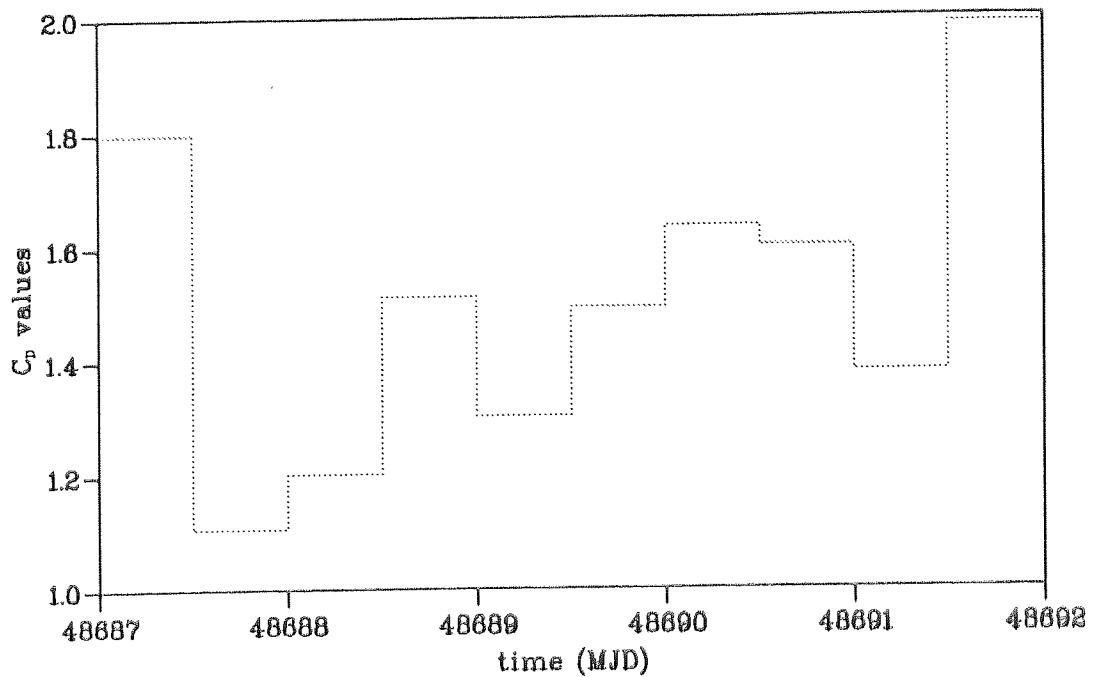


Figure 2.2: An example of the step function for drag scale factors over the period MJD 48687 to MJD 48692.

being possessed of a lower RMS value without being distorted towards any particular geographical region. The RMS, or Root Mean Square, is defined as the square root of the mean of the squared differences between observed data and calculated equivalents:

$$\sqrt{\frac{1}{\sum w_i} \sum_{i=0}^n w_i (O_i - C_i)^2}$$

and is a statistical measure of how well the model fits the data (the sample variance estimate). A lower RMS is generally associated with a better *fit* — this does not always imply a better model. Initial studies which employed multiple drag scale factors in the step function form, for instance Seasat studies [Rothwell, 1989], solved for C_D values on a daily basis. However, by 1992 the frequency had increased to as many as eight a day, for instance for the French satellite SPOT-2 [Nouël *et al.*, 1991]. Such a practice leads to increasing correlations between solution parameters, calling into question the quality, or indeed reality, of the solution. Indeed, where correlations reach a value of one, linear dependencies between solution parameters may exist: potentially making the matrix N non-invertible [Chatfield and Collins, 1986]. Thus, it is not generally sufficient to use

the RMS alone as a measure of the absolute quality of the solution, though it may be able to give indications of a relative improvement.

Early during the work for this thesis, several attempts were made to solve for continuous drag scale factors in the form of a simple polynomial function, or as some sinusoidally varying curve. Such attempts proved unsuccessful, since the resultant RMS values were no better than those obtained using a daily step function, even when the order of the polynomial was greater than the length of the arc in days. This failure was traced to the prevalence of negative scale factors at both ends of the most of the long-arcs tested. The physical significance of these negative values is that the atmosphere is actually accelerating the satellite in its direction of motion; clearly an unrealistic event. It was found that the problem arose because of the lack of constraints on the curve at either end of the long-arc, there being no data outside the arc to fix the drag scale factors.

With the need to improve drag modelling, via concepts embodied later in this thesis (see Chapters 3 and 7), it became essential to produce some form of continuous (though not necessarily smooth) model for C_D . The obvious method, given the failure of an explicitly continuous analytic form, was to use several scale factors and rates of change which were connected to each other. This resulted in the saw-tooth regime illustrated in Figure 2.3. In contrast to the previous failures, this attempt to model the drag scale factors with a continuous function was found to work at least as well as the step function approach. The SATAN-A suite was therefore modified as follows.

First, the initial solution set, P^0 , was altered by removing all references to a drag-rate. Then an additional drag scale factor was included at the start epoch, $t_0 = 0$, and the ORBPRED and ORBCORR programs were amended to read this modified parameter set. A major distinction between step and saw-tooth approaches is the difference in which the programs interpret the time values associated with each scale factor. In the former, the associated time value dictates the *end* of the period of validity of the scale factor (the beginning being given by the expiration of the previous such factor). Conversely, with the saw-tooth technique, the associated time value is actually the time at which the fixed value pertains, since between any two successive associated time values, t_i and t_{i+1} say, the drag

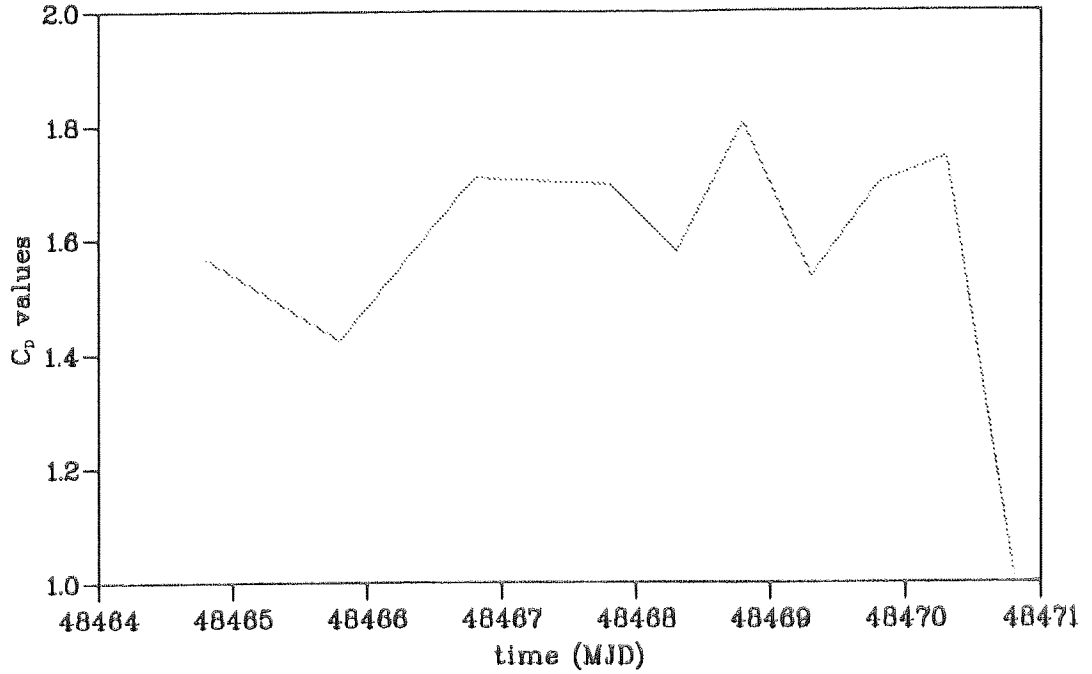


Figure 2.3: The saw-tooth approach to computing drag scale factors over the period MJD 48464.8 to MJD 48470.8.

scale factor $C_D(t)$ is given by

$$C_D(t) = C_{D_i} + \left(\frac{t - t_i}{t_{i+1} - t_i} \right) (C_{D_{i+1}} - C_{D_i}) \quad \forall t \in [t_i, t_{i+1}). \quad (2.11)$$

The necessary partial derivatives, $\frac{\partial}{\partial C_D} \underline{F}$, are computed from Equation 2.11 within the orbital prediction program, just as was effected before this alteration. However, for each computation time t there are now *two* partial derivatives, made with respect to each of the two C_D values on either side of this time. Since the only occurrence of C_D within the force \underline{F} acting on the satellite is in the component due to atmospheric resistance, \underline{F}_D , the required derivatives are obtained by differentiating Equation 2.5 where C_D is defined by Equation 2.11. Thus,

$$\frac{\partial \underline{F}}{\partial C_{D_i}} = -\frac{1}{2} \rho \left(\frac{t_{i+1} - t}{t_{i+1} - t_i} \right) A_D v_r \underline{v}_r$$

and

$$\frac{\partial \underline{F}}{\partial C_{D_{i+1}}} = -\frac{1}{2} \rho \left(\frac{t - t_i}{t_{i+1} - t_i} \right) A_D v_r \underline{v}_r$$

are the required partial derivatives with respect to the two drag scale factors. The only other changes required by ORBPRED and ORBCORR involved ensuring

that the indices of these scale factors and their associated time values matched and that references to them allowed for the removal of the drag-rate parameter.

2.6 Station coordinates

The second major change made to the SATAN-A suite of programs involved the station coordinates used to determine laser range measurements within the orbital correction program (ORBCORR). This alteration was necessitated by the increasing accuracy in the predicted orbits. Prior to this study, a single file of station coordinates had been used for periods of half a year or more, as for instance in the case of Seasat [Rothwell, 1989]. However, solutions to station coordinates are sought at regular intervals by various groups (such as the RGO, NASA etc.) using data sets which include information from higher altitude satellites such as Lageos (orbiting at an altitude of more than 6000 km) which are negligibly affected by atmospheric resistance.

Station coordinate solutions are made up of two vectors, namely the earth-fixed location of the monument (or marker) position and a correction for the displacement between this and the actual point of the laser beam's beginning (or radar antenna location for DORIS doppler data). The latter may be measured locally and values are computed regularly, stored centrally for all types of stations (not just laser sites) and made available to users around the globe. These values are then included in the periodic solutions made from observation data, so that monument solutions may be calculated. The monument solutions will vary due to Earth deformations and crustal motion. The former are allowed for by computing the effect of Earth tides due to sun and moon in both the prediction and correction programs. Crustal motion was hitherto not allowed for, so that arcs beginning at different epochs were converged with respect to a single fixed set of station coordinates. It is this shortcoming that this modification seeks to address.

It may be possible that levels of accuracy attained in orbital predictions may eventually necessitate station coordinates being computed within the prediction and correction programs themselves. However, comparing the magnitudes of current accuracies in orbit predictions with those of actual crustal motions suggests that it is satisfactory to produce a set of station coordinates correct to an approx-

imate central date of whichever long-arc is being converged. This should mean that the errors with respect to the station coordinates are at a minimum at this central point and increase towards either end of the arc.

Thus, a program was written which took a set of monument solutions pertinent to the given period (i.e lying before and as close as possible to the start epoch of a given arc), the correction vector file and *a file of station velocities* (again produced by groups such as NASA and RGO and collated centrally). This enables the station positions to be computed from the relevant monument-correction pair and then adjusted to a value at the central date of the arc, by including a velocity term under the assumption that

$$\underline{x}(t) = \underline{x}(0) + \underline{v}t$$

(where \underline{v} is the stored velocity vector). Further, since this routine is run before the orbit prediction and correction programs, no modifications to the latter were required.

Chapter 3

Surface Force Modelling

3.1 Errors in modelled surface-forces

In long-arc precise orbit determination for low Earth satellites, such as ERS-1, large errors may occur as a result of mismodelling of both the direct solar radiation pressure and aerodynamic resistance forces. It has been suggested by, among others, Klinkrad *et al.* [1990] that any improvements in the gravity field will be severely restricted in terms of their usefulness — assuming that the determination of such improvements is not directly impeded — until a similar level of accuracy is attained in these and other non-gravitational forces. It is further recognised that despite the sophistication of recent thermospheric models, such as MSIS83 [Hedin, 1983], MSIS86 [Hedin, 1987] and DTM [Barlier *et al.*, 1977], which consider the number densities of individual atmospheric constituents, little overall progress appears to have been made in modelling the neutral air density [Renard 1990; Ridgway *et al.*, 1990; Ries, 1992]. Indeed the simpler Jacchia 71 model [Jacchia, 1972], based primarily on satellite drag data, is considered to be the equal of the more sophisticated MSIS83 model in most orbit determinations.

Since thermospheric models may produce atmospheric densities which are in error by as much as 50% to 100%, it is not possible to circumvent this weakness in these *skin forces* [Klinkrad *et al.*, 1990] totally. However, the area component of these and other skin forces may be improved by considering particle-surface interactions for the respective incident fluxes [Herrero, 1985; Marshall *et al.*, 1991; Moore and Sowter, 1991]. This chapter will focus on the two skin-forces which are of greatest magnitude, namely aerodynamic resistance (combining both the

drag and lift forces of Section 2.2.4) and direct solar radiation pressure [Klinkrad *et al.*, 1990, p.2].

Errors in the aerodynamic resistance force arise from uncertainties in the atmospheric density, the area perpendicular to the relative velocity of the satellite (ρ and A_D respectively in Equation 2.5 of Section 2.2.4) and the characteristic behaviour of the atmospheric particles incident on the satellite's surfaces. Most methods currently used to circumvent such uncertainties work by introducing additional solution parameters into the force model of Chapter 2. For example, multiple drag coefficients, C_D , over specified time intervals improve the orbital fit by reducing the sum of squares of the residuals. However, employed in excessive numbers, such parameters lose any physical significance by absorbing errors in density, effective area, and other along-track forces (such as gravity field effects and solar-radiation pressure) [Rothwell, 1989]. Similarly, errors in the force due to direct solar radiation pressure arise predominantly from inaccuracies in both the visible area perpendicular to the sun-satellite vector and in the reflectivity conditions which translate into uncertainties in the product $C_R A_R$.

An attempt is made here to model surface areas, and hence skin forces, so that the derived scale factors C_D will be multiplicative constants for air density alone. This will only be perfectly achieved if the surface area and interaction coefficients can be modelled exactly. However, it may be approximated if the areas can be determined sufficiently accurately. The approach adopted here considers individual flux units and computes forces from the corresponding differences between incident and post-impact momentum where the surface interactions are described along probabilistic lines. The aim is to develop a series of force or area tables which may then be accessed from the prediction program (which will interpolate between tabulated values), rather than computing the forces directly at every step of the numerical integration process.

In this chapter the relevant momentum-exchange equations which are to replace the previous equations of Section 2.2 are elaborated. Then the theory required to determine the surface areas for use in these equations is described. Finally, a brief test of the resulting software is made; further validation of the area tables and momentum exchange equations being made using several long-arcs of the satellites ERS-1 and SPOT-2 in the Chapters 4 and 6 respectively.

3.2 Surface forces considered in terms of the momentum exchanged

Satellite skin forces, such as direct solar radiation pressure and atmospheric resistance, may be computed by relating the force to the opposing change in momentum effected by that force. Thus, considering the total force on the satellite as a result of the sum of momentum changes in all incident flux units, we have

$$\underline{F} = - \sum_{\substack{\text{incident} \\ \text{flux units}}} (m\underline{v} - m\underline{u})$$

where \underline{u} and \underline{v} are the incident and post-impact flux velocities respectively, measured relative to the satellite, and m is the mass of one unit of flux. Assuming that the flux forms a parallel beam which is not affected by reflected units and that only the first impact of each flux unit need be considered, then the number of incident units is proportional to the visible surface area, A , and the previous equation becomes

$$\underline{F} = k \sum_{\substack{\text{visible} \\ \text{surfaces}}} A (m\underline{u} - m\underline{v})$$

where the constant of proportionality, k , relates the force to the density of the incident flow. Given these assumptions, each of the two main skin forces may be considered in turn.

3.2.1 Direct solar radiation pressure

For any Earth satellite, the assumption that direct solar radiation forms a parallel flux is immediately justified by the distance between sun and satellite. The other main assumption, that only the first impact need be considered, is imposed on the grounds that inaccuracies in the geometric model of the satellite and uncertainties in the surface-particle interactions outweigh any potential increase in accuracy arising from the inclusion of multiple impacts. This justification is employed for both direct solar radiation pressure *and* aerodynamic resistance forces.

Now, let E_0 be the flux at the Earth's surface, then the flux emitted from the sun is roughly $E_0 \bar{d}_{se}^2$, reversing the inverse square law; \bar{d}_{se} being the mean sun-earth distance. Whence, the flux incident on the satellite is

$$\frac{E_0 \bar{d}_{se}^2}{d_{se}^2}$$

where d_{ss} is the sun-satellite distance. This equation is a measure of the absolute energy of the incident photons, whence the magnitude of the incident *momentum* per unit area may be written (for speed of light c),

$$\frac{E_0 \bar{d}_{se}^2}{d_{ss}^2 c}$$

Now, radiation striking a satellite surface may be absorbed, reflected or transmitted with probabilities a , r and t respectively. Reflection and transmission may be further separated into specular and diffuse cases providing probabilities r_s , t_s , r_d and t_d . These probabilities measure the proportions of flux reacting in a given way and satisfy

$$a + r_s + r_d + t_s + t_d = 1 \quad (3.1)$$

where the values of these coefficients are specific to a given surface, or part surface, of a satellite.

Next, suppose that the flux has incident direction \underline{d} , subtending an angle θ_i with a given surface normal \underline{n} , as illustrated in Figure 3.1. Then the total incident

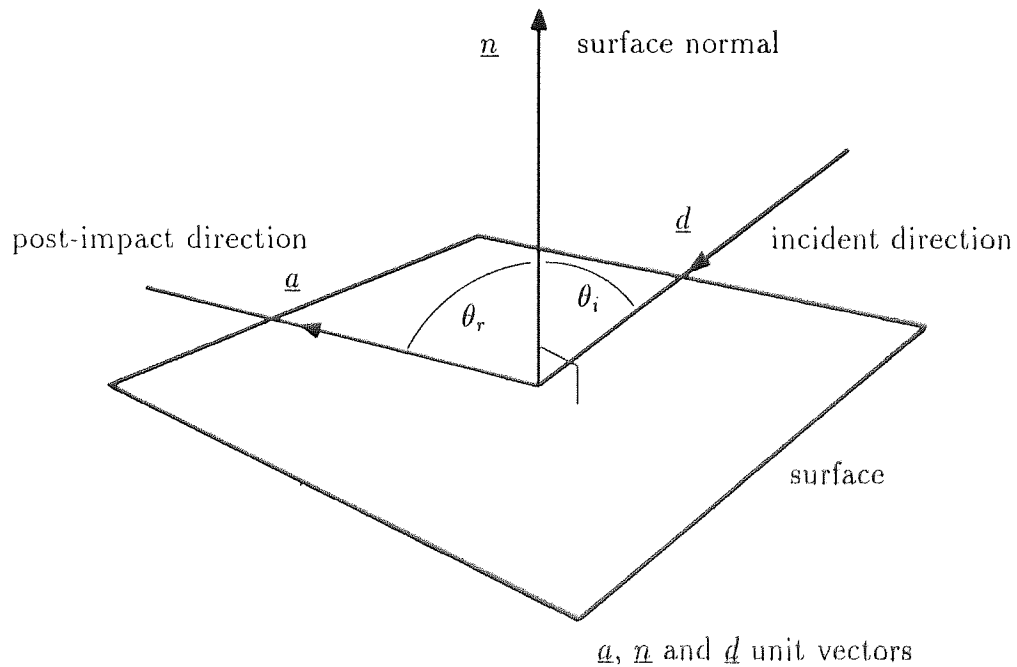


Figure 3.1: Incident and post-impact solar flux on a plane surface.

momentum per unit area is

$$\frac{E_0 \bar{d}_{se}^2}{d_{ss}^2 c} \underline{d}$$

and the post-impact value may be computed by taking each surface-reaction in turn.

For absorption the post-impact velocity is zero, whilst for direct transmission the velocity is unaltered. For the proportion r_s , the tangential component of momentum is unchanged while the normal component is reversed and, from Figure 3.1, $\theta_r = \theta_i$. Thus, comparing normal and tangential components for this proportion, the post-impact direction, \underline{a} , satisfies

$$\underline{a} \cdot \underline{n} = -\underline{d} \cdot \underline{n}$$

$$\text{and } \underline{a} - (\underline{a} \cdot \underline{n})\underline{n} = \underline{d} - (\underline{d} \cdot \underline{n})\underline{n}$$

whence

$$\underline{a} = \underline{d} - 2(\underline{d} \cdot \underline{n})\underline{n}$$

$$= \underline{d} + (2 \cos \theta_i)\underline{n}$$

and the post-impact momentum arising from the specularly reflected proportion r_s is

$$\frac{E_0 \bar{d}_{se}^2}{d_{ss}^2 c} r_s (\underline{d} + 2 \cos \theta_i \underline{n}).$$

For the proportion r_d , a completely diffuse reaction is assumed, in the sense that the reflected photons are distributed with a conical beam, centred on the surface normal, of half angle $\pi/2$. The resultant tangential component of post-impact momentum is zero by symmetry, while the normal component is given by [Schamberg, 1959, pp.64-67],

$$\frac{E_0 \bar{d}_{se}^2}{d_{ss}^2 c} \frac{2r_d}{3} \underline{n}.$$

Finally, for diffusely transmitted solar flux the same assumptions are made as for the diffusely reflected proportion. Thus, since the post-impact direction is opposite to that of this last case, the same result obtains but with r_d replaced by $-t_d$.

Differencing the sum of these post-impact momenta from the incident value, yields a total flux momentum change per unit area of a given satellite surface. To obtain the momentum change over the whole surface, this expression is simply multiplied by the visible plane area perpendicular to the incident flow, $A_S \cos \theta_i$. Thus, by the arguments at the beginning of Section 3.2, the force on a given

surface of a satellite, due to direct solar radiation pressure, can be written as

$$\underline{F}_R = \frac{E_0 \bar{d}_{se}^2}{d_{ss}^2 c} A_S \cos \theta_i \left((1 - t_s - r_s) \underline{d} - 2 \left(r_s \cos \theta_i + \left(\frac{r_d - t_d}{3} \right) \right) \underline{n} \right). \quad (3.2)$$

3.2.2 Free molecular aerodynamics

Analogously to direct solar radiation pressure, derivation of the aerodynamic force on a satellite may be made from consideration of the incident and post-impact momenta of the atmospheric flux particles. Consider a single uncharged particle moving with an average velocity \underline{u} relative to the satellite. Let this velocity subtend an angle θ_i with some given surface normal, \underline{n} . Further, assume a post-impact velocity \underline{v} subtending an angle θ_r with the same normal, as in Figure 3.2. The resulting force on the satellite, due to this single incident particle, may be

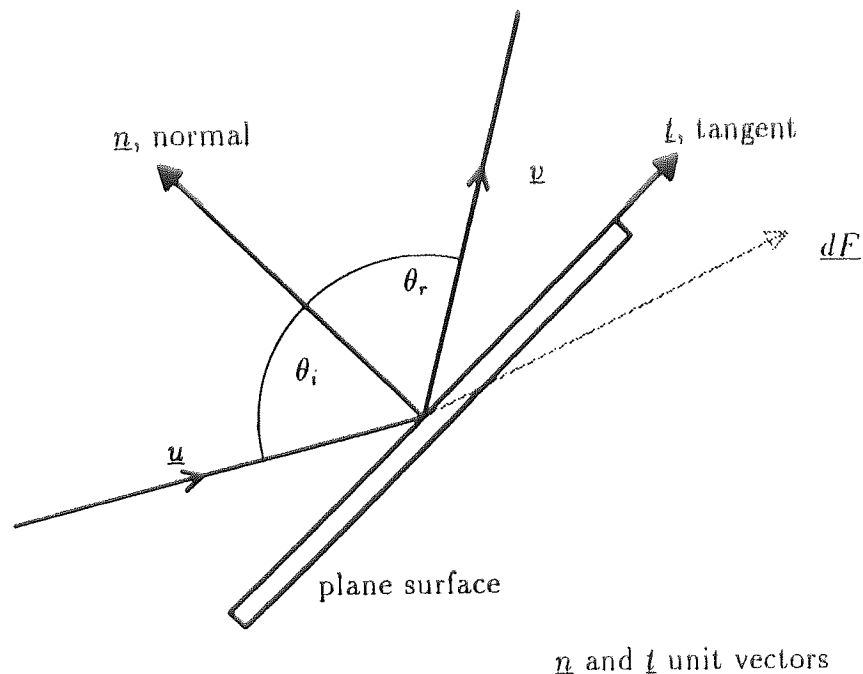


Figure 3.2: Force from a single aerodynamic particle on a flat plate.

written in terms of its normal and tangential components of momentum (p and τ), or equivalently (in the manner of Section 3.2), in terms of momentum change where the particle has a mass m , thus:

$$\begin{aligned} \underline{dF} &= -p\underline{n} + \tau\underline{t} \\ &= -(m\underline{v} - m\underline{u}). \end{aligned} \quad (3.3)$$

The values of the momentum components may then be found from scalar products,

$$\begin{aligned} p &= (m\underline{v} - m\underline{u}) \cdot \underline{n} = m(v \cos \theta_r + u \cos \theta_i) = p_r + p_i \\ \tau &= -(m\underline{v} - m\underline{u}) \cdot \underline{t} = m(u \sin \theta_i - v \sin \theta_r) = \tau_i - \tau_r \end{aligned}$$

where the subscripts i and r denote incident and reflected (or post-impact) respectively.

To compute the incident momentum on a given surface, it is first necessary to find the number of particles striking a unit surface in a unit time. With \underline{u} defined as above, let $\underline{\omega}$ be the velocity vector of a particular particle, relative to the satellite. Then the number of particles, dN , moving at velocities between $\underline{\omega}$ and $\underline{\omega} + d\underline{\omega}$ is given by

$$dN = f(\underline{\omega}) d\omega_x d\omega_y d\omega_z \quad (3.4)$$

for $\underline{\omega}$ in some Cartesian coordinate system with components ω_x , ω_y and ω_z . The function, $f(\underline{\omega})$, given by Schidlovskiy [1967] for conditions of free-molecular flow, is

$$f(\underline{\omega}) = n \left(\frac{2\pi RT}{M} \right)^{-3/2} \exp \left(\frac{-|\underline{\omega} - \underline{u}|^2}{2RT/M} \right) \quad (3.5)$$

where n is the number density of the rarefied gas (in this case the atmosphere), R the specific gas constant, T the absolute temperature and M the gas's mean molecular mass.

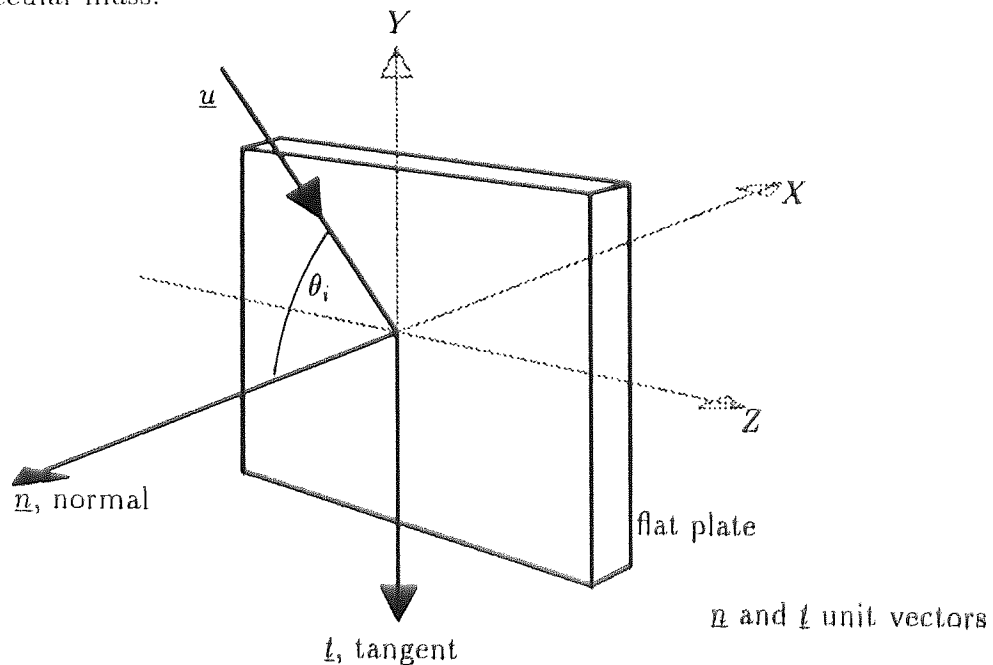


Figure 3.3: The incident velocity \underline{u} and the Cartesian system for the particular velocity $\underline{\omega}$.

Let the Cartesian system for $\underline{\omega}$ be chosen so that the vector \underline{u} lies in the XY -plane (as in Figure 3.3) making an angle θ_i with the surface normal \underline{n} (which lies along the negative X -axis). Then Equation 3.5 becomes

$$f(\underline{\omega}) = n \left(\frac{2\pi RT}{M} \right)^{-3/2} \exp \left(\frac{-(\omega_x - u \cos \theta_i)^2 - (\omega_y + u \sin \theta_i)^2 - \omega_z^2}{2RT/M} \right) \quad (3.6)$$

where $u = |\underline{u}|$. From Equations 3.4 and 3.6 it follows that the number of particles striking a unit area in unit time is

$$\int_{\underline{\omega}: \omega_x > 0} \omega_x f(\underline{\omega}) d\underline{\omega}$$

where the restriction on the integral arises from the fact that ω_x must be positive in order for the particle to collide with the surface at all. Hence the incident momentum may be expressed in terms of the normal and tangential momentum coefficients, by

$$p_i = \int_{\underline{\omega}: \omega_x > 0} \omega_x (m\omega_x) f(\underline{\omega}) d\underline{\omega}$$

$$\tau_i = \int_{\underline{\omega}: \omega_x > 0} \omega_x (m\omega_y) f(\underline{\omega}) d\underline{\omega}.$$

Evaluating these integrals yields the following [Schaaf and Chambré, 1958, p.701]

$$p_i = \frac{\rho RT}{M} \frac{\Pi(s \cos \theta_i)}{\sqrt{\pi}} \quad (3.7)$$

$$\tau_i = \frac{\rho RT}{M} \frac{X(s \cos \theta_i)}{\sqrt{\pi}} s \sin \theta_i$$

where the aerodynamic speed ratio, s , is given by

$$s = \frac{u}{\sqrt{2RT/M}}$$

and the functions Π and X are defined by

$$X(x) = e^{-x^2} + x\sqrt{\pi}(1 + \operatorname{erf}(x))$$

$$\Pi(x) = xX(x) \frac{\sqrt{\pi}}{2} (1 + \operatorname{erf}(x))$$

with the error function

$$\operatorname{erf}(x) = \frac{2}{\sqrt{\pi}} \int_0^x e^{-t^2} dt.$$

Just as for direct solar radiation pressure, the proportional coefficients of Equation 3.1, describing the surface-particle reaction, are used to produce the post-impact momenta from the incident values of Equation 3.7.

Taking each proportion in turn, as before, it can be seen that the fraction of incident particles which is absorbed has a zero post-impact momentum, all its incident momentum being transferred into an equivalent negative momentum of the satellite. Conversely, the post-impact momentum of those fractions which undergo specular reflection or direct transmission give post-impact momentum coefficients

$$p_r = -r_s p_i$$

$$\tau_r = r_s \tau_i$$

and

$$p_r = t_s p_i$$

$$\tau_r = t_s \tau_i$$

respectively.

Considering the proportion r_d which is diffusely reflected, it is again assumed that this forms a conical beam of half-angle $\pi/2$ centred on the surface normal. So, as for direct solar radiation pressure, the post-impact tangential component will be zero ($\tau_r = 0$). However, the speed of the reflected particles still has to be determined (whereas photons are assumed to have the same incident and post-impact speed, namely that of light). It is assumed that this speed lies between a minimum arising as a consequence of the surface temperature (T_S), i.e.

$$\frac{1}{2} \sqrt{\frac{2\pi RT_S}{M}}$$

and the incident value. The actual post-impact momentum of this fraction of the incident particles may then be obtained by varying the proportions which travel at each of these two limiting speeds.

Next, suppose a proportion σ is reflected at the speed imbued by the surface temperature, then the post-impact momentum of the whole of this diffusely reflected proportion is

$$p_r = \frac{\rho RT}{M} \left(\frac{\sigma r_d}{2} \sqrt{\frac{T_S}{T}} X(s \cos \theta_i) \right) + \frac{2p_i}{3} (1 - \sigma) r_d. \quad (3.8)$$

A similar result is obtained for the diffusely transmitted proportion, by simply replacing r_d in Equation 3.8 with $-t_d$, (exactly as was effected in the case of direct solar radiation pressure in Section 3.2.1).

Finally, the values of p and τ required by Equation 3.3 may now be determined by combining their respective components from all these gas-surface interaction modes. Thus, the total normal and tangential components of the aerodynamic force may be written

$$p = \frac{\rho RT}{M} \left(\left[1 - t_s + r_s + \frac{2}{3}(1 - \sigma)(r_d - t_d) \right] \frac{\Pi(s \cos \theta_i)}{\sqrt{\pi}} + \frac{\sigma(r_d - t_d)}{2} \sqrt{\frac{T_S}{T}} X(s \cos \theta_i) \right) \quad (3.9)$$

$$\tau = \frac{\rho RT}{M} \left([1 - t_s - r_s] \frac{X(s \cos \theta_i)}{\sqrt{\pi}} s \sin \theta_i \right).$$

Whence, from Equation 3.3, the total force on a given surface having visible effective area $A_S \cos \theta_i$ is simply

$$\underline{F}_d = A_S \cos \theta_i (-p\underline{n} + \tau\underline{t}) \quad (3.10)$$

with p and τ defined by the previous equation (3.9).

3.3 The GUESS area-table software

In order to utilise Equations 3.2 and 3.10 in place of the existing equations of the SATAN-A suite (namely 2.6 and 2.5), their constituent variables must be estimated, evaluated, or known. In practice, the surface interaction coefficients (Equation 3.1) fall into the first category with values being a combination of estimate and theory for a region of space where there is little empirical evidence [Ries, 1992]. Other values are well known (E_0 , c and M), measurable (R and T , hence s) or modelled (ρ). For full evaluation of these two equations, the only other variables required are A_S , θ_i and \underline{d} . The aim here is to produce values of A_S , tabulated by \underline{d} , where \underline{d} is defined by two angles. In the case of aerodynamic resistance, it will also prove necessary to consider an additional angle, giving the rotation of the solar array. A suite of programs, GUESS (Geometry-Utilising Estimation of Satellite Surfaces) has been developed to produce just such a set of tables. In addition modifications have been made to the existing SATAN-A suite to utilise the derived tables in the orbit prediction process.

The GUESS software works from a user-defined geometric model comprising a discretization of the satellite into planar triangular or quadrilateral elements.

Each element consists of a surface normal, a given area, the appropriate number of vertices and the necessary surface interaction coefficients (Equation 3.1). In addition, the geometric input file contains the satellite's mass, locations of centre-of-mass and instrumentation (such as the laser retroreflector array) and solar panel axis of rotation (given as a point and a direction). The solar array itself is then stored in any arbitrary position from which the software computes its true location and orientation.

An advantage of this discretization is that it allows for unrestricted complexity in the geometric model, the only practical restraint being available processing time. Conversely, despite the fact that errors will undoubtedly increase as the model increasingly deviates from reality, a more accurate shape incurs correspondingly larger uncertainties in the less well known surface interaction coefficients. (since a greater number of these will require estimation). Further, the above assumptions of parallel flux and single impact give rise to errors in the modelled forces. Thus, increasing the model accuracy is only valuable where it results in an improvement in the computed force which outweighs the errors imposed by these other limitations.

The satellite model used by GUESS is constructed in a system fixed in the

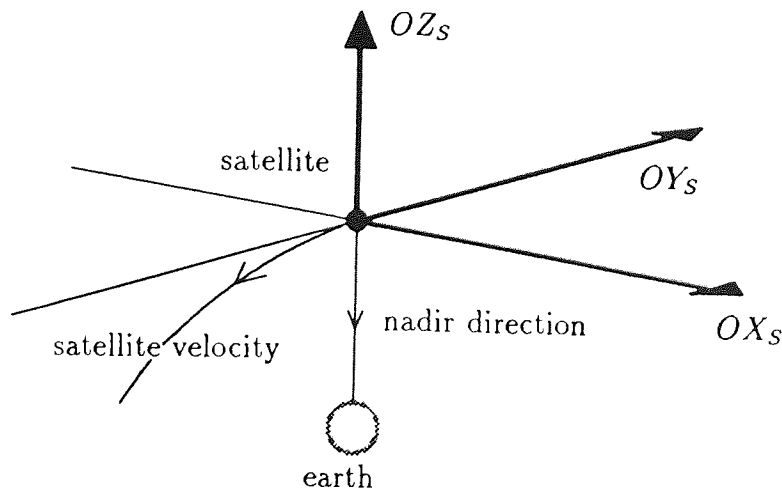


Figure 3.4: The satellite-fixed coordinate system.

satellite ($OX_S Y_S Z_S$). Any system would be acceptable in theory but in practice (to minimise the necessary modifications of the existing software) the following one was chosen. The OZ_S -axis lies in the nadir pointing direction, which in the case of most altimetric satellites will be normal to the satellite surface which most

closely faces the Earth. Then, the OX_S -axis is the vector (or cross) product of the OZ_S -axis and the satellite velocity vector. The product is taken in such a way as to cause the OY_S -axis to oppose as closely as possible the satellite's direction of travel (velocity vector). The three axes thus obtained form the right-handed system illustrated in Figure 3.4.

The next section describes what goes on in the GUESS package, in particular detailing how the geometric file is used to compute the visible areas for each surface element of the geometric model of the satellite over a range of angles.

3.4 Evaluation of the area tables: theory

The program begins by rotating the whole model into a coordinate system based on the solar array axis of rotation which is defined ($OX_A Y_A Z_A$) as follows,

$$\begin{aligned} \underline{OZ}_A &= \underline{a} \\ \underline{OX}_A &= \begin{cases} \underline{OX}_S & \text{if } \underline{OY}_S \parallel \underline{a} \\ \underline{OY}_S \times \underline{a} & \text{otherwise} \end{cases} \\ \underline{OY}_A &= \underline{OZ}_A \times \underline{OX}_A \end{aligned} \quad (3.11)$$

where \underline{a} is the direction vector of this axis and the origin of the new system is given by some point on this axis, \underline{p} say, (given as a position vector in the satellite fixed system within the geometric input file).

The normals, \underline{n} , and vertices, \underline{v} , in the geometric input file are rotated to this new system using the relationships,

$$\underline{n}_A = (\underline{n}_S \cdot \underline{OX}_A) \underline{OX}_A + (\underline{n}_S \cdot \underline{OY}_A) \underline{OY}_A + (\underline{n}_S \cdot \underline{OZ}_A) \underline{OZ}_A$$

$$\underline{v}_A = ((\underline{v}_S - \underline{p}) \cdot \underline{OX}_A) \underline{OX}_A + ((\underline{v}_S - \underline{p}) \cdot \underline{OY}_A) \underline{OY}_A + ((\underline{v}_S - \underline{p}) \cdot \underline{OZ}_A) \underline{OZ}_A.$$

This procedure simplifies the rest of the program as, in this new system, the sun position need only be defined by one angle: namely that by which the solar panels must be rotated about the OZ_A -axis to move them from their stored position to a sun-pointing one.

Since the incident flux vector still requires two angles to be fully defined, this means that the tables will be in at most three angles (one for the sun rotation

vector and two for the incident flux vector). Indeed, for direct solar radiation pressure only two angles will be necessary, since one of these is also the required angle of rotation for the solar array (see Figure 3.5). The solar array is rotated

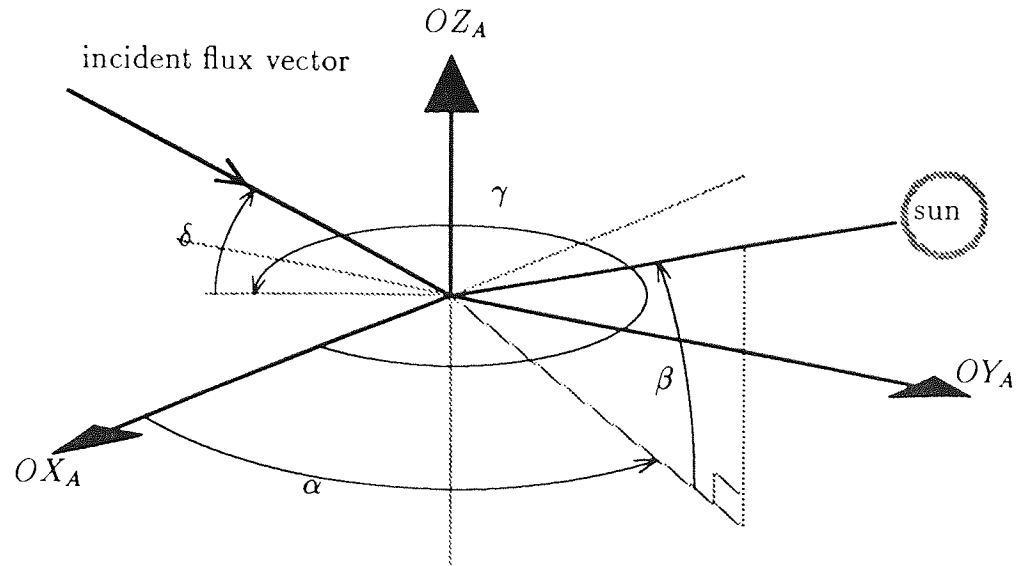


Figure 3.5: The angles defining both the sun position (α, β) and the incident flux vector (γ, δ).

through an angle θ where

$$\theta = \alpha - \arctan\left(\frac{n'_{Ax}}{n'_{Ay}}\right), \quad (3.12)$$

α being defined in Figure 3.5 and

$$\underline{n}'_A = n'_{Ax}\underline{OX}_A + n'_{Ay}\underline{OY}_A + n'_{Az}\underline{OZ}_A$$

the normal of the sun-facing side of the solar panels in its stored position in the axial system (defined by Equation 3.11). Equation 3.12 simply states that the rotation angle is the difference between the sun angle α and the fixed angle of the relevant surface normal, measured in a plane perpendicular to the rotation axis.

The model now lies in the $OX_A Y_A Z_A$ system, correctly orientated with respect to the sun. The next step in the GUESS programs is to project this geometry into a plane perpendicular to the incident flux vector (defined by angles γ and δ of Figure 3.5). The projection is carried out by considering the incident unit flux vector to be the OZ_V -axis of a third coordinate system, $OX_V Y_V Z_V$, with

$$\underline{OX}_V = \begin{cases} \underline{OX}_A & \text{if } \underline{OY}_A \parallel \underline{OZ}_V \\ \underline{OY}_A \times \underline{OZ}_V & \text{otherwise} \end{cases}$$

$$\underline{OY}_V = \underline{OZ}_V \times \underline{OX}_V$$

defining the other two axes, in a manner analogous to the previous coordinate change. However, as the normals and vertices are now all position vectors, i.e. given from the same origin, they may be easily converted to this new system using the single relationship

$$\underline{x}_V = (\underline{x}_A \cdot \underline{OX}_V) \underline{OX}_V + (\underline{x}_A \cdot \underline{OY}_V) \underline{OY}_V + (\underline{x}_A \cdot \underline{OZ}_V) \underline{OZ}_V$$

where $\underline{x}_{\text{system}}$ represents either a normal or a vertex ($_{\text{system}=V}$ or $_A$ for projected and axial systems respectively). The origin remains unchanged as any plane perpendicular to the incident flux vector is appropriate.

At this point, the projected surface elements consist of groups of vertices lying in the $OX_V OY_V$ -plane of the $OX_V Y_V Z_V$ system, with the OZ_V coordinate representing the “height” of the vertex above this plane. In consequence, each projected surface element may be entirely and closely enveloped by a rectangular box lying in the same plane and having sides parallel to the OX_V and OY_V axes. In addition, all such boxes may be entirely and closely contained within a single larger rectangle as illustrated in Figure 3.6. The visible area is then calculated by

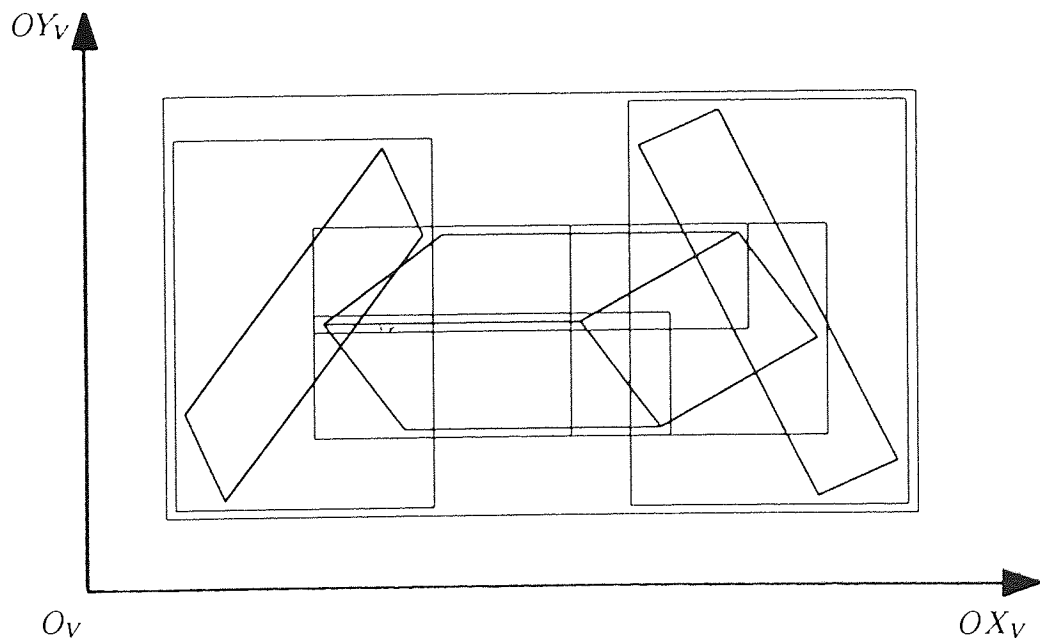


Figure 3.6: Enclosing the projected surface elements in boxes within the projective $OX_V OY_V$ -plane.

sub-dividing the larger box into a square-grid of pre-determined mesh size. Each

square in the grid is centred on some point, $\underline{q} = (q_x, q_y)$ say, which may be associated with an incident flux particle travelling on a path parallel to the OZ_V -axis and passing through this point. Taking each such point in turn the program tests whether or not it lies within none, one, or more than one of the projected surfaces by considering a number of conditions. Each condition must be met before the next is tested. Failure at any stage means that point does not lie within this projected surface, hence that the particle associated with this point does not hit this element. In this event, take the next surface element or, when all have been considered, the next grid point.

Thus, for any point and any surface element, the program first determines whether or not the point lies within the relevant small enveloping rectangle of that element (see Figure 3.6). This is effected by comparing the values of q_x and q_y with the edges of the rectangle. Secondly, the program deduces whether or not the point lies inside the wedge defined by two adjacent edges of the projected surface element (see Figure 3.7). Here the projected vertices have been labelled \underline{u} , \underline{v} , \underline{w} and \underline{x} (in an anti-clockwise manner). If the point lies in the wedge then

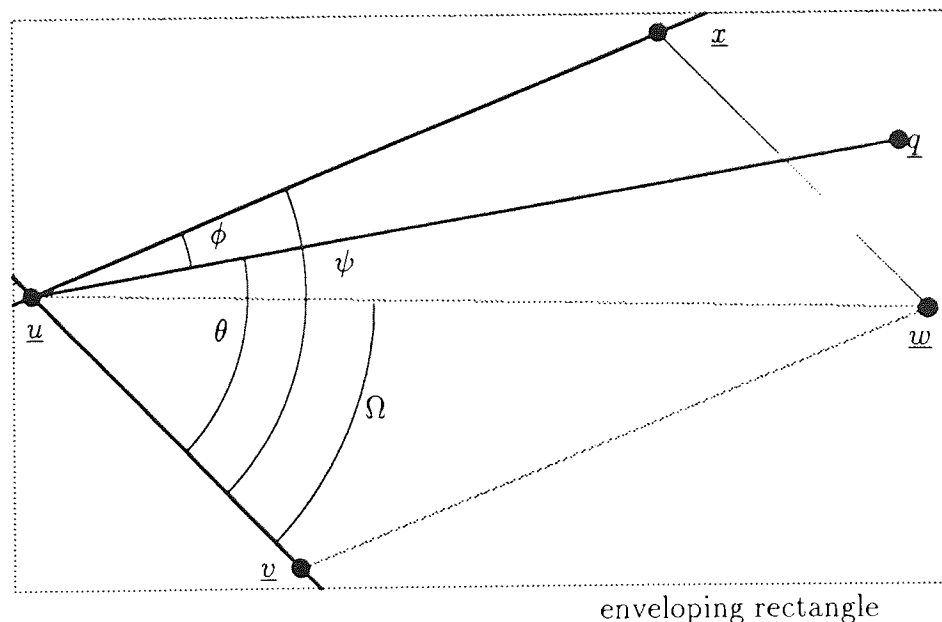


Figure 3.7: The wedge associated with a projected surface element and the angles θ , ϕ , ψ and Ω .

the angles θ , ϕ and ψ of Figure 3.7 satisfy $\theta + \phi = \psi$, hence

$$\begin{aligned} \arccos \left(\frac{(\underline{v} - \underline{u}) \cdot (\underline{x} - \underline{u})}{|\underline{v} - \underline{u}| |\underline{x} - \underline{u}|} \right) &= \arccos \left(\frac{(\underline{q} - \underline{u}) \cdot (\underline{v} - \underline{u})}{|\underline{q} - \underline{u}| |\underline{v} - \underline{u}|} \right) \\ &+ \arccos \left(\frac{(\underline{q} - \underline{u}) \cdot (\underline{x} - \underline{u})}{|\underline{q} - \underline{u}| |\underline{x} - \underline{u}|} \right) \end{aligned}$$

which actually implies that the point lies in the X -shaped region limited by the extended edges $\underline{v} - \underline{u}$ and $\underline{x} - \underline{u}$ (forming two wedges joined at the point \underline{u}). However, because of the way in which the enveloping box is chosen, the point cannot lie in the smaller wedge (on the side of \underline{u} opposite to the projected surface element) since the spacing between \underline{u} and the edge of the enveloping rectangle is less than half the grid spacing. Thus, this condition is equivalent to saying that the point does indeed lie in the wedge of Figure 3.7.

Thirdly, the program determines which three vertices form the smaller wedge in which the point lies (only necessary for quadrilateral surface elements). Again, referring to Figure 3.7, it may be seen that the point lies in the wedge formed by the vertices \underline{u} , \underline{v} and \underline{w} if $\theta < \Omega$ and in that formed by \underline{u} , \underline{w} and \underline{x} otherwise. In either event, the three vertices are re-labelled \underline{u} , \underline{v} and \underline{w} so that Figure 3.8 pertains. Referring to this figure, the point of intersection of a line through \underline{u} and

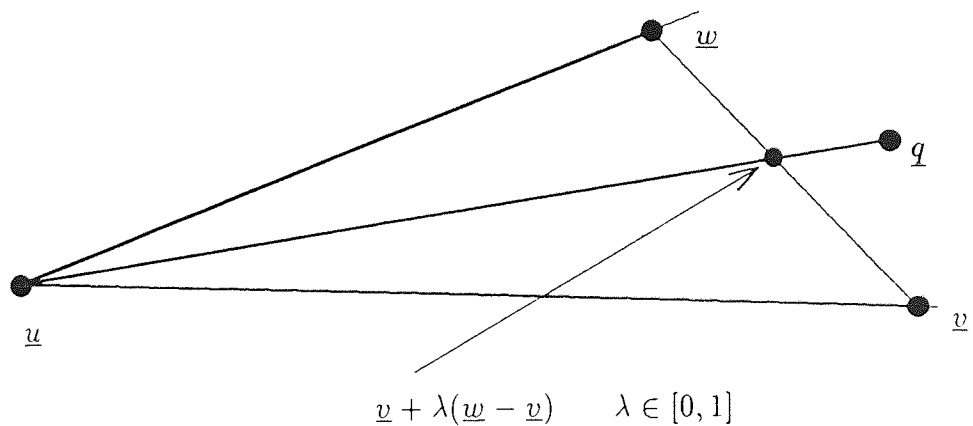


Figure 3.8: The vector equation for a point on the edge of a triangle.

\underline{q} with the edge of the triangle $\underline{v} - \underline{w}$ is such that

$$\underline{u} + \mu(\underline{q} - \underline{u}) = \underline{v} + \lambda(\underline{w} - \underline{v}) \quad (3.13)$$

for real numbers μ and λ with $\lambda \in [0, 1]$.

Now, the point \underline{q} lies within the triangle formed by these three vertices (hence within the projected surface element) if and only if $\mu \geq 1$. Whence, by writing

Equation 3.13 as a pair of simultaneous equations in μ and λ and substituting in for λ so that

$$\mu = \frac{(\underline{u}_x - \underline{v}_x)(\underline{v}_y - \underline{w}_y) - (\underline{u}_y - \underline{v}_y)(\underline{v}_x - \underline{w}_x)}{(\underline{u}_x - \underline{q}_x)(\underline{v}_y - \underline{w}_y) - (\underline{u}_y - \underline{q}_y)(\underline{v}_x - \underline{w}_x)},$$

μ may be evaluated, thus indicating whether or not the point lies inside the projected surface element.

The argument so far will determine which surface elements the path of an incident flux particle will intersect but not which of those it will actually strike — clearly it will only strike one. Where a point lies inside more than one projected surface element, the program considers the OZ_V components of the elements in question. Let \underline{n}_V be normal to a surface element in the $OX_V Y_V Z_V$ system and let \underline{v}_V be any of its vertices, then

$$\underline{n}_V = n_{Vx} \underline{OX}_V + n_{Vy} \underline{OY}_V + n_{Vz} \underline{OZ}_V$$

and the equation for the plane in this system in which the surface element lies is

$$n_{Vx}x + n_{Vy}y + n_{Vz}z = \underline{n}_V \cdot \underline{v}_V.$$

Hence,

$$z = \left(\frac{\underline{n}_V \cdot \underline{v}_V - n_{Vx}q_x - n_{Vy}q_y}{n_{Vz}} \right)$$

gives the “height” of the point of intersection of the particle’s path and the surface element above the projective plane. For a particle associated with the point \underline{q} in the manner described above, the incident surface element is that with the greatest z -value of all those surface elements intersected by the particle’s path.

The number of intersections (N_{int}) and of hits (N_{hit}) are summed over all points \underline{q} for each surface element. Then, for any given element, the visible projected area ($A_{v,p,i}$) perpendicular to the incident flux may be given as a proportion of the total projected area

$$A_{v,p,j} \approx \frac{N_{hit,j}}{N_{int,j}} A_j \cos \theta_{i,j} \quad (3.14)$$

for surface element j where the actual surface area is A_j and $\theta_{i,j}$ is the incidence angle at this surface. Noting that $A_{v,p,j}$ is the $A_S \cos \theta_i$ of Equations 3.2 and 3.10, Equation 3.14 may be written as

$$A_S \approx \frac{N_{hit,j}}{N_{int,j}} A_j$$

with the level of approximation governed by the accuracy of the model and area estimation procedure (i.e. N_{hit} and N_{int}).

3.5 Further developments

The previous section described in some detail how the visible areas are determined for use in the skin force equations (3.2 and 3.10). However, consideration of the former equation indicates that further computation may be made prior to the orbital determination procedure (thereby reducing the number of required calculations within the adapted programs). Indeed, Equation 3.2 may be decomposed into two parts, namely

$$A_S \cos \theta_i \left([1 - t_s - r_s] \underline{d} - 2 \left[r_s \cos \theta_i + \left(\frac{r_d - t_d}{3} \right) \right] \underline{n} \right) \quad (3.15)$$

and

$$\frac{E_0 \bar{d}_{sc}^2}{d_{sc}^2 c},$$

the first of which depends only upon the geometry of the satellite model and the angles of incidence. Hence, Equation 3.15 may be evaluated regardless of specific values of planetary and satellite ephemeris, and atmospheric conditions. Since the aim is to tabulate over a range of angles, then interpolate between the tabulated values within the prediction process, storing values of Equation 3.15 rather than the simple areas will greatly reduce both storage size and computation time. The storage will be reduced because, for each pair of angles, instead of an area for each surface element of the model only one vector is required. Unfortunately, no similar decomposition is possible for Equation 3.10 because of the atmospheric components which are time and space related.

The surface-interaction coefficients (t_s, r_s, t_d, r_d, a) also have to be estimated in some way, as does the momentum exchange coefficient σ . Since these values are typically satellite dependent, details of their estimation for ERS-1 will be included in the next chapter (Chapter 4) and for SPOT-2 in Chapter 6, where the respective orbits and results are discussed. However, the following method for choosing values for the aerodynamic resistance coefficients may be applicable in general.

Consider the normal and tangential momentum exchange coefficients given by Sowter [1989, p.10]

$$\sigma_n = \frac{p_i - p_r}{p_i - p_w}$$

$$\sigma_t = \frac{\tau_i - \tau_r}{\tau_i}$$

where p_w is the theoretical normal momentum arising from the incident surface temperature T_S , all the other variables being previously defined (with indices as above). Then, comparing Sowter's [1989, p.11] equations for p and τ with those of Equation 3.9 above, it is possible to obtain a system of simultaneous equations in the coefficients of Equation 3.1 and the momentum exchange coefficients σ_n and σ_t . Indeed, there are in fact two distinct equations for σ_n alone:

$$\begin{aligned}\sigma_t &= 1 - t_s - r_s \\ \sigma_n &= 1 + t_s - r_s - \frac{2}{3}(1 - \sigma)(r_d - t_d) \\ \sigma_n &= \sigma(r_d - t_d).\end{aligned}\tag{3.16}$$

Now, experimental work (such as that cited by Schaaf and Chambré [1958, p.695] and, more recently, that done on the ANS-1 satellite, [Moore and Sowter, 1991]) indicates that in certain instances, σ_t may be expected to take a value close to one. Also, by considering the thermal accommodation coefficient used by Smoluchowski in 1898 and again by Knudsen in 1911 [Schaaf and Chambré, 1958, p.695], it is possible to infer that σ_n similarly lies close to unity. Further, for satellites such as ERS-1, SPOT-2 etc. the proportion of the transmitted aerodynamic flux is zero. Thus,

$$t = t_d + t_s = 0$$

which in turn implies that both t_d and t_s are equal to zero. Hence, using the simultaneous Equations 3.16,

$$r_s = 0$$

in order that σ_t attain a value of unity. Therefore, either $1 - \sigma = 0$ or $r_d = 0$. Clearly,

$$r_d \neq 0$$

since otherwise σ_n would also be zero. Thus,

$$r_d = 1$$

$$\sigma = 1$$

$$a = 0$$

fully defining the aerodynamic interaction coefficients for use throughout the rest of this simulation. There is no similar approach for direct solar radiation since more is known about light-surface interactions and there is more variety in the way photons react with different satellite surfaces. Effectively, because more is known, the models used are more involved.

3.6 Verification of the GUESS software

The GUESS software was tested on a number of plane and solid objects to ensure that the areas produced matched those theoretically expected (given simple geometric considerations). For all shapes tested (plane rectangle and triangle, cuboid and trapezoid) the results were exactly as theoretically predicted. That is to say, the software produces true areas for convex solids. The only limitation is that the grid spacing needs to be smaller than the smallest face of the solid — so that at least some points fall inside each visible surface element. However, it is recognized and should be emphasized that such accuracy is unlikely to be attained with very complex shapes, or where there is complicated overlapping.

Chapter 4

ERS-1 orbits

4.1 The ERS-1 satellite

The first European remote-sensing satellite, ERS-1, was launched on the 16th of July 1991 into a near circular orbit of inclination 98.5° . Of the on board instrumentation, a single frequency radar altimeter provides continuous monitoring of the ocean surface between latitudes 81.5° N and 81.5° S. To enable orbit determinations, the satellite was also equipped with a retro-reflector array for precise ranging from the network of laser stations (illustrated in Figure 4.1). The altimeter data can also be used as tracking data, either directly as height measurements or elaborated to form crossover differences. In addition, ERS-1 carries a synthetic aperture radar antenna (SAR), two sun acquisition sensors, three (fore, mid and aft) wind scatterometer antennae (WSA) and the solar array — which provides electrical power to the satellite. The ERS-1 satellite is illustrated in Figure 4.2.

For optimal usage of the altimetric data, precise positioning of the satellite is necessary to an accuracy commensurate with that of the altimeter, particularly in the radial direction; namely 5 cm or less. However, such a goal is currently unrealistic since ERS-1 suffers from the problems described in the last chapter, in that surface forces are often in error by more than the gravitational ones. Further, for ERS-1, these errors are compounded by the high solar activity currently experienced in the early 1990's, the low altitude of around 780 km and the high surface-to-mass ratio of the satellite. In order to try and alleviate these difficulties, the method of Chapter 3 has been applied to this satellite.

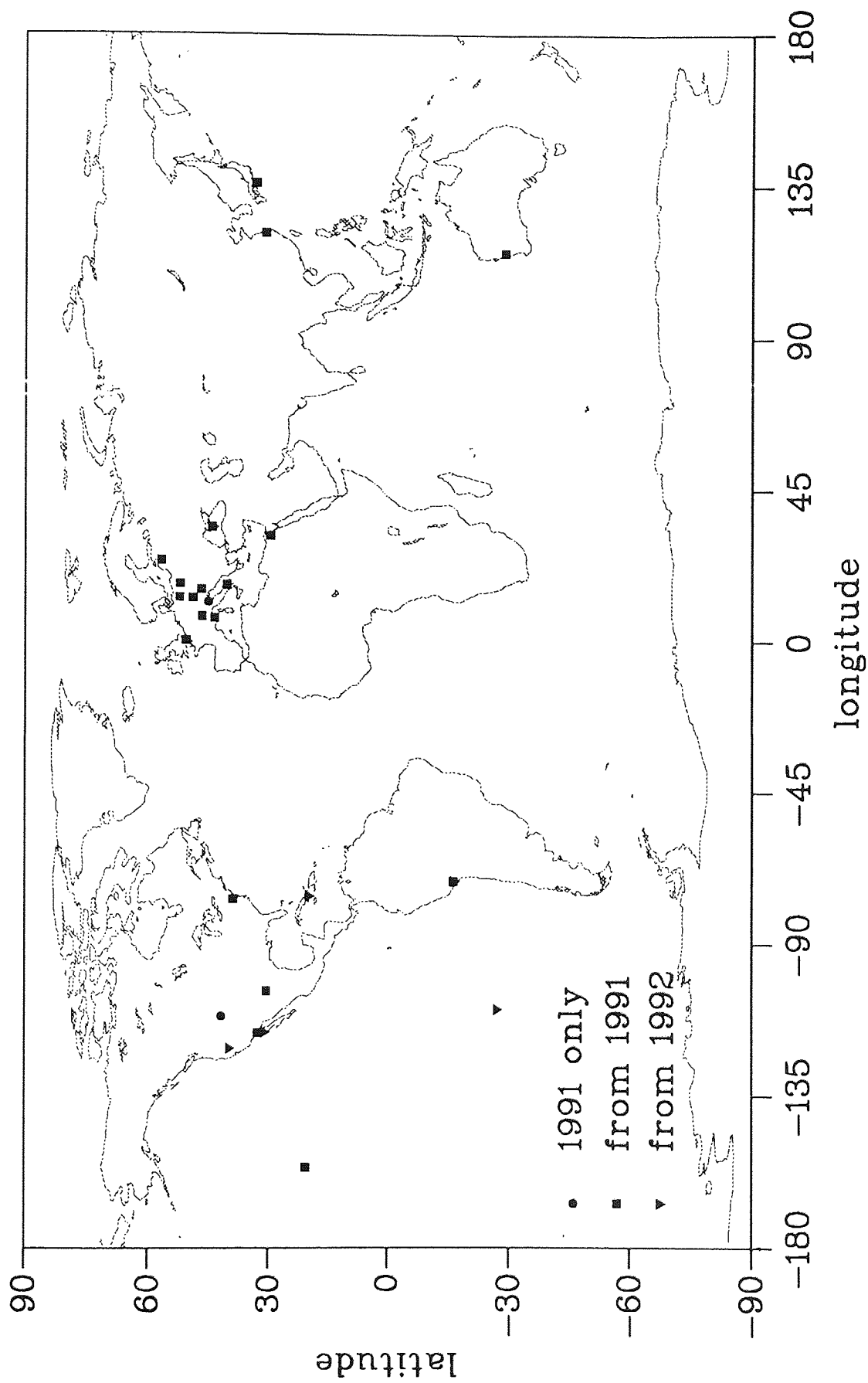


Figure 4.1: The network of laser stations ranging to ERS-1.

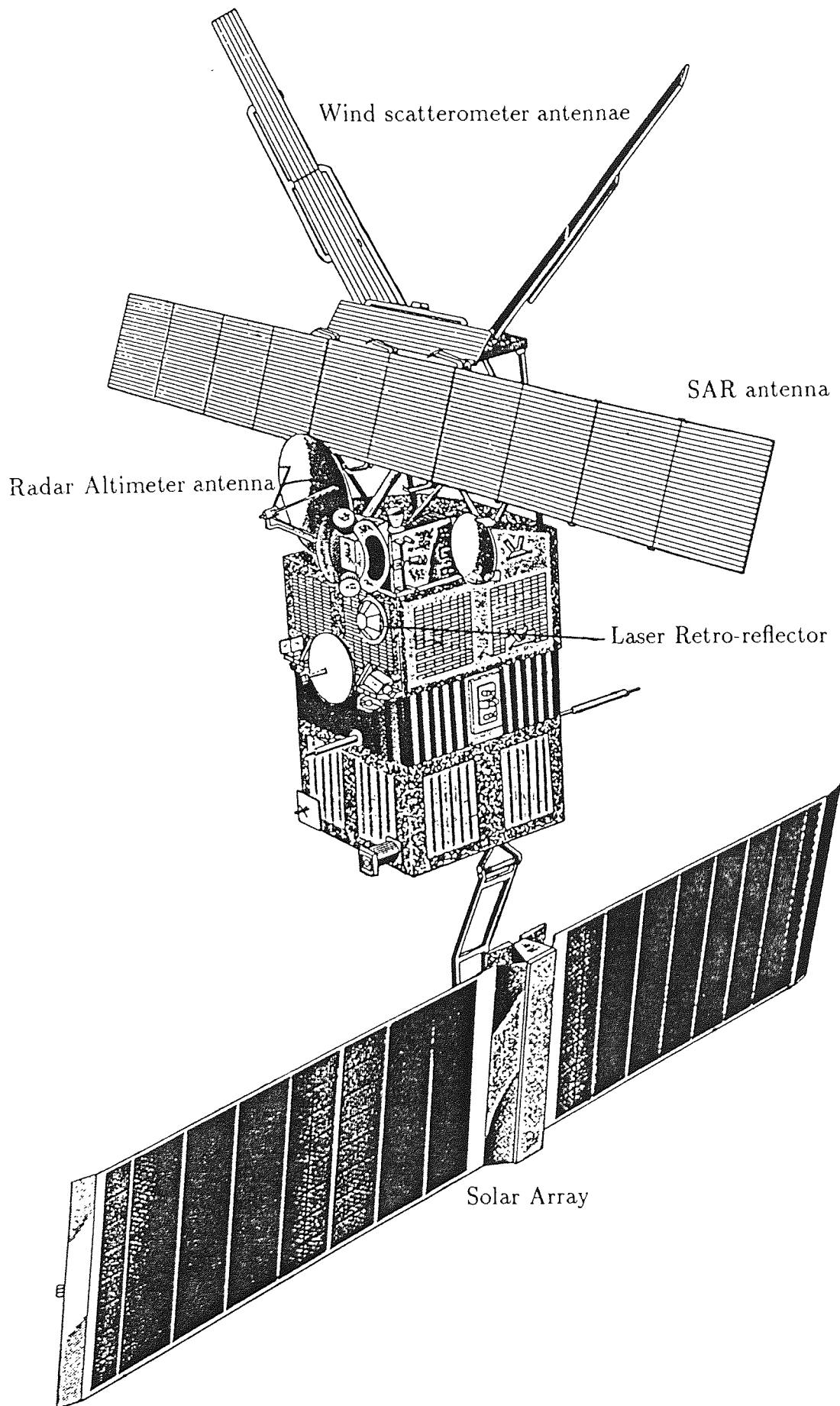


Figure 4.2: The ERS-1 satellite.

4.2 A geometric model of ERS-1

To apply the method of Chapter 3, it is first necessary to model the satellite and its surface characteristics, also estimating the variables required for the evaluation of Equations 3.10 and 3.2. Beginning with the area aspect of this problem, the satellite structure has been reduced to a composite of planar quadrilateral elements in accordance with the requirements of the GUESS software of Chapter 3. These surface elements have been chosen to simplify the model as far as is realistically possible, while retaining the basic shape, dimensions and surface characteristics of the satellite itself. The minimum extent of this simplification was further governed by the available processing time.

Essentially, the model adopted for ERS-1 comprises a trapezoidal box surmounted by a number of planes, as illustrated in Figure 4.3. Thus, the box approximates the satellite module and payload and the planes the WSA, SAR and solar array. With the exception of the single sloping face, each of the surface elements of the box lies perpendicular to one of the axes of satellite-fixed coordinate system of Figure 3.4 (Section 3.3). Further, all six box surface elements are estimated so that, viewed along the relevant *perpendicular* axis, the modelled cross-sectional area equals the true value (i.e. of the actual satellite).

The SAR and three WSA antennae are each represented by two surface elements, of equal area, placed back-to-back. The only difference between the two elements of such a pair lies in the opposing directions of the outward pointing normal vectors. The solar array is made up of four such surface elements, forming two perpendicularly intersecting planes (each plane comprising a back-to-back pair of surface elements as for the WSA and SAR). One of these two planes represents the solar panel surface (and its back) and the other (far smaller) the thickness of the central portion which attaches the array to the satellite module, as viewed along the line of the solar panels. Hence, the minimum end-on area possessed by the true solar array is also reflected in the geometric model.

Each of the model's surface elements is stored in a record within the geometric input file (required by the GUESS software) as four vertices, a full plane area and an outward-pointing normal vector in the satellite-fixed system of Chapter 3. Since the solar array rotates, the vertices and normals of this portion of the model

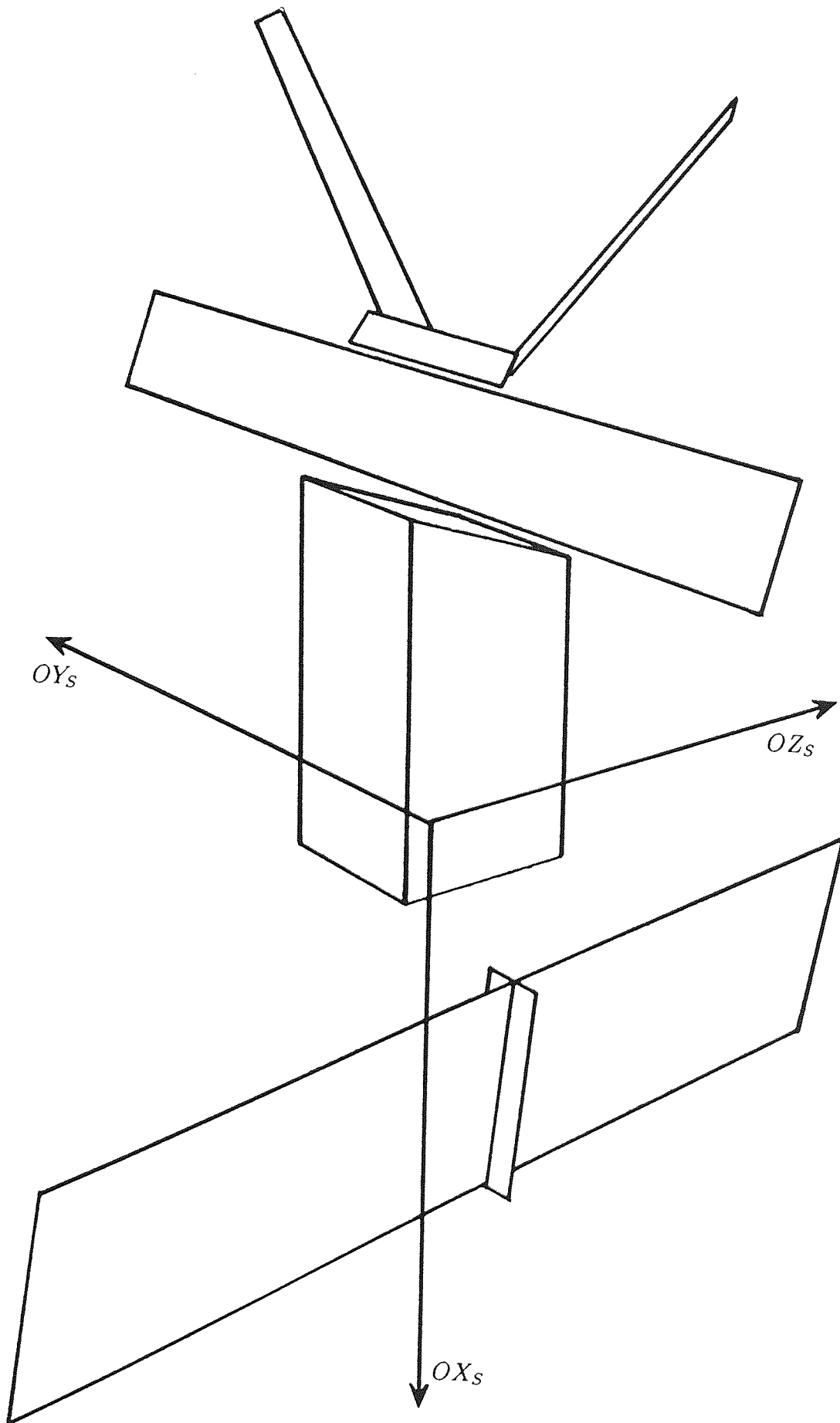


Figure 4.3: The ERS-1 model and satellite-fixed coordinate system.

will vary. However, for compatibility with the GUESS software the solar panel face is nominally fixed in any attainable position (for instance aligned as closely as possible to one of the system's axes). This fixes the four vertices and normal for this element. The vertices and normals of the other three elements may then be computed relative to the stored position of the fixed solar panel element. Thus, the geometry of the whole array is internally consistent. From this stored position, the *true* position may be attained by rotating the whole array about the axis of rotation.

For ERS-1, the solar array rotates about a single axis lying parallel to the OX_S -axis of the satellite-fixed system, $OX_S Y_S Z_S$, (illustrated in Figure 4.3) and passing through a point, O_A say, on the positive OZ_S -axis. Thus, the relationship between the satellite-fixed and axial systems of Chapter 3 is as illustrated in Figure 4.4. Though the axis of rotation of the solar array, hence OZ_A , is parallel

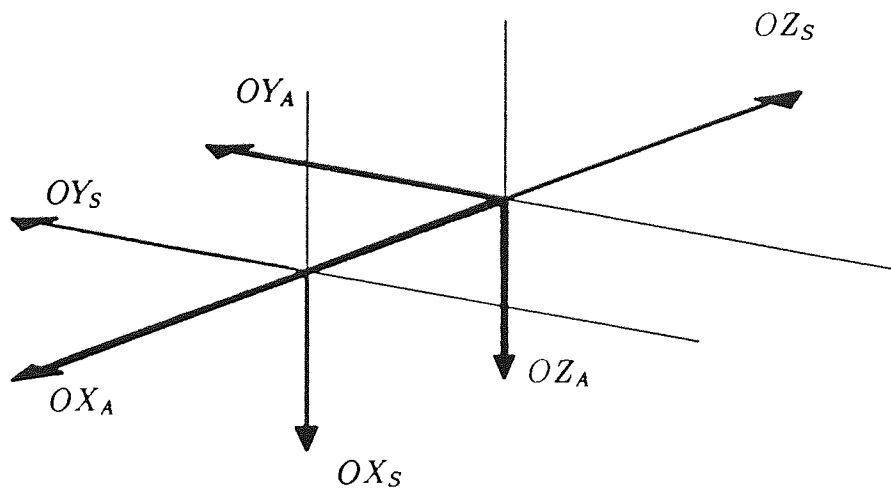


Figure 4.4: Satellite-fixed and axial systems for ERS-1.

to OX_S for ERS-1, such a relationship is not necessary to the GUESS software which may be employed for a solar array axis of rotation pointing in any direction and lying through any point in the satellite fixed system, $OX_S Y_S Z_S$.

In addition to the model's geometry, the input file for the GUESS software must include the satellite's identity, mass and the location (in the satellite fixed system) of the satellite's centre of mass, laser retro-reflector array, altimeter and

any other instrumentation used for tracking data — and therefore necessary to the programs in the SATAN-A suite. The values of these have been extracted from ERS-1 documentation [Pieper, 1988 and Renard, 1990]. Furthermore, the GUESS software requires the coefficients a , t_s , t_d , r_s , r_d and σ of Equations 3.1 and 3.8 which describe the behaviour of incident flux particles at the satellite's surface. These are derived as follows, drawing largely on values given in the same documentation as above.

For the atmospheric resistance force of Equation 3.10 these coefficients are determined just once and are the same for all model surface elements. The method of determination has already been described in Section 3.5 above. However, for direct and reflected solar radiation pressure, the necessary coefficients, namely a , t_s , t_d , r_s , and r_d must be computed independently for each surface element of the model. Further, values are required for both direct and earth-reflected light and that fraction of the solar flux re-emitted by the earth as infra-red radiation. Since, as stated by Equation 3.1, these coefficients sum to unity, it is only necessary to specify four of the five variables within the input file. The values of the four chosen coefficients (r_d is omitted), are evaluated for each surface element of the geometric model from the same documentation as the satellite mass etc. above. However, since each model element may relate to more than one region on the satellite's surface, an average of the coefficients of the relevant contributing regions is made, weighting each stored coefficient by the proportion of the contributing region's area to that of the surface-element being considered.

As well as the area, vertices, normal and interaction coefficients, each record in the geometric input file is required to contain values of two extreme temperatures so that a surface temperature T_S may be computed from the formula

$$T_S = T_{S_{min}} + \nu T_{S_{max}}$$

where ν is a shadow factor describing the position of the satellite with respect to the earth's shadow ($T_{S_{min}}$ defining the temperature when fully in shadow and $T_{S_{max}}$ that in full sunlight). For each surface s , the values of the minimum and maximum are obtained in a similar manner to the solar radiation pressure coefficients (i.e. as a weighted average) from the same documentation as before.

4.3 Area tables for ERS-1

Having produced the geometric input file as described above, the GUESS software was used to determine tables for both the direct solar radiation pressure and aerodynamic resistance forces acting on ERS-1. In addition to the data held in the geometric file, the GUESS software requires a grid size to be defined and some limits on the possible angles describing the incident flux direction; the choice of which is further explained below. The grid size adopted for shooting flux particles/rays at the projected satellite model's surface elements was 50 mm by 50 mm. This had been found to produce accurate results for the test objects, was sufficiently small that the WSA would register accurately and yet was also large enough so that the computation time was less than the available maximum.

In addition, it was necessary to justify the assumptions made in the GUESS software for ERS-1, namely that the incident atmospheric flux is parallel and that only the first impact of each particle need be considered. Now, for satellites orbiting at heights of around 700km to 900km, such as ERS-1, it may be assumed that the ratio of satellite to atmospheric velocity, together with the rarefaction of the atmosphere, are concomitant with a state of *free molecular flow* [Schaaf and Chambré, 1958]. In such a state, the gas acts as a group of independent particles, where the reflected particles do not impede the incident stream. Thus, this incident stream may be taken to have a parallel average velocity. Further, for ERS-1, the single impact approximation is made on the basis of results from studies carried out by MATRA [Renard, 1990]. These indicate that computing the forces as a result of single impacts gives a degradation in accuracy of about 5% over a multiple impact model. However, the computation time is more than halved by such an approximation. Thus, given the limited accuracy of the geometric model of the satellite, it was decided that any potential increase in accuracy derived from multiple impacts was outweighed by the decrease in computation time associated with the single impact assumption.

For direct solar radiation pressure, the sun-to-satellite vector (which defines the sun's position required to rotate the solar array to its correct orientation) is also the incident flux vector. Thus, for each surface element of the geometric model, the visible areas were tabulated in just two angles, namely α and β of

Figure 3.5, over a $5^\circ \times 5^\circ$ grid covering the unit sphere centred on the satellite. It is emphasized that these angles are measured in the *axial* system of Chapter 3 and *not* the satellite-fixed system.

The areas thus produced were then employed (along with the normal vectors and interaction coefficients) in Equation 3.15 of Chapter 3 to produce a *quasi-force* for each surface element of the model. For each pair of angles (α , β) the resultant values were summed over all surface elements so that, rather than having eighteen entries (one for each surface element of the model) there were just three — describing a *quasi-force* vector in the axial system. This can then be easily converted into the direct solar radiation pressure force vector (within the orbit prediction program) using the scale factor

$$\frac{E_0 \bar{d}_{se}^2}{d_{ss}^2 c}$$

of Section 3.5.

The visible areas (produced above) were also employed to compute the effective total area perpendicular to the incident flux direction over a more widely spaced grid ($22.5^\circ \times 15^\circ$). The values of this total area, see Table 4.1, illustrate the variation experienced over the range of incident flux angles. Table 4.1 also confirms the variations in total area that are to be expected of ERS-1. First, the total area is greatest for small values of β , which is where the solar panels (inclined at an angle of about 20° to the OZ_A -axis) contribute most; up to a maximum of 28 square metres. Further, at such angles the body area is almost 8 square metres, as opposed to the end-on (along the OZ_A -axis) area of just 4 square metres — or even less. Secondly, there is a corresponding minimum in total area for large values of β , for precisely the opposite reasons. Indeed, the lowest areas (in the table) are obtained for $\beta = -75^\circ$ because at this point, the incident vector is almost edge-on to the solar panels — for all values of α . In addition, since the SAR is also inclined at a similar angle, neither it nor the solar panels contribute markedly to the total area, which is largely composed of the body component (at a similar low due to its being viewed almost along its length). Thirdly, the variation with α for any given β is mostly due to the differing contribution of the SAR. This varies from a maximum of 10 square metres, at values of α which lie along the SAR surface normal to a minimum of zero, when $\alpha = \pm 90^\circ$ and the SAR is edge-on to the

β	-90°	-75°	-60°	-45°	-30°	-15°	0°	15°	30°	45°	60°	75°	90°
α													
0.0°	13.6	12.1	20.5	31.5	39.3	44.1	46.7	46.9	43.7	37.5	29.4	21.4	13.7
22.5°	13.8	12.0	21.0	32.3	40.4	45.3	47.9	48.1	44.8	38.4	30.2	21.9	13.7
45.0°	14.1	11.6	20.1	30.7	38.8	43.5	46.0	46.2	43.1	37.4	29.7	21.9	14.1
67.5°	14.2	10.5	17.7	27.0	34.1	39.3	41.4	41.8	39.5	35.0	29.3	21.7	14.2
90.0°	14.3	9.2	15.4	23.0	29.2	33.3	34.7	37.6	37.6	34.6	28.5	21.4	14.3
112.5°	14.2	9.2	15.7	23.2	31.1	37.5	41.4	43.6	42.5	38.2	30.3	22.0	14.2
135.0°	14.3	8.9	15.3	25.6	34.7	41.9	46.0	47.8	47.0	41.6	31.8	22.2	14.3
157.5°	14.0	8.4	15.8	26.6	36.4	43.8	47.9	49.6	48.7	42.8	33.6	21.8	13.9
180.0°	14.9	7.7	15.0	25.8	35.4	42.6	46.7	48.4	47.6	42.0	33.3	22.9	14.9
202.5°	14.0	8.4	15.8	26.6	36.4	43.8	47.9	49.6	48.7	42.8	33.6	21.8	14.0
225.0°	14.3	8.9	15.3	25.6	34.7	41.9	46.0	47.8	47.0	41.6	31.8	22.2	14.3
247.5°	14.2	9.2	15.7	23.2	31.1	37.5	41.4	43.6	42.5	38.2	30.3	22.0	14.2
270.0°	14.3	9.2	15.4	23.0	29.2	33.3	34.7	37.6	37.6	34.6	28.5	21.4	14.3
292.5°	14.2	10.5	17.7	27.0	34.1	39.3	41.4	41.9	39.5	35.0	29.3	21.7	14.2
315.0°	14.1	11.6	20.1	30.7	38.8	43.5	46.0	46.2	43.1	37.4	29.7	21.9	14.1
337.5°	13.8	12.0	21.0	32.3	40.4	45.3	47.9	48.1	44.8	38.4	30.2	22.0	13.7
360.0°	13.6	12.1	20.5	31.5	39.3	44.1	46.7	46.9	43.7	37.5	29.4	21.4	13.7

Table 4.1: Cross sectional area for ERS-1 (in square metres) as viewed from the sun.

incident vector. Finally, it may be noted that the three WSA contribute almost negligible amounts to the cross-sectional area at all incident angles.

In addition to these general variations it is of interest to note the variation in area with varying α when $\beta = \pm 90^\circ$. Each of these angles represent a theoretical sun lying along the rotation axis of the solar array. In such a position, the array cannot meaningfully rotate because the sun vector has no component outside the array axis with which to define a rotation angle. However, because of asymmetries in the model, rotating the solar array does *in fact* give different total areas which, as can be seen, vary by as much as 0.83 square metres (about 8% of the total effective area for these values of β). Since the tables generated by the GUESS software (*not these illustrative tables*) were to be used for interpolation, it was

deemed better to rotate the array, so that the singularity represented by $\beta = \pm 90^\circ$ could be approached from different directions, and the varying areas thus obtained for the varying values of α enable meaningful interpolations to be made about these singularities. Also of interest, though not visible in Table 4.1, is the fact that for the same values of α , the areas obtained for $\beta = +90^\circ$ and $\beta = -90^\circ$ are only the same, in general, to two decimal places. This gives some measure of error arising from round off within the computational process — probably as a result of the overlapping mechanism — since for a fixed α , the total areas obtained from $\beta = \pm 90^\circ$ should be identical.

For the aerodynamic resistance force, the visible area tables for the model's surface elements were derived in much the same way. However, for these tables, there were *three* angles required rather than two. Two of these, (γ and δ of Figure 3.5) defined the incident flux vector. The third, α — one of the sun position angles — was sufficient to determine the necessary rotation angle of the solar array. The fact that just one angle suffices to correctly rotate the solar array to a sun-pointing position is a direct result of the seemingly involved approach of Chapter 3 using an axial coordinate system as well as a satellite-fixed one.

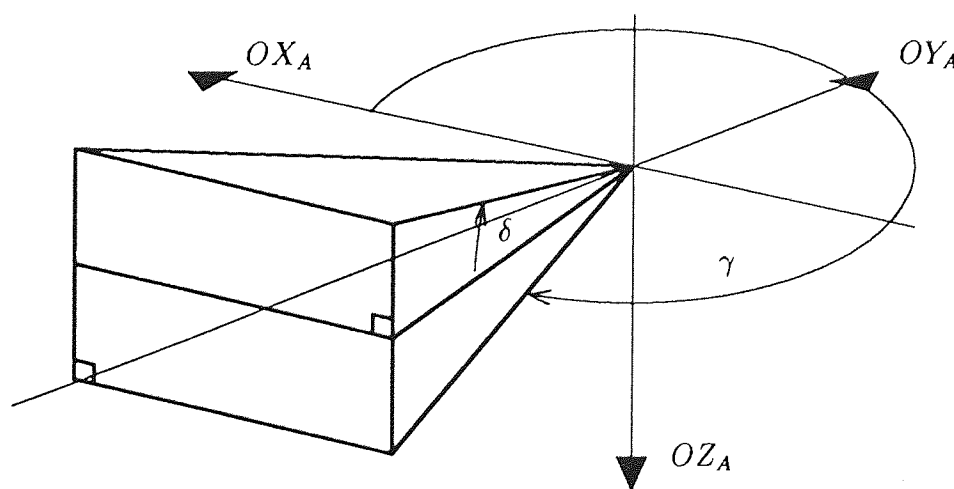


Figure 4.5: Region of interest for the aerodynamic flux incident on ERS-1.

For ERS-1, it was found that the angles γ and δ never deviated from either the $OX_A - OY_A$ -plane or the $OY_A - OZ_A$ -plane by more than 5° . Equivalently, the incident flux vector (defined by these angles) was found to be always within

$\pm 5^\circ$ of the $-OY_S$ -axis (i.e. the $-OY_A$ -axis — see Figure 4.4). This relationship is equivalent to the statement that the relative velocity of the satellite with respect to an atmosphere rotating with the earth (assumptions made in the atmospheric model of the orbital prediction program) never deviates from its absolute velocity vector (both vectors lying in the same reference frame) by more than about 5° . This restriction, illustrated in Figure 4.5, was determined empirically by studying three months of laser tracking data for ERS-1 (from August to October 1991, inclusive) and confirms the pre-launch results of van der Wenden [1985].

γ	$\delta = -5^\circ$			$\delta = 0^\circ$			$\delta = +5^\circ$		
	265°	270°	275°	265°	270°	275°	265°	270°	275°
α									
0.0°	12.45	9.65	11.73	11.83	8.91	11.83	11.73	9.66	12.47
22.5°	22.58	19.29	18.83	22.05	17.94	17.65	21.79	17.87	16.81
45.0°	30.85	28.10	28.13	30.33	26.78	26.97	30.04	26.66	26.07
67.5°	35.94	33.99	34.76	35.44	32.68	33.62	35.12	32.54	32.71
90.0°	37.09	36.05	37.71	36.59	34.74	36.59	36.26	34.59	35.66
112.5°	34.13	33.99	36.56	33.62	32.68	35.44	33.32	32.53	34.49
135.0°	27.51	28.10	31.47	26.97	26.78	30.33	26.70	26.66	29.43
157.5°	18.21	19.29	23.21	17.65	17.94	22.04	17.43	17.87	21.18
180.0°	11.11	9.65	13.07	11.83	8.91	11.83	13.08	9.66	11.13
202.5°	21.17	17.89	17.43	22.04	17.94	17.65	23.21	19.28	18.22
225.0°	29.40	26.66	26.70	30.33	26.78	26.97	31.48	28.10	27.51
247.5°	34.49	32.54	33.31	35.44	32.68	33.63	36.57	33.99	34.13
270.0°	35.64	34.60	36.26	36.59	34.74	36.59	37.72	36.05	37.11
292.5°	32.68	32.54	35.12	33.62	32.68	35.44	34.76	33.99	35.96
315.0°	26.08	26.66	30.02	26.97	26.78	30.33	28.13	28.10	30.85
337.5°	16.81	17.89	21.79	17.66	17.94	22.04	18.83	19.28	22.59
360.0°	12.45	9.65	11.73	11.83	8.91	11.83	11.73	9.66	12.47

Table 4.2: Cross sectional area for ERS-1 (in square metres) as viewed along the incident aerodynamic flux vector.

Analogously to solar radiation pressure, a file containing the visible areas for each surface element of the satellite's geometric model was produced over

a $5^\circ \times 5^\circ \times 5^\circ$ grid in the three angles (α , γ and δ). However, as was discussed in Section 3.5, no further elaboration was possible and this file was used as input for the orbital prediction routine. Again similarly to solar radiation pressure, these areas were also used to produce a table of total effective cross-sectional areas over a reduced grid of $22.5^\circ \times 5^\circ \times 5^\circ$, the contents of which are shown in Table 4.2.

Considering this table, it can be seen that (as was the case with Table 4.1, for direct solar radiation pressure) the effective total cross-sectional areas produced exhibit variations in a manner that might be expected for ERS-1. Because of the limited variation in angles γ and δ , the main constant contribution to the cross-sectional area is due to the body and measures approximately 8 square metres. The SAR contributes almost nothing, since the incident flux vector lies almost parallel to it for all angles considered. Similarly, the WSA component of the cross-sectional area is also negligible. Thus, the greatest part of the variation evidenced in Table 4.2 arises as a result of the rotation of the solar array and hence registers as a variation with angle α . Here, as expected, the maximum area is obtained when the solar panel lies perpendicular to the flux (at α values of 90° and 270°) and minima occur when the two are parallel (α equals 0° or 180°).

It must be emphasized that both Table 4.1 and 4.2 are for illustrative purposes only, neither of them being employed in the orbital determination process. However, these tables *do* allow some confirmation of the credibility of the results of the GUESS software for ERS-1.

4.4 Precise orbit determinations for ERS-1 using GUESS tables

Before these tables could be used for precise orbit determination of the ERS-1 satellite, the SATAN-A suite had to be extensively modified. However, despite the extent of the necessary changes, the actual implementation was reasonably straightforward and may be summarized as follows.

First, the format of the observation data needed altering, since from 1989 most laser tracking data was in the MERIT II format, rather than MERIT I previously used. Secondly, subroutines to read in both sets of tables as well

as the satellite's geometric model file were written, storing the area/vector data in arrays for later use. Thirdly, a second atmospheric resistance subroutine was written, initially to be run as an option (instead of using the existing drag routine). Fourthly, the existing solar radiation subroutine was modified to take the stored data where this option was chosen. Further, this same routine was modified in the reflected radiation section where satellite areas were incorporated into the thirteen element model (see Section 2.2.6). Finally, we note that the partial derivatives are effectively the same, namely of the form

$$\frac{\partial F}{\partial C_D} = \frac{\partial F_D}{\partial C_D}$$

$$\frac{\partial F}{\partial C_R} = \frac{\partial F_R}{\partial C_R}$$

so that no changes to the correction program are required. Having amended the orbit determination package, it was tested on over three months of laser tracking data from the launch date in late July until early November 1991, comprising over twenty distinct long-arcs, each typically six days in length.

Each long-arc was determined using the 50×50 GEM-T3A gravity field and associated tidal models within the J2000 inertial reference system. GEM-T3A was derived from the GEM-T3 normal equations [Lerch *et al.*, 1992] with additional DORIS tracking data from the French satellite SPOT2 (see Chapter 6 for more information on SPOT2 and DORIS). The atmospheric density was modelled using the MSIS83 model due to Hedin [1983] and combined with saw-tooth drag scale factors to produce the aerodynamic resistance force. The station monument solutions were derived from three months of Lageos data (August 1991 to October 1991) by the Royal Greenwich Observatory. These, together with the relevant corrections from the eccentricity vector file were used to compute the station coordinates relevant to the given arcs. Each arc also estimated a number of drag scale factors, C_D , and a single solar reflectivity coefficient, C_R .

It was found that the saw-tooth approach was less robust than the old step function. This was because it was far more sensitive to the relative locations of data and nodal points. Indeed, totally unrealistic scale factors were obtainable, *especially* in *sparsely* tracked orbits, simply by locating the nodal points so that the slope joining two successive C_D values ran at an extreme angle through the

intervening clumps of data. Thus, the scale factors were chosen to ensure that the period between any two nodes always contained some laser data and further, that not all the laser data lay predominantly closer to one node than the other. In addition, the number of scale factors was limited so as to keep the correlations between solution parameters as low as possible. This led to a mix of daily and half-daily values (for the time between nodes), with an occasional quarter-daily period where such was deemed necessary (and realistic) to converge the orbit.

For each arc, the orbit was converged both with and without the GUESS tables. Where such tables *were* used, the aerodynamic resistance and direct solar radiation pressure forces were computed using Equations 3.10 and 3.2 respectively. Where these tables *were not* used, constant values for A_D and A_R were used in conjunction with the original Equations 2.5 and 2.6 of Chapter 2.

Before attempting any detailed analysis of the results, a simple check was carried out on each orbit with the GUESS tables in use. This check consisted of printing out the total area which lay perpendicular to the direction of travel at any time. An example of this for just one long-arc is illustrated in Figure 4.6 which clearly shows the expected two-cycle per earth-revolution variation that is

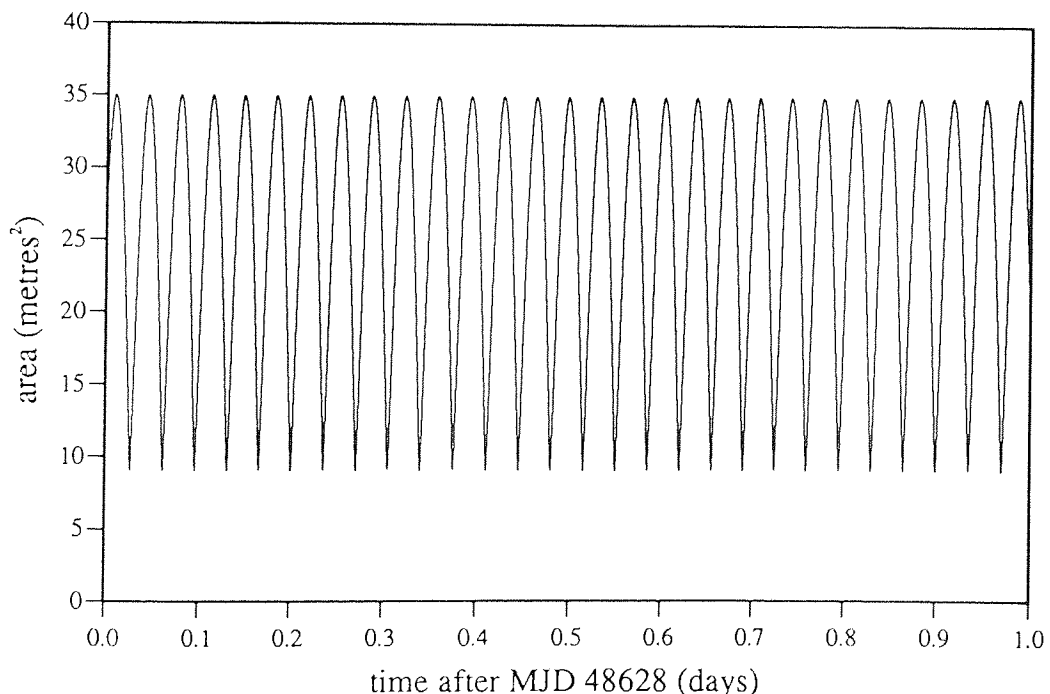


Figure 4.6: An example of the variation in the effective cross-sectional area of ERS-1 over part of the long-arc from MJD 48628 to MJD 48633.

a result of the solar panel rotation. As such it confirms the pattern already seen

in the illustrative Table 4.2 and further suggests that the model solar array is effectively mimicking reality.

A further elaboration of the solution process enabled the results to indicate the existence of any geographical bias that occurred in the converged orbits. This elaboration consisted on simply considering the tracking data both as a single

Arc Dates (MJD)	$N(C_D)$	Data used: stations/passes/observations			
		total	area A	area B	area C
48459.80 – 48463.60	5	8/19/277	6/17/259	2/2/18	0/0/0
48464.80 – 48470.80	10	13/48/678	8/36/541	3/7/100	2/5/37
48468.80 – 48474.80	10	14/48/663	9/39/550	3/7/93	2/2/20
48474.80 – 48481.60	12	16/49/570	9/32/355	5/12/158	2/5/57
48481.50 – 48486.90	9	17/51/678	11/38/502	4/8/99	2/5/77
48486.90 – 48492.90	16	15/54/660	10/38/505	4/11/94	1/5/61
48492.90 – 48498.90	13	15/55/723	9/42/524	4/9/130	2/4/69
48496.80 – 48502.80	11	12/54/742	9/45/607	2/5/64	1/4/71
48500.80 – 48506.80	11	14/61/855	9/48/722	4/10/95	1/3/38
48506.88 – 48512.80	7	12/34/448	7/19/240	3/12/155	2/3/53
48512.80 – 48518.80	10	16/50/701	9/30/452	5/14/153	2/6/96
48515.30 – 48521.30	10	16/60/760	9/34/430	5/18/209	2/8/121
48522.60 – 48525.60	5	10/24/363	6/12/211	3/9/90	1/3/62
48525.50 – 48532.00	7	12/34/512	7/21/367	4/11/131	1/2/14
48532.00 – 48538.00	11	12/42/542	7/26/270	4/14/236	1/2/36
48537.80 – 48543.80	11	11/37/434	6/25/277	4/11/145	1/1/12
48543.80 – 48549.80	8	10/23/277	5/15/168	4/5/55	1/3/54
48546.80 – 48552.90	9	6/21/260	3/15/159	2/3/35	1/3/66
48553.40 – 48560.30	9	9/21/316	5/13/179	3/7/113	1/1/24
48560.37 – 48566.80	8	8/15/201	4/6/67	3/6/77	1/3/57
48566.80 – 48573.80	7	6/13/146	3/8/91	2/4/30	1/1/25

Table 4.3: Solution details for converged ERS-1 long-arcs, July to October inclusive, 1991.

set *and* as arising from three mutually exclusive geographical regions. For this analysis the chosen regions were (A) Europe and the Mediterranean, (B) the USA

and the north Pacific and (C) the southern hemisphere. All these stations are clearly illustrated in the SLR network map (see Figure 4.1). The main reason for this subdivision into distinct regions is that where all or most of the tracking data for a given arc lies within one region, the orbital solution is often pulled so as to minimise the residuals over this region — at the expense of accuracy elsewhere. By considering the relative RMS values for different areas and relating these to the overall RMS value, it should be possible to monitor such bias, should any arise. In addition, by watching for this eventuality, it may prove possible (for instance by judicious choice of nodal points for the drag scale factors) to constrain or decrease any such geographical bias.

The solution details for each long-arc determined are presented in Table 4.3. This table contains the dates of the start and end of each arc, the number of nodal C_D values solved for, and the data accepted in the solution (some observations are necessarily rejected in the convergence process — the numbers given refer to the final data values accepted by the process). The accepted data are tabulated, both for the whole dataset and for each geographical region, as the number of contributing SLR tracking stations, the number of passes tracked and the number of normal points provided. These normal points are derived and provided by the RGO from the full dataset (which would be too large to use without such preprocessing). A pass of SLR data is simply a series of normal points from a single station's observations, the latter arising from a single "overhead" pass of the satellite.

Having converged the long-arcs, a comparison of the RMS obtained for each arc from the two approaches was made, the results of which are tabulated in Table 4.4. It is clear from this table, that in all but two of the twenty-one converged long-arcs the use of GUESS tables has reduced the RMS of fit. Further, for these two exceptions, the differences between the results obtained with and without GUESS tables are very small. Thus, it would seem that the use of GUESS tables really does result in a better orbital prediction model than simply using a constant area-to-mass ratio for the ERS-1 satellite.

Looking at the results for the three geographical regions, it appears in general that the orbits where GUESS tables have been used show less variation in RMS between each region than the equivalent solutions without GUESS tables. The

obvious exception to this is the arc from MJD 48525.5 to MJD 48532.0 where region C attains a vastly different RMS value both from the other regions and

Arc Dates (MJD)	RMS of fit (cm), total (A,B,C)			
	with GUESS tables		without GUESS tables	
48459.80 – 48463.60	26.50	(24.7, 45.3, —)	25.05	(23.3, 43.4, —)
48464.80 – 48470.80	27.68	(23.2, 42.9, 35.3)	46.99	(48.2, 38.1, 50.9)
48468.80 – 48474.80	26.09	(22.3, 42.9, 19.4)	34.55	(30.7, 48.7, 51.5)
48474.80 – 48481.60	28.36	(23.9, 35.1, 32.6)	40.40	(32.9, 47.2, 58.5)
48481.50 – 48486.90	28.29	(21.4, 44.6, 38.7)	37.71	(26.5, 47.8, 70.8)
48486.90 – 48492.90	24.58	(23.2, 29.2, 27.8)	55.63	(44.9, 76.3, 88.7)
48492.90 – 48498.90	22.07	(23.1, 18.7, 19.9)	53.67	(46.2, 46.8, 99.3)
48496.80 – 48502.80	35.68	(29.9, 33.0, 68.3)	60.98	(40.4, 68.0, 144.1)
48500.80 – 48506.80	22.31	(18.5, 39.9, 26.3)	41.16	(34.1, 62.4, 79.8)
48506.88 – 48512.80	53.15	(39.7, 72.7, 40.8)	64.97	(47.1, 80.7, 83.5)
48512.80 – 48518.80	26.91	(22.3, 35.4, 30.9)	31.24	(26.5, 39.8, 35.9)
48515.30 – 48521.30	37.13	(28.1, 39.6, 56.0)	37.29	(23.6, 36.2, 67.0)
48522.60 – 48525.60	32.48	(27.5, 43.5, 29.2)	31.07	(25.2, 43.3, 27.8)
48525.50 – 48532.00	37.04	(38.3, 35.2, 0.1)	69.63	(67.5, 69.1, 114.4)
48532.00 – 48538.00	47.52	(47.5, 46.3, 55.1)	69.16	(65.2, 67.6, 101.0)
48537.80 – 48543.80	31.64	(32.9, 28.6, 35.8)	36.41	(40.2, 25.7, 51.4)
48543.80 – 48549.80	35.65	(34.5, 40.7, 33.6)	75.30	(78.1, 64.4, 76.8)
48546.80 – 48552.90	47.85	(54.6, 38.3, 32.7)	96.59	(105.2, 79.0, 82.3)
48553.40 – 48560.30	87.35	(87.2, 85.9, 94.6)	169.23	(165.1, 163.1, 220.3)
48560.37 – 48566.80	61.29	(49.1, 74.7, 53.5)	121.88	(94.8, 124.8, 144.1)
48566.80 – 48573.80	32.61	(17.7, 62.6, 19.2)	33.51	(20.4, 62.7, 18.4)
mean	35.10	(31.3, 42.5, 35.7)	46.93	(49.4, 60.7, 79.4)
σ	16.70	(16.9, 18.2, 20.8)	21.24	(35.2, 32.7, 47.8)

Table 4.4: The Root Mean Square of fit (in centimetres) for the converged ERS-1 long-arcs by solution method and geographical location.

between the two solutions. This is easily explained by considering Table 4.3 which shows that for this arc there is only one contributing station in this region providing just two passes of data. Thus, the solution is largely determined by the

other laser tracking stations in both cases — which is why the RMS is so different between regions. The vast difference between the value of 0.1 cm where GUESS tables are used and 114.4 cm is merely due to chance, since this station does little to affect the solution, so is an exception in each case.

Secondly, in most cases, the European/Mediterranean group seems to have the smallest RMS of the three regions. This implies that the resulting orbit is

Arc Dates (MJD)	Value of coefficient C_R	
	with GUESS tables	without GUESS tables
48459.80 – 48463.60	1.01	1.56
48464.80 – 48470.80	1.03	1.58
48468.80 – 48474.80	1.00	1.58
48474.80 – 48481.60	1.04	1.60
48481.50 – 48486.90	1.04	1.63
48486.90 – 48492.90	1.05	1.69
48492.90 – 48498.90	1.02	1.64
48496.80 – 48502.80	1.02	1.61
48500.80 – 48506.80	1.02	1.60
48506.88 – 48512.80	1.04	1.64
48512.80 – 48518.80	1.06	1.71
48515.30 – 48521.30	1.05	1.64
48522.60 – 48525.60	0.99	1.66
48525.50 – 48532.00	1.06	1.69
48532.00 – 48538.00	1.08	1.69
48537.80 – 48543.80	1.06	1.74
48543.80 – 48549.80	1.06	1.64
48546.80 – 48552.90	1.06	1.65
48553.40 – 48560.30	1.39	2.51
48560.37 – 48566.80	1.17	1.76
48566.80 – 48573.80	1.48	2.67

Table 4.5: The value of the solar radiation coefficient, C_R , solved for both with and without GUESS generated tables.

probably biased towards this area, at least to some extent — an observation which

is further corroborated by the relevant means and standard deviations. However, the differences between this and the second group (USA and north Pacific) are small and in several cases where GUESS tables have been used the situation is in fact reversed. Further, there is no correlation between these occurrences and those instances where the second group contributes a larger proportion of the accepted tracking data (see Table 4.3). So it is unlikely that the variations in RMS between these two groups can be attributed to the orbit being pulled over a region. Rather, it is probable that they simply reflect the differing fit of the data between these two areas.

In addition to the RMS of fit, the solution factors C_D for drag and C_R the solar reflectivity coefficient, were also considered. Table 4.5 illustrates the solution values of the variable C_R for the twenty-one long-arcs, both with and without GUESS area tables. It is immediately clear that the value of C_R is significantly diminished in all arcs where GUESS tables have been used. Further, in all but the last three long-arcs considered the value of C_R where such tables have been used is very close to 1 — indicating that the modelled radiation forces are potentially closer to the true value, since they require little or no scaling. All three exceptions fall in the period when the quantity of tracking data for ERS-1 was diminishing, towards the end of 1991. This is illustrated further by the relevant values in Table 4.3. Considering further the RMS of fit of these three arcs (Table 4.4), it is clear that the converged orbits are not as well defined as those lying earlier in 1991.

As a final consideration, the values of the solution drag scale factors, C_D were plotted for each arc, so that the differences arising from the use of GUESS area tables could be seen. A selection of the twenty-one graphs thus obtained is shown in Figure 4.7. The only consistent factor in all these graphs, is that the C_D values obtained in those arcs where GUESS tables have been used are lower than those where they have not. A few arcs do not display this general trend, but only at the ends of the relevant long-arc period.

It would thus seem, from the evidence of these twenty-one converged long arcs, that the use of GUESS area tables may diminish the RMS of fit of the residuals to the data and may also result in solar reflectivity coefficient, C_R , that is consistently close to one. In addition, the drag scale factors, C_D , attained are also lower

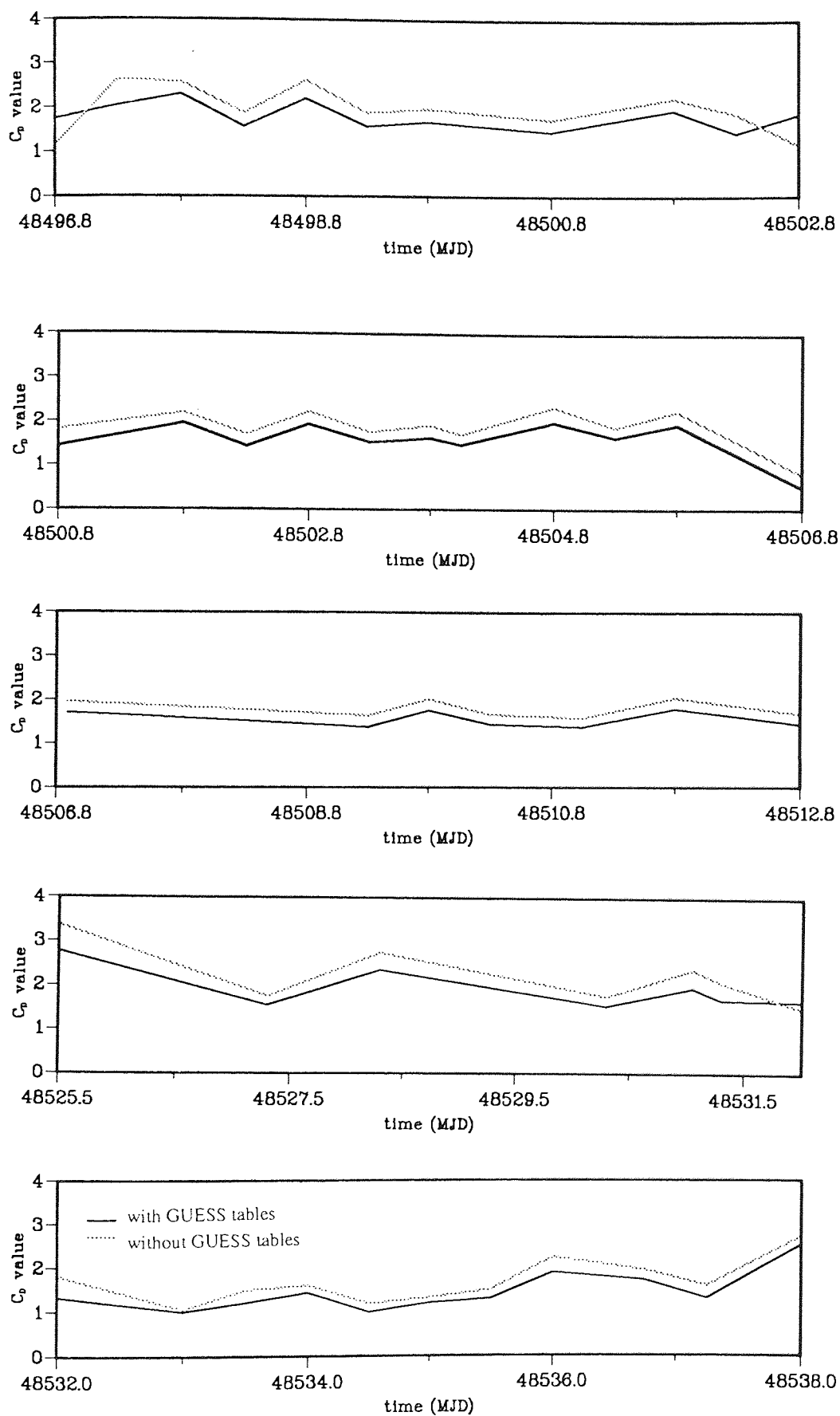


Figure 4.7: The converged drag-scale factors with and without GUESS tables for a selection of the long-arcs considered.

than the corresponding values where the GUESS generated tables have not been employed. From these results, it is suggested that, for ERS-1, GUESS tables may produce improved orbits in terms of the general fit of the data, the consistency of the scale factor C_R and the diminished C_D values. However, given the similar variations obtained by these drag scale factors, comparing arcs converged with and without GUESS tables, it is not clear to what extent the tables have removed error in the surface areas. Nor is it clear that the remaining scaling factors absorb errors due solely to mismodelling of the atmospheric density.

Chapter 5

Long-Arc Refinement using Dual-Crossover Data

5.1 Non-dynamic long-arc refinement

It has been seen, in Chapter 2, how precise orbit determination is effected at Aston. It has also been shown, in Chapter 4, how some improvement may be achieved in the determination of long-arc orbits for ERS-1 by using a dynamic force model based upon momentum changes. In this chapter, an alternative, *non-dynamic*, method for improving ERS-1 orbits will be considered. This approach derives the radial heights empirically, rather than from the dynamic equations of motion upon which the force model of Chapter 2 is based. For this reason the technique has been termed *non-dynamic*.

The aim of this chapter is to simulate the refinement of the ERS-1 orbits by using height residuals from a second satellite, namely TOPEX/Poseidon. These residuals are then used to solve for coefficients in an analytic expression for radial orbit error, so that corrections may then be added back into the long arc orbits.

5.2 Altimetry and dual-crossovers

For ERS-1 the principal tracking data types are laser-ranging and radar-altimetry. In contrast to the range recovered from laser data, altimetry provides a *normal* height between the satellite radar antenna and some closest point on the earth's surface. Since steep slopes can be the cause of non-normal measurements, as the

beam width at the earth's surface may be measured in square kilometres, this data type is more accurate over level surfaces, such as the sea and, until recently its use as a measurement was restricted to such areas. However, it is also now used to discover topographical and other information about certain areas of ice sheets, flat land and inland water, see for instance Rapley *et al.*, [1992]. The major advantage of altimetry over laser-range data is its greater geographical density, which arises from its not being constrained to fixed sites on land masses, while its main weakness arises from this same lack of precision in the point on the earth's surface at which the measurement is made.

To partially circumvent this problem of geographically related error, it is possible to difference pairs of altimeter measurements which occur over the same ground point. This is achieved by differencing the altimeter measurements at the intersection of an *ascending* and a *descending* ground-track. Each such difference is called a (single-) crossover and does not suffer from geoid error which, being constant at a given point, cancels out. Indeed, all such time-independent geographically related error terms cancel, leaving only time-varying errors [Sandwell *et al.*, 1986]. This cancellation also extends to those solution parameters which are similarly geographically related. Thus, such parameters cannot be determined from this data source alone but require some additional constraints for solution. The relevant deficiencies are elaborated upon in Section 5.6 below.

Dual-crossovers extend the concept of the single-crossover to points where the altimeter measurement of *two* satellites are differenced. Thus, the *ascending* ground-track belongs to one satellite and the *descending* one to another. One benefit of dual-crossovers is that several parameters which were insoluble (Section 5.6) using solely single-crossover data become soluble with dual-crossover data. Further, these dual-crossovers may enable the accuracy of the more poorly determined orbits of one satellite to be improved relative to the more accurate ones of the other. In the case of ERS-1 and TOPEX/Poseidon, the latter orbits the earth at a much higher altitude and is therefore not subject to the same atmospheric or gravitational problems as ERS-1. Thus, it is hoped that TOPEX/Poseidon will provide more accurate orbits by which those of ERS-1 may be refined.

Several authors have discussed dual-crossovers including Born *et al.* [1986] who examined improvement in the radial ephemeris of the planned U.S. Navy

satellite N-ROSS, whilst Shum *et al.* [1990] outlined a procedure for refining ERS-1 orbits using TOPEX/Poseidon. However, both these studies were undertaken prior to the launch dates of the satellites involved, when the exact period of simultaneous operation and orbital characteristics were still unknown. With both ERS-1 and TOPEX/Poseidon operational, it became opportune to examine the dual-crossover technique as pertinent to the repeat cycles of their orbits.

5.3 Simulating the crossover data

For the purposes of this study simulated data were used, since at the time of writing no TOPEX/Poseidon and ERS-1 altimetry data were available for the same period. For each satellite the method of simulation was first to estimate a start vector, comprising position and velocity at some epoch, from known observed orbital elements. These were then used to produce *true* and *perturbed* ephemerides in the following manner.

For ERS-1 the *true* ephemeris were produced by iterating the usual parameter set (the method is described in Chapter 2) using the MSIS83 atmospheric density model [Hedin, 1983], half-daily drag coefficients, the area tables derived in Chapter 3 and the GEM-T3 gravity field which is complete to degree and order fifty [Lerch *et al.*, 1992]. Ocean tides were modelled using the GEM-T2 tide model and all other forces and models are as outlined in Section 2.2. The ephemeris were calculated at thirty second intervals over the six days from MJD 48500 to MJD 48506, during which time ERS-1 was treated as if in its thirty-five day repeat mode. It is to be stressed that this assumption was made solely for the purposes of this simulation and that it does invalidate any results. In this mode the satellite makes 501 complete earth orbits in the time the earth takes to make 35 complete revolutions. In addition, the inclination was assumed to have an actual value of 98.53 degrees and the right ascension at MJD 48500 was taken to be 247.07002 degrees.

In comparison, the satellite TOPEX/Poseidon has an altitude of around 1335 km, thus, for simplicity, atmospheric drag was eliminated. Otherwise the *true* ephemeris were derived using exactly the same conditions as for ERS-1 except for a constant value for the surface area (required to compute the solar radiation pres-

sure). The ephemeris were again computed every thirty seconds, but over the *ten* days from MJD 48498 to MJD 48508. This period just exceeds the 9.91553 days (approximately) required for TOPEX/Poseidon to make one complete ground-track, comprising 127 revolutions, during which time the earth revolves 10 times. The values of inclination and right ascension at MJD 48498 were fixed at 66.039 degrees and 99.92398 degrees respectively.

These two sets of *true* ephemeris were used to produce two sets of simulated laser data using coordinates of the ten actual laser-ranging stations which observed ERS-1 during the simulation period in September 1991. The procedure assumes (i) a given number of passes for each station, (ii) full visibility throughout each station's range and (iii) that the laser observations also occur at thirty second intervals — like the *true* ephemeris. Given these assumptions, preliminary points were generated for each satellite using the *true* ephemerides. These preliminary points were then used as input for the prediction-correction routine of Chapter 2 and were subsequently adjusted by adding on the residuals thus obtained. For TOPEX/Poseidon the number of laser points was left unrestricted under the above assumptions. However, for ERS-1 they were limited to a set where the numbers of passes and observations for each station matched those actually obtained over the simulation period (as illustrated in Table 5.1).

A second set of ephemeris was then derived using these laser points as input observations. The gravity field was altered to the PGS4591 model field (based on the GEM-T3 normal equations plus some DORIS Doppler tracking of the SPOT-2 satellite), also complete to degree and order fifty, though it was restricted to terms of degree and order of thirty or less for the satellite TOPEX/Poseidon. Such a restriction was made necessary by the fact that the two gravity fields are almost identical for satellites at the inclination of TOPEX/Poseidon. Thus, in order to produce a sufficiently different set of *perturbed* ephemeris some alteration or limitation of PGS4591 was required. In addition, for ERS-1 the atmospheric density model was altered to the Jacchia 71 model [Jacchia, 1972], though half-daily drag coefficients and the same GUESS generated area tables were used.

These new models were converged against the simulated laser-range data from the *true* ephemeris using the orbital determination package. This produced two new state vectors, each comprising satellite position and velocity, at MJD 48500

Station ID number	Number of Passes	Number of Observations
1953	3	27
1884	5	75
7831	4	51
7542	9	156
1181	7	123
7839	9	164
7835	1	4
7090	3	38
7840	10	112
1863	4	20
7105	1	11
7110	2	18
7939	1	13
7810	2	24
7210	2	12
7046	1	7
total	64	855

Table 5.1: Numbers of laser-range passes and observations for ERS-1 between MJD 48500 and MJD 48506.

for ERS-1 and MJD 48498 for TOPEX/Poseidon. From these vectors two sets of *perturbed* ephemeris were evaluated and, for each satellite, the *true* and *perturbed* ephemerides were then compared in the radial, along-track and cross-track directions (as illustrated in Figures 5.1 and 5.2). The ephemeris comparison resulted in radial root-mean-square differences of the order of 58 cm for ERS-1 and 13 cm for TOPEX/Poseidon which are comparable with early results achieved for ERS-1 and with expected values for TOPEX/Poseidon. However, for ERS-1, later developments have shown some improvement (see Chapter 4).

Using the *true* and *perturbed* ephemerides, single and dual-crossovers were then derived as follows. First, from each ephemeris file approximate equator crossings were found. These points were then used to produce first estimates of the actual crossover locations. These, in turn, were employed as the starting

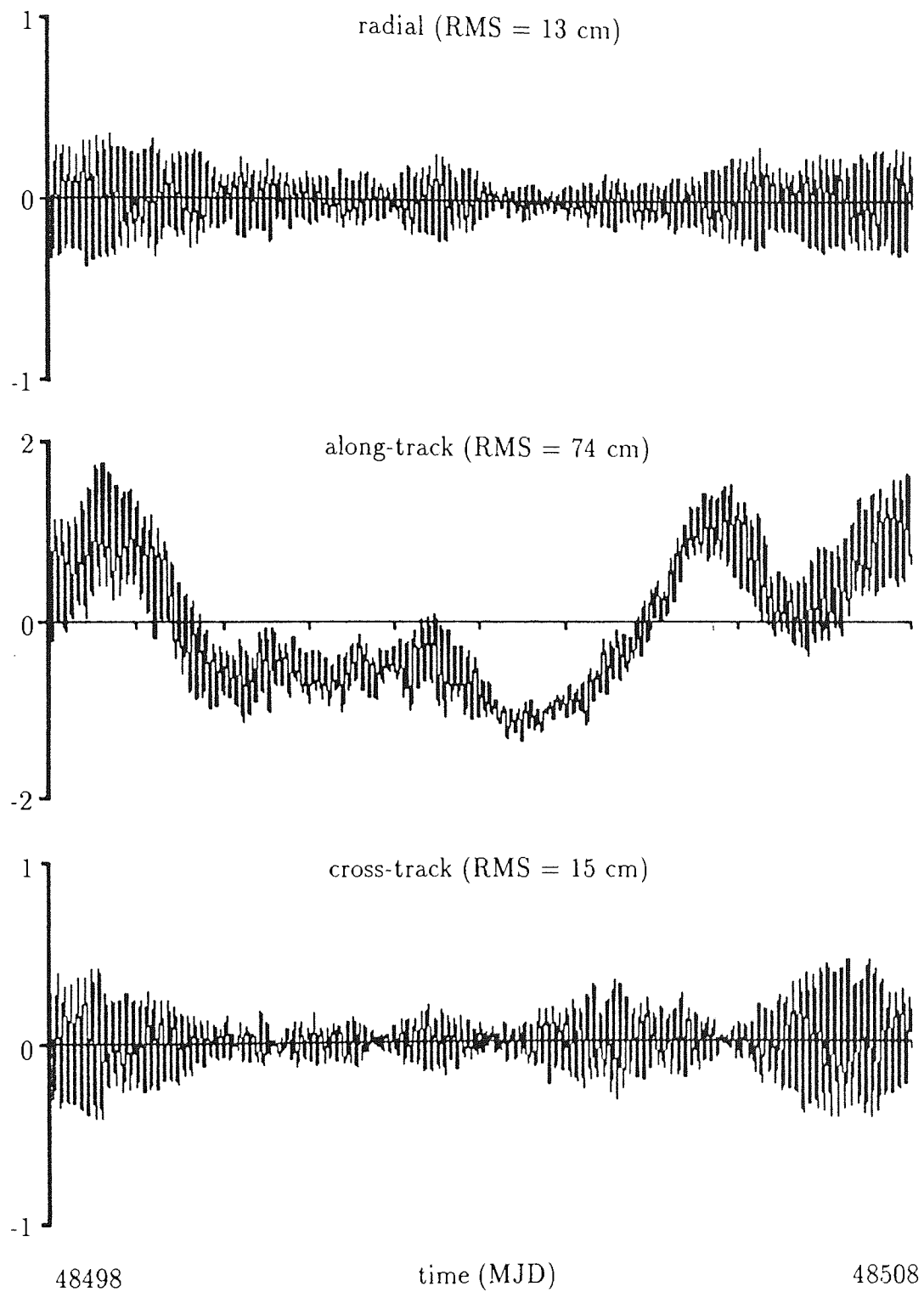


Figure 5.1: A comparison of simulated true and perturbed ephemerides for the satellite TOPEX/Poseidon.

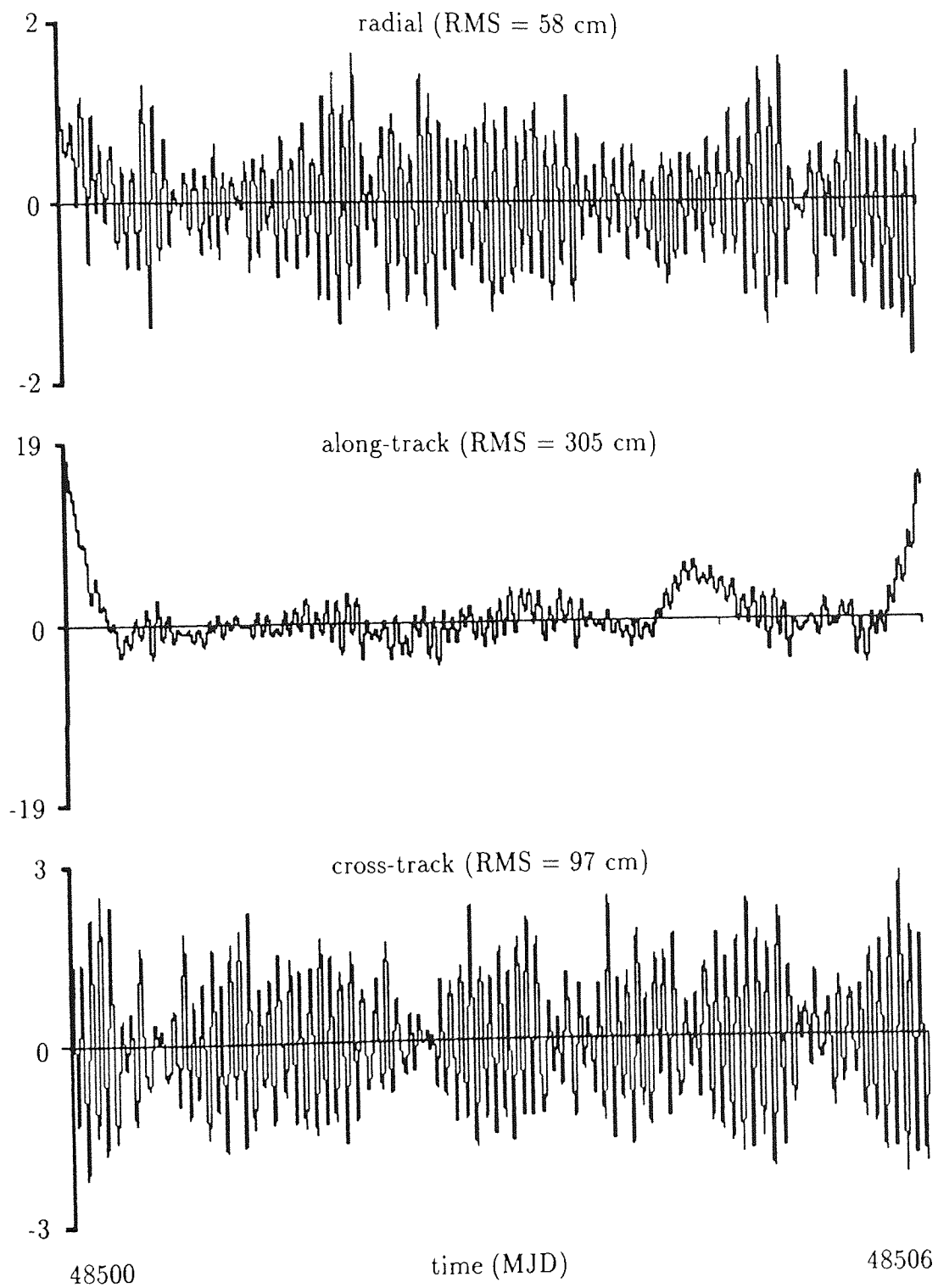


Figure 5.2: A comparison of simulated true and perturbed ephemerides for the satellite ERS-1.

values for iterative schemes which interpolate within the ephemeris to produce more accurate crossover points consisting of a radial difference, two times and the latitude and longitude of the point in the earth fixed reference frame. The actual details of this process vary from single to dual-crossovers as follows.

For both types of crossovers, the equator crossings are determined by linear interpolation between pairs of successive ephemeris points which straddle the equator. These may be easily picked up since an equator crossing results in a change in the sign of the Z-coordinate in the earth-fixed system. From here the methods differ somewhat.

For single-crossovers, taking each hemisphere and every pair of ground-tracks in that hemisphere in turn, a first approximation of the crossover longitude is given by

$$\frac{\lambda_1 + \lambda_2 + \lambda_3 + \lambda_4}{4}$$

where the λ_i denote the longitudes of the equator crossing points. From this first approximation, a more precise crossover location is made by iterating within the ephemeris until latitude and longitude match, as follows. Let (ϕ, λ) be the desired latitude-longitude pair at the crossover point. Further, let $(\phi(t_i), \lambda(t_i))$ and $(\phi(t_j), \lambda(t_j))$ be the best available approximations at times t_i and t_j respectively. Then

$$\begin{aligned} \phi &\approx \phi(t_i) + \Delta t_i \frac{d\phi(t_i)}{dt} \\ &\approx \phi(t_j) + \Delta t_j \frac{d\phi(t_j)}{dt} \end{aligned}$$

with similar expressions for λ [Rowlands, 1981]. By writing this in matrix notation,

$$\begin{pmatrix} \frac{d\phi(t_i)}{dt} & -\frac{d\phi(t_j)}{dt} \\ \frac{d\lambda(t_i)}{dt} & -\frac{d\lambda(t_j)}{dt} \end{pmatrix} \begin{pmatrix} \Delta t_i \\ \Delta t_j \end{pmatrix} = \begin{pmatrix} \phi(t_j) - \phi(t_i) \\ \lambda(t_j) - \lambda(t_i) \end{pmatrix}$$

we may solve for refinements Δt_i and Δt_j to t_i and t_j respectively. This procedure is iterated to convergence, using values of ϕ , $\frac{d\phi}{dt}$ etc. derived by interpolating within the satellite ephemeris.

Next the normal height was calculated at this point for each of the *true* and *perturbed* ephemerides. These four values were then combined to produce one simulated single-crossover difference. The single-crossover differences were then stored for each satellite, along with the two crossover times and both the latitude

and longitude. These data subsequently became input for the adopted orbital refinement procedure. The differences between the crossover times found for the *true* and *perturbed* orbits were negligible in all computed crossovers.

The initial estimates for dual-crossover locations are made using a geometric method where each of four cases is considered in turn (Northern/Southern hemisphere, descending/ascending ERS-1 arc). The first case will be explained in detail below and the general form of all the relevant equations (thus covering the other three cases) will then be given in Equation 5.1.

At a time t_a^T the ground-track of the satellite TOPEX/Poseidon intersects the equator at longitude λ_a^T in an ascending manner. It passes through the crossover point at a time Δt^T later by which time the earth has revolved about its axis by an angle $\Delta t^T \dot{\omega}$; $\dot{\omega}$ being the rotation rate of the earth. Therefore, the great circle formed by the orbital plane of this satellite intersects the equator at longitude $\lambda_a^T - \Delta t^T \dot{\omega}$, making an angle i^T (the inclination angle of TOPEX/Poseidon) with the same. The angle of arc of this great circle, between equator and dual-crossover point, is U^T .

Similarly, at time $t_d^E - \Delta t^E$ the ground-track of ERS-1 passes through the dual-crossover point, descending to intersect the equator at longitude λ_d^E a time Δt^E later. By this time the earth has again rotated through an angle $\Delta t^E \dot{\omega}$ so that

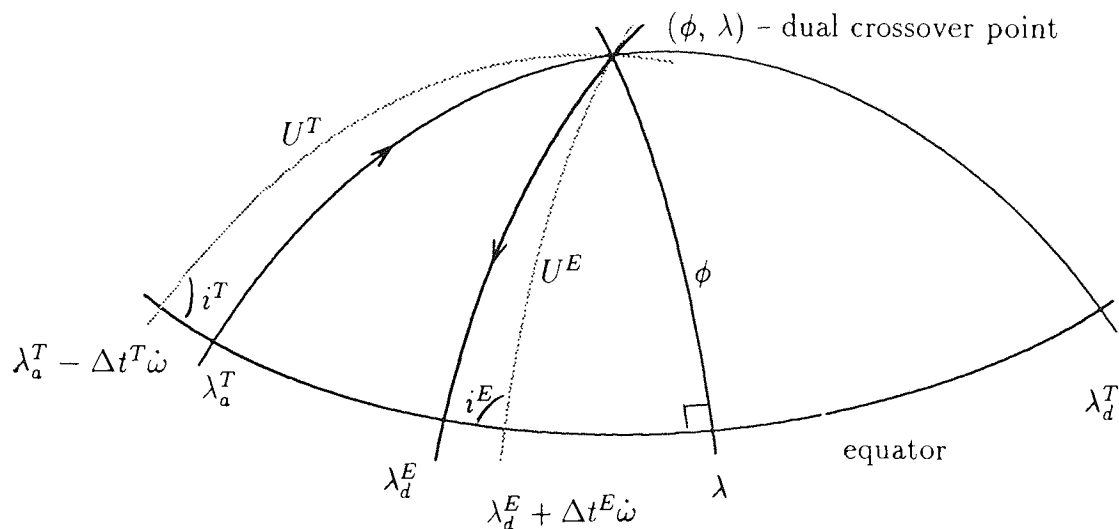


Figure 5.3: Geometric estimation of a dual-crossover point (Northern hemisphere, ERS-1 descending arc).

the great circle formed by the orbital plane of ERS-1 through the crossover point

intersects the equator at longitude $\lambda_d^E + \Delta t^E \dot{\omega}$ with an angle i^E (the corresponding inclination of ERS-1). The angle of arc between dual-crossover point and equator is U^E (see Figure 5.3). Using trigonometric relationships on spherical triangles the times Δt^E and Δt^T may be computed to give first estimates of the dual-crossover times $t_a^T + \Delta t^T$ and $t_d^E - \Delta t^E$ as follows.

Let the initial values of Δt^E and Δt^T be zero and define Δ to be the angle between the points where the relevant great-circles of ERS-1 and TOPEX/Poseidon intersect with the equator. Then, considering Figure 5.3, the angle Δ is given by

$$\begin{aligned}\Delta &= (\lambda_d^E + \Delta t^E \dot{\omega}) - (\lambda_a^T - \Delta t^T \dot{\omega}) \\ &= \lambda_d^E - \lambda_a^T + \dot{\omega}(\Delta t^E + \Delta t^T)\end{aligned}$$

and U^E and U^T are fully determined by

$$\begin{aligned}\cot U^E &= (\cos i^T \sin i^E + \cos \Delta \cos i^E) / \sin \Delta \\ \cot U^T &= (\cos i^E \sin i^T + \cos \Delta \cos i^T) / \sin \Delta\end{aligned}$$

since both are less than π radians. New values of Δt^E and Δt^T are then computed from

$$\Delta t^s = \frac{U^s \text{period}^s}{2\pi}$$

where $s = E$ or T and the process is repeated until the values of Δt^E and Δt^T converge.

From the converged values, the longitude of this crossover point may be determined by considering its sine and cosine which are:

$$\begin{aligned}\cos(\lambda - (\lambda_d^E + \Delta t^E \dot{\omega})) &= \frac{\cos U^E}{\cos \phi} \\ \sin(\lambda - (\lambda_d^E + \Delta t^E \dot{\omega})) &= -\cot i^E \tan \phi\end{aligned}$$

whence the longitude may be uniquely determined as

$$\lambda = (\lambda_d^E + \Delta t^E \dot{\omega}) + \arctan\left(\frac{-\cos U^E \sin U^E}{\cos i^E}\right).$$

The latitude is determined from the spherical sine rule and consideration of the hemisphere of the current case. Thus,

$$\phi = \arcsin(\sin U^E \sin i^E)$$

and for each dual-crossover the first estimate consists of latitude ϕ and longitude λ at times $t_d^E + \Delta t^E$ for ERS-1 and $t_a^T - \Delta t^T$ for TOPEX/Poseidon. The other three cases require a similar set of equations, with minor variations, and the general equations which may be used for all four cases are given by

$$\begin{aligned}
\Delta &= \delta_{hem} (\lambda_{dir}^E - \lambda_a^T) + \dot{\omega} (\Delta t^T - \delta_{dir} \Delta t^E) \\
\cot U^E &= (\cos i^T \sin i^E - \delta_{dir} \cos \Delta \cos i^E) / \sin \Delta \\
\cot U^T &= (-\delta_{dir} \cos i^E \sin i^T + \cos \Delta \cos i^T) / \sin \Delta \\
\lambda &= \lambda_{dir}^E - \delta_{dir} \delta_{hem} \left(\Delta t^E \dot{\omega} + \arctan \left(\frac{-\cos U^E \sin U^E}{\cos i^E} \right) \right) \\
t^E &= t_{dir}^E + \delta_{dir} \delta_{hem} \Delta t^E \\
t^T &= t_{dir}^E + \delta_{hem} \Delta t^T
\end{aligned} \tag{5.1}$$

where

$$\begin{aligned}
\delta_{hem} &= \begin{cases} 1 & \text{Northern hemisphere} \\ -1 & \text{Southern hemisphere} \end{cases} \\
\delta_{dir} &= \begin{cases} 1 & \text{ERS-1 ascending} \\ -1 & \text{ERS-1 descending} \end{cases}
\end{aligned}$$

From first approximations of the dual-crossover points determined in this manner, more precise locations are found by iterating within the ephemeris until latitude and longitude match using a similar method to that for single-crossovers [Rowlands, 1981]. As above this may be written in matrix notation,

$$\begin{pmatrix} \frac{d\phi(t^E)}{dt}, & -\frac{d\phi(t^T)}{dt} \\ \frac{d\lambda(t^E)}{dt}, & -\frac{d\lambda(t^T)}{dt} \end{pmatrix} \begin{pmatrix} \Delta t^E \\ \Delta t^T \end{pmatrix} = \begin{pmatrix} \phi(t^T) - \phi(t^E) \\ \lambda(t^T) - \lambda(t^E) \end{pmatrix}$$

where $(\phi(t^E), \lambda(t^E))$ and $(\phi(t^T), \lambda(t^T))$ are the best available approximations to the true dual-crossover point, (ϕ, λ) . The matrix equation yields refinements to the respective crossover times, t^E and t^T . By interpolating within the satellite ephemeris and partial derivatives at the new times $t^E + \Delta t^E$ and $t^T + \Delta t^T$ new best values for $(\phi(t^E), \lambda(t^E))$ and $(\phi(t^T), \lambda(t^T))$ are obtained. Iteration of the scheme converges upon the true latitude and longitude.

Having determined the dual-crossover points, the crossover heights were calculated at each point for both the *true* and *perturbed* orbits. These values were differenced to produce one simulated dual-crossover residual and all such differences were stored, along with the two epochs and the latitude and longitude. The

variation between the dual-crossover epochs for the *true* and *perturbed* orbits were negligible in all cases. The simulated crossover points were then sorted into those that lay over the oceans and those that lay over land. The latter group were eliminated and the remaining data retained for the solution procedure. The retained simulated data is summarized in Table 5.2. It is important to note that no time

Satellite	period (MJD)	repeat period days	data type	number
ERS-1	48500 to 48506	35	single crossover differences	4288
TOPEX/Poseidon	48498 to 48508	10	single crossover differences	10013
ERS-1 and TOPEX/Poseidon	union of the above	—	dual crossover differences	13664

Table 5.2: Summary of simulated crossover data used.

restriction was placed on the separation of the epochs used to calculate either dual or single crossovers. Further, the geographical distributions of single satellite crossovers for ERS-1 and TOPEX/Poseidon and of dual satellite crossovers are illustrated in Figures 5.4 to 5.6. The incomplete ERS-1 distribution (Figure 5.4) is a result of the fact that all data lies in just six days of the thirty-five day repeat cycle assumed in the simulation process. In comparison, the TOPEX/Poseidon dataset (Figure 5.5) represents all crossovers in a complete repeat period of that satellite. Further, these figures show that all crossovers are concentrated towards the higher latitudes, being sparser in the equatorial regions. This is simply a result of the geometry of the repeat ground-tracks forcing closer spacing when an equal number of tracks crosses the circumference of a smaller circle (as occurs as the latitude deviates increasingly from the equator). Residuals for the crossover differences, as input to the non-dynamic refinement procedure detailed in Section 5.5 below, were computed by differing the normal height measurements relative to the WGS84 reference ellipsoid from the *true* and *perturbed* simulated ephemerides.

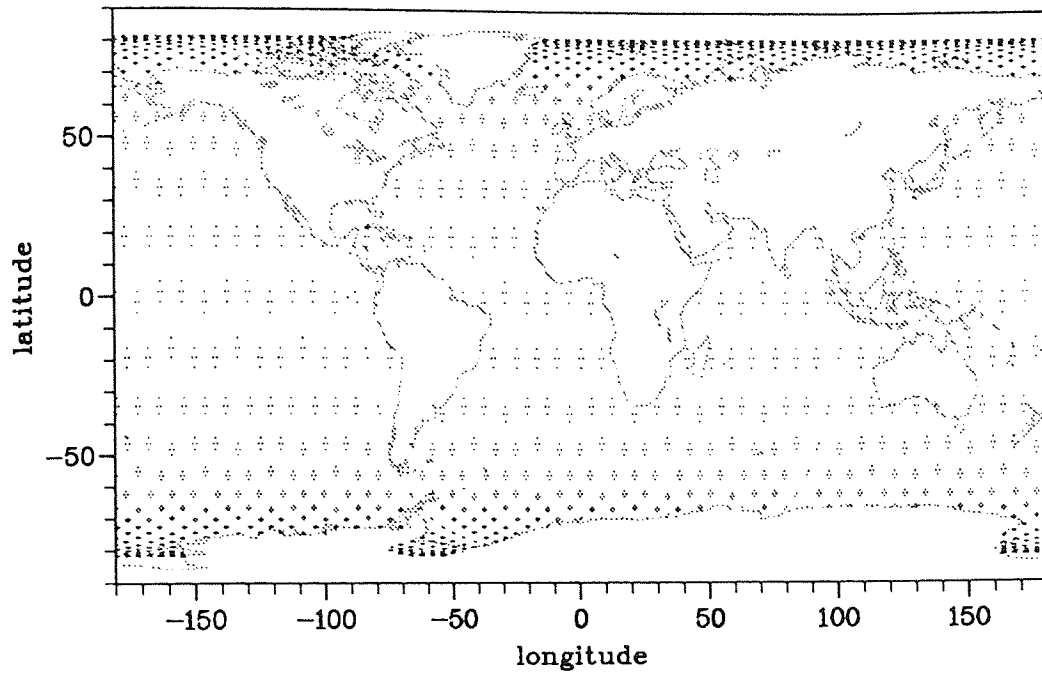


Figure 5.4: Geographic location of simulated single-crossovers over the oceans for ERS-1.

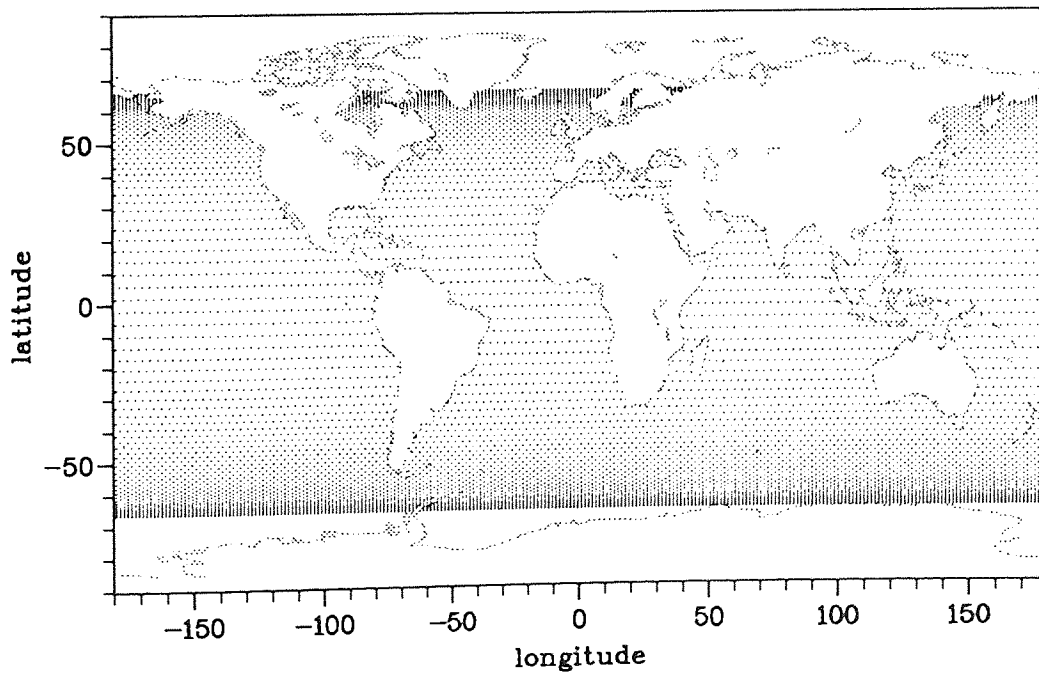


Figure 5.5: Geographic location of simulated single-crossovers over the oceans for TOPEX/Poseidon.

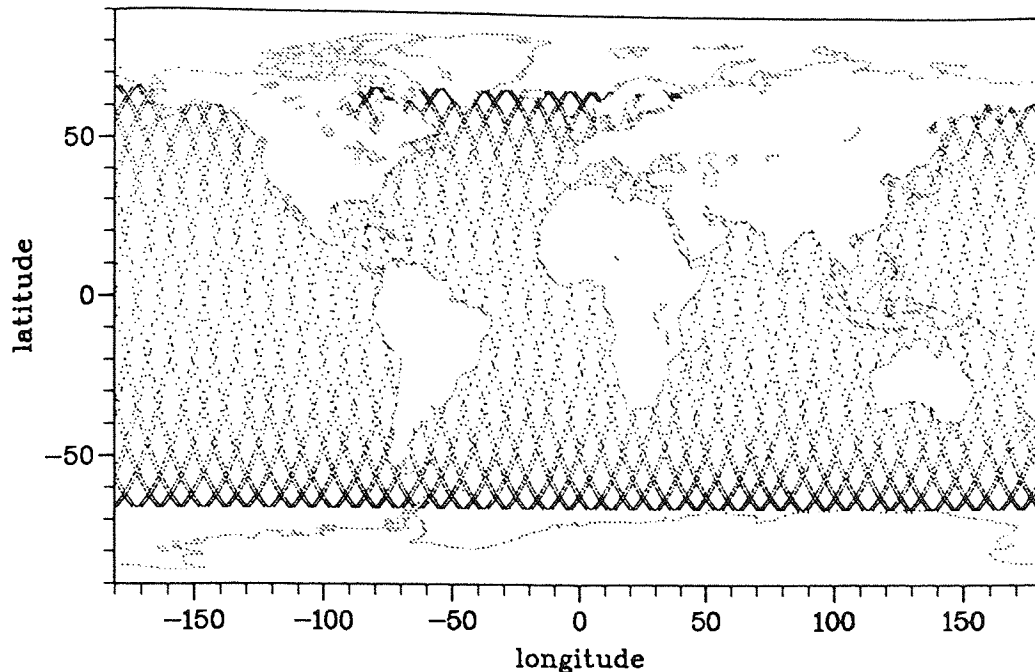


Figure 5.6: Geographic location of simulated dual-crossovers over the oceans for ERS-1 and TOPEX/Poseidon.

5.4 The determination of an analytic expression for the radial error

It is desired that the error in the radial direction, Δr , be expressed in an analytic form in order that the chosen non-dynamic method for refining long-arc orbits of ERS-1 can be tested. This error may be considered to arise from errors in the various modelling coefficients used in the force model of Section 2.2. By deriving expressions for the error due to each contributory factor in turn, an equation for the general form of the total radial error may be determined.

Let the radial distance r be expressed in Keplerian elements

$$r = \frac{a(1 - e^2)}{(1 + e \cos f)}$$

where a is the semi-major axis, e the eccentricity and f the anomaly of the instantaneous orbital ellipse [Kaula, 1966, p.21]. This may be written more simply in terms of the eccentric anomaly E as follows

$$r = a(1 - e \cos E)$$

[Rosborough and Tapley, 1987]. Now the mean anomaly M is related to E by

Kepler's equation,

$$M = E - e \sin E$$

[Kaula, 1966, p.22] and it is possible to express $\cos E$ as an infinite series in terms of $\cos nM$ as follows,

$$\cos E = -\frac{e}{2} + \sum_{n=1}^{\infty} \frac{2}{n^2} J'_n(ne) \cos nM$$

where J_n is a Bessel function of the first kind and the ' indicates differentiation with respect to e [Smart, 1953]. It is thus possible to express the radial distance r in terms of this mean anomaly M and, up to and including terms in order e^2 , r is given by

$$r = a \left(1 - e \cos M + \frac{e^2}{2} - \frac{e^2}{2} \cos 2M \right) + O(e^3)$$

[Moore and Rothwell, 1990, p.190]. Now, making small changes in a , e and M , namely Δa , Δe and ΔM respectively, results in a small change Δr in the radial distance r . After some computation this may be expressed as

$$\begin{aligned} \Delta r = & \Delta a \left(1 - e \cos M + \frac{e^2}{2} - \frac{e^2}{2} \cos 2M \right) + ae \Delta M \sin M - a \Delta e \cos M \\ & + ae \Delta e + ae^2 \Delta M \sin 2M - ae \Delta e \cos 2M + O(e^3). \end{aligned} \quad (5.2)$$

Taking each force acting on the satellite in turn (these were considered in some detail in Section 2.2) and considering errors in the model coefficients, it is possible to derive an analytic form for Equation 5.2 as follows.

From Section 2.2.1 the gravitational force may be expressed as arising from a potential V , written as a sum of frequency terms. Separating this into central and perturbing components provides the following expression for the total potential V

$$V = \frac{\mu}{r} + R$$

where R is given by

$$R = \frac{\mu}{a} \sum_{m=0}^{\infty} \sum_{k=-\infty}^{\infty} \sum_{q=-\infty}^{\infty} \gamma_{k,m} \left(\overline{C}_m^{kq} \cos \psi_{k,m,q} + \overline{S}_m^{kq} \sin \psi_{k,m,q} \right)$$

\overline{C}_m^{kq} and \overline{S}_m^{kq} being functions of the real-valued inclination functions $F_{lmp}(i)$ and the eccentricity functions $G_{l,p,q}(e)$ [Kaula, 1966, pp.34-37]. In addition, $\gamma_{k,m}$ is given by

$$\gamma_{k,m} = (-1)^{\frac{k-m+1}{2}}$$

and $\psi_{k,m,q}$ by

$$\psi_{k,m,q} = \omega + (k + q)M + m(\Omega - \theta) + (k - m)\frac{\pi}{2}. \quad (5.3)$$

From the above expression for the perturbing force R , the error in the gravity field coefficients may be considered to result in an error ΔR in this force. This error may also be expressed in terms of the Keplerian elements a , e and M by considering the relevant planetary equations of Lagrange (as given for example by Kaula [1966, p.29]), namely:

$$\begin{aligned} \frac{da}{dt} &= \frac{2}{na} \frac{\partial F}{\partial M} \\ \frac{de}{dt} &= \frac{(1 - e^2)}{na^2 e} \frac{\partial F}{\partial M} - \frac{\sqrt{(1 - e^2)}}{na^2 e} \frac{\partial F}{\partial \omega} \\ \frac{dM}{dt} &= \frac{-(1 - e^2)}{na^2 e} \frac{\partial F}{\partial e} - \frac{2}{na} \frac{\partial F}{\partial a} \end{aligned} \quad (5.4)$$

where $F = V - T$ is the force function, T being the kinetic energy. Substituting for V and T gives F in terms of R ,

$$F = \frac{\mu}{2a} + R$$

whence Equations 5.4 may all be written in terms of R by replacing F with R in all but the last. For the variation of M with respect to time, $\frac{dM}{dt}$, noting that

$$\frac{-2}{na} \frac{\partial}{\partial a} \left(\frac{\mu}{2a} \right) = \frac{\mu}{na^3} = n$$

(from Kepler's third law, for example [Borowitz and Beiser, 1967, p.187]) we have the expression

$$\frac{dM}{dt} = n - \frac{(1 - e^2)}{na^2 e} \frac{\partial R}{\partial e} - \frac{2}{na} \frac{\partial R}{\partial a}.$$

These equations may now be solved for Δa , Δe and ΔM using the method of linear perturbations [Kaula, 1966, pp.39-41] which assumes the existence of a mean ellipse described by the elements \bar{a} , \bar{e} , $\bar{\omega}$ and \bar{M} on a mean precessing plane defined by $\bar{\Omega}$ and \bar{i} . These mean elements may be determined from the osculating values with short periodic oblateness terms removed using the method of Gooding [1981]. Further, where the eccentricity is small $\bar{\omega}$ is ill-defined so that the required linearity of $\frac{d}{dt}\bar{\omega}$ and $\frac{d}{dt}\bar{M}$ does not occur. In this case the approach taken by Cook

[1966] may be employed which uses the fact that $\overline{\omega + M}$ is well defined. Hence, $\frac{d}{dt}\overline{\omega}$ and $\frac{d}{dt}\overline{M}$ may be found indirectly from $\frac{d}{dt}\overline{\omega + M}$ which is linear. Alternatively, where the orbit is frozen, or where \bar{i} is equal to the critical inclination, 63.4° [Cook, 1966], then $\frac{d}{dt}\overline{\omega} = 0$ and $\frac{d}{dt}\overline{M} = \frac{d}{dt}\overline{\omega + M}$. From here on the mean elements will be used unless otherwise specified, but the bars will be dropped for ease of notation (for example \bar{a} will be written simply as a).

Now, using the method of linear perturbations the error Δx , for any element x , may be expressed as

$$\Delta x = \int_{t_0}^t \frac{d\Delta x}{dt} dt$$

and replacing R , M , a and e in Equations 5.4 by ΔR , ΔM , Δa and Δe gives

$$\begin{aligned} \Delta a &= \frac{2}{na} \int_{t_0}^t \frac{\partial \Delta R}{\partial M} dt \\ \Delta e &= \frac{\sqrt{(1-e^2)}}{na^2e} \int_{t_0}^t \left(\sqrt{(1-e^2)} \frac{\partial \Delta R}{\partial M} - \frac{\partial \Delta R}{\partial \omega} \right) dt \\ \Delta M &= \Delta n - \frac{1}{na} \int_{t_0}^t \left(\frac{(1-e^2)}{ae} \frac{\partial \Delta R}{\partial e} + 2 \frac{\partial \Delta R}{\partial a} \right) dt \end{aligned} \quad (5.5)$$

where Δn may be derived in a similar manner:

$$\Delta n = \int_{t_0}^t \frac{d\Delta n}{dt} dt = -\frac{3n}{2a} \Delta a.$$

If x is any of the terms R , M , a , or e , then Δx may be expressed as a sum of terms, each arising from one frequency component in the expansion for V :

$$\Delta x = \sum_{k,m,q} \Delta x_{k,m,q}.$$

In addition, the partial derivatives of ΔR with respect to a , e , ω and M may be also be expressed in this way. Thus, for the terms ω and M which only appear in the expansion of $\psi_{k,m,q}$,

$$\begin{aligned} \frac{\partial \Delta R}{\partial M} &= \sum_{k,m,q} (k+q) \Delta R_{k,m,q} \\ \frac{\partial \Delta R}{\partial \omega} &= \sum_{k,m,q} k \Delta R_{k,m,q}. \end{aligned}$$

Next, considering the semi-major axis a , we see that it only occurs as an inverse power of l in the coefficients \overline{C}_m^{kq} and \overline{S}_m^{kq} [Wnuk, 1990]. Similarly, the eccentricity

e only appears in the eccentricity functions $G_{l,p,q}(e)$. Hence, for a and e , the required partial derivatives of ΔR are given by

$$\frac{\partial \Delta R}{\partial a} = \sum_{k,m,q} \frac{-(l+1)}{a} \Delta R_{k,m,q}$$

and

$$\frac{\partial \Delta R}{\partial e} = \frac{\mu}{a} \sum_{k,m,q} \gamma_{k,m} \left(\overline{C}_m^{kq} \cos \psi_{k,m,q} + \overline{S}_m^{kq} \sin \psi_{k,m,q} \right).$$

Still using the method of linear perturbations, it is assumed that a , e and i , hence n also, are constant over the time period of interest. So the only time-varying parts of $\Delta R_{k,m,q}$ are the sine and cosine of the angle $\psi_{k,m,q}$. Now by regular manoeuvring, the orbit of ERS-1 is effectively frozen, hence for ERS-1 $\dot{\omega} \approx 0$ and, without loss of generality, it may be assumed that $\omega = \pi/2$. Similarly, the argument of perigee of TOPEX/Poseidon's orbit is maintained at 90° [Marshall *et al.*, 1992], so that it too is in a frozen orbit and again $\dot{\omega} \approx 0$. Hence the terms $\dot{\omega}$, \dot{M} , $\dot{\theta}$ and $\dot{\Omega}$ are *all* constant, whence so is $\dot{\psi}_{k,m,q}$. Thus, temporarily dropping the subscripts k,m,q , the following relationship results:

$$\frac{\partial \Delta R}{\partial x} = A \sin \psi + B \cos \psi$$

for suitable constants A and B . This expression may be integrated:

$$\begin{aligned} \int_{t_0}^t (A \sin \psi + B \cos \psi) dt &= \int_{t_0}^t (A \sin \psi + B \cos \psi) \frac{d\psi}{\dot{\psi}} dt \\ &= \int_{t_0}^t \frac{A \sin \psi + B \cos \psi}{\dot{\psi}} d\psi \\ &= \frac{1}{\dot{\psi}} \left[B \sin \psi(t) - A \cos \psi(t) \right]_{t_0}^t \end{aligned}$$

enabling solutions of Δa , Δe and ΔM to be found, since all are sums of the terms

$$\int \frac{\partial \Delta R_{k,m,q}}{\partial x}$$

and hence of

$$\int (A \sin \psi + B \cos \psi).$$

It follows that the desired solutions to Δa , Δe and ΔM are formed as sums of terms [Moore and Rothwell, 1990, p.190]

$$\Delta a_{k,m,q} = \left(\frac{2\mu\gamma_{k,m}(k+q)}{na^2\dot{\psi}_{k,m,q}(t_0)} \right) [\Xi(t) - \Xi(t_0)]$$

$$\Delta e_{k,m,q} = \left(\frac{\mu\gamma_{k,m}(2q(1-e^2) - ke^2)}{2na^3e\dot{\psi}_{k,m,q}(t_0)} \right) [\Xi(t) - \Xi(t_0)]$$

$$\Delta M_{k,m,q} = \left(\frac{3\mu\gamma_{k,m}(k+q)t}{a^3\dot{\psi}_{k,m,q}(t_0)} \Xi(t_0) \right) + \left(\frac{\mu\gamma_{k,m}}{a^2\dot{\psi}_{k,m,q}(t_0)} \right) \times$$

$$\left[\left(\frac{3(k+q)}{\dot{\psi}_{k,m,q}(t_0)a} - \frac{2}{na} \right) + \left(\frac{1}{nae} \frac{\partial}{\partial e} + \frac{2}{n} \frac{\partial}{\partial a} \right) \right] [\Upsilon(t) - \Upsilon(t_0)]$$

respectively, where

$$\Xi(t) = \left(\overline{C}_m^{kq} \cos \psi_{k,m,q}(t) + \overline{S}_m^{kq} \sin \psi_{k,m,q}(t) \right)$$

$$\text{and } \Upsilon(t) = \left(\overline{S}_m^{kq} \cos \psi_{k,m,q}(t) - \overline{C}_m^{kq} \sin \psi_{k,m,q}(t) \right)$$

define the functions $\Xi(t)$ and $\Upsilon(t)$. The partial differential operators in this equation act solely on \overline{S}_m^{kq} and \overline{C}_m^{kq} as there are no a or e terms in $\psi_{k,m,q}(t)$.

By including the assumption that $\dot{\omega} = 0$, the derivative of Equation 5.3 with respect to time gives the following result,

$$\dot{\psi}_{k,m,q} = (k+q)\dot{M} + m(\dot{\Omega} - \dot{\theta}).$$

Next, the sum in k, m, q may be simplified by gathering all terms with similar $(k+q)$ and resetting k to equal this new summation variable (i.e. $k+q \mapsto k$). Further, by measuring ψ relative to its initial position $\psi(t_0)$ we may write

$$\begin{aligned} \psi_{k,m}(t) &= \psi_{k,m}(t_0) + \dot{\psi}_{k,m} \times t \\ &= \left(k\dot{M} + m(\dot{\Omega} - \dot{\theta}) \right) \times t. \end{aligned} \quad (5.6)$$

Then, if Δr_G denotes the radial error contribution from this source (gravitational potential) it can be shown that (combining the relevant terms and writing in a more accessible form — see also Moore and Rothwell [1990, pp.191–192])

$$\Delta r_G(t) = \sum_{k,m} (A_{k,m} \cos \psi_{k,m}(t) + B_{k,m} \sin \psi_{k,m}(t)) + C_2 t \quad (5.7)$$

measured relative to some value $\Delta r_G(t_0)$, where the secular term $C_2 t$ arises from those instances when $\dot{\psi}_{k,m,q}(t_0) = 0$.

The force due to atmospheric drag was given by Equation 2.5 of Chapter 2. In order to determine the error in this model it was further assumed that (i) the drag scale factor, C_D , cross-sectional area, A_D and satellite speed, v , are constant

in the region of interest, (ii) lift forces are negligible and (iii) the density error may be expressed by

$$\Delta\rho = \Delta\rho_p \left(\exp \left(\frac{(r_p - r)}{H} \right) \right)$$

where the subscript p denotes the perigee and H is some constant representing the density scale height [Moore and Rothwell, 1990, p.193]. Now

$$r - r_p = ae(1 - \cos E)$$

and so, expanding the exponential as a power series in $\frac{ae}{H}(1 - \cos E)$ results in

$$\Delta F_D = -\Delta\rho_p \left(1 - \frac{ae}{H} + \frac{ae \cos E}{H} \right) \frac{C_D A_D v^2}{2} + O(e).$$

This equation may [Moore and Rothwell, 1990, p.193] be elaborated in a similar manner to Equation 5.2 for the gravitational error by using the Gaussian form of Lagrange's planetary equations and deriving equations for Δa , Δe and ΔM in terms of $\Delta\rho_p$, H , a , e and E . Given a small eccentricity, say $e \leq 0.002$, the relevant expression for Δr_D is

$$\Delta r_D(t) = -a^2 C_D A_D \Delta\rho_p (E(t) - E(t_0)) \left(1 - \frac{ae}{H} - \frac{ae}{2H} \cos E(t) \right)$$

(plus periodic terms of n cycles/rev) where E increases by 2π for each revolution [Moore and Rothwell, 1990, p.194]. This error may thus be re-written in the following general form:

$$\Delta r_D(t) = C_1 + C_3 (t - t_*) \sin M(t) + \sum_{n,0} (A_{n,0} \cos \psi_{n,0}(t) + B_{n,0} \sin \psi_{n,0}(t)) \quad (5.8)$$

for some suitable epoch t_* .

The final force to consider (Section 2.2) is that due to solar radiation pressure. This force is complicated by the satellite geometry, making the following assumptions necessary [Aksnes, 1976]. The cross-sectional area, A_D , is assumed constant, the force is taken along the sun-earth line, the penumbra is referred to by the eccentric anomalies of the umbral entry and exit points with respect to the sun-centre and the mismodelling is represented by

$$\Delta F_R = \Delta C_R \frac{A_D P}{m \mu} \left(\frac{a_0}{r_0} \right)^2$$

where C_R is the solar reflectivity coefficient, m the satellite mass and P the force per unit area exerted at the earth by the sun when its geocentric distance r_0 equals

its mean distance a_0 . Then the components Δa , Δe and ΔM may be determined with respect to the number of satellite revolutions from some initial epoch [Aksnes, 1976]. Thus, given that much of the secular along-track error is absorbed into the drag coefficients [Moore and Rothwell, 1990], the dominant form of the radial error due to the mismodelling of solar radiation pressure is a sinusoidal variation in E or M of increasing amplitude superimposed upon a secular change as evidenced by the *bow-tie* pattern of error seen when estimating the solar coefficient C_R in orbit determinations [Colombo, 1984]. Thus, the resulting general form of the radial error from this force is

$$\Delta r_R(t) = C_3(t - t_*) \sin M(t) + C_4(t - t_*) \cos M(t) \quad (5.9)$$

for some suitable epoch t_* .

The only other source of radial error considered here is that due to errors in the state vector which may be considered as errors in the initial Keplerian elements a_0 , e_0 , etc. Thus, simply substituting small changes in these elements into Equation 5.2 provides the following

$$\begin{aligned} \Delta r_I &= \Delta a_0(1 - e \cos M) - a \Delta e_0(\cos M - e + e \cos 2M) \\ &+ ae \left(\Delta M_0 - \frac{3n}{2a} \Delta a_0(t - t_0) \right) (\sin M + e \sin 2M) + O(e^2). \end{aligned}$$

Now the terms $\cos M$ and $\cos 2M$ are equivalent to the terms $\cos \psi_{1,0}$ and $\cos \psi_{2,0}$ respectively and there is a similar relationship between the $\sin nM$ and $\sin \psi_{n,0}$ terms. So the general form of the contribution of this term to the radial error is

$$\begin{aligned} \Delta r_I(t) &= \sum_{k=0}^2 (A_{k,0} \sin \psi_{k,0}(t) + B_{k,0} \cos \psi_{k,0}(t)) \\ &+ C_1 + C_3(t - t_0) \sin M(t) + C_5(t - t_0) \sin 2M(t). \end{aligned} \quad (5.10)$$

Totalling Equations 5.7, 5.8, 5.9 and 5.10 gives the following general analytic form for the radial error:

$$\begin{aligned} \Delta r(t) &= \sum_{k,m} (A_{k,m} \sin \psi_{k,m}(t) + B_{k,m} \cos \psi_{k,m}(t)) \\ &+ C_1 + C_2 t \\ &+ C_3(t - t_*) \sin M(t) + C_4(t - t_*) \cos M(t) \\ &+ C_5(t - t_*) \sin 2M(t) \end{aligned} \quad (5.11)$$

for some suitable epoch t_* . This expression is the simplest form for the radial error; several contributing effects being subsumed into the same terms. For instance, the dominant one cycle-per-revolution orbital error arising from gravitational and initial state vector errors (Δr_G and Δr_I above) is contained within the frequency dependent summation. Also, unlike Rapp *et al.* [1991], no additional term is added to absorb resonance effects.

Equation 5.11 may be used to provide expressions for single and dual-crossover differences. For a single-crossover with epochs t_1 and t_2 respectively, the radial error (crossover residual) is simply the difference in the value of Equation 5.11 at these two times. This is given by

$$\begin{aligned}
\Delta r_{SXO} = & \sum_{k,m} (A_{k,m} [\sin \psi_{k,m}(t_2) - \sin \psi_{k,m}(t_1)] \\
& + B_{k,m} [\cos \psi_{k,m}(t_2) - \cos \psi_{k,m}(t_1)]) \\
& + C_2(t_2 - t_1) \\
& + C_3 [(t_2 - t_*) \sin M(t_2) - (t_1 - t_*) \sin M(t_1)] \\
& + C_4 [(t_2 - t_*) \cos M(t_2) - (t_1 - t_*) \cos M(t_1)] \\
& + C_5 [(t_2 - t_*) \sin 2M(t_2) - (t_1 - t_*) \sin 2M(t_1)] \quad (5.12)
\end{aligned}$$

for some suitable epoch t_* which, in this simulation, was taken to be the mid-point of the period of interest. Thus, secular effects will be at a minimum at this point, and reach maxima at those times furthest from t_* . This should give rise to a *bow-tie* pattern corresponding to that caused by the element of error in the solar radiation coefficient C_R . For dual-crossovers the equation for the modelled radial error is

$$\begin{aligned}
\Delta r_{DXO} = & \sum_{k,m} (A_{k,m}^T \sin \psi_{k,m}^T(t^T) - A_{k,m}^E \sin \psi_{k,m}^E(t^E) \\
& + B_{k,m}^T \cos \psi_{k,m}^T(t^T) - B_{k,m}^E \cos \psi_{k,m}^E(t^E)) \\
& + C_1^T - C_1^E \\
& + C_2^T(t^T) - C_2^E(t^E) \\
& + C_3^T(t^T - t_*^T) \sin M(t^T) - C_3^E(t^E - t_*^E) \sin M(t^E) \\
& + C_4^T(t^T - t_*^T) \cos M(t^T) - C_4^E(t^E - t_*^E) \cos M(t^E) \\
& + C_5^T(t^T - t_*^T) \sin 2M(t^T) - C_5^E(t^E - t_*^E) \sin 2M(t^E) \quad (5.13)
\end{aligned}$$

where the superscripts E and T refer to ERS-1 and TOPEX/Poseidon respectively.

Further, since the two epochs t^T and t^E refer to different satellites, the constant terms, C_1 , do not cancel.

5.5 Method of solution

Having simulated the data (Section 5.3) and obtained expressions for the radial error (Equations 5.12 and 5.13), the refinement process solves for the unknown parameters of Equation 5.11 using simultaneous equations of the form

$$A\underline{x} = \underline{b} \quad (5.14)$$

where \underline{b} contains the simulated values, \underline{x} the best estimates of the unknown coefficients and each row of A is the transpose of

$$A_r = \left(\begin{array}{c} \vdots \\ \cos \psi_{km}^T(t^T) \\ \sin \psi_{km}^T(t^T) \\ \vdots \\ \delta_i \\ t^T \\ (t^T - t_*^T) \sin M^T(t^T) \\ (t^T - t_*^T) \cos M^T(t^T) \\ (t^T - t_*^T) \sin 2M^T(t^T) \\ \vdots \\ \kappa_i \cos \psi_{km}^E(t^E) \\ \kappa_i \sin \psi_{km}^E(t^E) \\ \vdots \\ \kappa_i \delta_i \\ \kappa_i t^E \\ \kappa_i (t^E - t_*^E) \sin M^E(t^E) \\ \kappa_i (t^E - t_*^E) \cos M^E(t^E) \\ \kappa_i (t^E - t_*^E) \sin 2M^E(t^E) \end{array} \right) \left. \begin{array}{l} \vphantom{\begin{array}{c} \vdots \\ \cos \psi_{km}^T(t^T) \\ \sin \psi_{km}^T(t^T) \\ \vdots \\ \delta_i \\ t^T \\ (t^T - t_*^T) \sin M^T(t^T) \\ (t^T - t_*^T) \cos M^T(t^T) \\ (t^T - t_*^T) \sin 2M^T(t^T) \\ \vdots \\ \kappa_i \cos \psi_{km}^E(t^E) \\ \kappa_i \sin \psi_{km}^E(t^E) \\ \vdots \\ \kappa_i \delta_i \\ \kappa_i t^E \\ \kappa_i (t^E - t_*^E) \sin M^E(t^E) \\ \kappa_i (t^E - t_*^E) \cos M^E(t^E) \\ \kappa_i (t^E - t_*^E) \sin 2M^E(t^E) \end{array}} \right\} \begin{array}{l} \text{TOPEX/Poseidon frequency terms} \\ \\ \text{other TOPEX/Poseidon terms} \\ \\ \text{as above for ERS-1} \end{array}$$

where δ_i is 0 for single-crossovers and 1 for dual-crossovers and κ_i is 1 for single-crossovers and -1 for dual-crossovers.

In practice it may be impossible to determine \underline{x} precisely, due to noise in the data, thus the final solution $\hat{\underline{x}}$ may be of the form

$$\hat{\underline{x}} = \underline{x} - \underline{\Delta x}$$

where $\hat{\underline{x}}$ is the best attainable solution and $\underline{\Delta x}$ is an error term. In addition, it may require more than one iteration to determine such a best solution:

$$\begin{aligned} \hat{\underline{x}}_1 &= 0 & + & \underline{\Delta x}_1 \\ &\vdots & & \\ \hat{\underline{x}}_{n+1} &= \hat{\underline{x}}_n & + & \underline{\Delta x}_{n+1} \\ \hat{\underline{x}}_{n+i} &= \hat{\underline{x}}_{n+1} & & \forall i \in \mathbb{N}. \end{aligned} \tag{5.15}$$

In order to solve Equation 5.14 the effect of a prior solution is first removed,

$$A\underline{\Delta x}_i = \underline{b} - A\hat{\underline{x}}_{i-1}. \tag{5.16}$$

Then the least squares solution for a set of m equations in n unknowns, where $m \geq n$, is given by

$$A^t A \underline{\Delta x}_i = A^t (\underline{b} - A\hat{\underline{x}}_{i-1}),$$

where the normal matrix $N = A^t A$ is symmetric positive definite and thus invertible. Whence, the following expression for $\underline{\Delta x}_i$ pertains:

$$\begin{aligned} \underline{\Delta x}_i &= (A^t A)^{-1} A^t (\underline{b} - A\hat{\underline{x}}_{i-1}) \\ &= (A^t A)^{-1} A^t \underline{b} - \hat{\underline{x}}_{i-1} \end{aligned}$$

which may be added to the previous best solution to obtain the new version as in Equation 5.15. In this simulation the quantity of data was large in proportion to the number of solution parameters and, more importantly, entirely noise free. Thus, a converged solution was found in a single run of the program, with a zero starting vector.

In order to calculate the matrix A all values of $\psi_{k,m}$, together with the mean anomaly M must be determined at every observation time. These values were computed as follows. First, for each pair of integers (k, m) , $\psi_{k,m}$ was evaluated using Equation 5.6. This in turn required that $\dot{\psi}_{k,m}$ first be determined as follows. A satellite orbiting the earth with period T performs some N_s revolutions while

the earth rotates some N_e times relative to the ascending node Ω . Hence, [Moore and Rothwell, 1990, p.188],

$$\dot{M}T = 2\pi N_s$$

and

$$(\dot{\theta} - \dot{\Omega})T = 2\pi N_e \quad (5.17)$$

so

$$\frac{(\dot{\theta} - \dot{\Omega})}{\dot{M}} = \frac{N_e}{N_s}$$

whence

$$\dot{\psi}_{k,m} = \dot{M} \left(k - m \frac{N_e}{N_s} \right). \quad (5.18)$$

From error analysis it can be seen that some of the frequencies, $\dot{\psi}_{k,m}$, do not make significant contributions to the radial error and, further, that the magnitude of their contribution decreases as the frequency departs from the dominant value of one cycle-per-revolution. For the purposes of this simulation an upper limit was set at two cycles-per-revolution which (at the time of this study) was a generally accepted value for analytic expansions of this type (see, for instance, Wagner [1985]). The relevant (k, m) pairs may then be determined by restricting Equation 5.18 to this limit and noting that \dot{M} alone gives a one cycle-per-revolution frequency. Given integers k and m several distinct pairs may produce the same frequency, yet only one of these is required. A search through increasing values of m , where k is limited by the value of m was made, until all the frequencies below two cycles per revolution were found. Only the lowest (k, m) pair which produces a given frequency was stored, along with that frequency. Since the expression for \dot{M} is simply

$$\dot{M} = \frac{2\pi N_s}{T},$$

$\dot{\psi}_{k,m}$ is now fully determined for all (k, m) of interest and hence, by Equation 5.6, so is $\psi_{k,m}(t)$.

It remains necessary only to compute $M(t)$. Now, as noted above, $\omega = \pi/2$ whence

$$U = \omega + f \approx \omega + M = \frac{\pi}{2} + M$$

and thus,

$$M \approx U - \frac{\pi}{2}.$$

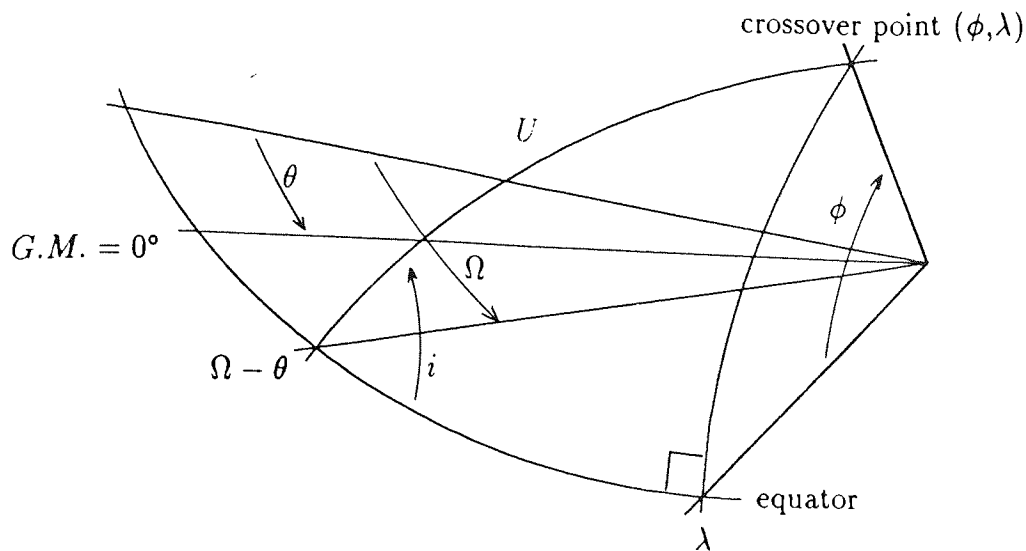


Figure 5.7: Computation of the length of arc U .

So to determine U is to determine M . Considering Figure 5.7 and applying spherical trigonometry to the right-angled triangle [Todhunter and Leathem, 1903] provides

$$\begin{aligned}\cos U &= \cos \phi \cos (\lambda - (\Omega - \theta)) + \sin \phi \sin (\lambda - (\Omega - \theta)) \cos \frac{\pi}{2} \\ &= \cos \phi \cos (\lambda - \Omega + \theta).\end{aligned}$$

Also

$$\cot \phi \sin (\lambda - \Omega + \theta) = \cot i$$

and

$$\frac{\sin \phi}{\sin i} = \sin U,$$

whence

$$\sin U = \frac{\cos \phi \sin (\lambda - \Omega + \theta)}{\cos i}.$$

Now, i was assumed to be fixed and both λ and ϕ are retained, along with the crossover times, within the input file of Section 5.3. So U may be determined when Ω and θ are evaluated which is effected by the single determination procedure:

$$\theta'(t) = \theta(t) - \Omega(t) = \theta(t_0) - \Omega(t_0) + \dot{\theta}' \times t$$

the value of $\dot{\theta}' = \dot{\theta} - \dot{\Omega}$ being derived using Equation 5.17. Hence, the matrix $N = A^t A$ is now fully determined.

5.6 Modifications to the solution procedure

This section outlines further restrictions which need to be placed on the matrix inversion procedure, outlined in the previous section. They fall into two categories: those which were expected from crossover theory and those which arose from the experimental process.

It is recognised [Moore and Rothwell, 1990] that using single-crossovers as the sole data type means that several harmonic terms cannot be solved for, either because they are geographically dependent, or because they are members of a set which are linearly dependent. Thus, the constant or $\psi_{0,0}$ term and the $\cos \psi_{k,0}$ terms cannot be solved for since they are geographically dependent. So, in a crossover difference these terms cancel, resulting in rows or columns of zero elements in the matrix N . This means, in turn, that the matrix is non-invertible and hence no solution can be found for these terms. Similarly, where linear dependencies exist between the parameters, then the number of these exceeds the row space of the matrix N [Sernesi, 1993] which again becomes singular (non-invertible), thus preventing a solution from being found (since no unique solution exists). For the adopted upper limit on the frequencies, namely two cycles-per-revolution, the linearly dependent sets for single-crossovers are the groups of sines and cosines of the following (bracketed) sets of $\psi_{k,m}$:

$$\begin{aligned} &(\psi_{1,1}, \psi_{-1,1}), \\ &(\psi_{2,1}, \psi_{0,1}, \psi_{-2,1}), \\ \text{and } &(\psi_{2,2}, \psi_{0,2}, \psi_{-2,2}), \end{aligned}$$

as established by Sandwell *et al.* [1986]. It is not possible to solve for all the terms of a single group, rather, to allow solution of any of them, *one* term must be fixed and the others may then be determined. For example, if it is desired to solve for $\cos \psi_{2,1}$ then either $\cos \psi_{0,1}$ or $\cos \psi_{-2,1}$ must be fixed by setting the relevant row/column in the matrix A to zero and the diagonal element of the same to one. This effectively suppresses the solution of the *fixed* coefficient. Alternatively, additional data from, for instance, precise altimeter measurements over non-oceanic reference surfaces (such as transponders, inland lakes etc.) may be used to resolve these deficiencies. However, using such a process still does not allow for the accurate evaluation of the defective frequencies [Wagner and Melchioni, 1989].

There are equivalent limitations when using dual-crossover data. For instance, only one constant ($\cos \psi_{0,0}^T$ or $\cos \psi_{0,0}^E$ or C_1^E or C_1^T) may be solved for, since any two or more constants must by necessity be linearly dependent, thus giving rise to singularities in the matrix N . The same situation arises with the $\cos \psi_{k,0}$ terms. Here, for any integer k , it can be shown that there is a linear relationship between the values for the two satellites. First, considering Figure 5.3,

$$\sin U^E \sin i^E = \sin U^T \sin i^T$$

whence, since $\omega = \pi/2$,

$$\cos M^E = \left(\frac{\sin i^T}{\sin i^E} \right) \cos M^T \equiv K \cos M^T.$$

Thus, the cosines of the one cycle-per-revolution terms of each satellite are linearly dependent and only one of them can be solved for. A similar dependency arises with the cosines of the two cycle-per-revolution terms:

$$\begin{aligned} \cos 2M^E &= 2 \cos^2 M^E - 1 \\ &= 2K^2 \cos^2 M^T - 1 \\ &= K^2 \cos 2M^T + (K^2 - 1) \end{aligned}$$

where the cosines of the two cycle-per-revolution terms and the constant are linearly dependent, so only two of these can be solved for. Higher values of k provide other $\cos \psi_{k,0}$ terms which display similar dependencies. However, such values here give rise to frequencies which lie above the adopted upper limit. Further deficiencies in the solution may be isolated as follows, using an approach based on that developed by Sandwell *et al.* [1986] for single-crossovers.

Considering a set of dual-crossovers, any radial form which is solely a function of the geographic ground-track position, i.e. latitude and longitude, is unobservable. Let such a form be $\Delta r_{null} = \Delta r_{null}(\phi, \lambda)$. Expanding this form in spherical harmonics we have

$$\Delta r_{null} = \sum_{l=0}^{\infty} \sum_{m=0}^l (C_{l,m} \cos m\lambda + S_{l,m} \sin m\lambda) P_{l,m}(\sin \phi).$$

This expression may then be converted into Keplerian elements [Moore and Ehlers, 1993] as follows. First define the term

$$\Delta r_{l,m} = (C_{l,m} \cos m\lambda + S_{l,m} \sin m\lambda) P_{l,m}(\sin \phi).$$

Then, using Kaula's transformation, [Kaula, 1966, pp.34-37],

$$\Delta r_{l,m} = \sum_{k=-l}^l F_{lm \frac{l-k}{2}}^*(i) (A_{l,m} \cos m\psi_{k,m} + B_{l,m} \sin m\psi_{k,m})$$

where

$$A_{l,m} = \begin{cases} C_{l,m} & l-m \text{ even} \\ -S_{l,m} & l-m \text{ odd} \end{cases}$$

$$B_{l,m} = \begin{cases} S_{l,m} & l-m \text{ even} \\ C_{l,m} & l-m \text{ odd} \end{cases}$$

the $F_{lm \frac{l-k}{2}}^*(i)$'s being the real-valued inclination functions of Kaula and \sum^* denoting that the summation be made incrementing k by 2 each time. To see how this links in with the frequencies, consider the case where $l = m = 1$. Then

$$\begin{aligned} \Delta r_{1,1} &= F_{1,1,1}(i) (C_{1,1} \cos \psi_{-1,1} + S_{1,1} \sin \psi_{-1,1}) \\ &+ F_{1,1,0}(i) (C_{1,1} \cos \psi_{1,1} + S_{1,1} \sin \psi_{1,1}) \end{aligned}$$

where the (1,1) surface harmonics map completely into the $(k,m) = (1,1)$ and $(-1,1)$ orbital frequencies for both ERS-1 and TOPEX/Poseidon. Conversely, the solution for the (1,1) and $(-1,1)$ frequencies for both satellites is thus restricted since there are linear dependencies between them (multiple rows of the matrix being connected by identical solution coefficients $C_{1,1}$ and $S_{1,1}$). The solution procedure is therefore deficient if all coefficients of the sine (or equivalently cosine) of

$$(\psi_{1,1}^T, \psi_{-1,1}^T, \psi_{1,1}^E, \psi_{-1,1}^E)$$

are sought simultaneously. Extending this analysis for other values of k and m permits further deficient combinations to be identified. Consideration of such combinations, for instance [Moore and Ehlers, 1993] shows that in all other deficient frequency groupings, one or more elements is outside the two cycle-per-revolution limit. Since, for a solution, it is sufficient to fix one element of a group in order to solve for the others, this limit effectively excludes other deficiencies from being a hindrance to *this* study.

Given all these considerations, certain terms were suppressed in the solution so that the matrix inversion procedure described in Section 5.5 above could be employed successfully. The necessary suppressions were effected by setting all elements in the row and column relating to the suppressed variable to zero. Then

the diagonal element was set to unity and the relevant parameter in the right hand side of Equation 5.16 to zero, i.e. $(\underline{b} - A\hat{x}_i)_j = 0$ where i denotes any prior solution and j is the parameter suppressed. Where terms from only one satellite needed suppression, those from TOPEX/Poseidon were chosen, since the primary purpose of this simulation was to refine ERS-1 long-arc orbits to accuracies comparable with those of TOPEX/Poseidon.

Thus, the complete list of suppressed variables consisted of, the constants arising from the frequency terms where $(k, m) = (0, 0)$,

$$A_{0,0}^E, B_{0,0}^E, A_{0,0}^T, B_{0,0}^T$$

the TOPEX/Poseidon explicit constant (in most cases),

$$C_1^T$$

the cosine coefficients of the $(k, 0)$ terms for TOPEX/Poseidon,

$$A_{-1,0}^T, A_{-2,0}^T$$

and the sine and cosine coefficient of *one* of the set discovered by the Sandwell method (again for TOPEX/Poseidon),

$$A_{-1,1}^T, B_{-1,1}^T.$$

After these suppressions, there remained just 253 distinct frequencies for the satellite TOPEX/Poseidon, giving rise to a total of 504 sine and cosine terms requiring solution.

5.7 Discussion of results

Solutions were sought for three situations: (S1) using dual-crossover data only and solving for just the ERS-1 parameters (i.e. suppressing all the TOPEX/Poseidon parameters), (S2) solving for the same ERS-1 parameters but increasing the dataset to include ERS-1 single-crossover data and (S3) further expanding the dataset with TOPEX/Poseidon single-crossover data and then solving for all parameters of both satellites. In all three cases the C_1^T constant was suppressed and the C_1^E constant solved for. For all three cases, where solutions were sought

converged values were obtained in just one iteration of the software routines, due to the fact that the simulated input data was, of course, noise free. For output, each such iteration produced a set of solution parameters, the correlations between them, the square roots of the eigenvalues of the matrix N^{-1} and a set of calculated ephemeris from the solution parameters. Since the matrix N^{-1} is also the variance-covariance matrix of the solution parameters, the variance estimates of these parameters are simply the eigenvalues of the matrix [Bonford, 1980, pp.712 – 720]. Thus, the equivalent standard errors may be obtained by taking the square root of each eigenvalue. In addition to these factors, the root-mean-square (RMS) of fit of these calculated ephemeris to the input values was computed, giving a measure of the improvement obtainable in ERS-1 long-arc orbits by adding radial corrections derived from dual-crossover data.

When such solutions were initially attempted it was found that the matrix became ill-conditioned, as a result of the closeness of the solution frequencies of ERS-1 (of which there were 1002 between zero and two cycles-per-revolution). This is because, for a satellite completing N_s revolutions in its repeat period T , the frequencies are effectively multiples of a common value [Moore and Ehlers, 1993]; namely $\frac{1}{N_s}$ cycles-per-revolution. Thus, the ERS-1 frequencies take values $\frac{i}{501}$ for integers i . These are clearly closer together than the corresponding values of $\frac{i}{127}$ for the satellite TOPEX/Poseidon (which did not exhibit this problem). This was further exacerbated for ERS-1, as the period considered was only *part* of the repeat cycle (6 days out of 35). Because of the closeness of the solution frequencies for ERS-1, pseudo-dependencies arose as a result of computational approximation. So the matrix inversion procedure produced high correlations between several of the solution parameters $A_{k,m}$ and $B_{k,m}$ (notably for higher values of m) as the matrix N approached an approximately singular state (i.e. tended to a non-invertible matrix).

This problem was circumvented by reducing the number of ERS-1 solution frequencies through a restriction of the value of m , and hence of k , in the frequency determination process. A limit of $m = 42$ was chosen empirically after attempts to produce a full solution for higher values of m had failed. As a result of this limit, just 170 of the possible 1002 ERS-1 frequencies lying below two cycles per revolution were solved for, giving rise to 340 sine and cosine terms.

A second factor which came to light after initial solutions were found was the high standard error of 47 cm attached to the C_2^T term (i.e. the *time* term for TOPEX/Poseidon). This is illustrated in Figure 5.8. This error, determined from

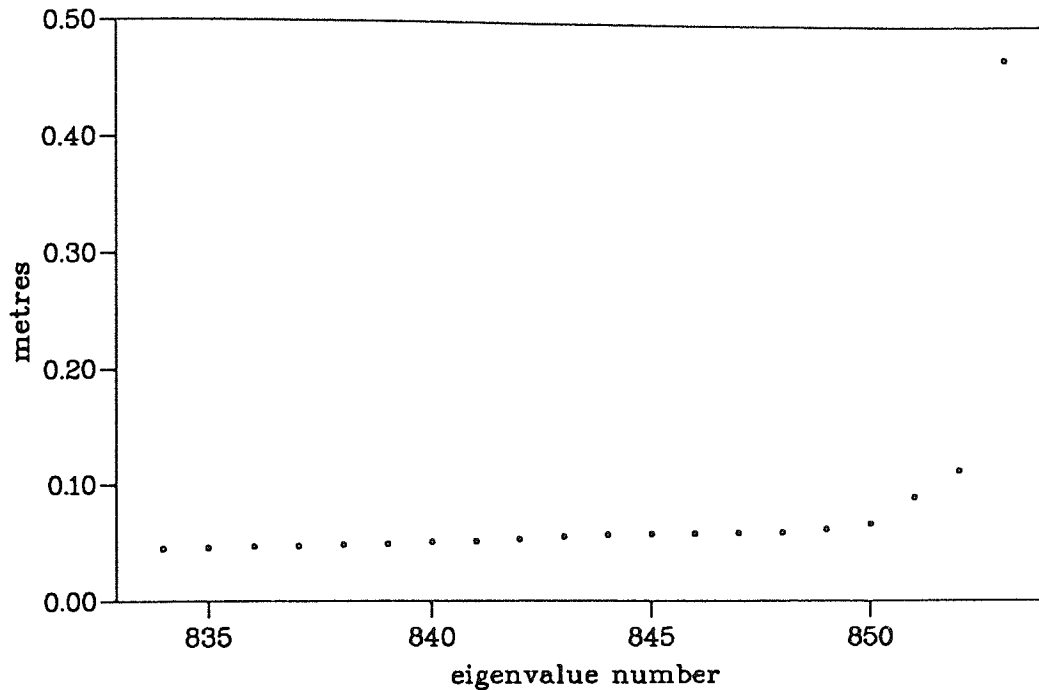


Figure 5.8: Some of the higher standard errors for the solution S3, prior to suppressing the parameter C_2^T .

the variance-covariance matrix N^{-1} indicates a weakness in the solution. This is particularly true since (i) the corresponding eigenvector had only the one C_2^T term as a major contributor and (ii) the standard error is greater than the initial 13 cm radial error estimate for TOPEX/Poseidon. Indeed, it is almost as great as the corresponding 58 cm *a priori* radial error estimate for ERS-1. As a result it was decided to suppress the C_2^T term in solution. It was noted that this did not degrade the root-mean-square (RMS) of fit of the solution but did result in a decrease in the correlations between parameters and removed the 47 cm standard error. Having made these modifications (limiting m for ERS-1 and suppressing the C_2^T term for TOPEX/Poseidon) there were just 345 solution parameters sought for the ERS-1 solutions (S1 and S2 above) and 852 for the joint case (S3).

For each solution, the radial correction was recovered by employing the solution parameters within Equation 5.11 and removed from the simulated or *a priori* values that are illustrated in Figures 5.1 and 5.2. This removal provided residuals of fit of the correction procedure to the simulated radial error, the RMS of which

are presented in Table 5.3. In all instances, there has been a marked improvement

solution	RMS (cm)		
	radial residuals		dual-crossover residuals
	ERS-1	TOPEX/Poseidon	
<i>a priori</i>	58.38	13.50	59.53
S1	6.82	—	12.00
S2	4.64	—	12.21
S3	4.87	3.09	2.69

Table 5.3: RMS of fit of the calculated radial error, from the unconstrained solutions, to the simulated values.

after modelling for a radial correction. The dual-crossover column indicates the diminution in the difference between true and perturbed dual-crossover heights,

$$\left(h_t^T - h_t^E\right) - \left(h_p^T - h_p^E\right).$$

This occurs as a result of the smaller difference between h_t and h_p after the computed corrections have been included.

Considering solution set S1, Figure 5.9 illustrates the radial residuals after correction. As indicated in Table 5.3, this has an RMS value of 6.82 cm corresponding to the 12.0 cm RMS of fit of the corrected set to the dual-crossover data. The value of 6.82 cm is significantly lower than the 13.50 cm *a priori* estimate for the error in the TOPEX/Poseidon radial ephemeris. This would appear to mean that the inaccuracies in the TOPEX/Poseidon ephemeris have not totally contaminated the ERS-1 solution parameters. Also, evident in Figure 5.9 is a three day beat (which results from the close proximity in ground-tracks after this period) and a number of arcs where the residuals still exceed 20 cm. Consideration of Figure 5.10 also shows a number of standard errors in excess of 6 cm. Thus while the RMS of fit after refinement is acceptable, there is clearly a level of uncertainty in the solution parameters, indicating that the solution is potentially inaccurate in certain circumstances.

By including ERS-1 single-crossovers in the dataset, but again only solving for the ERS-1 parameters, the RMS of fit is further reduced to some 4.64 cm. The radial residuals of this solution (S2) are depicted in Figure 5.11, which again sug-

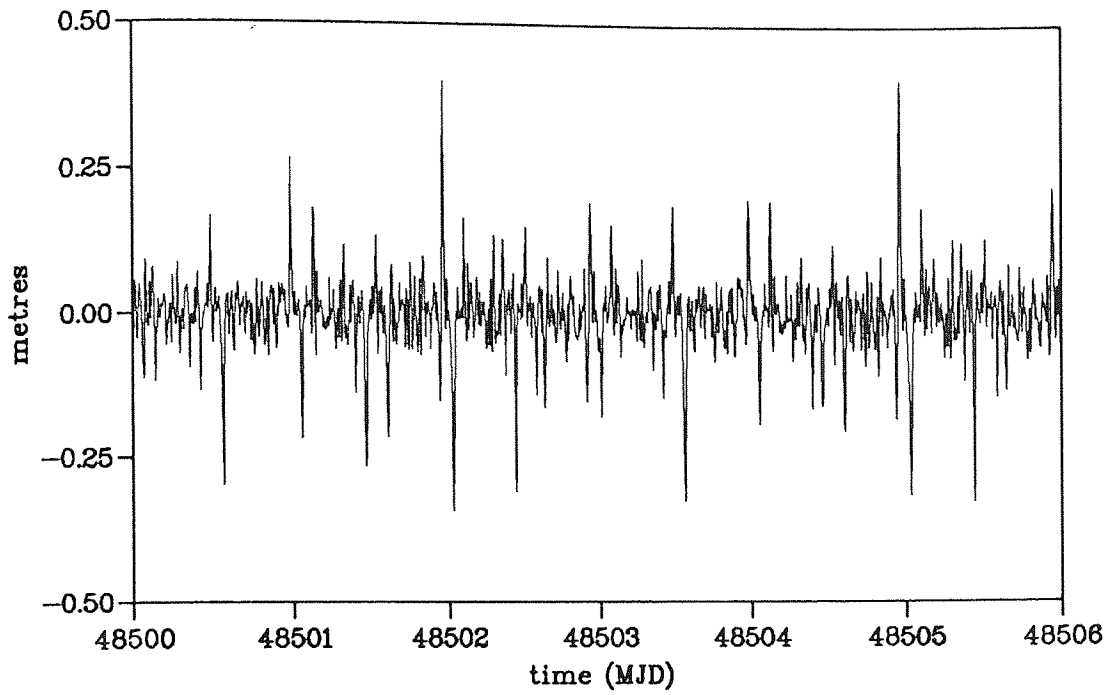


Figure 5.9: ERS-1 radial residuals after correction for the solution S1.

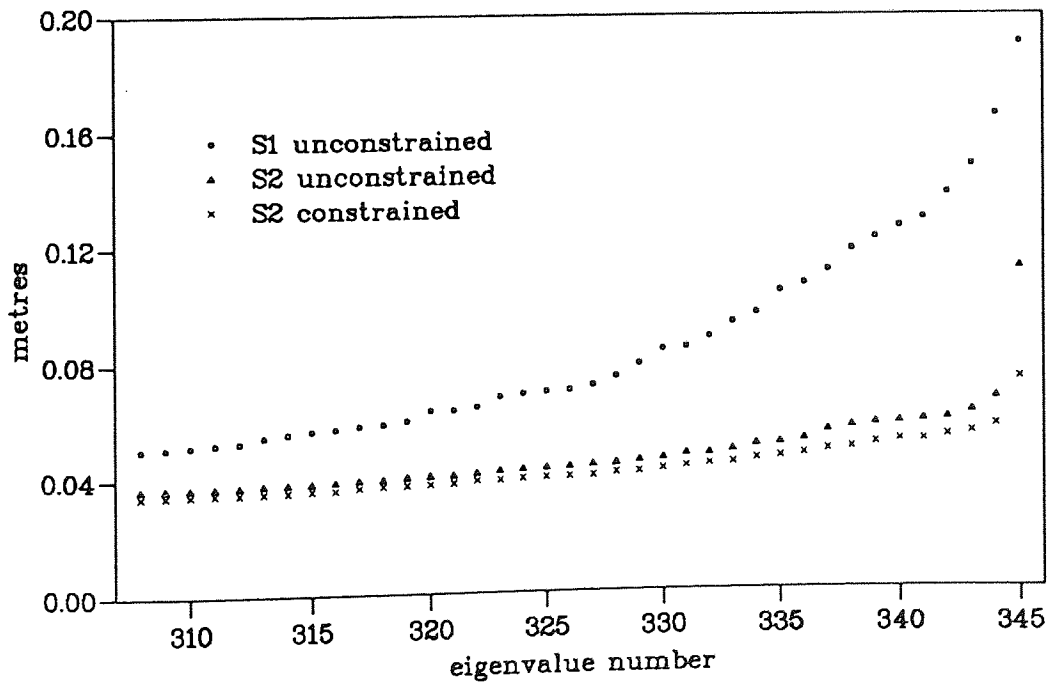


Figure 5.10: The highest standard errors for solutions to ERS-1 parameters.

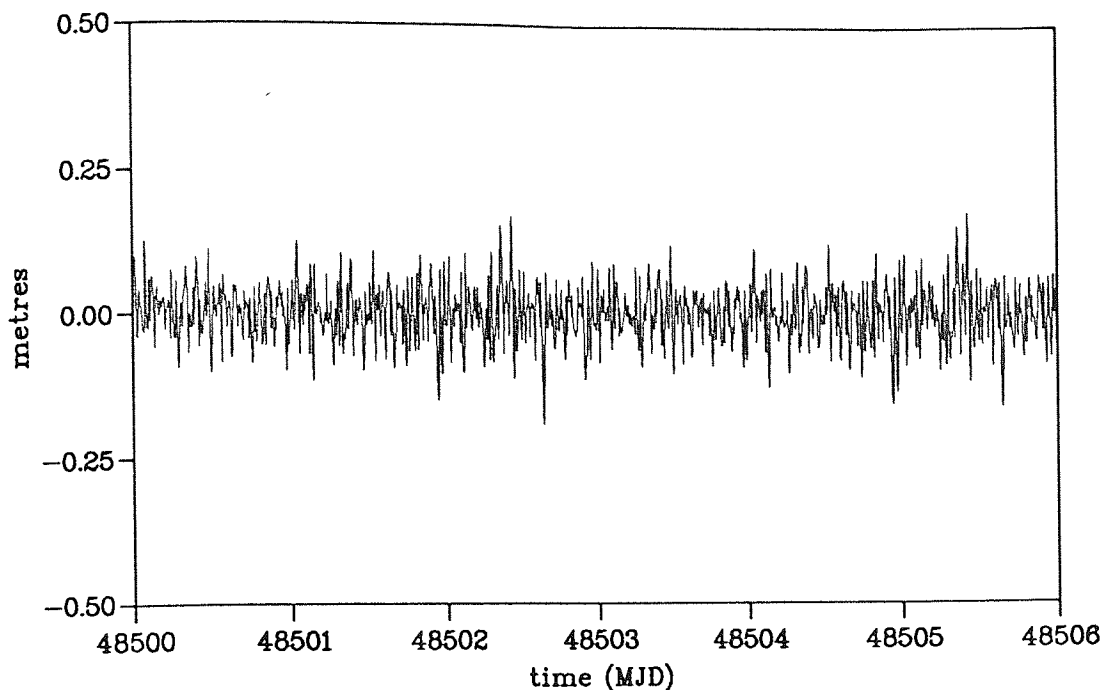


Figure 5.11: ERS-1 radial residuals after correction for the solution S2.

gests a three day repeat pattern and still possesses some points where the residuals are larger than 15 cm. The addition of the single-crossover data appears, from the improved results, to overcome some of the deficiencies in the dual-crossover dataset. Any future work with real dual-crossover data ought to consider the reasons behind this improvement; the geographical expansion of the dataset not necessarily providing the only explanation.

Further, some measure of the amount of absorption of TOPEX/Poseidon radial error into the ERS-1 solution is deduced by considering the 12.0 cm RMS of fit after correcting for the dual-crossover data. Taking the value of 4.64 cm achieved for ERS-1, a simple differencing of squares implies that the remaining error in the dual-crossovers (due to TOPEX/Poseidon) is approximately 11 cm — close to the *a priori* value of 13.5 cm. This indicates that there is a low incidence of absorption of the TOPEX/Poseidon error, opening up the potential to solve simultaneously for parameters of both satellites. The improvement in solution as attained by S2 over S1 is also illustrated in the diminished standard errors of Figure 5.10. A uniform improvement is displayed with only three such errors exceeding the 6 cm mark. The eigenvector connected with the 11 cm standard error was investigated through analysis of its component parameters, but no single contributing frequency or other value dominated; rather the vector was composed

of a large subset of the set of solution parameters.

The third solution, S3, added the TOPEX/Poseidon single-crossover data to the existing dataset and attempted the simultaneous solution suggested by this previous result. As stated above, this solution procedure solves for the previously specified 852 parameters to avoid singularities in the matrix N . The radial residuals after solution are depicted in Figure 5.12 for ERS-1 and 5.13 for TOPEX/Poseidon. The residuals for ERS-1 have increased slightly from those

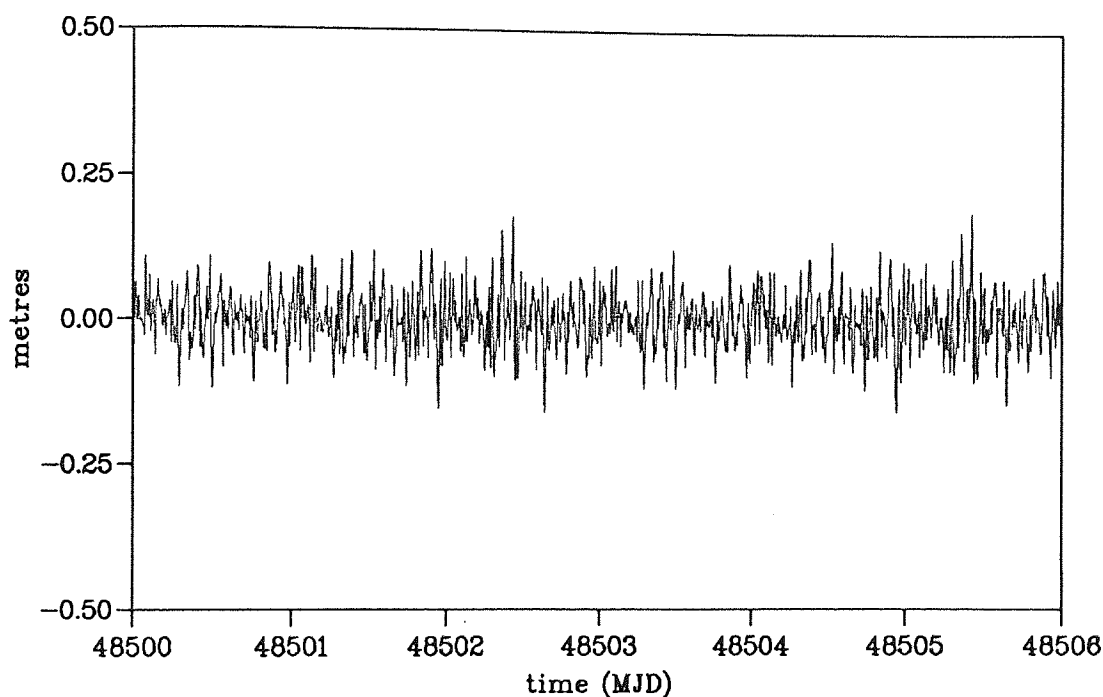


Figure 5.12: ERS-1 radial residuals after correction for the solution S3.

obtained for solution S2. However, none of them now exceed 20 cm, and the increase in RMS from 4.64 cm to 4.87 cm is reflected in slightly greater variation elsewhere. The TOPEX/Poseidon radial residuals exhibit an RMS of just 3.09 cm, indicating a significant improvement over the *a priori* 13.5 cm value. The residual plot for TOPEX/Poseidon also shows a clear daily cycle — giving ten almost identical occurrences of the same pattern over the simulation period. In addition to the improvement in the TOPEX/Poseidon residuals, the RMS of fit to the dual-crossover data has diminished to 2.69 cm. The standard deviations of the dominant eigenvectors are plotted in Figure 5.14. Investigating these eigenvectors indicated that those associated with the greatest uncertainties were largely composed of ERS-1 parameters; the dataset being adequate to resolve the TOPEX/Poseidon parameters.

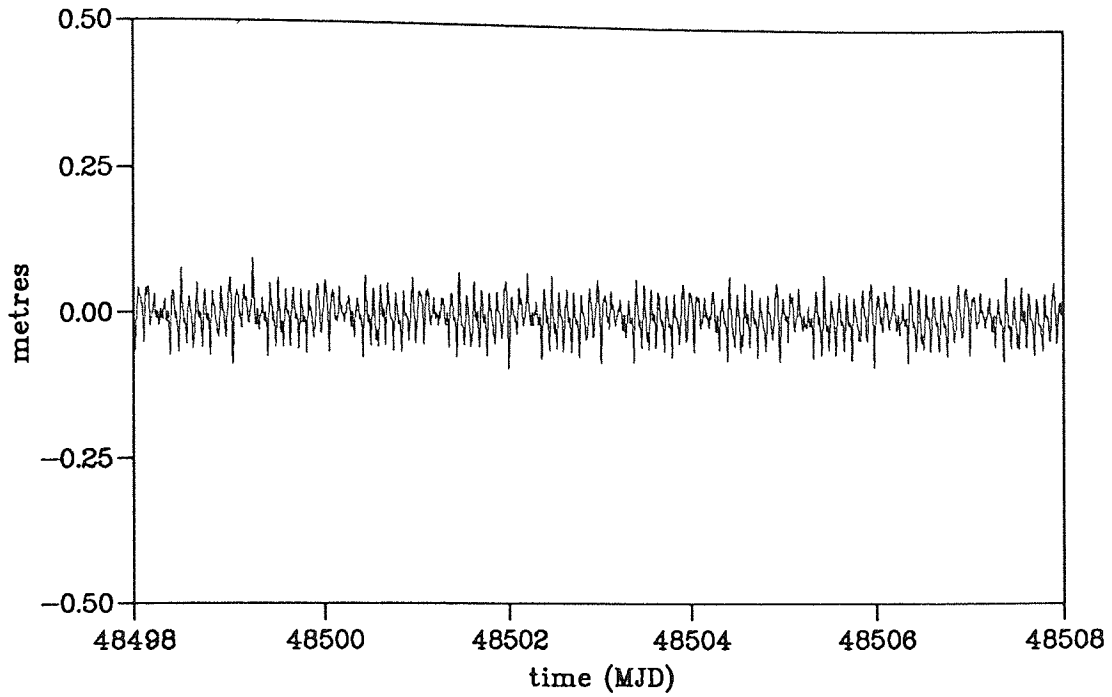


Figure 5.13: TOPEX/Poseidon radial residuals after correction, for the solution S3.

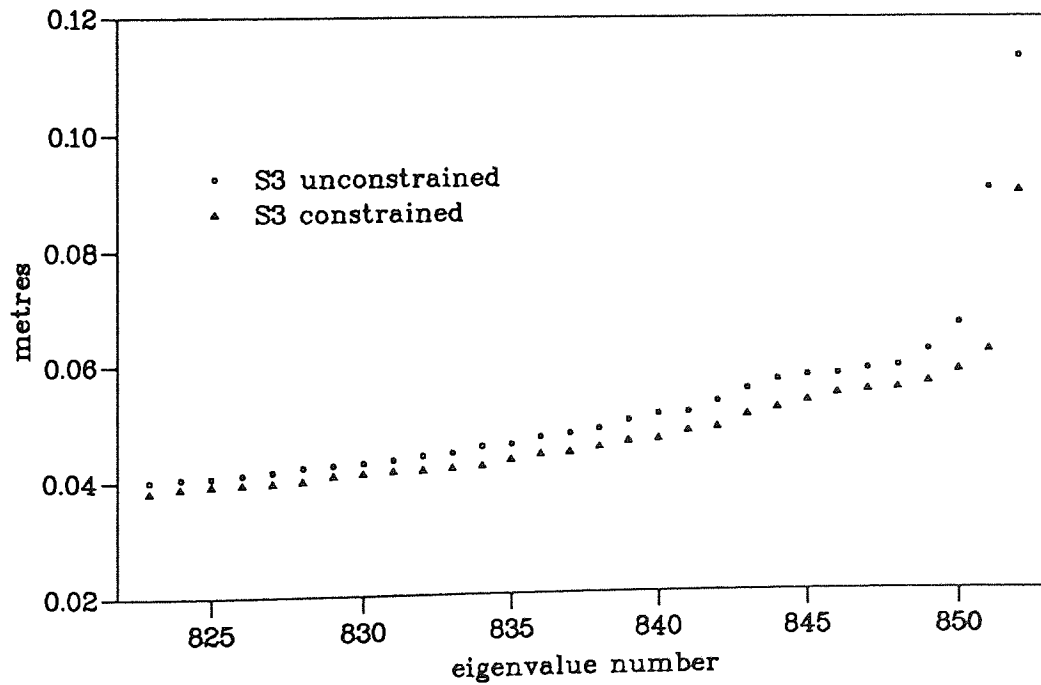


Figure 5.14: The highest standard errors for the simultaneous solutions.

So far the matrix N had been unconstrained. However, certain of the standard errors (illustrated in Figures 5.10 and 5.14) are relatively large when considered in relation to adjacent values. Further, in contrast to the case of the 47 cm standard error attained prior to the suppression of the C_2^T parameter, none of the associated eigenvectors show significant contributions from any given solution parameters. Thus, in order to reduce these values and so improve the level of confidence in the solution the matrix N was constrained.

Reduction in correlation between solution frequencies has been achieved by, among others, Wagner and Melchioni [1989] and Moore and Gray [1991], with the addition of mild constraints. The form of constraints adopted here was employed in a least squares collocation technique. Since it is generally accepted, for example Wagner [1985], that the greatest contribution to the radial error arises from the one cycle-per-revolution term, $\psi_{1,0}$, this parameter is given the greatest freedom and all other frequency terms are constrained to a greater extent. Thus, those frequencies farthest from one cycle-per-revolution (zero and two cycles-per-revolution in this case) are given the least freedom. The parameters for each satellite are weighted independently which enables a distinction to be made between the confidence held in orbits of the two satellites.

The constraints for the frequencies were selected by considering the achieved or expected variations in the orbital standard deviations. Thus, it was assumed that the orbit of ERS-1 had a sample standard deviation of between 10 cm and 50 cm (based upon converged RMS values using GEM-T2) as compared with a range of 4 cm to 20 cm for TOPEX/Poseidon (from predicted estimates). These ranges were converted to minimum and maximum constraints by first dividing throughout by a value of $20\sqrt{2}$ — taken to be a typical crossover weight — and then using the constraint formula $w = 1/\sigma^2$ (see Figure 5.15). It must be noted that *all* these values are merely *suggested* values, since this study is only a simulation. However, within this study at this time, it was felt that the constraints thus obtained matched orbital RMS values achieved for ERS-1 six-day arcs, using the same gravity fields as used for the simulated data. The overall effect is to restrict the solution, by encouraging absorption of ill-determined signatures into frequencies close to the dominant one cycle-per-revolution term.

The constraints were further adapted to include some measure of the relative

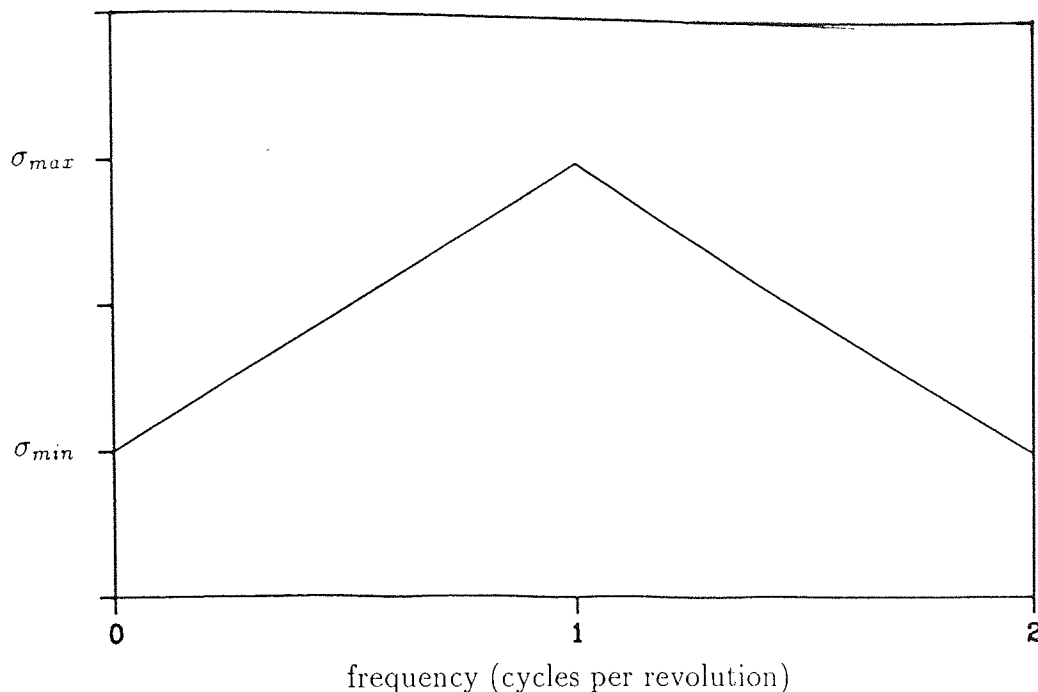


Figure 5.15: Illustrating the triangular weighting procedure.

number of data points included by multiplying them by the factor

$$\frac{N_{obs}}{N_{param}}$$

where N_{obs} is the number of observations (for a given satellite) and N_{param} is the number of solution parameters sought. The non-frequency terms $\{C_i : i = 1, 5\}$ were also constrained to give some measure of the relationship between the two satellites. These constraints reflected the estimated relationship between ERS-1 and TOPEX/Poseidon, given that the latter is considered to possess more accurate orbits. Thus, the non-frequency terms of ERS-1 were left unconstrained, whereas those of TOPEX/Poseidon were constrained to 2 cm. The principle here is that ERS-1 error dominates and by constraining the parameters of the two satellites in this way, the ERS-1 parameters are forced to absorb errors which might otherwise corrupt the better known TOPEX/Poseidon values.

The RMS of fit attained using the constrained versions of solution techniques S2 and S3 (presented in Table 5.4) were obviously not as low as those of the unconstrained set, since the constrained parameters are less free to find a minimising solution. In addition to this, there was another cause of the higher RMS values, which becomes clear when considering the residual plots, as illustrated in Figures 5.16 and 5.17. These figures both have large *tails* at either end of the simulation period. If these tails are removed, the RMS is diminished to values

solution	RMS (cm)		
	radial residuals		dual-crossover residuals
	ERS-1	TOPEX/Poseidon	
S2	8.02	—	14.13
S3	6.53	3.73	4.35

Table 5.4: RMS of fit of the calculated radial error, from the constrained solutions, to the simulated values.

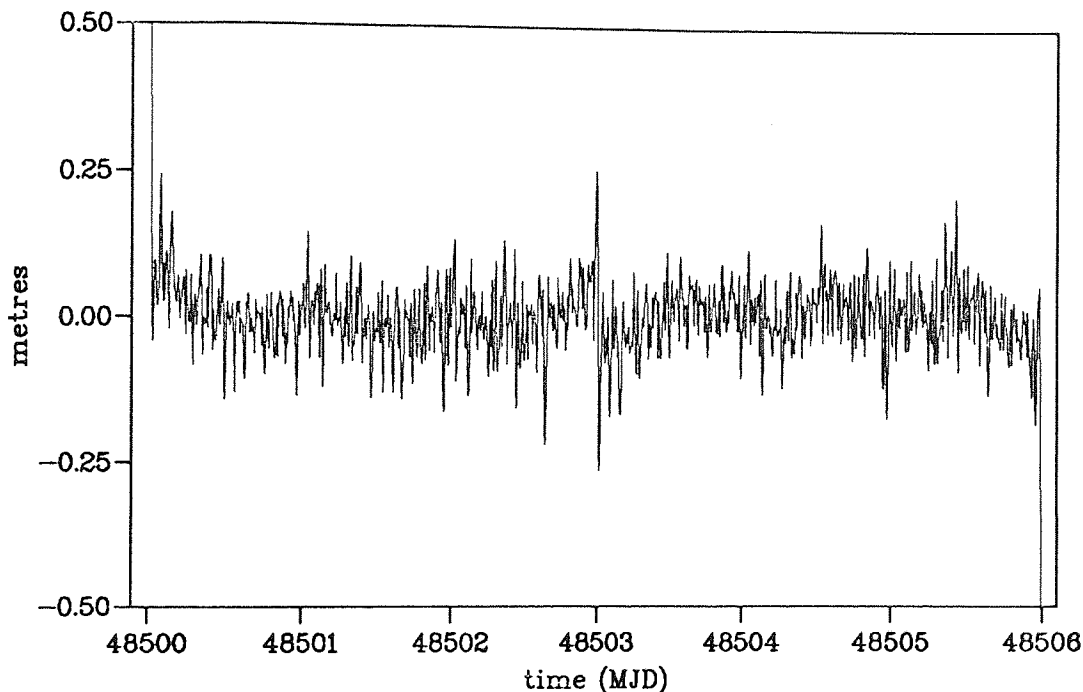


Figure 5.16: ERS-1 radial residuals after correction, for constrained version of the solution S2.

of 5.66 cm and 5.33 cm for solutions S2 and S3 respectively; still larger than the equivalent unconstrained results. The different RMS values for the ERS-1 solutions with and without the tails, are probably due to the lack of data beyond the simulation period; meaning that the solution at the ends of the period is not restricted to realistic values. In the unconstrained solution, there are no visible tails since the errors are absorbed throughout the solution, due to the minimising process. However, when seeking a constrained solution, these errors cannot be so freely absorbed and the tails become apparent. In contrast to the RMS increase in the constrained solution, the standard errors achieved (illustrated in Figures 5.10 and 5.14) show a uniform improvement (decrease). Thus there is more confidence

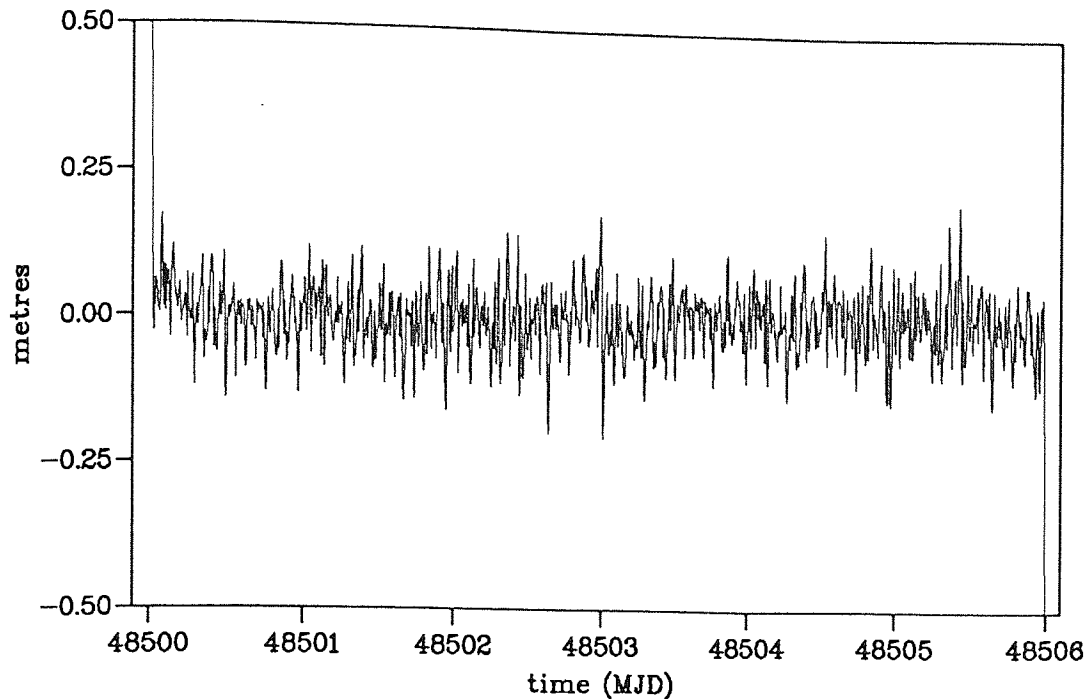


Figure 5.17: ERS-1 radial residuals after correction, for constrained version of the solution S3.

in the constrained solution; at least in that portion of the period lying between the *tails* exhibited by the residuals.

5.8 Conclusions

In conclusion, these results indicate that a conceptually simple technique is able to reduce the radial orbit error of ERS-1 through the addition of dual-crossover residuals with TOPEX/Poseidon. The addition of ERS-1 single-crossovers further improves the solution, resolves some of the remaining outlying points and improves confidence in the solution, as measured by the standard errors of the covariance matrix. The use of the mild constraint approach detailed above (which characterises the known form of the radial error) also reduces the formal uncertainty in the solution. However, the presence of tails in the residuals may indicate that the real uncertainty has increased despite the greater confidence in individual coefficients. Conversely, as these tails lie at the ends of the simulation period, they may simply indicate a problem with the simulation technique, possibly one of over-constraining certain frequencies. Clearly, one solution to this problem would be to exclude the arc ends — a procedure which is already in common

use in orbital convergence work. In addition, this simulation shows that solution of parameters for the simultaneous refinement of ERS-1 and TOPEX/Poseidon is possible, though certain parameters have to be suppressed due to dependencies and geographic unobservables within the parameter set. These unrecoverable components have been identified under the assumptions of the simulation.

A further development may be to replace the simple constraint model used here with a more complex approach. In particular the variance of the gravitational component of the radial error at a specific frequency can be derived from the covariance matrix of the global gravity field model used in the long-arc analyses to derive the crossovers.

The study has implicitly assumed that the temporal errors associated with crossovers are negligible or random in nature. More specifically, it has been assumed that errors due to atmospheric corrections (dry and wet troposphere, ionosphere, inverse barometer effect) and dynamic ocean topography make no net contribution to the radial refinement. For TOPEX/Poseidon, the microwave radiometer (TOPEX) allows a water vapour induced delay to be determined. Further, the ionospheric correction may be derived for TOPEX from the dual frequency altimeter, and for Poseidon from the solid state altimeter (using the DORIS tracking network — see Chapter 6). Thus, the source of major error in the crossover data is likely to be in ocean tides and other ephemeral ocean dynamic features, e.g. eddies. It may be that refining the ERS-1 orbit only will be preferred by users of this technique to avoid any possible contamination of the more precise TOPEX/Poseidon dataset.

Chapter 6

Tracking the French satellite

SPOT-2

6.1 Introducing the next two chapters

In the previous two chapters attempts have been made to improve ERS-1 orbits. In Chapter 4 this was effected by adopting the techniques of Chapter 3; modifying the aerodynamic and direct solar radiation pressure components of the force model and utilising the GUESS area table generating software. Subsequently, in Chapter 5, an approach was made using transferred data from a second satellite (in this instance, TOPEX/Poseidon — which is not affected by atmospheric density to the same extent as ERS-1). Thus, each attempt aimed to reduce the uncertainties that arise from errors in atmospheric modelling combined with sparse tracking data. In this and the following chapter a further attempt is made, using information from the SPOT-2 satellite. In contrast to the previous approach, this does *not* avoid the atmospheric problems of ERS-1, but rather, by possessing a far denser tracking dataset, aims to correct for along-track errors.

This chapter is purely preparatory. It begins with a brief outline of the SPOT-2 satellite and the DORIS tracking system. Following this, the modifications required by the SATAN-A suite, in order to enable it to process the DORIS Doppler range-rate data, are described. Thirdly, using the GUESS software of Chapter 3, area tables are produced from a geometric model of SPOT-2 (in a similar manner to those obtained for ERS-1 in Chapter 4) and several precise long-arc orbits are determined for periods in 1990 and 1992. It is intended that this will provide a

further example of the ability of area tables produced by the GUESS software to improve the fit of long-arc precise orbits. Then, in the next chapter, the third attempt to refine ERS-1 orbits will be made using SPOT-2 data.

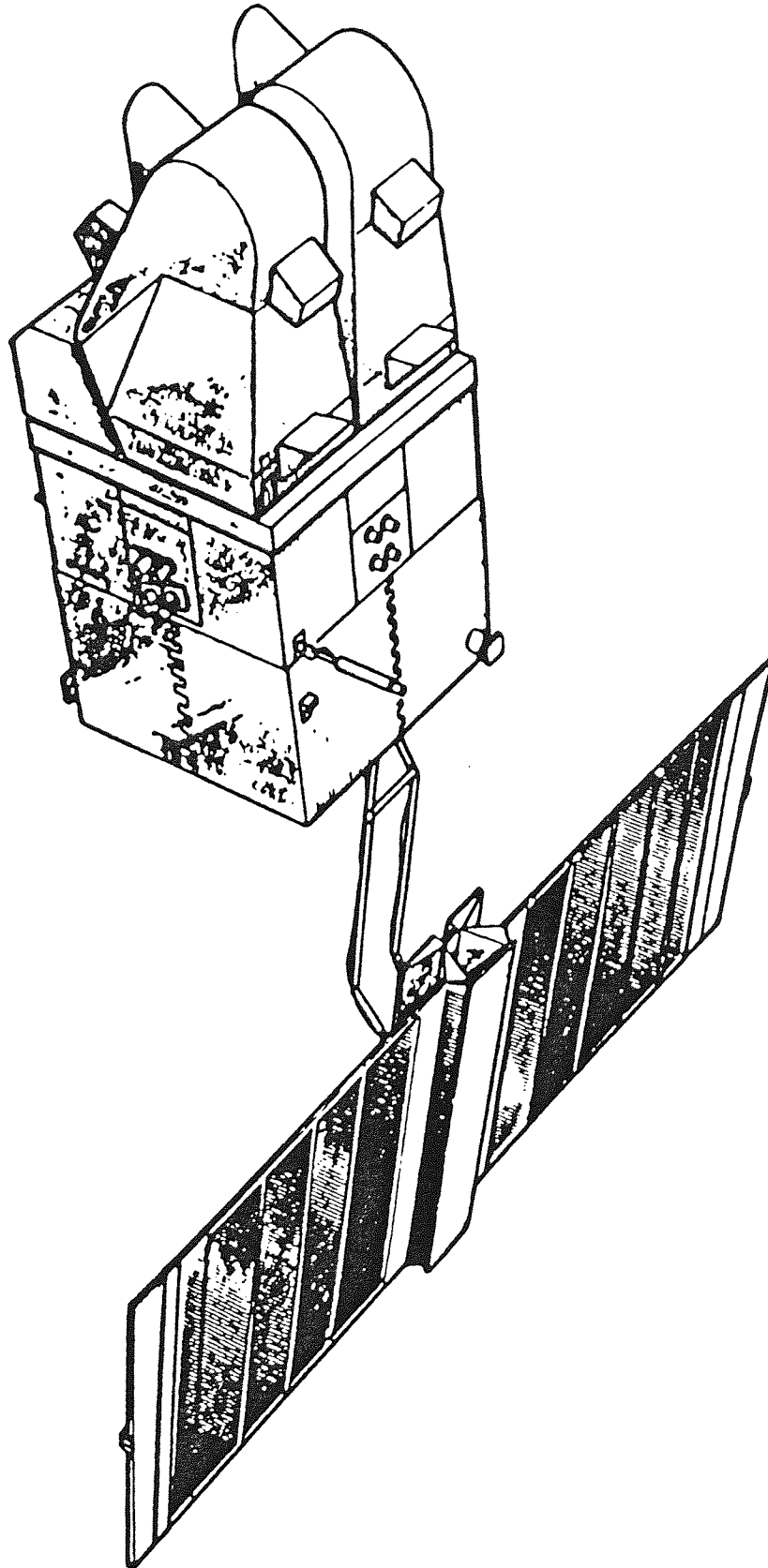
6.2 SPOT-2 and the DORIS system

The French satellite SPOT-2 was launched in March 1990 from an Ariane launch vehicle into a sun-synchronous orbit of low eccentricity ($e < 0.01$) at an inclination of 98.6° and an approximate altitude of 832 km. It repeats its ground-track every twenty-six days and is maintained in this orbit by manoeuvres whenever necessary.

The satellite module and solar array attachment (illustrated in Figure 6.1) are identical to those of ERS-1, though the actual solar panel dimensions are slightly smaller (about 19.5 square metres as opposed to a value of 28.5 for ERS-1). The payload consists of two high resolution visual imagers and the on-board segment of the DORIS tracking system (developed by CNES at Toulouse); the latter being experimental at the time of launch [Nouël, 1991]. This segment, now confirmed as being fully operational by over two years of successful tracking, comprises an omnidirectional antenna, an ultra stable oscillator (USO) and storage and processing facilities.

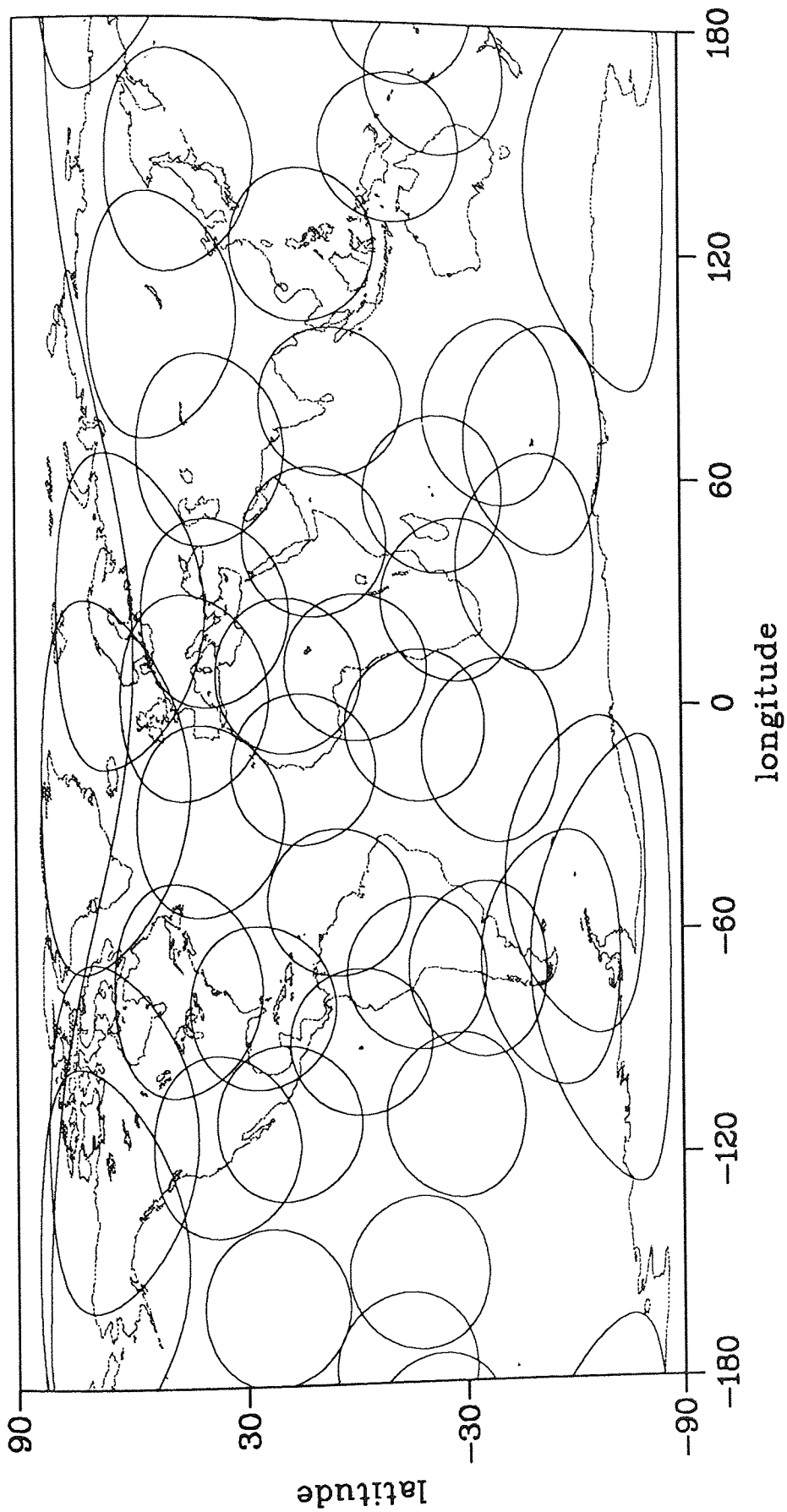
The ground segment of DORIS is made up of a network of beacons each of which falls into one of two categories: either an orbit determination beacon (ODB) or a ground location beacon (GLB). ODBs are all sited at fixed, well known locations and are used to determine the orbit of SPOT-2. As Figure 6.2 illustrates, these provide an almost uniformly global coverage; the system being programmed to receive at an elevation of just 10° [Dorrer, 1991]. The GLBs, on the other hand are not used for orbit determination but rather to locate positions on, and hence movements of, the earth's surface. Such measurements are relative to the satellite orbit, as determined by the ODBs. In addition to these two groups, there is a master beacon at Toulouse, used to update the on-board processor for each orbit, and a receiving station at Aussaguel which downloads the stored data (once every twelve hours for SPOT-2) and transfers it to Toulouse for further processing.

Each ground station (ODB or GLB) comprises three meteorological sensors as well as its own USO and the DORIS antenna. These sensors measure the local



SPOT-2

Figure 6.1: The SPOT-2 satellite.



DORIS ORBIT DETERMINATION BEACONS
 FEBRUARY 1992

Figure 6.2: Positioning and coverage of DORIS orbit determination beacons by February 1992.

atmospheric pressure, air temperature and relative humidity, to provide information for the meteorological messages which are sent to the satellite. Every ODB transmits continuously at two frequencies of 401.125 MHz and 2036.125 MHz (maintained by the stability of the USO), interrupting these signals every 10 seconds to broadcast the current meteorological information. In contrast, the GLBs may not transmit continuously but have to be operated on a pre-selected time slot basis. The reason for this is that if two GLBs were to transmit at the same time from a similar location they would interfere at the satellite in such a way as to prevent proper reception and processing. Thus, only one such beacon may transmit a signal at any one time and the satellite must have been informed which beacon is sending by a message from the master beacon at Toulouse. This problem does not occur with the ODBs because their spacing is such that where two signals do reach the satellite, the Doppler effect causes them to be so dissimilar that they do not disrupt the operation of the on-board segment.

The on-board processor works by comparing the received frequencies, which differ from the emitted ones due to Doppler effects, with those of its own USO, namely 401.25 MHz and 2036.25 MHz respectively. The higher of these is then used to compute the beacon-spacecraft range-rate and, in the same way, the lower is employed to eliminate errors due to the ionospheric propagation effect. The theory and methodology of such a technique is explained in the next section.

6.3 The Doppler effect and beats: some theory

The Doppler effect is a well known phenomenon relating the difference between emitted and received frequencies to the relative motions of source and receiver. For example, if the receiver is receding from the source (i.e. their separation is increasing), the apparent wavelength increases as the number of complete waves received in any given time interval decreases (the velocity of the signal remaining unchanged). This corresponds to a received frequency which is lower than the emitted one [Borowitz and Beiser, 1967, p.435]. For mutually approaching source and receiver the opposite result pertains, as illustrated in Figure 6.3.

For electromagnetic radiation, such as the radar signal of the DORIS system, the speed is equal to that of light, c . Thus, the relationship between received (f_r)

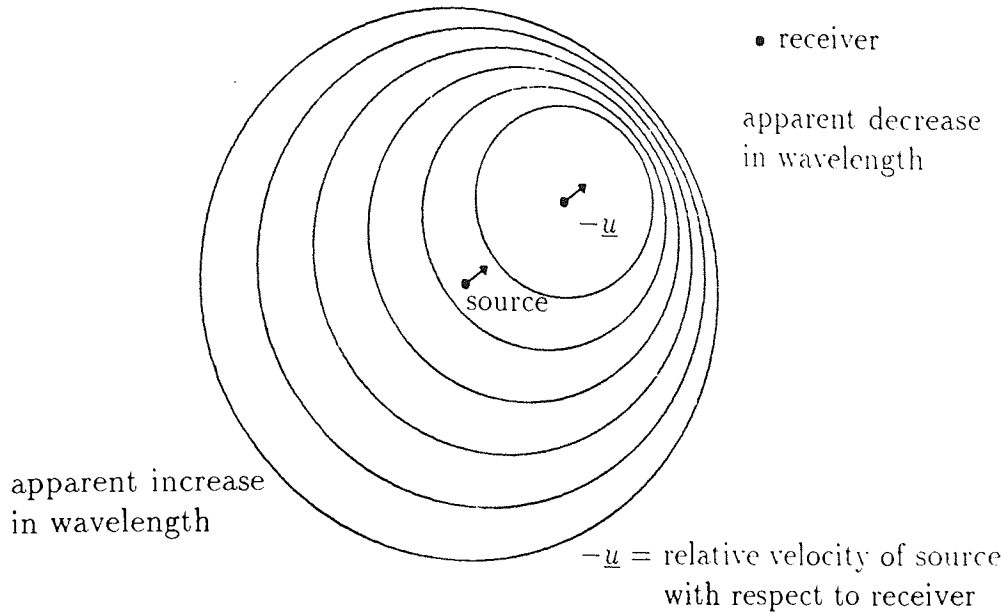


Figure 6.3: The Doppler effect.

and emitted (f_b) frequencies is given by

$$f_r = f_b \left(\frac{1 - u/c}{\sqrt{1 - u^2/c^2}} \right) \quad (6.1)$$

where u is the magnitude of the relative velocity of the receiver with respect to the source, measured positive for an increasing separation and negative otherwise [Borowitz and Beiser, 1967, p.437].

Expanding Equation 6.1 in terms of powers of u/c by means of the binomial theorem, gives

$$\begin{aligned} f_r &= f_b (1 - u/c) \left(1 + u^2/2c^2 + 3u^4/8c^4 + \dots \right) \\ &= f_b \left(1 - u/c + u^2/2c^2 - u^3/2c^3 + \dots \right) \end{aligned}$$

from which, by consideration of the relative magnitudes of f_b , u and c (noting that $u \ll c$ for SPOT-2), terms of order $(u/c)^4$ and above may be neglected. Indeed, even the term in $(u/c)^3$ produces negligible computational effect at the levels of precision currently available within the SATAN-A suite (as described in Chapter 2). In practice, the DORIS system simplifies even this and, neglecting all non-Newtonian terms, employs the expression

$$f_r = f_b (1 - u/c) \quad (6.2)$$

which is corrected for relativistic effects (thereby including the $(u^2/2c^2)$ term) within the adapted orbital correction program (see Section 6.4).

The received frequency is not measured directly, but rather by comparison with the on-board reference frequency, f_s . This is effected by considering the composite wave, created by the interference between received and reference frequencies. These interact to give a wave of constant frequency $(f_s + f_r)/2$ and varying amplitude. The amplitude varies from zero, when the interference is destructive to some maximum value. Thus, we may consider a second wave of constant amplitude which envelopes the composite one, as illustrated in Figure 6.4, [Borowitz and Beiser, 1967, p.431]. The frequency of this enveloping wave is $|f_s - f_r|$ and,

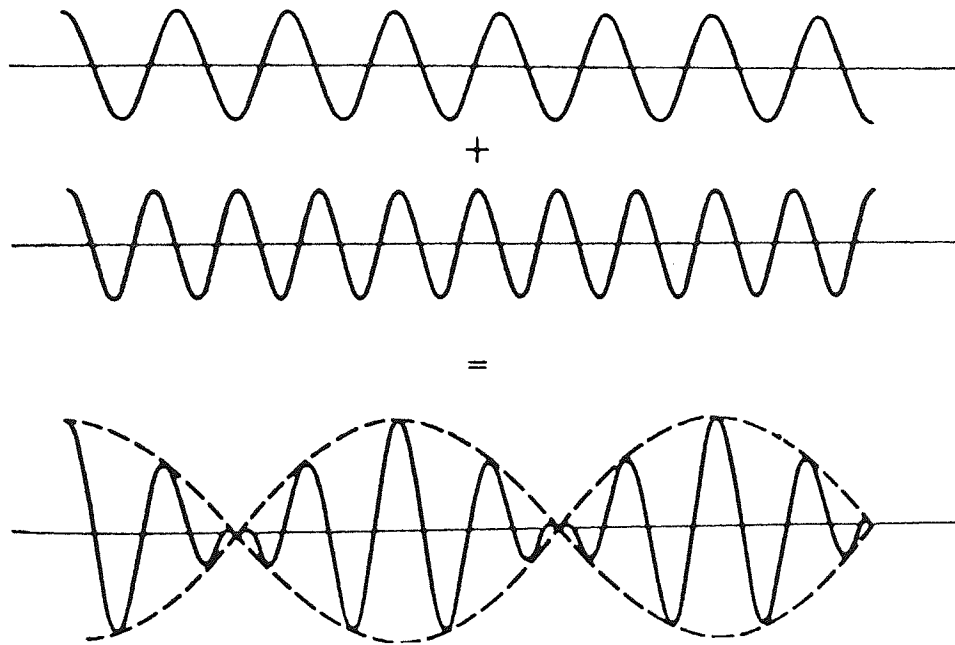


Figure 6.4: An example illustrating how two frequencies may interact to produce beats.

where the two interfering frequencies which produce it are sufficiently close, it provides an audible pulsating signal, from which the name *beats* is derived. Even in the non-audible range, beats are still detectable by instrumentation and it is the number of such beats which the DORIS system counts, over some measured time interval, Δt , lying between successive meteorological broadcasts.

By careful choice of f_s and f_b it is possible to ensure that either the received frequency exceeds that of the on-board USO ($f_s > f_r$) or vice versa ($f_s < f_r$) at all times. In addition, by maintaining the beacon frequency close to that of the satellite ($f_s \approx f_b$), the magnitude of the number of beats (N) may be restricted,

increasing the ease of counting. This number is given by the expression

$$N = \int_{t_0}^{t_0+\Delta t} |f_s - f_r| dt$$

where the frequencies of the USOs on the SPOT-2 satellite and in the DORIS beacons satisfy $f_s > f_r$. Substituting for f_r in this expression, using Equation 6.2, results in the following equation for N ,

$$N = (f_s - f_b) + \frac{f_b}{c} \int_{t_0}^{t_0+\Delta t} u dt \quad (6.3)$$

which is the equation used by the on-board DORIS segment to evaluate N and hence the observed values to be used as data for orbit determinations. Further, by the definition of u above (as the rate of change of the satellite-beacon separation, $\frac{d\rho}{dt}$) it is possible to expand the final integral term of Equation 6.3 as follows,

$$\begin{aligned} N &= (f_s - f_b) + \frac{f_b}{c} \int_{t_0}^{t_0+\Delta t} \dot{\rho}(s) ds \\ &= (f_s - f_b) + \frac{f_b}{c} (\rho(t_0 + \Delta t) - \rho(t_0)). \end{aligned} \quad (6.4)$$

Now, each record of the data files produced by CNES for SPOT-2 contains the values of

$$\begin{aligned} &t_0, \\ &\Delta t, \\ \text{and } &\frac{c}{f_b \Delta t} (N - (f_s - f_b)) \end{aligned}$$

where the last of these represents the observed range-rate value, $O_i(t_0)$ — the subscript i denoting the sequential record number and t_0 being the observation time. Further, the corresponding calculated value $C_i(t_0)$ — required by the weighted least squares procedure of Section 2.3 — is found from Equation 6.4 to be

$$C_i(t_0) = \frac{\rho(t_0 + \Delta t) - \rho(t_0)}{\Delta t} \quad (6.5)$$

thus completing the description of and theory behind the DORIS Doppler system. The next section elaborates upon the necessary amendments to the orbital determination package and the corrections which must be made to these observed and calculated values for precise orbits to be calculated.

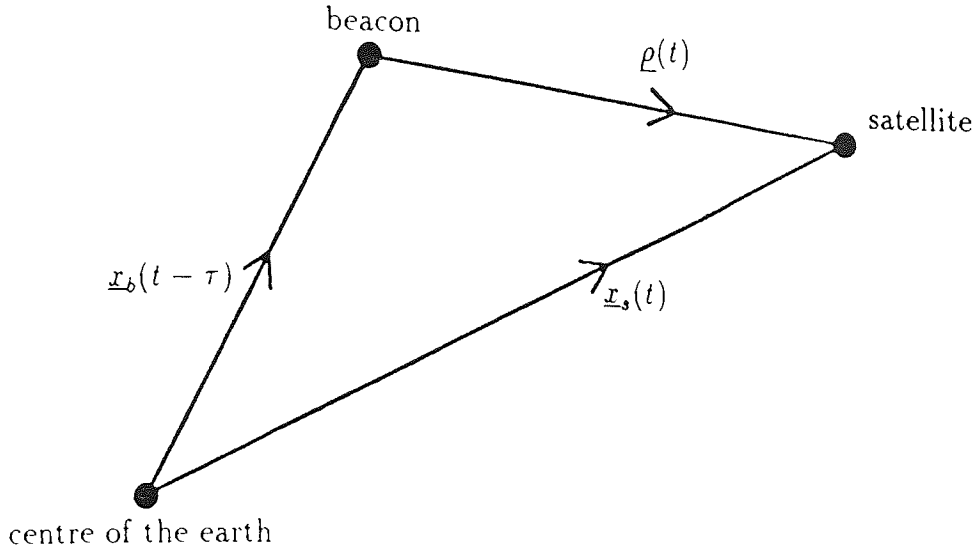


Figure 6.5: The satellite-beacon range vector.

6.4 Amending the SATAN-A package

It may be recalled from Chapter 2 that the prediction program (ORBPREP) takes as its basic input a file of observation times, t , and determines both a position, $\underline{x}(t)$, and velocity vector, $\dot{\underline{x}}(t)$, as well as partial derivatives, $\frac{\partial}{\partial p_k} \underline{x}(t)$, for each of the input times and all the model parameters, p_k , for which a solution is being sought. From these values, the correction program (ORBCORR) computes a calculated value, $C_i(t)$, and its partial derivatives, $\frac{\partial}{\partial p_k} C_i(t)$, corresponding to every observation, $O_i(t)$. These are then used to form the normal equations and hence correct the prior parameters.

For DORIS Doppler data, the basic calculated value, C_i is defined by Equation 6.5, which corresponds to an observed range-rate measurement. Thus, in order to evaluate C_i , the range vector $\underline{\rho}$ (illustrated in Figure 6.5) must first be determined from

$$\underline{\rho}(t) = \underline{x}_s(t) - \underline{x}_b(t - \tau)$$

where \underline{x}_s and \underline{x}_b denote the satellite and beacon position vectors respectively (in some inertial reference frame) and τ is the *propagation* time (that is the time taken for the signal to travel from the beacon to the satellite). In its existing form the prediction program already produces the satellite position vector, $\underline{x}_s(t)$ and the equivalent value for the beacon, $\underline{x}_b(t - \tau)$, is determined within the correction

program, by iterating in τ until the range ρ and the propagation time τ both satisfy

$$\rho = \tau c.$$

Having produced both these position vectors, the range may be computed at times t and $t + \Delta t$ using

$$\rho(t) = |\underline{\rho}(t)|$$

whence, by substitution into Equation 6.5, the range-rate may be found.

From a consideration of this equation, it is clear that *two* dates are required to obtain *one* calculated range-rate. Thus, the input file of dates must contain two records for every one observation record in the Doppler data file; namely the time at the start of the beat count, t say, and that at the end of the same, $t + \Delta t$ (given a count duration Δt , as above). If this condition is met, the prediction program requires no alterations other than those normally incurred for the inclusion of any new satellite; namely determining area tables, including satellite specific data such as mass, and so forth. More importantly, the adoption of the DORIS Doppler data does not, by itself, result in any change in the prediction program (all changes arising solely from satellite variations rather than tracking-data differences).

Conversely, the correction routine, which is structured in a manner that takes each type of tracking data in turn, requires several adjustments. These must enable it to read and process (adding the stored corrections to the raw values) the new observation format, add several additional computed corrections to both observed and calculated values and produce the partial derivatives of the range-rate for use in the normal equations. Each of the necessary amendments will be considered in turn.

The first alteration was simply effected by changing a format statement. Thus, the DORIS Doppler data records could be read and the corrections (ionospheric, tropospheric and phase centre effect) added where necessary to the raw observed value. As has been mentioned above, the ionospheric corrections are computed from the Doppler effect on the lower beacon frequency (Section 6.3) and the tropospheric corrections from the meteorological message (Section 6.2). The phase centre effect is the DORIS equivalent of a centre-of-mass correction, allowing for the offsets between beacon location and antenna and between satellite antenna and centre-of-mass. This correction has been computed in such a way that it may

be added directly to the observed range-rate, requiring no further computation. These corrections produce an observation for each record which is then used by the modified correction program.

There are three other corrections made, all of which are added to the basic calculated range-rate of Equation 6.5. One of them, the relativistic correction, could equivalently be *removed* from the observed value: the effect on the residual ($O_i - C_i$) being the same. The other two corrections made are constant offsets for the error in the USO frequencies and that in the tropospheric correction term from the data record. Both these corrections must be added to the calculated range-rate as they will be solved for in the correction program (thus requiring partial derivatives of the calculated range-rate with respect to each correction).

Because each USO (of both satellite and beacons) does drift slightly from its nominal value, the true emitted and satellite reference frequencies will differ from the nominal values which are used to determine the beat count (Equation 6.3). However, it is not possible to solve directly for all the drifts in both satellite and beacon USO's at once. Indeed, analogously to the solution of station coordinates, *one* frequency error must be fixed in order to solve for the drifts in the others. Thus, it is assumed that the satellite reference frequency, f_s , is *true* and that all the error lies in the beacon USOs. This will mean that any correction obtained also includes the error in the satellite USO frequency. Current practice indicates that solving for a constant drift in each pass (computed as a ratio of the error in beacon frequency to the nominal frequency) is a satisfactory way of dealing with this error [Nerem *et al.*, 1991].

Now, because the nominal observed range-rate O_i^n is obtained from using the true beat count but nominal values of the USO frequencies f_b^n and f_s^n , it differs from the true observed value O_i^t as follows:

$$\begin{aligned} O_i^n &= \left(\frac{N}{\Delta t} - (f_s^n - f_b^n) \right) \frac{c}{f_b^n} \\ &= \left((f_s^t - f_b^t) - (f_s^n - f_b^n) + \frac{f_b^t}{c} O_i^t \right) \frac{c}{f_b^n} \end{aligned}$$

superscripts t and n denoting true and nominal respectively. This expression is then simplified by the assumption that all the error lies in the beacon frequency,

i.e. $f_s^n = f_s^t$, thus resulting in the equation,

$$O_i^n = \left(f_b^n - f_b^t + \frac{f_b^t}{c} O_i^t \right) \frac{c}{f_b^n}.$$

Whence O_i^t may be written

$$\begin{aligned} O_i^t &= \frac{c}{f_b^t} \left(\frac{f_b^n}{c} O_i^n + (f_b^t - f_b^n) \right) \\ &= O_i^n \left(\frac{f_b^n}{f_b^t} \right) + c \left(\frac{f_b^t - f_b^n}{f_b^t} \right) \\ &= O_i^n + O_i^n \left(\frac{f_b^n}{f_b^t} - 1 \right) + c \left(\frac{f_b^t - f_b^n}{f_b^t} \right) \\ &= O_i^n + \Delta_{\text{USO}} \end{aligned}$$

where

$$\Delta_{\text{USO}} = O_i^n \left(\frac{f_b^n - f_b^t}{f_b^t} \right) + c \left(\frac{f_b^t - f_b^n}{f_b^t} \right)$$

is the required correction to the observed value to allow for the frequency drift in the USOs.

Since it is the calculated value which requires correcting, this term must be modified and then removed from the uncorrected variable C_i . Thus, retaining the above superscript conventions,

$$\begin{aligned} C_i^t &= C_i - \Delta_{\text{USO}} \\ &= C_i - O_i^n \left(\frac{f_b^n - f_b^t}{f_b^t} \right) - c \left(\frac{f_b^t - f_b^n}{f_b^t} \right) \\ &\approx C_i - C_i \left(\frac{f_b^n - f_b^t}{f_b^t} \right) + c \left(\frac{f_b^n - f_b^t}{f_b^t} \right) \\ &= C_i - C_i \left(\frac{\beta}{c} \right) + \beta \end{aligned} \tag{6.6}$$

where

$$\beta = c \left(\frac{f_b^n - f_b^t}{f_b^t} \right)$$

is the required frequency bias correction. The parameter β is solved for once per pass over the long-arc, within the orbit correction program of Section 2.3. The approximation used in Equation 6.6 is justified since any error will be absorbed by the solution parameter, β .

The computation of the tropospheric correction term for each pass is far more straightforward. It is simply provided by scaling the existing correction term in

the data records, Δ_{trop} , by a parameter K_{trop} and adding this to the calculated value (C_i),

$$C_i^t = C_i + K_{\text{trop}} \Delta_{\text{trop}} \quad (6.7)$$

with the parameter K_{trop} being solved for in the usual manner (see Section 2.3).

The sole remaining correction term is a relativistic one. This is required to allow for the fact that Equation 6.2 was limited to Newtonian mechanics, whereas the velocities involved necessitate the inclusion of the effect of relativity. This correction term is given by Boucher [1978] in terms of an adjustment to the beat count N :

$$\Delta N = \frac{-\Delta t f_b}{c^2} \left(\left(\frac{GM_e}{|\underline{x}_b(t-\tau)|} - \frac{GM_e}{|\underline{x}_s(t)|} \right) - \left(\frac{|\dot{\underline{x}}_s(t)|^2 - |\dot{\underline{x}}_b(t-\tau)|^2}{2} \right) \right)$$

where G and M_e are the gravitational constant and mass of the earth respectively (as in Chapter 2) and all other variables are already defined in this chapter. As with the frequency bias above, this equation results in a correction to the observed value O_i^n , given by

$$\begin{aligned} O_i^t &= O_i^n - \frac{c\Delta N}{f_b\Delta t} \\ &= O_i^n - \frac{1}{c} \left(GM_e \left(\frac{1}{|\underline{x}_b(t-\tau)|} - \frac{1}{|\underline{x}_s(t)|} \right) - \left(\frac{|\dot{\underline{x}}_s(t)|^2 - |\dot{\underline{x}}_b(t-\tau)|^2}{2} \right) \right) \end{aligned}$$

which translates to a correction to the computed value by replacing O_i with C_i in this last equation and altering the first minus after the equality to a plus term.

Thus the required correction is,

$$+\frac{1}{c} \left(GM_e \left(\frac{1}{|\underline{x}_b(t-\tau)|} - \frac{1}{|\underline{x}_s(t)|} \right) - \left(\frac{|\dot{\underline{x}}_s(t)|^2 - |\dot{\underline{x}}_b(t-\tau)|^2}{2} \right) \right).$$

This concludes the description of all corrections which are made to the observed and calculated range-rates.

The next step in amending the SATAN-A suite, is to evaluate and include the relevant partial derivatives, $\frac{\partial C_i}{\partial p_k}$, within the orbital correction program. Using the range-rate definition of Equation 6.5, these may be expressed as follows,

$$\frac{\partial C_i}{\partial p_k} = \frac{\partial \dot{\rho}}{\partial p_k} = \frac{1}{\Delta t} \left(\frac{\partial \rho(t+\Delta t)}{\partial p_k} - \frac{\partial \rho(t)}{\partial p_k} \right)$$

which requires the further evaluation of the partial derivatives of the range, $\frac{\partial \rho}{\partial p_k}$, at times t and $t + \Delta t$. These in turn can be found by expanding the derivative

in a similar fashion as is used for other partial derivatives within the correction program; namely

$$\frac{\partial \rho}{\partial p_k} = \sum_{j=1}^3 \frac{\partial \rho}{\partial x_{s_j}} \frac{\partial x_{s_j}}{\partial p_k}$$

where $\underline{x}_s = (x_{s_1}, x_{s_2}, x_{s_3})$ is the satellite position vector. Thus, the partial derivative of the range-rate with respect to any parameter p_k is given by

$$\frac{C_i}{\partial p_k} = \frac{1}{\Delta t} \sum_{j=1}^3 \left(\frac{\partial \rho(t + \Delta t)}{\partial x_{s_j}(t + \Delta t)} \frac{\partial x_{s_j}(t + \Delta t)}{\partial p_k} - \frac{\partial \rho(t)}{\partial x_{s_j}(t)} \frac{\partial x_{s_j}(t)}{\partial p_k} \right).$$

Further, $\rho^2 = \sum_{j=1}^3 (x_{s_j} - x_{b_j})^2$, so the partial derivative of the range with respect to an element in the satellite vector is just

$$\frac{\partial \rho}{\partial x_{s_j}} = \frac{(x_{s_j} - x_{b_j})}{\rho}$$

and then the desired partial derivative of the range-rate can be written

$$\frac{\partial \dot{\rho}}{\partial p_k} = \sum_{j=1}^3 \left(\frac{(x_{s_j}(t + \Delta t) - x_{b_j}(t + \Delta t))}{\Delta t \rho(t + \Delta t)} \frac{\partial x_{s_j}(t + \Delta t)}{\partial p_k} - \frac{(x_{s_j}(t) - x_{b_j}(t))}{\Delta t \rho(t)} \frac{\partial x_{s_j}(t)}{\partial p_k} \right)$$

where the values of $\frac{\partial x_{s_j}}{\partial p_k}$ are determined, as usual, within the orbit prediction program (ORBRED). This completes the determination of the necessary partial derivatives for all the force model parameters of Section 2.2.

In addition to these, the correction program requires expressions for the partial derivatives of the additional parameters; namely the tropospheric and frequency bias scale factors, K_{trop} and β respectively. Since these do not contribute to the force model, they are calculated entirely within the correction program, unlike those which have just been determined.

The partial derivative of the range-rate with respect to the frequency bias β , is provided by differentiating Equation 6.6:

$$\frac{\partial C_i}{\partial \beta} = 1 - \frac{C_i}{c}$$

which is approximately equal to one, due to the relative magnitudes of C_i and c . The partial derivative with respect to the tropospheric correction may be obtained similarly from Equation 6.7 and is found to be

$$\frac{\partial C_i}{\partial K_{\text{trop}}} = \Delta_{\text{trop}}$$

Which completes the determination of *all* the partial derivatives.

The final amendment to be made to the correction routine arises from the large number of factors produced when solving for both tropospheric and frequency bias corrections on every pass. The number of these terms means that the time taken for the matrix inversion is significantly increased over solutions where such parameters are not sought. However, it was found that this increase in computation time could be diminished by noting that each of these correction terms contributes *solely* to the diagonal elements of the normal matrix. Whence, the inverse of the relevant portion of the matrix might be found by inverting the individual diagonal elements. The following method of decomposing the matrix into diagonal and non-diagonal blocks was thus adopted.

Consider the following partitioning of a symmetric positive definite matrix,

$$\begin{pmatrix} A & B & C \\ B^t & D_1 & E \\ C^t & E & D_2 \end{pmatrix} \begin{pmatrix} \underline{x} \\ \underline{y} \\ \underline{z} \end{pmatrix} = \begin{pmatrix} \underline{p} \\ \underline{q} \\ \underline{r} \end{pmatrix}$$

where D_1 , D_2 and E are all diagonal matrices and the superscript t here denotes the matrix transpose. Further, \underline{x} , \underline{y} and \underline{z} are subsets of the unknown solution parameters and \underline{p} , \underline{q} and \underline{r} are known. This gives rise to an equivalent system of simultaneous vector equations:

$$A\underline{x} + B\underline{y} + C\underline{z} = \underline{p} \quad (6.8)$$

$$B^t\underline{x} + D_1\underline{y} + E\underline{z} = \underline{q} \quad (6.9)$$

$$C^t\underline{x} + E\underline{y} + D_2\underline{z} = \underline{r} \quad (6.10)$$

whence, from Equation 6.10,

$$\underline{z} = D_2^{-1} (\underline{r} - C^t\underline{x} - E\underline{y}). \quad (6.11)$$

Substituting this expression for \underline{z} into Equation 6.9 we have

$$(B^t - ED_2^{-1}C^t)\underline{x} + (D_1 - ED_2^{-1}E)\underline{y} = \underline{q} - ED_2^{-1}\underline{r} \quad (6.12)$$

which provides the following equation for \underline{y}

$$\underline{y} = (D_1 - ED_2^{-1}E)^{-1} (\underline{q} - ED_2^{-1}\underline{r} - (B^t - ED_2^{-1}C^t)\underline{x}). \quad (6.13)$$

Combining Equations 6.11 and 6.8 in a manner analogous to that by which Equation 6.12 was determined, the following result holds

$$(A - BD_2^{-1}C^t)\underline{x} + (B - CD_2^{-1}E)\underline{y} = \underline{p} - CD_2^{-1}\underline{r} \quad (6.14)$$

and by combining these last two expressions, Equations 6.13 and 6.14, we obtain an equation of the form

$$M\underline{x} = \underline{s}$$

where

$$M = (A - CD_2^{-1}C^t) - (B - CD_2^{-1}E)(D_1 - ED_2^{-1}E)^{-1}(B^t - ED_2^{-1}C^t)$$

and

$$\underline{s} = \underline{p} - CD_2^{-1}\underline{r} - (B - CD_2^{-1}E)(D_1 - ED_2^{-1}E)^{-1}(\underline{q} - ED_2^{-1}\underline{r})$$

which allows \underline{x} to be determined by inverting M (which is only as large as the matrix A). Then, by substituting back into Equations 6.12 and 6.11 in turn, both \underline{y} and \underline{z} may also be found.

While this may *seem* a more involved technique than inverting the full matrix, the actual computations employed are in fact far simpler, since the inverse of a diagonal matrix is simply another diagonal matrix composed of the inverses of the original elements. Thus, not only are all the matrices which require inverting far smaller than the full matrix, but also only one of the six distinct sub-matrices needs inverting as a unit rather than through simple element inversion. This is due to the fact that most of the necessary inversions are of the diagonal matrices, their transposes, or products of these two types — all of which are still diagonal matrices.

6.5 Producing area tables for SPOT-2

Having completed the amendments to the SATAN-A package, detailed in the previous section, the next step in incorporating DORIS tracking data was to produce area tables for SPOT-2 from the GUESS software of Chapter 3. In order to compute these tables, the SPOT-2 satellite (illustrated in Figure 6.1 above) was first modelled geometrically as a trapezoidal box with a solar array composed of two intersecting planes, as depicted in Figure 6.6. As such, it is thus very similar to the ERS-1 model (Figure 4.3), lacking only the scatterometer antennae and the SAR. The other major difference is that the sloping face is oriented in the opposite way to that of ERS-1 and the slope is greater (i.e. deviates more from a

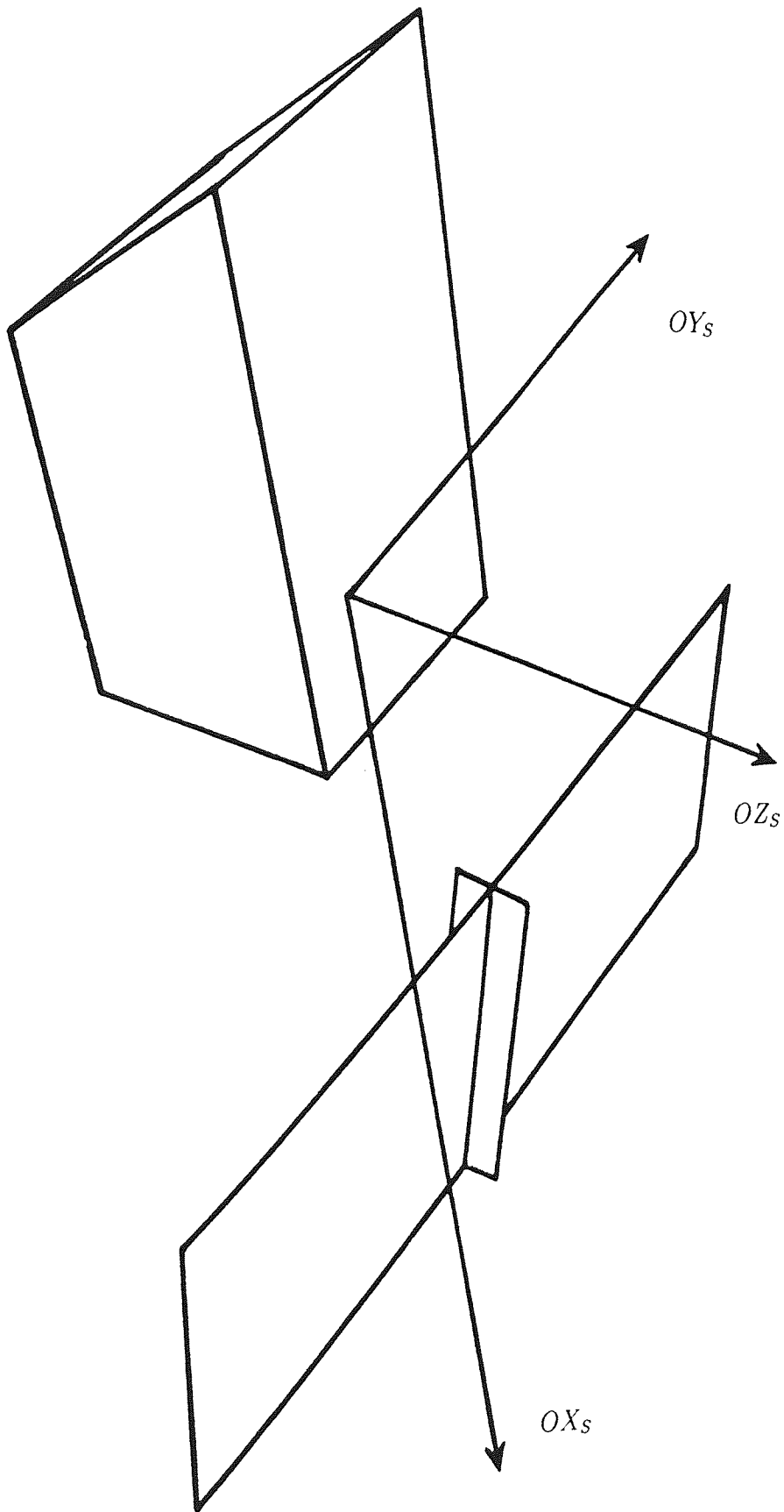


Figure 6.6: The geometric model of SPOT-2 in the satellite-fixed system.

cuboid). The whole of the geometry of SPOT-2 (both areas and normal vectors) was determined from this model.

The other variables which are required by the GUESS software (i.e. surface interaction coefficients, satellite mass and instrument locations) were estimated or computed in a manner analogous to their derivation for ERS-1 in Chapter 4. The aerodynamic coefficients employed were the same as those used for ERS-1, as suggested by the discussion at the end of Chapter 3, while the solar radiation coefficients were derived using data received from CNES.

The GUESS software was run on the input file and area tables were produced

β	-90°	-75°	-60°	-45°	-30°	-15°	0°	15°	30°	45°	60°	75°	90°
α													
0.0°	8.9	6.9	10.4	17.3	22.2	25.7	27.4	28.1	27.0	24.0	20.1	15.1	8.9
22.5°	8.8	7.3	11.5	18.5	23.8	27.4	29.2	29.9	28.5	25.3	21.1	15.6	8.8
45.0°	8.7	7.3	11.7	18.6	23.9	27.6	29.4	30.0	28.7	25.5	21.5	15.7	8.7
67.5°	8.4	7.0	11.2	17.6	22.6	26.1	27.9	28.6	27.6	25.5	21.2	15.0	8.4
90.0°	8.6	6.3	9.9	15.5	20.1	23.3	24.9	26.6	26.6	24.6	20.1	14.2	8.6
112.5°	8.5	6.8	10.4	16.3	21.1	25.2	27.9	29.5	29.1	26.3	21.0	14.2	8.5
135.0°	9.0	6.9	10.5	16.3	22.2	26.7	29.4	31.0	30.4	27.0	21.1	14.2	8.9
157.5°	9.2	6.6	9.9	16.0	22.0	26.5	29.2	30.8	30.3	26.6	20.7	14.2	9.2
180.0°	9.3	6.1	8.8	14.8	20.5	24.8	27.4	29.1	28.7	25.2	20.0	14.2	9.3
202.5°	9.2	6.6	9.9	16.0	22.0	26.5	29.2	30.8	30.3	26.6	20.7	14.2	9.2
225.0°	9.0	6.9	10.5	16.3	22.2	26.7	29.4	31.0	30.4	27.0	21.1	14.2	9.0
247.5°	8.5	6.8	10.4	16.3	21.1	25.2	27.9	29.5	29.1	26.3	21.0	14.2	8.5
270.0°	8.6	6.3	9.9	15.5	20.1	23.3	24.9	26.6	26.6	24.5	20.0	14.2	8.6
292.5°	8.4	7.0	11.2	17.6	22.6	26.1	27.9	28.6	27.6	25.5	21.2	15.0	8.4
315.0°	8.6	7.3	11.7	18.6	23.9	27.6	29.4	30.0	28.7	25.5	21.5	15.7	8.6
337.5°	8.8	7.3	11.5	18.5	23.8	27.4	29.2	29.9	28.5	25.3	21.1	15.6	8.8
360.0°	8.9	6.9	10.4	17.3	22.2	25.7	27.4	28.1	27.0	24.0	20.1	15.1	8.9

Table 6.1: Cross sectional area for SPOT-2 (in square metres) as viewed from the sun.

which were then used by the ORBPRED program to determine the relevant forces. Since the SATAN-A suite had already been adapted to accept these tables (Chap-

γ	$\delta = -5^\circ$			$\delta = 0^\circ$			$\delta = +5^\circ$		
	265°	270°	275°	265°	270°	275°	265°	270°	275°
α									
0.0°	9.45	8.23	9.03	8.90	7.91	8.91	9.04	8.23	9.45
22.5°	16.28	14.38	13.62	15.79	13.58	12.83	15.48	13.28	12.25
45.0°	21.86	20.33	19.90	21.37	19.53	19.12	21.04	19.21	18.48
67.5°	25.28	24.29	24.38	24.82	23.51	23.60	24.46	23.16	22.94
90.0°	26.06	25.68	26.36	25.59	24.90	25.59	25.23	24.54	24.92
112.5°	24.07	24.29	25.59	23.24	23.16	24.15	23.59	23.51	24.81
135.0°	19.60	20.33	22.16	19.11	19.53	21.37	18.79	19.21	20.73
157.5°	13.31	14.38	16.59	12.83	13.58	15.79	12.55	13.30	15.17
180.0°	8.72	8.22	9.75	8.90	7.91	8.91	9.75	8.23	8.73
202.5°	15.18	13.28	12.55	15.79	13.58	12.84	16.59	14.38	13.31
225.0°	20.73	19.20	18.79	21.38	19.53	19.11	22.17	20.33	19.60
247.5°	24.16	23.17	23.25	24.81	23.51	23.59	25.59	24.29	24.06
270.0°	24.92	24.54	25.23	25.59	24.90	25.59	26.37	25.68	26.06
292.5°	22.94	23.17	24.46	23.59	23.51	24.81	24.37	24.29	25.29
315.0°	18.48	19.20	21.04	19.11	19.53	21.37	19.90	20.33	21.86
337.5°	12.24	13.30	15.49	12.83	13.58	15.79	13.62	14.38	16.28
360.0°	9.45	8.23	9.03	8.90	7.91	8.91	9.04	8.23	9.45

Table 6.2: Cross sectional area for SPOT-2 (in square metres) as viewed along the incident aerodynamic flux vector.

ter 3), only minor alterations (involving the identification of SPOT-2 as an acceptable satellite) were required. As a quick visual confirmatory check that the geometry was credible and the GUESS software valid for a second satellite (having previously tested it on ERS-1 alone), tables analogous to Tables 4.1 and 4.2 were produced. These tables, 6.1 and 6.2 respectively, display the total effective cross-sectional area perpendicular to the incident flux vector over the range of angles attained in the case of SPOT-2.

Considering first the table for solar radiation (displayed over a $22.5^\circ \times 15^\circ$ grid in Table 6.1), the observed and expected variations again correspond (as was the case for ERS-1) — thus providing more confirmation that the GUESS software

works satisfactorily. For instance, the total area is smallest for those values of β (namely $\beta = -70^\circ$) which are farthest from the value of 20° which is the angle between the solar panels and the axis of rotation of the solar array. In contrast, where β approximates this angle, the cross-sectional area reaches its maximum, since at this value the solar panel is contributing its largest amount; namely its full plane area.

In addition, there is a variation in area with the angle α . However, this is less marked for SPOT-2 than for ERS-1 since there is no SAR. Thus, only that component of the total area which is contributed by the main body of SPOT-2 varies in α for any given value of β . Given the shape of the SPOT-2 geometric model (as illustrated in Figure 6.6), this variation means that the maximum values of the cross-sectional area will be attained when $\alpha = 0^\circ$ or 180° — since the trapezium edges offer the minimum area when rotating about the body in α for a fixed β . Corresponding minima thus occur at α values of 90° and 270° . Finally, we note that this table shows similar variations to those displayed by Table 4.1 for ERS-1 when $\beta = \pm 90^\circ$. As for ERS-1, these points correspond to a sun position lying *on* the solar axis of rotation, and the cause of this variation has been considered already in Chapter 4.

Again, similarly to ERS-1, it was found that the $-OY_S$ -axis of SPOT-2 did not deviate from the incident atmospheric flux vector by more than $\pm 5^\circ$. Thus, for the aerodynamic resistance force, the visible areas are illustrated in Table 6.2 over a $5^\circ \times 5^\circ \times 22.5^\circ$ grid in the three angles α , γ and δ of Figure 3.5. As in the case of direct solar radiation pressure, this illustrative table displays the variations that would be expected for SPOT-2.

The constant contribution to the total area, just over 7 square metres, arises from the body of the model. The variability is almost all due to the rotation of the solar array, hence (as for ERS-1) registers as variation with the angle α . Thus, as expected, the maximum area is obtained when the solar panel lies perpendicular to the incident flux vector (for instance, $\alpha = 90^\circ$ or 270° for $\delta = \gamma = 0$) and corresponding minima occur when these two are most nearly parallel ($\alpha = 0^\circ$ or 180° for the same δ and γ). It is again emphasized that these tables are for illustrative purposes only and that they were *not* used in this form within the orbit determination program.

6.6 Precise orbit determinations for SPOT-2

In order to confirm that the SATAN-A adaptation works, several long-arc SPOT-2 orbits were converged over periods within May 1990 and January and February 1992. Table 6.3 summarizes the time span of each arc as well as the numbers of

Arc Dates (MJD)	Number of C_D 's sought	Data included		
		stations	passes	observations
48016.0 – 48021.0	21	27	435	16729
48021.0 – 48026.0	21	27	425	16465
48628.0 – 48633.0	20	37	525	17219
48633.0 – 48638.0	21	37	573	18513
48638.0 – 48643.0	21	37	593	19219
48645.0 – 48650.0	20	36	526	17390
48667.0 – 48672.0	20	40	573	18843
48672.0 – 48677.0	20	40	593	19523

Table 6.3: Solution details for converged SPOT-2 long-arcs, May 1990 and January and February 1992.

DORIS tracking beacons, passes and range-rate measurements included in the solution. Each arc was converged relative to the GEM-T3A gravity field, associated ocean tide model and MSIS83 thermospheric model in the J2000 inertial reference system. Values of solar activity F10.7 and geomagnetic indices K_p have been plotted for the relevant months in Figures 6.7 and 6.8 respectively; highlighting the long-arc periods. In addition, each arc was converged both with and without the area tables (described above) in order to further confirm that the GUESS software works. In each case, the drag scale factors were solved for using the linear variation (*saw-tooth*) approach described in Section 2.5. In most instances twenty or twenty-one nodal values were solved for, the first two being separated by either six or twelve hours and the rest lying just six hours apart.

It is possible to solve realistically for so many drag scale factors for SPOT-2 due to the density of the DORIS tracking data combined with the almost global coverage that this system offers. DORIS Doppler data does not suffer from either the sporadic nature of laser range data, nor the geographical bias that arises

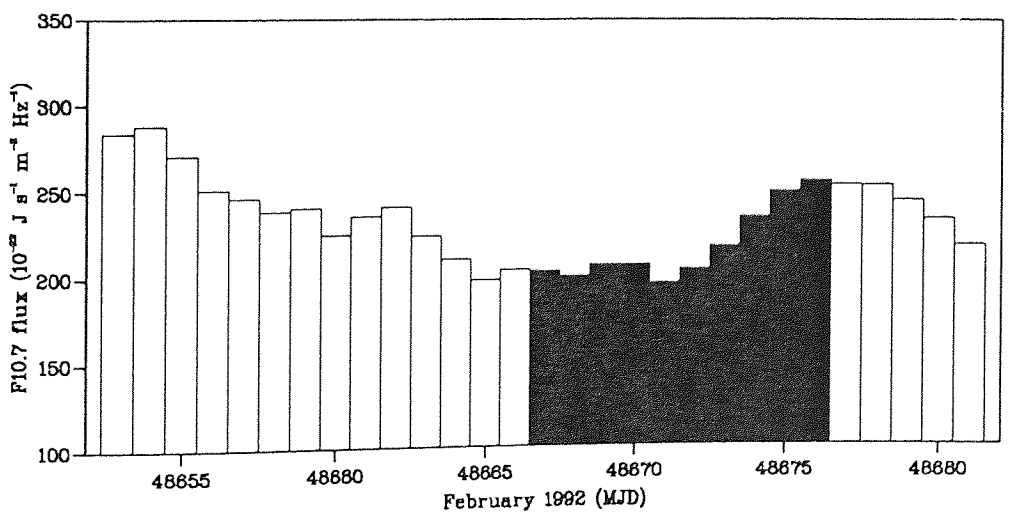
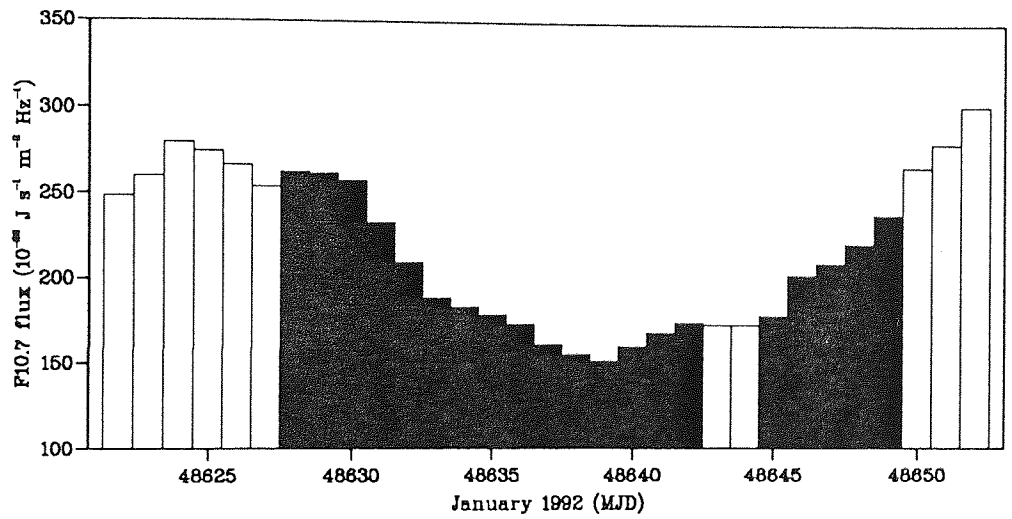
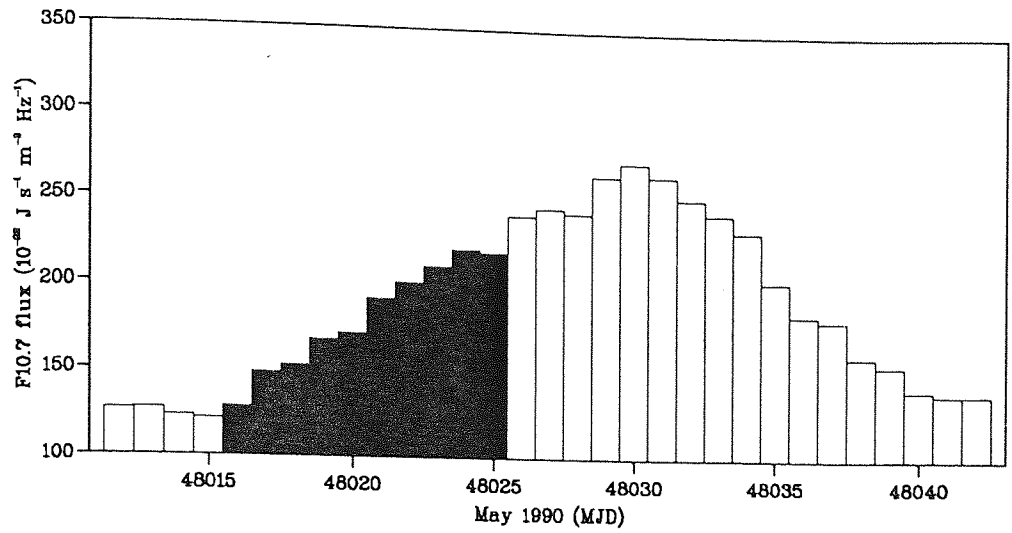


Figure 6.7: Solar Flux F10.7 for May 1990 and January and February 1992, emphasizing the converged long-arc periods.

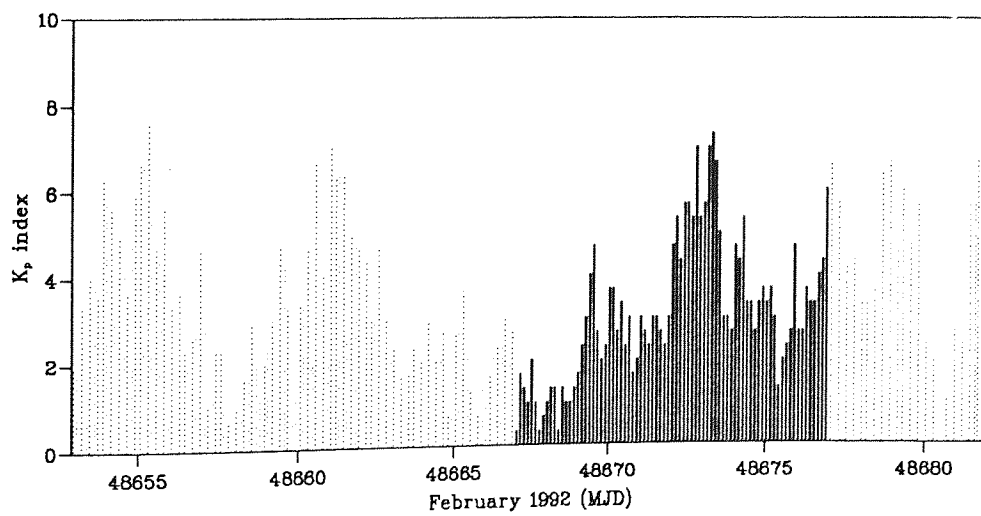
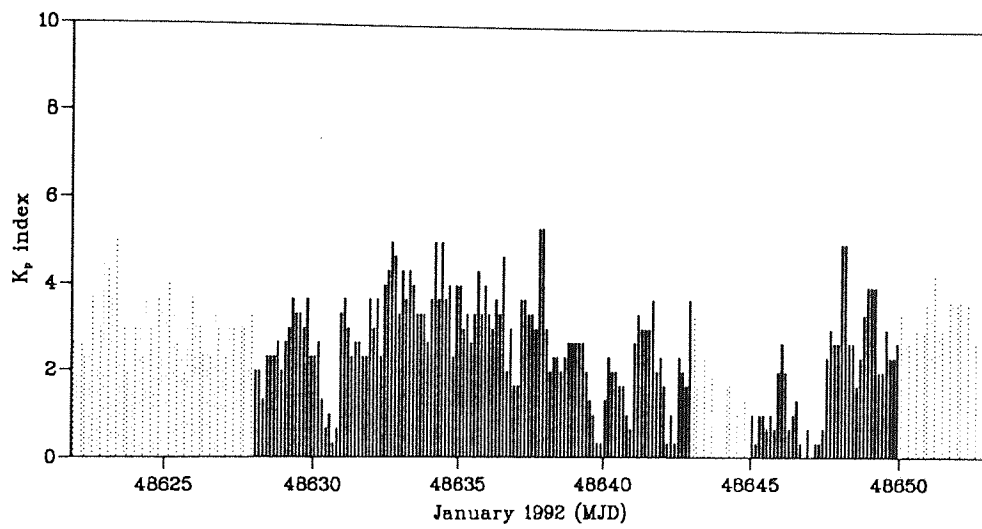
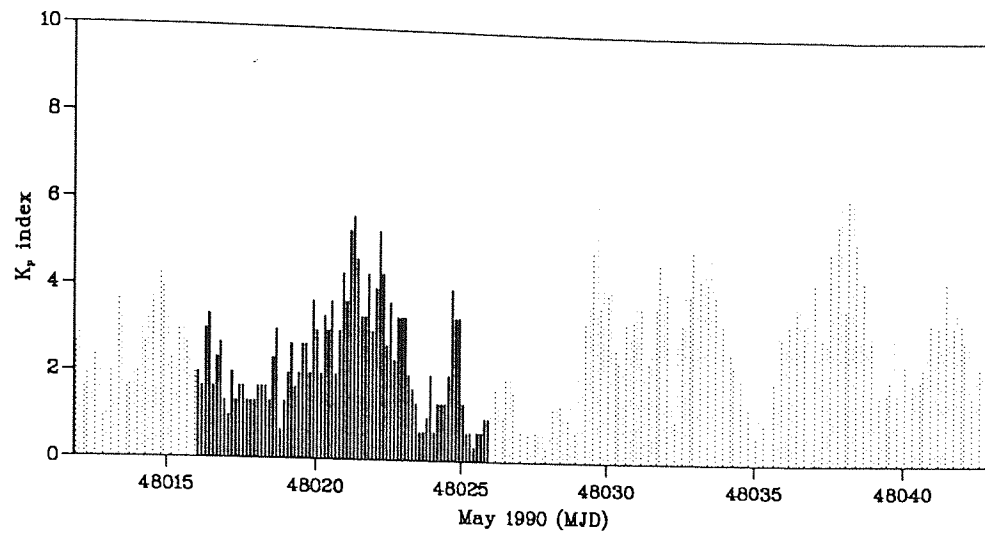


Figure 6.8: Geomagnetic indices for May 1990 and January and February 1992, emphasizing the converged long-arc periods.

from the fewer laser stations. There was therefore no point in dividing the ODBs into separate geographical groups (as had been done for ERS-1 in Chapter 4). Every long-arc orbit was converged by solving for the standard initial state vector (position and velocity), multiple drag scale factors (as indicated in Table 6.3), station frequency offsets per pass, and a single solar reflectivity coefficient. The tropospheric pass corrections, K_{trop} , were not sought, since it had been found that the gain in fitting the model to the data did not reflect the increased expenditure of time taken for their solution. Further, there is no real indication that this correction satisfactorily explains the error in the tropospheric adjustment in the data records. So the model may better fit the data, but does not necessarily offer a more satisfactory explanation of the satellite's behaviour.

The RMS values presented in the column headed "with GUESS tables" of Table 6.4 may be further diminished through more rigorous rejection criteria (i.e. by

Arc Dates (MJD)	Root Mean Square of fit (mm/second)	
	with GUESS tables	without GUESS tables
48016.0 – 48021.0	1.74	1.64
48021.0 – 48026.0	1.68	2.19
48628.0 – 48633.0	1.82	3.51
48633.0 – 48638.0	1.71	2.62
48638.0 – 48643.0	1.16	1.20
48645.0 – 48650.0	1.76	2.33
48667.0 – 48672.0	1.14	1.68
48672.0 – 48677.0	2.02	3.75

Table 6.4: The Root Mean Square of fit for the SPOT-2 long-arcs both with and without GUESS generated tables in millimetres per second.

rejecting a larger number of observations). Such an approach allows RMS values of about 1.1 millimetres per second to be attained — comparable with results presented at the DORIS Day conference in Toulouse in October 1991 [Nouël, 1991]. In addition, when the tropospheric correction *was* solved for (once every pass), the RMS was further reduced to around the 0.7 millimetres per second range — again comparable with the results of other groups [Nouël, 1991]. This comparability of results verifies the modifications to the SATAN-A suite. Further, Table 6.4 indi-

cates that in all but the first long-arc (in May 1990) the use of Guess generated tables reduces the RMS of fit of the data to the model. Considering also the C_D coefficients for each long-arc, Figure 6.9 illustrates clearly that the same pattern of drag scale factors pertains for both solution procedures. Though the absolute values of the scale factors obtained with GUESS tables are less than those without the tables, the relative variations (with respect to the mean C_D value) are very similar. The only deviations from this pattern occur at the ends of the long-arc periods where the solution is not as well constrained. The existence of this pattern reflects the fact that the underlying modelled density varies in the same manner for both solution procedures. Further, the area is probably being modelled more accurately with the GUESS tables, but the two-cycle-per-revolution variation in the modelled area does not show in the C_D values, obtained linearly over several revolutions.

As a further consideration, the use of GUESS tables for SPOT-2 orbits leads to lower values of the solar radiation coefficient C_R . Indeed, as is illustrated in

Arc Dates (MJD)	Value of coefficient C_R	
	with GUESS tables	without GUESS tables
48016.0 – 48021.0	1.063	1.998
48021.0 – 48026.0	1.050	2.001
48628.0 – 48633.0	1.224	2.269
48633.0 – 48638.0	1.063	1.998
48638.0 – 48643.0	1.096	2.072
48645.0 – 48650.0	1.197	2.235
48667.0 – 48672.0	1.141	2.133
48672.0 – 48677.0	1.237	2.320

Table 6.5: The value of the solar radiation coefficient, C_R , solved for both with and without GUESS generated tables.

Table 6.5, the resultant values are all approximately equal to unity, indicating that the modelled solar radiation pressure force required little or no scaling in the orbital determination process. Also, the C_R coefficient often absorbs along-track error arising from aerodynamic force mismodelling (as well as along-track error from other sources) Thus, the fact that $C_R \approx 1$ may imply that the modelled along-

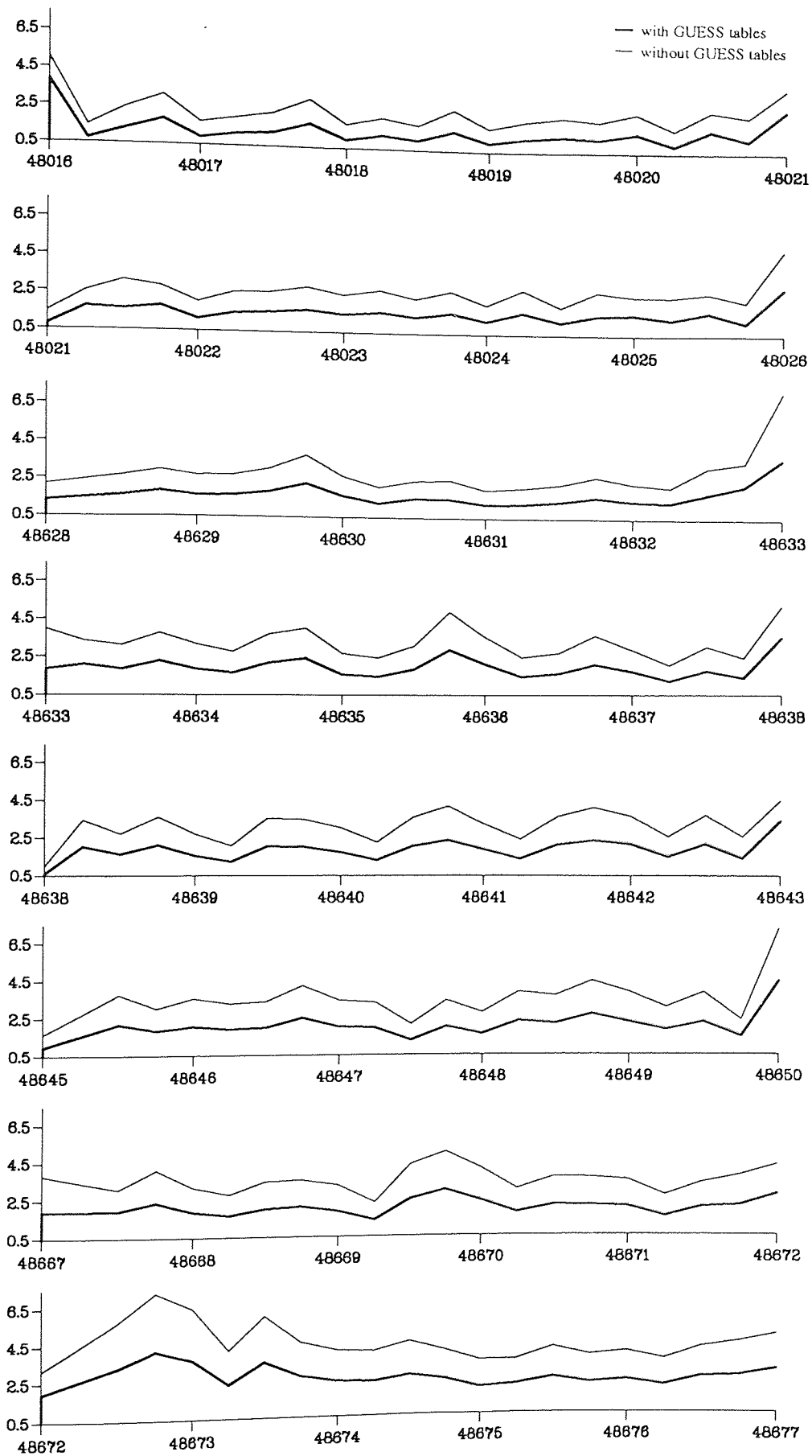


Figure 6.9: Drag-scale factors, C_D , for the eight SPOT-2 long-arcs considered.

track force *has* seen some improvement — due to the inclusion of GUESS tables and the momentum exchange approach of Chapter 3 — in the components arising from the aerodynamic resistance force and the direct solar radiation pressure force.

However, these results do show that the orbital determination process has been successfully converted for use with SPOT-2 DORIS Doppler tracking data. Thus, the third suggested technique for refining ERS-1 long-arc orbits may now be tested; as is the aim of the next chapter.

Chapter 7

Improving ERS-1 orbits with SPOT-2 tracking data

7.1 Correcting for density mismodelling

Having modified the orbital determination programs of Chapter 2 so that SPOT-2 orbits could be determined and having produced area tables for this satellite using the GUESS software described in Chapter 3, another attempt to improve ERS-1 orbits can be made. As was discussed in Section 3.1, precise orbit determination for ERS-1 suffers from the limited available knowledge and models of atmosphere. Further, at least during the early stages of its life, during 1991 and 1992, there is a sparsity of laser tracking data, which exacerbates this problem.

Many of the techniques currently practised in an attempt to overcome both these factors involve solving for additional parameters. For example, multiple drag scale factors may be sought at diminishing intervals, often every six hours or less [Ries *et al.*, 1991]. Another example is the increasingly common approach of solving for an explicit one-cycle-per-revolution term, often as factors of the sine and cosine of this variation,

$$\Delta\rho = [C_D + \bar{S} \sin(\omega + M) + \bar{C} \cos(\omega + M)] \quad (7.1)$$

[Shum *et al.*, 1990]. Here, \bar{S} and \bar{C} are the scale factors, ω is the argument of perigee of the satellite orbit and M is the mean anomaly of the same. Equation 7.1

gives a correction to the modelled atmospheric density in the form of a scale factor,

$$\rho = \rho_{\text{modelled}} \Delta\rho$$

but the correction may also be applied directly to the force model by solving for slightly modified values of the coefficients, \bar{S} and \bar{C} , for instance,

$$\underline{F} = -\frac{1}{2}C_D A \rho v \underline{v} + \bar{S} \sin(\omega + M) + \bar{C} \cos(\omega + M) \quad (7.2)$$

[Ehlers and Moore, 1993]. However, for ERS-1, the unfavourable spread of tracking data, often combined with an overall sparsity of the same, may mean that solution of such additional parameters is unrealistic. It is a fact that satellite laser range (SLR) data is concentrated in the northern hemisphere; mainly the U.S.A. and western Europe. This geographical bias allows the determination procedure to minimise errors around the SLR tracking stations at the expense of errors elsewhere along the arc; the existence and magnitude of which cannot be properly assessed using SLR tracking data alone. Further, where the SLR data *are* sparse, this problem is exacerbated by solving for additional parameters as described above. Thus, for ERS-1, it is often the case that with SLR data alone, credible drag scale factors may only be solved for on a daily, or at most half-daily, basis.

In order to ameliorate this problem for ERS-1, a recent feasibility study was conducted by CNES [Deleuze and Nouël, 1992]. This established that drag scale factors derived from the satellite SPOT-2 could be utilised to improve ERS-1 long-arc orbits. As is evident from the descriptions of ERS-1 and SPOT-2 given in Chapters 4 and 6 respectively, their orbits have many similarities. In particular, their inclination angles (98.5° for ERS-1 and 98.6° for SPOT-2) and orbital eccentricities (0.001 or less) are extremely close and the major difference lies in the 50km that separates their altitudes. For a first approximation, these orbital similarities mean that both satellites experience similar variations in the atmospheric density over a given long-arc period. Further, the quantity and spacing of the DORIS Doppler tracking data for SPOT-2 is such that drag scale factors may be realistically estimated at intervals of six hours or less.

In this chapter, a method is presented which attempts to recover information about the effect of atmospheric resistance on SPOT-2 and then to use this to

improve ERS-1 precise orbits. However, unlike the study made by CNES, this improvement is realised through employing along-track acceleration corrections; the dominant portion of the aerodynamic resistance force lying in this direction. The corrections are first verified on SPOT-2, before appropriate modifications (which allow for density variations due to the differences in position of the two satellites) are made and the corrections applied to ERS-1 orbits.

Because of the way GUESS generated tables have been seen to improve the orbits of both ERS-1 and SPOT-2, they will be used throughout this chapter as part of the usual orbital determination procedure. Thus, it will be assumed that the along-track acceleration correction represents density mismodelling rather than miscalculation of the surface area, or gas-surface interaction. The next two sections deal with the method by which the along-track acceleration corrections are derived, together with the results obtained when the derived corrections were applied to SPOT-2. The fourth section then utilises these results to improve on current ERS-1 orbits.

7.2 Along-track acceleration corrections

Various authors have attempted to improve on aerodynamic force modelling by the extraction of information from long-arc analyses. Moore and Rothwell [1990] and Ridgway *et al.* [1990] examined laser range and Doppler range-rate residuals from Seasat tracking data as a possible method of recovering relative atmospheric density corrections to an underlying thermospheric model. Alternatively, Rothwell and Moore [1991] and Nuth *et al.* [1991] attempted to modify selected parameters within such a model, but with only limited success due to the relative insensitivity of near circular orbits to thermospheric variability and the coarseness of the model's atmospheric input parameters (i.e. solar activity F10.7 and geomagnetic indices K_p). Given the near continuous temporal tracking of SPOT-2 from the DORIS network, the methodology of Ridgway *et al.* [1990] has been modified, as detailed below.

If \ddot{T} denotes the along-track acceleration due to the atmospheric resistance, i.e. the acceleration due to drag, then the change in the semi-major axis, a , arising

from this acceleration may be expressed [King-Hele, 1987] as

$$\frac{da}{dt} = \left(\frac{2a^2 v}{\mu} \right) \ddot{T}$$

where μ is the product of the gravitational constant and the earth's mass. Thus, using Kepler's third equation: $n^2 a^3 = \mu$ where n is the mean motion of the satellite,

$$\frac{dn}{dt} = - \left(\frac{3n}{2a} \right) \frac{da}{dt}$$

and hence

$$\frac{dn}{dt} = - \left(\frac{3nav}{\mu} \right) \ddot{T}$$

where v is the velocity. By restricting the theory to a circular orbit, a not unreasonable approximation for ERS-1 and SPOT-2 given their low eccentricities, the orbital radius becomes equal to the semi-major axis i.e. $a = r$. Thus, $v = an$ and $\mu = v^2 a$, so the derivative $\frac{dn}{dt}$ may be written

$$\begin{aligned} \frac{dn}{dt} &= - \left(\frac{3n}{v} \right) \ddot{T} \\ &= - \left(\frac{3}{a} \right) \ddot{T} \end{aligned} \quad (7.3)$$

It follows that, by taking small changes in both sides of Equation 7.3 (and denoting these changes by the Δ function) we may express the along-track acceleration correction, $\Delta \ddot{T}$, in terms of an along-track position correction, ΔT , as follows:

$$\begin{aligned} \Delta \ddot{T} &= - \frac{1}{3} a \frac{d}{dt} \Delta n \\ &= - \frac{1}{3} \frac{d}{dt} a \Delta n \\ &= - \frac{1}{3} \frac{d}{dt} \Delta v \\ &= - \frac{1}{3} \frac{d^2}{dt^2} \Delta T. \end{aligned} \quad (7.4)$$

Continuing to follow Ridgway *et al.*, the along-track position correction ΔT may be determined empirically from tracking data residuals. In the context of SPOT-2, these are just range-rate residuals, $\Delta \dot{\rho}(t_0)$, and may be expressed as the difference between the observed ($_{obs}$) and calculated ($_{cal}$) range-rates. Thus,

$$\Delta \dot{\rho}(t_0) = \dot{\rho}_{obs}(t_0) - \dot{\rho}_{cal}(t_0^*)$$

where t_0 is the epoch of the observed range-rate $\dot{\rho}_{obs}$ and the along-track correction is identified as a timing error δt in the epoch t_0^* for the derived range-rate, i.e. $t_0 = t_0^* + \delta t$. Hence,

$$\Delta\dot{\rho}(t_0) \approx \dot{\rho}_{obs}(t_0) - \dot{\rho}_{cal}(t_0) + \ddot{\rho}(t_0)\delta t \quad (7.5)$$

and the residual may be approximated by an offset and timing error, i.e. a bias and tilt. The required timing error is in fact the gradient of best fitting straight line through the points gained by plotting $\Delta\dot{\rho}$ against $\ddot{\rho}$ for each pass. One example of such a plot, taken from a single pass in the middle of a five day SPOT-2 long-arc MJD 48628 to MJD 48633 (January 7th to the 11th inclusive, 1992), is illustrated

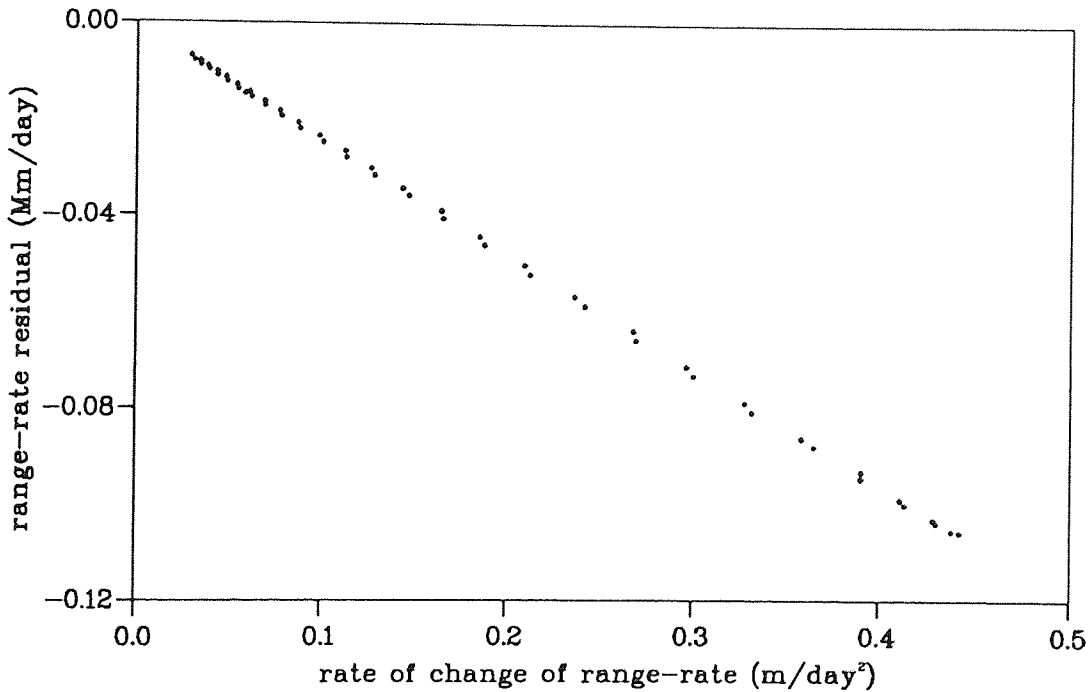


Figure 7.1: Example slope for a single pass of range-rate residuals.

in Figure 7.1.

In order to compute δt the value of the rate of change of range-rate, $\ddot{\rho}$ must first be determined. To this end, the file of range-rate residuals, produced by the orbit determination procedure, was constructed so that the i^{th} record contained an epoch, t_i , a residual, $\Delta\dot{\rho}(t_i)$, a range-rate value, $\dot{\rho}(t_i)$ and the satellite's relative velocity in the along-track direction, v_i . For each pass the mean values of time, \bar{t} , and satellite velocity, \bar{v} , were determined by taking the sample mean of the values of t_i and v_i respectively over all the records in that pass. In addition, the value of $\ddot{\rho}(t_0)$ was computed by means of a linear approximation between adjacent values

of the range rate,

$$\begin{aligned}\ddot{\rho} &= \frac{d}{dt}\dot{\rho} \\ &\approx \frac{\dot{\rho}(t_{i+1}) - \dot{\rho}(t_i)}{t_{i+1} - t_i}.\end{aligned}$$

Similarly, the corresponding residual at this same *average* epoch was determined by averaging over the same two records,

$$\dot{\rho} = \frac{\dot{\rho}(t_{i+1}) + \dot{\rho}(t_i)}{2}.$$

For each pass thus treated, the slope, δt , was then obtained by solving Equation 7.5 using a matrix inversion method. The value of δt , combined with the average velocity of the same pass, \bar{v} , may then be used to produce the desired along-track correction

$$\Delta T = \bar{v}\delta t$$

which is associated with the epoch \bar{t} . Thus, a set of points of the form $(\bar{t}, \Delta T)$ is obtained over the whole of the long-arc; one for each pass within that arc. By fitting some curve through these points a second derivative may be determined which can then be used to evaluate the required along-track acceleration correction, $\Delta\ddot{T}$ from Equation 7.4.

7.3 Application of the above method to some SPOT-2 long-arcs

The preceding methodology was tested on three five-day SPOT-2 long-arcs in January and February 1992. The time span of each arc was chosen to avoid both SPOT-2 and ERS-1 manoeuvres so that the corrections derived for these three periods could later be modified for ERS-1 orbits. The number of DORIS tracking beacons, data passes and range-rate measurements included in the converged solutions are summarized in Table 7.1. For the sake of consistency, points which were rejected in the initial convergence of each SPOT-2 long-arc were removed from the observation file to ensure that they were *not* included in any of the subsequent variations.

Arc Dates (MJD)	Data included		
	stations	passes	observations
48628.0 – 48633.0	37	526	16994
48645.0 – 48650.0	36	526	17390
48667.0 – 48672.0	40	573	18843

Table 7.1: Summary of contributing stations, passes and range-rate measurements from SPOT-2.

As for the ERS-1 arcs of Chapter 4, the orbits were all converged relative to the GEM-T3A gravity field, associated ocean tide model and MSIS83 thermospheric model in the J2000 inertial reference system. Values of solar activity F10.7 and geomagnetic indices K_p for the relevant periods, may be seen in Figures 6.7 and 6.8 respectively of Chapter 6. The three long-arcs periods considered in this chapter lie within the highlighted regions of these figures, since they are three of the eight arcs converged in that chapter. Surface force modelling tables for SPOT-2 were derived using the GUESS software (again effected in the previous chapter). The drag scale factors were solved for using the linear variation, or saw-tooth, approach (Section 2.5) as was also used the ERS-1 long-arcs of Chapter 4. In each case, twenty nodal values were solved for, the first two separated by a twelve hour interval and the rest lying just six hours apart. All long-arc orbits were converged by solving for the standard initial state vector (for range-rate data): position and velocity, multiple drag scale factors, station frequency offsets per pass, and a single solar reflectivity coefficient.

To determine appropriate along-track acceleration corrections, the drag scale parameters for each arc were replaced by their statistical mean value, \bar{C}_D ; the orbits being re-computed holding all parameters fixed to obtain a set of range-rate residuals. These residuals reflect the actual difference between the modelled density scaled by the factor \bar{C}_D and that experienced by the satellite. Each pass of data was then analysed as described above to determine the set of points $(\bar{t}, \Delta T)$ for the whole of the long-arc. These are illustrated in Figure 7.2 for each of the three five-day SPOT-2 long-arcs converged.

Having obtained \bar{t} and ΔT for each pass over the whole arc, these data were smoothed in a two stage process to reduce noise prior to fitting a curve through

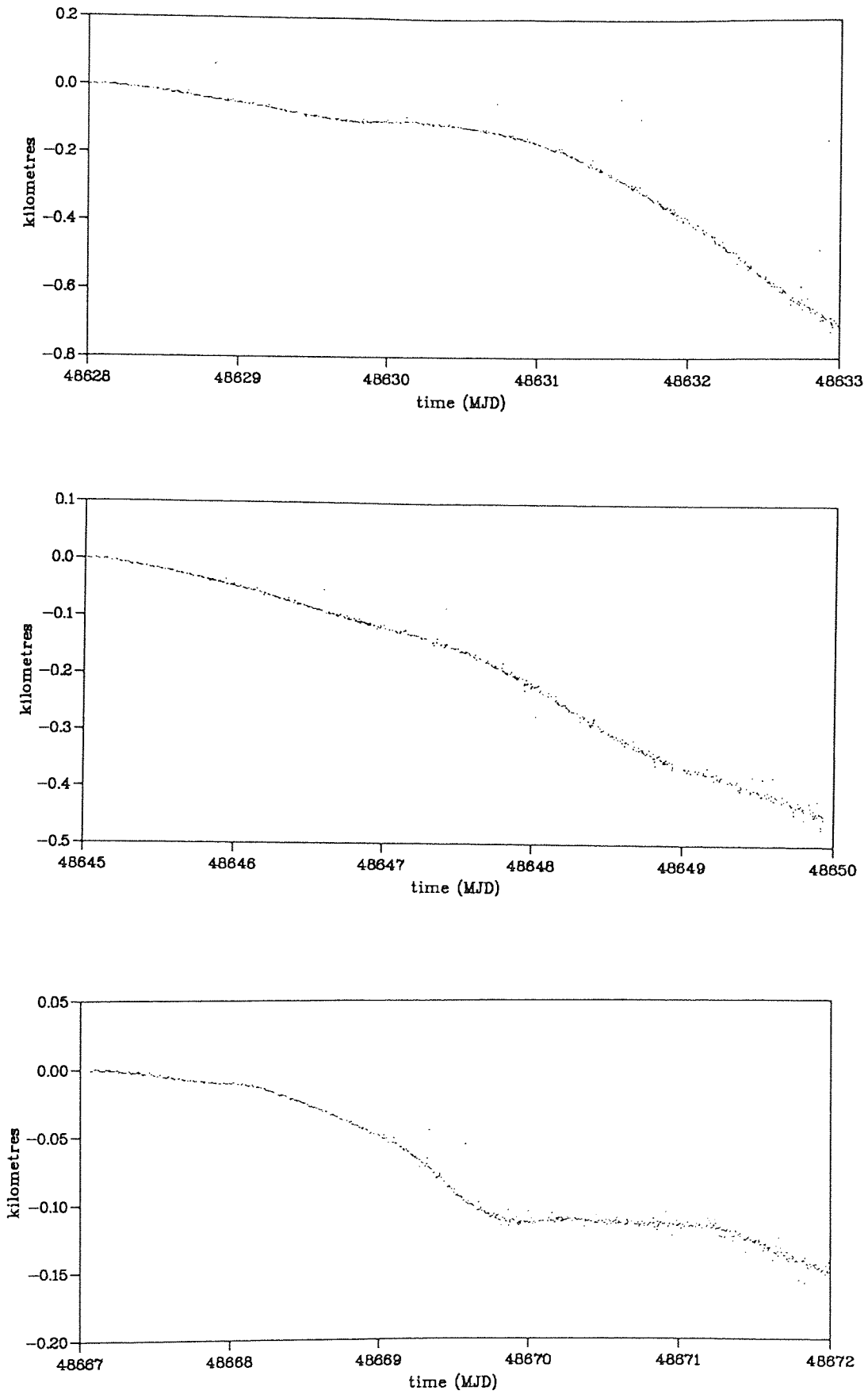


Figure 7.2: All $(\bar{t}, \Delta T)$ pairs, over three converged five-day SPOT-2 long-arcs.

the resulting data. Initial attempts to fit a curve to the unsmoothed data had met with little success due to the distorting effects of outlying data points, hence the need to reduce the dataset in this way. In the first stage outliers were removed by fitting a polynomial of the form

$$\Delta T = p(t) = \alpha_0 + \alpha_1 t + \dots + \alpha_n t^n$$

to all remaining points and excluding values beyond a specified rejection level. The process of fitting a polynomial and rejecting outliers was repeated, for a fixed rejection level and polynomial order, until no further points were excluded.

When fitting a polynomial to a set of points, it is found empirically that the RMS of the fitted curve to the data decreases in a continuous manner with a number of sharp step-like drops separated by regions of slower change, as the order of the fitted polynomial increases. Eventually, one of two situations pertains: either a sudden increase in the RMS occurs for an increase in order, implying that the polynomial is no longer well defined, or the decreases in RMS are of a magnitude smaller than is of interest (or of benefit) when compared with the increase in computing time taken to solve for the coefficients of the fitted polynomial. The order of the rejection polynomial, used to remove the outliers in the manner described in the previous paragraph, was either the greatest value before the RMS began to increase, or some lesser value lying just after one of the sharp decreases in RMS.

The rejection level, used to determine which points were outliers, was determined by considering the data (illustrated in Figure 7.2) and picking a value which removed those points clearly lying outside the main stream. In practice, too low a rejection level tended to reject so many points, especially at the end of a long-arc, that the polynomial determined by each subsequent iteration was substantially different from the previous solution. This again led to another large number of rejected points, so the subsequent solution again differed extensively. In the worst cases, a situation arose where no points were left in the last twenty percent of the arc, effectively preventing the remainder of the method from being implemented. The choice of rejection level was made so that this event did not occur, while the worst of the outliers were still removed.

Simply removing the outliers in this manner, did not prove sufficient to satisfactorily reduce noise in the data; some further smoothing being necessary. The

method chosen consisted of averaging all remaining accepted points over each orbital revolution to produce a single point $(\bar{t}, \Delta T)$ for each orbital period throughout the long-arc. This reduction eliminated the concern about extracting a smooth second derivative from a function described by noisy discrete values exhibiting a strong once per revolution signature. The smoothed data are plotted in Figure 7.3 for the same three five-day SPOT-2 long-arcs as previously.

The next step in the process, consisted of fitting a curve through these averaged points. The main consideration was that the second derivative (required by Equation 7.4) be continuous and, preferably, smooth. Thus, each trial curve was composed of a number of polynomials or splines (of cubic order or higher). Where multiple polynomials were tested, they were spliced at the connection points by setting the first *three* derivatives equal, thus ensuring the required smooth second derivative. In addition, the value of the fitted curve and its first derivative were both set to zero at the start of the long-arc; since at this point it is assumed that the along-track position is correct, any errors having been absorbed into the initial state vector. Figure 7.4 shows a detail of Figure 7.3, along with two curves, one an 11th order polynomial, the other a section of the spliced polynomial solution to the first test arc (from MJD 48628 to MJD 48633). This figure illustrates the improvement in fit that may be obtained by splicing polynomials, as against using a single polynomial.

Having fitted a curve to the along-track position correction points, the second derivative, $\frac{d^2}{dt^2} \Delta T$, was found and hence the along-track acceleration correction function derived using Equation 7.4. This function was then compared with the along-track acceleration corrections derived by differencing the *actual* along-track accelerations due to drag from the two SPOT-2 orbits; namely the converged orbit and that employing the fixed drag scale factor, \bar{C}_D . These differences were termed the *expected* along-track acceleration corrections, denoted $\Delta \ddot{T}_{\text{expected}}$, and are illustrated in Figure 7.5 (again for all three test arcs).

Given the method used to derive the along-track acceleration function, it was unrealistic to expect that the once-per-revolution variations in $\Delta \ddot{T}_{\text{expected}}$, would be matched. Indeed, a comparison of the expected acceleration corrections achieved both with and without GUESS tables, shows that this once-per-revolution variation, (exhibited by both curves, see Figure 7.6) is exacerbated by the twice-per-

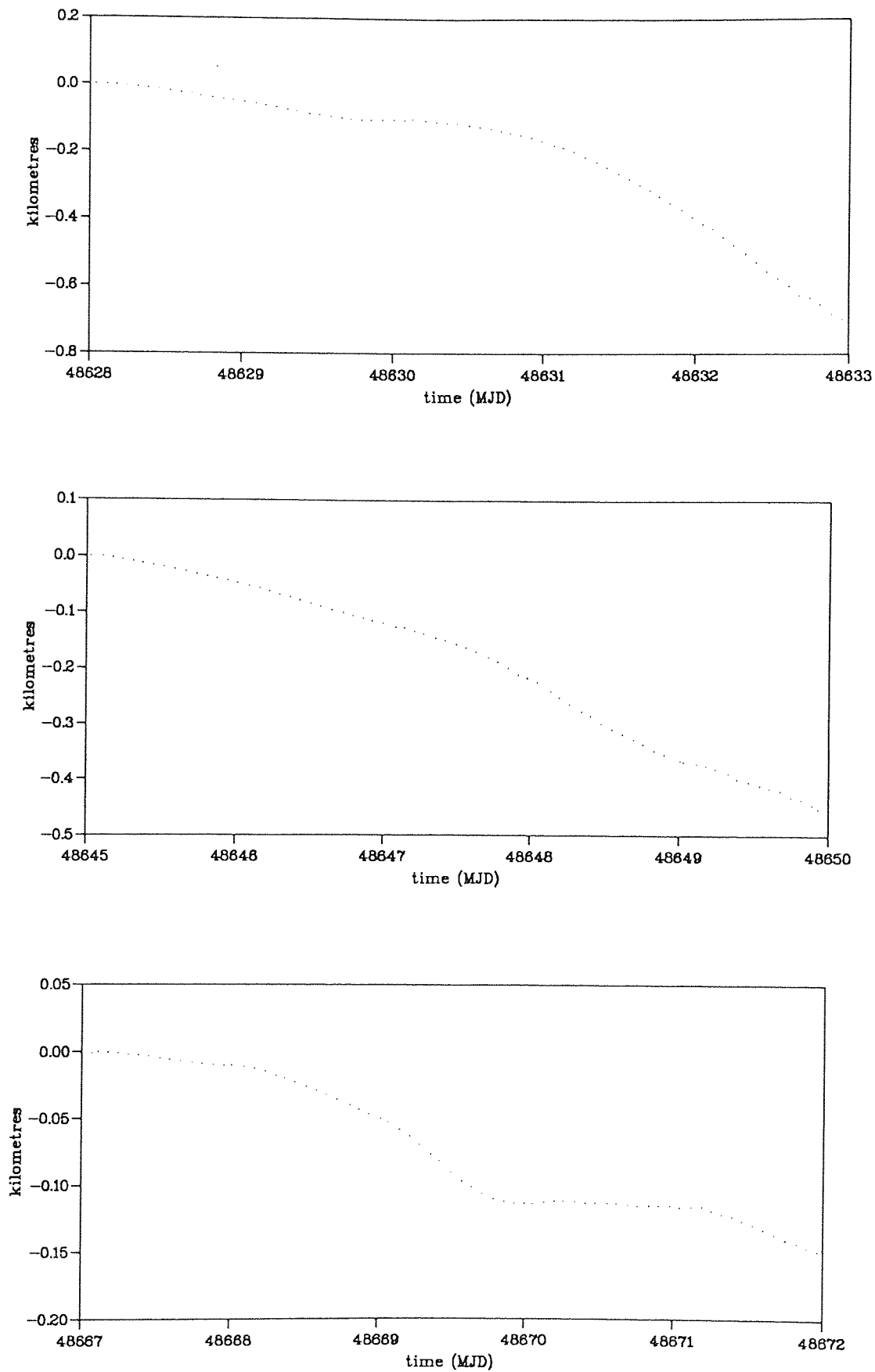


Figure 7.3: Smoothed $(\bar{t}, \Delta T)$ pairs, over the same three arcs.

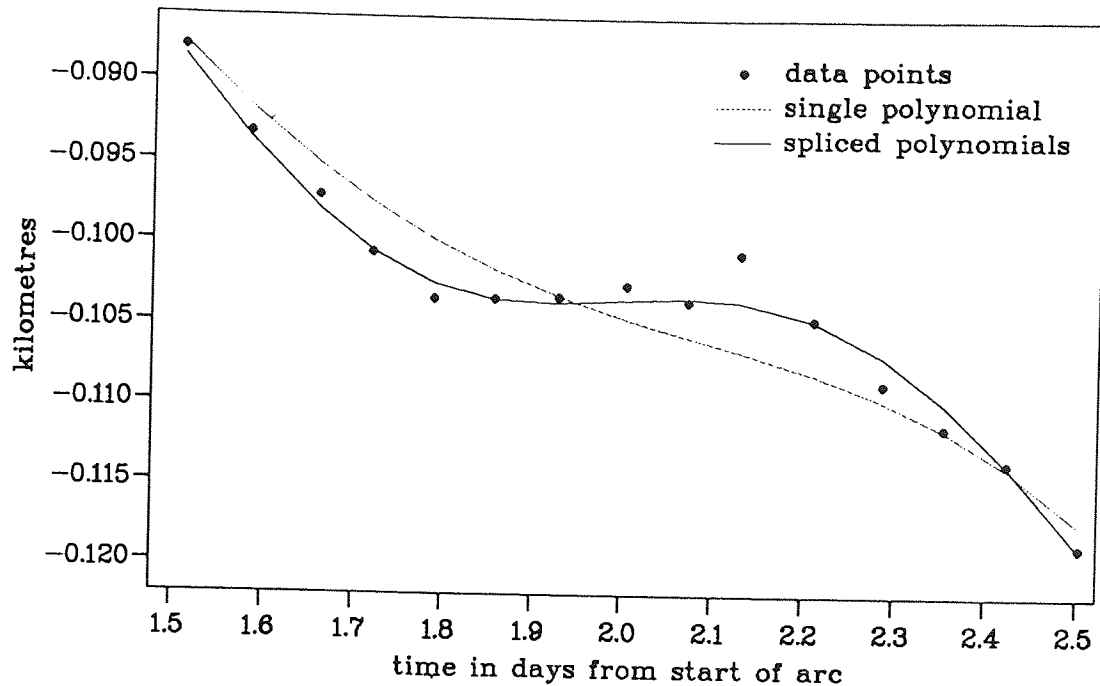


Figure 7.4: Detail of smoothed data showing single versus spliced polynomial fits from the SPOT-2 arc of MJD 48628 to MJD 48633.

revolution variation in the satellite area. Thus, in order for a solution curve to be judged satisfactory (prior to testing it on a SPOT-2 orbit), it had not only to fit the along-track position correction data but also needed to possess a complementary along-track acceleration correction curve that matched the *general trends* exhibited by the expected corrections. Once such a fit was obtained, a set of along-track acceleration values, $\Delta\ddot{T}_{\text{solution}}$, was computed from the fitted curve, at the times required by the orbital prediction routine. These computed corrections were saved for testing in that same routine.

The orbital prediction routine, already modified slightly in various stages of this thesis, was then further adapted to read in a file of along-track acceleration corrections and to add these corrections onto the computed along-track acceleration due to drag. For each arc tested, the computed acceleration corrections were output and stored at thirty second intervals; this being the integration step length employed in the orbit determination process. In addition, the along-track acceleration due to drag was output and stored both for the initial converged orbit and for that where the drag scale factors had been set to a mean value. This enabled the computation of $\Delta\ddot{T}_{\text{expected}}$ which was used to check that the adapted orbit program actually worked by adding the expected corrections back on to the

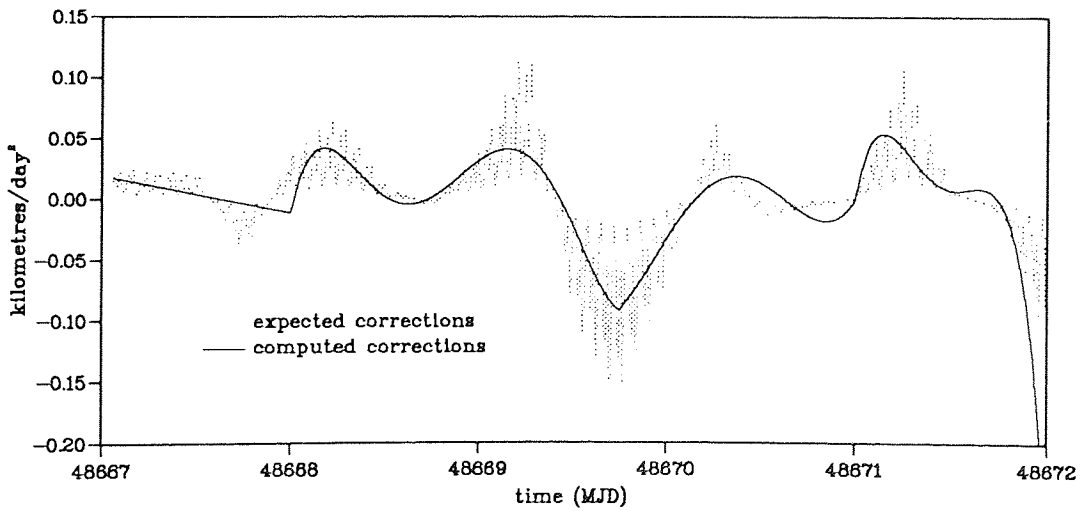
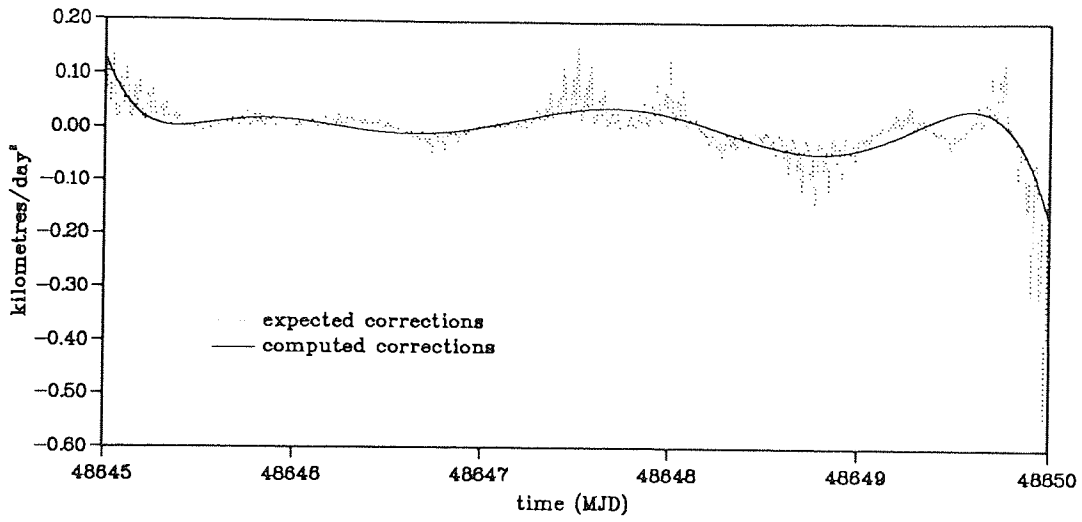
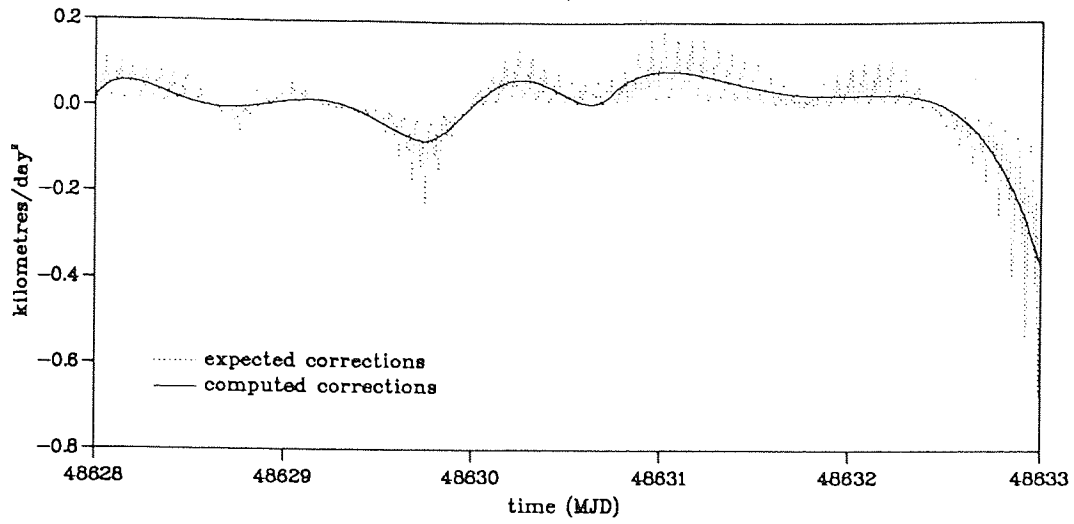


Figure 7.5: Expected corrections, using area tables, with computed solution, for the three SPOT-2 arcs.

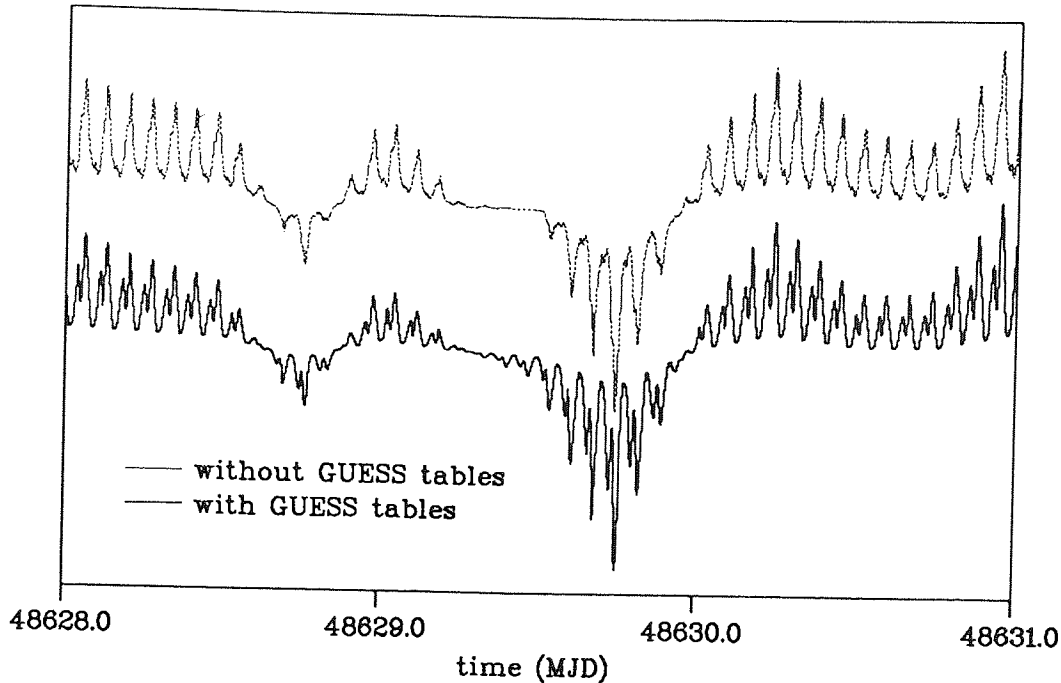


Figure 7.6: Comparison of expected corrections obtained with and without the use of GUESS tables from the arc starting on MJD 48628.

orbit produced from the average \overline{C}_D scale factor.

For the first arc (MJD 48628 to MJD 48633) the outliers were rejected using an 11th order polynomial and a rejection level of 60 metres which resulted in five of the initial set of 526 points being excluded after just two iterations (and no further points when a larger number of iterations was used). After averaging, taking the mean motion of SPOT-2 to be 14.208377 revolutions per day, there were just 71 data points. The solution curve chosen as best fitting these data was made up of three polynomials: one of order seven, valid for the first 1.75 days, then two of order six, with the connecting point 3.75 days after the start epoch. This particular combination of polynomials was chosen after considering several variations. It was found to produce a curve which more closely matched the data (see Figure 7.4) than any other of greater simplicity (i.e. lower order polynomials, or a lesser number of polynomials).

For the second arc (MJD 48645 to MJD 48650), the rejection polynomial was of the 10th order and the rejection level was just 20 metres. There were eight points rejected from an initial 526 and, averaging over the same period again resulted in 71 smoothed values. For this second arc, the rejection polynomial was found also found to provide a satisfactory solution curve, with correspondingly

adequate along-track acceleration corrections, $\Delta\ddot{x}_{\text{solution}}$.

For the third arc (MJD 48667 to MJD 48672), the rejection polynomial was of the 12th order and the rejection level was just 7 metres. There were thirteen points rejected from an initial 573 and, averaging over the same period resulted in 73 smoothed values. For this third arc, the solution curve was made up of four polynomials: one of order five, valid for the first day, then two of order seven, ending 3.75 days and 4.0 days, respectively, after the start epoch and finally one of order six.

The final RMS of fit of the initial SPOT-2 orbits, together with subsequent variations and confirmatory tests using both expected values and solutions for the along-track acceleration corrections, are given in Table 7.2. It should be emphasized that the addition of along-track corrections occurs *after* scaling so the *corrections themselves remain unaltered by the re-convergence process*. Considering

Arc dates (MJD)	RMS of fit (millimetres/second)		
	48628 – 48633	48645 – 48650	48667 – 48672
converged orbit	1.82	1.76	1.14
replacing C_D with \overline{C}_D	1092.31	894.36	345.83
then adding $\Delta\ddot{T}_{\text{expected}}$	1.85	2.20	13.16
then re-converging	1.82	1.75	1.14
replacing C_D with \overline{C}_D			
then adding $\Delta\ddot{T}_{\text{solution}}$	25.81	18.53	8.98
then re-converging	2.20	1.74	1.11

Table 7.2: RMS of orbital fits for SPOT-2 (millimetres/second).

this table, the first point to note is the RMS for the orbit where C_D was replaced with \overline{C}_D which indicates just how much the drag scale factors absorb density and other variations in an orbit. This table also indicates that the addition of $\Delta\ddot{T}_{\text{expected}}$ to the force model produces an orbital solution which is very close to the original converged solution, confirming again that the amended program works and, further, the validity of this along-track correction procedure. In addition, it is clear from the table that the level of fit obtained in the original converged solution cannot quite be matched by adding on the simple curve approximation for the along-track acceleration corrections, $\Delta\ddot{T}_{\text{solution}}$. Rather, it proved necessary to

re-converge the orbit, effectively solving for C_D again, to produce similar RMS values. This re-convergence process does not affect the along-track acceleration corrections, since these are added *after* scaling the uncorrected accelerations by C_D . It is for this reason that Table 7.4 gives differing values for the re-converged RMS of fit when differing along-track acceleration corrections are employed (one set is scaled for the height variation between ERS-1 and SPOT-2). Otherwise, if drag-scaling occurred after the corrections had been added, it might be expected that all re-converged orbits would give the same RMS of fit.

Figure 7.7 illustrates that adding on the along-track corrections resulted in a diminished variation in the drag scale factors over the long-arc period. This may imply that the variation in the error in the modelled aerodynamic resistance force is removable, with the GUESS tables providing more accurate areas and the along-track corrections absorbing the varying errors in the density model (known to be significant [Klinkrad *et al.*, 1990]). Thus, this approach may prove useful in separating the error components even if it did not directly benefit ERS-1 orbits.

7.4 Employing these SPOT-2 corrections within ERS-1 orbits

The analysis of SPOT-2 in the previous section has verified that the recovered along-track acceleration correction is a fair representation of the required acceleration. This section utilises the derived acceleration time series to improve along-track modelling of ERS-1. The same three five-day long-arcs were analysed for ERS-1, Table 7.3 summarizing the SLR data employed in converging these

Arc Dates (MJD)	Data included		
	stations	passes	observations
48628.0 – 48633.0	11	21	276
48645.0 – 48650.0	8	19	236
48667.0 – 48672.0	7	27	507

Table 7.3: Summary of contributing stations, passes and SLR measurements from ERS-1.

arcs. The first two arcs with epochs MJD 48628 and MJD 48645 were resolved

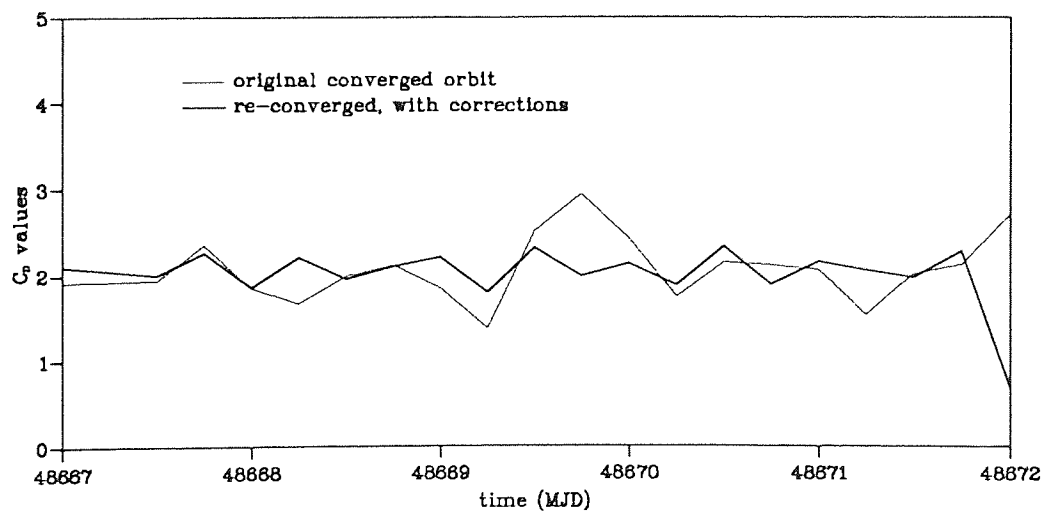
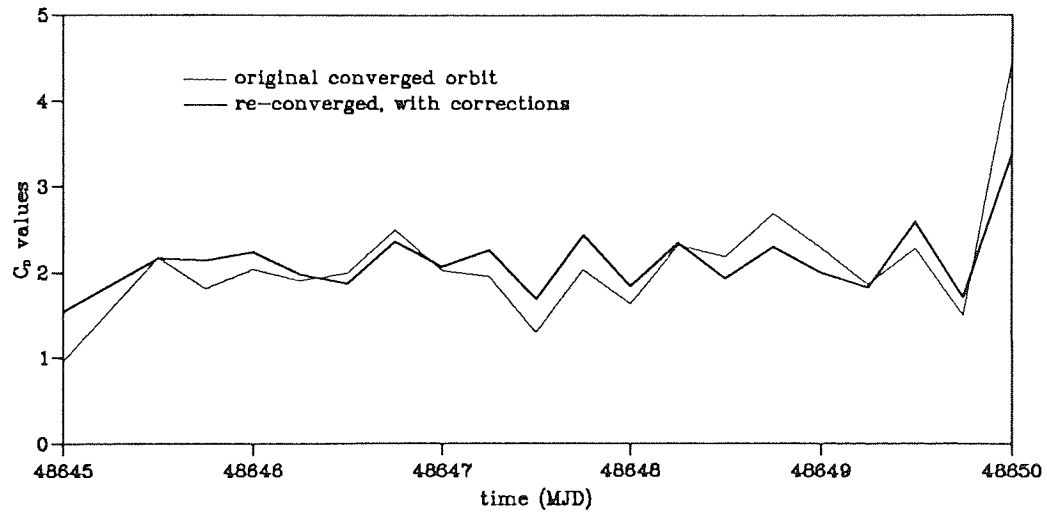
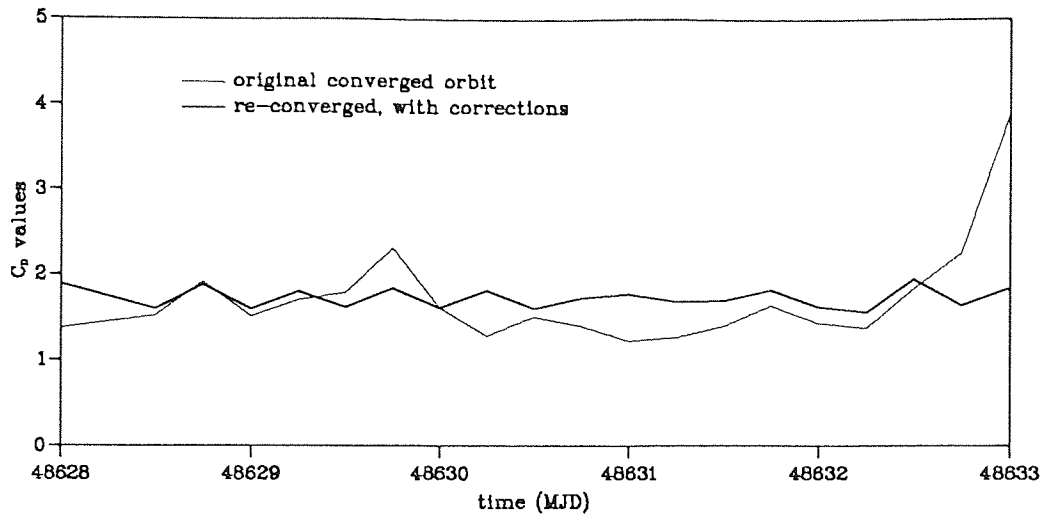


Figure 7.7: C_D values for SPOT-2.

with both twelve and twenty-four hour separations for the nodal drag scale factors (thus resulting in six and eleven such factors, respectively). The third arc, start epoch MJD 48667, was determined with the twenty-four hour separation only. This was because the correlations between solution parameters indicated that the twelve-hour separation over-parameterised the model; effectively leading to a non-determinable solution set. Other than this difference in the number of drag scale factors employed, the model components used for the ERS-1 precise orbit determinations were exactly the same as for SPOT-2; namely the GEM-T3A gravity field, the MSIS83 atmosphere and GUESS surface force tables.

Again analogously to the treatment of SPOT-2, each arc was first converged on its own, then re-converged with unscaled and scaled SPOT-2 along-track acceleration corrections respectively. The scale term employed was the ratio of the mean modelled (MSIS83) atmospheric densities (ρ),

$$\frac{\bar{\rho}_{\text{ERS-1}}}{\bar{\rho}_{\text{SPOT-2}}}$$

which approximates the density height variation between the two satellites. One alternative to scaling in this manner may be to solve for an explicit scaling term in the determination process [Ehlers and Moore, 1993].

The RMS of fit of the several solutions for ERS-1 are displayed in Table 7.4. It is important to emphasize that these values have been obtained using satellite laser

Arc dates (MJD)	RMS of fit (centimetres)				
	48628 – 48633		48645 – 48650		48667 – 48672
scale factors solved for	6	11	6	11	6
converged orbit	87.28	39.65	73.09	20.69	38.88
replacing C_D with \bar{C}_D then adding $\Delta\ddot{T}_{\text{solution}}$ then re-converging	55.02	34.20	40.88	20.68	35.42
the same, after first scaling $\Delta\ddot{T}_{\text{solution}}$ by $\bar{\rho}_{\text{ERS-1}}/\bar{\rho}_{\text{SPOT-2}}$	43.83	34.81	27.25	20.81	28.19

Table 7.4: RMS of orbital fits for ERS-1 (centimetres), using only SLR tracking data in the convergence process.

range (SLR) data *only* and thus may suffer from geographical bias. Indeed, the

main reason why the eleven drag scale factors could not be solved for on the third arc, despite this arc possessing nearly twice as many observations as either of the other two, was due to the smaller number of stations (and hence the *greater* bias). Considering Table 7.4, it appears that where a daily drag-scale factor is solved for, the correction procedure works well — indeed, rather better than might have been anticipated. This is evidenced by the much diminished RMS values obtained where scaled along-track corrections are added to the converged orbit. That the procedure does not give such vast benefits for the solutions where half-daily drag scale factors are employed, may be attributed to the fact that the RMS involved are already much lower.

However, it does not do to put much faith solely in the diminished RMS since this is an automatic consequence of applying the least-squares differential correction procedure to SLR data and increasing the number of solution parameters. Indeed, a decrease in the RMS of fit, given the limited geographical spread of the laser data is a poor indicator of radial accuracy, over-parameterisation leading to biased orbits with unrealistic fits over the laser sites at the expense of orbital accuracy elsewhere. A test of radial accuracy may be provided by the use of ERS-1 altimeter data, both as a height measurement relative to some reference ellipsoid and as a crossover difference. The latter provide the more exact measure, given reliance of altimetric heights on the accuracy of the geoid adopted. However, for ERS-1 in its three day repeat cycle, the number of useful crossovers is small, as they occur predominantly over land or ice at high latitudes.

Altimetry for the three arcs was acquired from NOAA where geophysical corrections were added to the ERS-1 fast delivery data supplied by ESA. The altimeter measurements were corrected for ionospheric and tropospheric refraction, instrumental effects and solid earth and ocean tides. An altimeter bias of -70 cm was added relative to an earth radius of 6378.1363 km and flattening f where $1/f = 298.257$. The geoid heights were derived from the JGM-1 gravity field complete to degree and order 70. JGM-1 is near state-of-the-art and is to be preferred, in general, to the previous GEM-T series. However, it was not available during the SPOT-2 analyses, hence the adoption of GEM-T3A for dynamic modelling. Sea-surface topography to degree and order 15 was taken from the GEM-T3 Geosat solution. An altimetric height database relative to the adopted reference ellipsoid

was achieved by incorporation of the geoid height, sea-surface topography height and altimeter bias into the corrected measurement. To reduce this dataset, 15 second normal points were then evaluated. Both altimeter and crossover data were added to the laser data to assess the orbits.

The results of fitting both crossover and altimeter data to the ERS-1 orbits are presented in Table 7.5, along with the RMS of the same fits when the original orbit

Arc dates (MJD)	RMS of fit (centimetres)				
	48628 – 48633		48645 – 48650		48667 – 48672
scale factors solved for	6	11	6	11	6
using only SLR data					
fit of altimetry	73.5	102.5	80.8	67.6	52.5
fit of crossovers	62.8	102.9	97.2	79.0	45.6
also including crossovers					
fit of altimetry	78.5	—	77.0	—	52.2
fit of crossovers	61.7	—	83.4	—	42.1

Table 7.5: RMS of fit of altimetry and crossover data for ERS-1 (centimetres) for the original converged orbits.

was converged with crossover data as part of data contributing to the solution. The first thing to note is the apparent ambiguity of the results. For instance, using SLR data only, the first arc is poorer radially with half-daily drag scale factors than with daily ones. However, the converse is true for the second arc — and no conclusion possible at all for the third. Further, the use of crossover data in the solution *obviously* improves the RMS of fit of crossover data, but has a similar effect on the fit of the altimetry only for the second and third arcs.

In conclusion, several points emerge from this study. Firstly, it is clear from the above results that SPOT-2 derived along-track acceleration corrections can be used to improve sparsely tracked ERS-1 precise orbits. The ERS-1 results may be improved by scaling explicitly for density variations and also by including direct altimetric or derived crossover data in the solution process. It is suggested that the lack of a one-cycle-per-revolution signal in the derived curve may be overcome by using an additional term such as is given in Equation 7.2, solving for \bar{S} and \bar{C} typically once over a six day long-arc. Further, it may prove advantageous to

solve for the density height scaling factor in solution. As a final point, the method itself may prove amenable to improvement also. Thus, for instance, the rejection and smoothing procedure may be automated and the curve fitting process may be similarly adapted by using quartic or higher order splines (cubic splines having been attempted with no success). Given the vast improvement to initial RMS of fit, with no degradation of radial accuracy, it would seem that this method was worthy of such further study.

Chapter 8

Conclusions

8.1 Modifications to the SATAN-A suite

This thesis contains three main attempts to refine ERS-1 long-arc orbits as well as additional modifications to the SATAN-A suite to facilitate these attempts. The alterations to the SATAN-A suite may be summarized as follows. First, the solution of drag scale factors was altered from the previous drag and drag-rate (C_D and \dot{C}_D) or step function options to a single saw-tooth method (incidentally retaining the drag and drag-rate option, given two nodal points). In the saw-tooth method, each drag scale factor is a node, connected to the two adjacent nodes by straight lines. This enables the scale factors to be defined continuously, thus facilitating both the dual-crossover and along-track acceleration refinement methods of Chapters 5 and 7 respectively. Indeed, the use of discontinuous drag scale factors had previously been seen to adversely affect both methods of refinement due to the production of finite discontinuities in the residuals. These jumps compromised the solution of the harmonic coefficients of Equation 5.11 and totally precluded the matching of the second derivative (of the derived solution curve) to the expected along-track correction curve as described in Section 7.3.

Secondly, an alternative model for both the aerodynamic resistance and direct solar radiation pressure forces was introduced. This was based on momentum exchange considerations (see also Klinkrad *et al.* [1990] and Sowter [1989]) rather than the simple deceleration approach previously employed. In order to adopt this model the GUESS area generating software was devised; the results of which could either be used to produce a total effective cross-sectional area (for use in the

original force models) or be employed with the momentum exchange approach. the application of area tables also constituted the first attempt to refine ERS-1 long-arc orbits.

Thirdly, the SATAN-A software was modified to include DORIS Doppler data which required an additional section in the correction program. Lastly, the fourth major alteration allowed the addition of explicit along-track acceleration corrections to be added during the prediction stage of the predictor-corrector process, within the skin-force subroutines. Together, these last two adaptations permitted the third attempt at ERS-1 long-arc precise orbit determination refinements to be made and tested.

8.2 A re-iteration of the main results obtained

The GUESS software was confirmed on several convex solids with ideal results, though such levels of accuracy were not expected with the more complex satellite geometries. However, the software did provide area tables for both ERS-1 and SPOT-2 which reflected the expected variations with sun position and viewing angle. Further, when employed in precise orbit determinations, these tables resulted in lower values of the RMS of fit in almost all long-arcs considered. Despite this, it is unclear exactly how accurate the tables are.

Though the variation in the drag scale factors was less with the GUESS tables for SPOT-2, this was not the case for ERS-1. However, the sparsity of the laser data for ERS-1 means that the change in pattern seen in the SPOT-2 scale factors was not really expected to be seen in those of ERS-1. This is because the drag scale factors are much more responsive to the positioning of the nodal points for ERS-1 where the data can be best described as occurring in discrete clumps. While the products $C_D A_D$ (for drag) and $C_R A_R$ (for direct solar radiation pressure) appear to be better determined with GUESS tables than without, it is still unrealistic to hope that the scale factors themselves (i.e. C_D and C_R) no longer absorb any errors due to mismodelling of the satellite areas. However, such errors should be small in relation to other errors e.g. those due to mismodelled density.

Regardless of these considerations, it does seem from the results of the use of GUESS tables that some form of satellite area tables can effectively reduce

the orbital RMS in long-arcs. So, one should either employ any existing satellite specific tables (e.g. those for Seasat and TOPEX/Poseidon) or generate tables by some other manner, for example using the GUESS software described in Chapter 3 (as has been done for ERS-1 and SPOT-2).

Considering next the dual-crossover simulation of Chapter 5, it was shown that by equating the radial residuals with the radial error, which may be expressed as a harmonic series plus a number of secular terms (see Equation 5.11), the coefficients of such an expression could be successfully solved for. Further, the resultant solutions could be substituted back into this same equation to provide corrections to the satellite ephemeris in the radial direction. The simulation showed that such a process effectively improved orbits of both ERS-1 and TOPEX/Poseidon. Indeed, the RMS of the ERS-1 orbits was reduced to below the initial level of that for TOPEX/Poseidon. It was also seen that by considering the standard errors arising from the covariance matrix, terms which weakened the solution (for instance by being heavily correlated with other terms) could be identified and suppressed.

The results of converging several SPOT-2 long-arcs in Chapter 6 indicated that the modifications for the inclusion of DORIS Doppler data were effective, at least in the case of this satellite. This chapter further confirmed that the GUESS software was beneficial to more than one satellite (as measured by the reduced RMS of the several converged long-arcs).

Given the capability of the SATAN-A suite to process this data type (the purpose of Chapter 6 being to provide just such a capability), it was then possible to apply the along-track acceleration correction method of Chapter 7, which method also proved successful in improving ERS-1 orbital determinations. The level of improvement attained from this method was seen to be governed largely by the number of solution parameters sought for ERS-1 and the presence or lack of altimetry in the solution. Thus, given the sparse laser tracking for the ERS-1 orbits, where half-daily drag scale factors were sought, the initial RMS was lower, and the improvement with along-track acceleration correction less. However, it was found (from the altimeter residuals) that in fact solving for daily scale factors was more realistic — and even then the orbit was probably biased towards the

laser stations. It seems clear from the results of using DORIS Doppler range-rate data that if PRARE had worked, ERS-1 orbits would not have required as much refinement as they undoubtedly have.

8.3 Directions of future work

Each of the attempts to refine ERS-1 orbits has been shown to work, either in practice or in simulation. However, taking each of them in turn, several suggestions for further modifications may be made.

First considering the GUESS software, it may prove necessary to employ three angles for the direct solar radiation pressure tables (as is already the case for the aerodynamic resistance force). This is due to the fact that the solar panels do not always point as closely to the sun as is possible, but rather may be slightly off-pointing. Reasons for this variation include pre-determined mechanical movement, only approximating the a sun-pointing position, and decisions to use an alternative scheme (as with TOPEX/Poseidon where the complex pattern of yaw and solar panel rotation was designed to maximise battery life). In order to employ new tables the orbital subroutines will need changing, as will some of the GUESS routines. However, the main GUESS program will be unaltered since it already accepts three varying angles. For the SATAN-A suite, the practical application will be possible with the “sun-pointing” angle determined from the equations of motion of the solar panels (such equations must exist where the panels are moving in a preset manner). It may also be possible to incorporate a thermal radiation element, to allow for forces arising from temperature differences, particularly those experienced by the solar array.

Considering next the dual-crossover simulation, the first necessity will be to test this procedure with real data. Such studies are in fact already underway and preliminary results are mixed. Some indicate similar levels of achievement, while others find that the improvement is not as marked as in the simulation [Carnochan *et al.*, [1993]. Further, there is potential for solving for more of the ERS-1 frequencies below the limit of two-cycles-per-revolution. Indeed, by using the covariance matrix for a constraint, rather than the elementary triangular procedure adopted in the simulation, and by considering a full thirty-five day dataset

(the ground-track repeat time), it is hoped that the high standard errors arising from the closeness of adjacent frequencies will be overcome. Further, the increasing body of work on dual-crossovers (for example Carnochan *et al.* [1993] and le Traon *et al.* [1993]) indicates yet other avenues of investigation — for instance, the possibility of their inclusion as part of the *dynamic* orbit determination process is also being investigated. It is hoped that such inclusion will improve sparse orbits just as altimetry was shown to by Rothwell [1989]. It should also be emphasized that the temporal problems of dual crossovers (i.e. problems arising from large time differences between intersecting groundtracks) have not been considered in the simulation, a fact which will have to be considered in dealing with real data. At the very least some restriction will need to be placed on the time difference between the ascending and descending arc. Similarly, any future work with real dual-crossover data ought to investigate the reasons behind the improvement obtained by including single-crossovers in the solution; the geographical expansion of the dataset not necessarily providing the only explanation.

Finally, the along-track acceleration correction method may be adapted so that the scaling factor is solved for, rather than given as was the case above — the ratio of the experienced average densities. In addition, the method of fitting the rejection polynomial may be automated by using an algorithm which determines the polynomial at which any further increase in order does not produce a sufficiently large decrease in the RMS of fit to merit its use. This automation could also include the choice of the rejection level (say three sample standard deviations — a common statistical measure of an outlier [Mood *et al.*, 1982]) so that a sufficient number of outlying points be rejected without distorting the remaining dataset and without allowing outlying points to remain. In addition to these considerations, the method of fitting the solution curve ideally requires less subjectivity. This could either be attained by attempting to automate the current approach — quite difficult given the number of options (how many polynomials to use and of what order and where to splice them together) or using some variation of the spline technique. If the latter was adopted, the spline functions would need to be quartic or quintic as the second differential of the cubic spline fit provides a ragged curve, thereby providing sudden jumps in the magnitude of the computed acceleration corrections. It should not be forgotten, that however much

the method is improved its final usefulness is limited by the availability of the SPOT-2 tracking data.

In conclusion though, each method has been shown to offer a successful way to refine ERS-1 orbits, though they all offer scope for further improvement through some additional modifications.

Bibliography

Aksnes, K. (1976) Short-Period and Long-Period Perturbations of a Spherical Satellite due to Direct Solar Radiation. *Celestial Mechanics*, vol.13, no.1, pp.89 – 104.

Astronomical Almanac, The. (1987) Edited jointly by the U.S. Naval Observatory and the Royal Greenwich Observatory. H.M.S.O./U.S. Government Printing Office, London/Washington, U.S.A.

Barlier, F., Berger, C., Falin, J. L., Kockarts, G. and Thuillier, G. (1978) A Thermospheric Model based on Satellite Drag Data. *Annales Geophysique*, vol.34, no.1, pp.9 – 24.

Bomford, G. (1980) *Geodesy*. Clarendon Press, Oxford.

Born, G. H., Tapley, B. D. and Santee, M. L. (1986) Orbit Determination using Dual Crossing Arc Altimetry. *Acta. Astronautica*, vol.13, no.4, pp.157 – 163.

Borowitz, S. and Beiser, A. (1967) *Essentials of Physics*. Addison-Wesley, Reading, Massachusetts, U.S.A.

Boucher, C. (1978) Relativistic Correction to Satellite Doppler Observation. In the proceedings of the meeting IAG-SSG4.45, *The Mathematical Structure of the Gravity Field*. Lagonissi, Greece.

Brouwer, D. and Clemence, G. M. (1961) *Methods of Celestial Mechanics*. Academic Press, London.

Burden, R. L. and Faires, J. D. (1989) *Numerical Analysis*. PWS-Kent, Boston, Massachusetts, U.S.A.

Carnochan, S., Moore, P., Ehlers., S., Lam, C. and Woodworth, P. (1993) *Improvement of Radial Positioning of ERS-1 through Dual Crossover Analysis with TOPEX/Poseidon*. Unpublished paper given at the second ERS-1 Symposium: Space at the Service of our Environment, 11 – 14/10/93, Hamburg, Germany.

Chatfield, C. and Collins, J. (1986) *Introduction to Multivariate Analysis*. Chapman and Hall, London.

Colombo, O. L. (1984) *Altimetry, Orbits and Ocean Tides*. NASA technical memorandum number 86180, greenbelt, Maryland, U.S.A.

Cook, G. E. (1965) Satellite Drag Coefficients. *Planetary and Space Science*, vol.13, no.10, pp.929 – 946.

- Cook, G. E. (1966) Perturbations of Near-Circular Orbits by the Earth's Gravitational Potential. *Planetary and Space Science*, vol.14, no.5, pp.433 – 444.
- Deleuze, M. and Nouël, F. (1992) *Improvement of the ERS-1 orbit using DORIS data on SPOT2*. Report produced for ESA/ESRIN by C.N.E.S., Toulouse, France.
- Dorrer, M. (1991) DORIS/SPOT2 Status. In *International DORIS Orbit Computation Workshop: Minutes*, C.N.E.S., Toulouse, France.
- Ehlers, S. and Moore, P. (1993) *Aerodynamic Force refinement to ERS-1 Orbits using Along-Track Accelerations from DORIS on SPOT2*, submitted for publication.
- Gooding, R. H. (1981) A Second-Order Satellite Orbit Theory, with Compact Results in Cylindrical Coordinates. *Phil. Trans. Royal Society*, vol.A299, no.1451, pp.425 – 474.
- Hedin, A. E. (1983) A Revised Thermospheric Model based on Mass Spectrometer and Incoherent Scatter Data: MSIS-83. *Journal of Geophysical Research*, vol.88, no.A12, pp.10170 – 10188.
- Hedin, A. E. (1987) MSIS-86 Thermospheric Model. *Journal of Geophysical Research*, vol.92, no.A3, pp.4649 – 4662.
- Herrero, F. A. (1985) The Lateral Surface Drag Coefficient of Cylindrical Spacecraft in a Rarefied Finite Temperature Atmosphere. *American Institute of Aeronautics and Astronautics*, vol.23, no.6, pp.862 – 867.
- Jacchia, L. G. (1972) Atmospheric Models in the Region from 110 to 2000 km. Pages 227 – 328 of *COSPAR International Reference Atmosphere 1972*. Akademie-Verlag, Berlin, West Germany.
- Kaula, W. M. (1966) *Theory of Satellite Geodesy: Applications of Satellites to Geodesy*. Blaisdell Publishing Company, Waltham, Massachusetts, U.S.A.
- King-Hele, D. G. (1987) *Satellite Orbits in an Atmosphere: Theory and Applications*. Blackie, Glasgow.
- Klinkrad, H., Koeck, Ch. and Renard, P. (1990) *Precise Satellite Skin Force Modelling by Means of Monte-Carlo Ray Tracing*. Draft of paper No. MP.1.2.5 given at COSPAR XXVIII, 1990, The Hague, The Netherlands.
- Lambeck, K. (1980) *The Earth's Variable Rotation: Geophysical Causes and Consequences*. Cambridge University Press, London.
- Lerch, F. J., Nerem, R. S., Putney, B. H., Felsentreger, T. L., Sanchez, B. V., Klosko, S. M., Patel, G. B., Williamson, R. G., Chinn, D. S., Chan, J. C., Rachlin, K. E., Chandler, N. L., McCarthy, J. J., Marshall, J. A., Luthcke, S. B., Pavlis, D. W., Robbins, J. W., Kapoor, S. and Pavlis, E. C. (1992) *Geopotential Models of the Earth from Satellite Tracking, Altimeter and Surface Gravity Observations: GEM-T3 and GEM-T3S*. NASA/GSFC technical report number 104555, Greenbelt, Maryland, U.S.A.

- Marshall, J. A., Rosborough, G. and Putney, B.** (1991) *Radiation Force Modelling for Satellite Precision Orbit Determination*. Unpublished paper given at the American Geophysical Union Spring Meeting, 30/05/91, Baltimore, Maryland, U.S.A.
- Marshall, J. A., Luthcke, S. B., Antreasian, P. G. and Rosborough, G. W.** (1992) *Modelling Radiation Forces Acting on TOPEX/Poseidon for Precision Orbit Determination*. NASA/GSFC technical report number 104564, Greenbelt, Maryland, U.S.A.
- Mood, A. M., Graybill, F. A. and Boes, D. C.** (1982) *Introduction to the Theory of Statistics*. McGraw Hill, London.
- Moore, P. and Ehlers, S.** (1993) Orbital Refinement of ERS-1 using Dual Crossover Arc techniques with TOPEX/Poseidon. *Manuscripta Geodaetica*, vol.18, pp.249 – 262.
- Moore, P. and Gray, R. D.** (1991) Global Non-Dynamic Improvement of Radial Positioning for Altimeter Satellites. *Advances in Space Research*, vol.11, no.6, pp.(6)130 – (6)130.
- Moore, P. and Rothwell, D. A.** (1990) A Study of Gravitational and Non-Gravitational Modelling Errors in Cross-Over Differences. *Manuscripta Geodaetica*, vol.15, pp.187 – 206.
- Moore, P. and Sowter, A.** (1991) Application of a Satellite Aerodynamics Model Based on Normal and Tangential Momentum Accommodation Coefficients. *Planetary and Space Science*, vol.39, no.10, pp.1405 – 1419.
- Nerem, S., Lerch, F. J., Williamson, R. G., Patel, G. B., Klosko, S. M., Chan, J. C. and Rodell, J. T.** (1991) An Evaluation of the DORIS Tracking System on SPOT2. In *International DORIS Orbit Computation Workshop: Minutes*, C.N.E.S., Toulouse, France.
- Nouël, F.** (1991) ed. *International DORIS Orbit Computation Workshop: Minutes*. C.N.E.S., Toulouse, France.
- Nouël, F., Berthias, J. P., Broca, P., Comps, A., Deleuze, M., Guitart, A., Jayles, C., Laudet, Ph., Pierret, C., Pradines, D., Taburian, D. and Valorge, C.** (1991) Orbit Determination with the DORIS/SPOT2 System — Preparing TOPEX: Evaluations with the DORIS/SPOT2 Data. In *International DORIS Orbit Computation Workshop: Minutes*, C.N.E.S., Toulouse, France.
- Nuth, V. J., Ries, J. C., Yuan, D. N., Shum, C. K. and Tapley, B. D.** (1991) *Modelling of Atmospheric Parameters for Precision Orbit Determination*. Unpublished paper given at the American Geophysical Union Spring Meeting, 28 – 31/05/91, Baltimore, Maryland, U.S.A.
- Pieper, B.** (1988) *ERS-1 Surface Properties*. ESA document number ER-TN-ESA-GS-0019. ESA/ESTEC, Noorwdwijk, The Netherlands.

Rapley, C. G., Baker, S. G., Birkett, C. M., Laxon, S. W., Ridley, J. K., Scott, R. F. and Strawbridge, F. (1992) ERS-1 Altimetry of Inland Water and Land. Pages 539 – 542 of *Proceedings of the First ERS-1 Symposium*. Cannes, France.

Rapp, R. H., Wang, Y. M. and Pavlis, N. K. (1991) *The Ohio State 1991 Geopotential and Sea Surface Topography by Harmonic Coefficient Model*. report 410, Department of Geodetic Science and Surveying, The Ohio State University, Columbus, Ohio, U.S.A.

Renard, P. (1990) *Final Report on Satellite Skin-Force Modelling*. MATRA technical report number S374/NT/100/89 produced under ESA contract number 7850/88/HGE-I, Toulouse, France.

Ridgway, J. R., Klosko, S. M. and Koblinsky, C. (1990) *Analysis of Seasat Residuals to Extract Atmospheric Drag Information*. Unpublished paper given at the Fall American Geophysical Union Meeting, 06/12/90, San Francisco, California, U.S.A.

Ries, J. C., Shum, C. K. and Tapley, B. D. (1991) DORIS Tracking Data Analysis. In *International DORIS Orbit Computation Workshop: Minutes*, C.N.E.S., Toulouse, France.

Ries, J. C. (1992) *Agenda of the First Meeting of IAG Special Study Group 2.130: Surface Force Modelling Effects on Satellite Orbits*. Unpublished agenda from the World Space Congress, 31/08/92, Washington D.C., U.S.A.

Rosborough, G. W. and Tapley, B. D. (1987) Radial, Transverse and Normal Satellite Position Perturbations due to the Geopotential. *Celestial Mechanics*, vol.40, no.1, pp.409 – 421.

Rothwell, D. A. (1989) *Precise Orbit Determination and Analysis from Satellite Altimetry and Laser Ranging*. Unpublished PhD. Thesis, The University of Aston in Birmingham.

Rothwell, D. A. and Moore, P. (1991) Atmospheric Density Parameters from Seasat Laser Ranging. *Advances in Space Research*, vol.11, no.6, pp.(6)131 – (6)136.

Rowlands, D. (1981) *The Adjustment of Seasat Altimeter Data and a Global Basis for Geoid and Sea-Surface Height Determination*. Report number 325, Department of Geodetic Science and Surveying, The Ohio State University, Columbus, Ohio, U.S.A.

Sandwell, D. T., Milbert, D. G. and Douglas, B. C. (1986) Global Non-Dynamic Orbit Improvement for Altimetric Satellites. *Journal of Geophysical Research*, vol.91, no.B9, pp.9447 – 9451.

Schaaf, S. A. and Chambré, P. L. (1958) Flow of Rarefied Gases. Pages 687 – 736 of *Fundamentals of Gas Dynamics*, edited by Howard W. Emmons. Oxford University Press, London.

- Schamberg, R.** (1959) *A New Analytical Representation of Surface Interactions for Hyperthermal Free Molecule Flow with Application to Neutral-Particle Drag Estimates of Satellites*. The RAND Corporation technical report number RM-2313, Santa Monica, California, U.S.A.
- Schidlovskiy, V. P.** (1976) *Introduction to the Dynamics of Rarefied Gases*. American Elsevier, New York, U.S.A.
- Schwiderski, E. W.** (1978) *Global Ocean Tides, Part I: A Detailed Hydrodynamical Interpolation Model*. NWSC/DL TR-3866.
- Shum, C. K., Yuan, D. N., Ries, J. C., Smith, J. C., Schutz, B. E. and Tapley, B. D.** (1990) Precision Orbit Determination for the Geosat Exact Repeat Mission. *Journal of Geophysical Research*, vol.95, no.C3, pp.2887 – 2898.
- Sernesi, E.** (1993) *Linear Algebra*, translated by J. Montaldi. Chapman and Hall, London.
- Sinclair, A. T. and Appleby, G. M.** (1986) *SATAN — Programs for the Determination and Analysis of Satellite Orbits from SLR data*. SLR technical note 9, RGO, Herstmonceaux.
- Smart, W. M.** (1953) *Celestial Mechanics*. John Wiley and Sons, Inc., New York, U.S.A.
- Sowter, A.** (1989) *Drag Coefficients with Applications to Satellite Orbits*. Unpublished PhD. Thesis, The University of Aston in Birmingham.
- Todhunter, I. and Leathem, J. G.** (1903) *Spherical Trigonometry*. MacMillan and Co., Ltd., London.
- le Traon, P. Y., Gaspar, P. and Makhmara, H.** (1993) *Using TOPEX/Poseidon Data to Enhance ERS-1 Orbit*. Unpublished paper given at the 18th EGS meeting, 3 – 7/05/93, Wiesbaden, Germany.
- Vonder Haar, T. H. and Suomi, V. E.** (1971) Measurements of the Earth's Radiation Budget from Satellites during a Five Year Period. *Journal of Atmospheric Science*, vol.28, no.3, pp.305 – 314.
- van der Wenden, E. F.** (1985) *De Geodyntabellen van de ERS-1 voor Luchtweerstand und Zonnestraling*. Unpublished paper, Ruimtevaarttechniek, Delft, The Netherlands.
- Wagner, C. A.** (1985) Radial Variations of a Satellite Orbit due to Geopotential Errors: Implications for Satellite Altimetry. *Journal of Geophysical Research*, vol.90, no.B4, pp.3027 – 3036.
- Wagner, C. and Melchioni, E.** (1989) On Using Precise Laser Ranges to Provide Vertical Control for Satellite Altimetric Surfaces. *Manuscripta Geodaetica*, vol.14, pp.305 – 338.
- Wnuk, E.** (1990) Precise Computation of Geopotential Orbit Perturbations for Very Low Earth Satellites. *Advances in Space Research*, vol.10, no.3–4, pp.(3)285 – (3)295.